UNIVERSITÀ DEGLI STUDI DI MILANO

DEPARTMENT OF PHARMACEUTICAL SCIENCES

PhD COURSE IN PHARMACEUTICAL CHEMISTRY

Design and Synthesis of New PET Radiotracers in Drug Discovery

TUTOR: Prof. Clelia DALLANOCE

PhD Thesis

Marco MASPERO

Matr. R12263

XXXIV cycle

PREFACE

In this manuscript, the scientific work that I've performed during my PhD studies is described. The foundations of this PhD project are found in an established collaboration between the Medicinal Chemistry laboratory of Prof. Clelia Dallanoce, University of Milan, Italy, and the Nuclear Medicine Unit of San Raffaele Hospital, Milan, Italy. In the recent years, the interest for new PET imaging agents able to early diagnose specific pathological conditions has grown, expanding therapeutic possibilities and improving patient care. Thus, these two research groups started collaborating on the synthesis of radiotracers targeting innovative biomarkers for the imaging of diseases for which suitable tracers are still missing. During the first two years of my PhD activity in Prof. Dallanoce's laboratory, I focused my attention on the fibrotic process, as it is the final pathological feature of many chronic diseases, and its early detection is an urgent clinical need that could improve the management of patients and increase the survival rate. Therefore, I selected a potential biomarker, and I've designed radiotracers for its specific targeting. Then, I was responsible for the "cold" section of the project, where I designed and synthesized various cold precursors, which were used for the preparation of radiotracers using different radiolabeling techniques. Together with these precursors, I synthesised the reference compounds, which are essential for the identification of the labelled products of the radiolabeling reactions. On the other hand, the "hot" section of the project, in which the radioactive nuclei are introduced in the structure of the precursors, was performed by the Nuclear Medicine Unit of San Raffaele Hospital, under the scientific supervision of Dr. Angela Coliva, to whom I'm most grateful. From the results of our research, two innovative radiolabeled compounds were selected and tested *in vitro* by the research group of Prof. Rosa Maria Moresco, University of Milano-Bicocca, Italy.

Besides its regular applications, the synergistic use of PET and other imaging techniques has recently drawn the interest of the scientific community, opening new perspectives for the treatment of diseases. With the desire to conduct leading-edge research in the imaging field, a collaboration with the University of Heidelberg was created, in particular with the research group of Molecular Imaging and Radiochemistry led by Prof. Dr. Carmen Wängler, Medical Faculty Mannheim, University of Heidelberg, Germany. One of their most recent researches is focused on the development of multimodal imaging agents that can be used *in vitro* and *in vivo* for the characterization of tumor cells, using multimodal imaging strategies and subsequently for patient-individualized endoradiotherapy. Thanks to this new collaboration, I could spend 9 months in Prof. Wängler's laboratories and, under her guidance together with the scientific support of Dr. Ralph Hübner, I could acquire specific knowledge in the radiochemical and biomolecular fields. As part of my PhD thesis, I prepared peptide-based dually labelled compounds suited for optical and PET imaging, which I radiolabeled with a beta-emitting radionuclide (^{68}Ga) for their application as PET tracers. I was also responsible for the evaluation of their chemical and optical properties, as well as for the *in vitro* evaluation of their binding affinities. This interdisciplinary, intense work represents a significant addition to my PhD research, the cherry on top of a three years long experience which gave me the instruments to become a more complete and independent scientist. I had the opportunity to follow many different projects not necessarily related to my PhD research (see the “side project” chapter at the end of the manuscript), I attempted to many scientific conferences, and I was able to write and publish many articles based on my research, which turned out to be essential gratifications for a not always easy work. The little everyday satisfactions helped me overcome the struggles and frustrations characterizing this job, and each passing day they draw me closer to the research world. A world in which I hope I can find my place in the future, and where I hope to make my own contribution.

I’m grateful for all the opportunities given to me by Prof. Dallanoce during these years, and I’ve appreciated the corrections and suggestions that I’ve received from Prof. Wängler and Prof. Moresco for the preparation of this thesis. I’m also indebted to the research groups of Milan and Mannheim, whose support helped me through these years of “sweat and tears”.

Marco Maspero

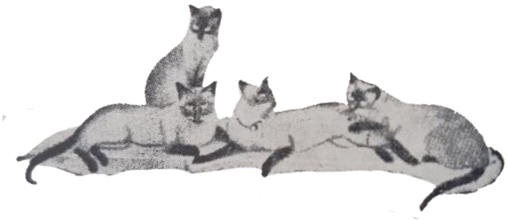

TABLE OF CONTENTS

CHAPTER ONE – Molecular imaging

CHAPTER TWO – Aim of the thesis

CHAPTER THREE – Experimental section

CHAPTER FOUR – Results and Discussion

CHAPTER FIVE – Conclusions and perspectives

CHAPTER SIX – Side project

BIBLIOGRAPHY

CHAPTER ONE

Molecular imaging

HISTORY OF IMAGING

Although the earliest known photograph to capture a human form was taken in Paris, France, in 1838 by Louis Daguerre, it was not until the 1895 that the first "medical" image was generated.[1, 2] It was the 8th of November of that year, German physic professor *Wilhelm Conrad Röntgen* was working with an evacuated glass Hittorf-Crookes's tube, studying cathode rays in his basement laboratory in Würzburg, Germany. In the dark of the room, he noticed that invisible rays were making a screen across the room glowing, and when he tried blocking the beam, he could see the bones of its own hand projected on the screen. Röntgen continued experimenting these unknown rays for several weeks, and on the 23rd of January 1896 he published a paper entitled "On a new kind of rays",[3] where he presented a 15-minute exposure of his wife's hand (*Anna Bertha Ludwig*) on a photographic plate (Figure 1.1). That picture represented the beginning of the studies on the X-rays, and with this the field of medical imaging was born.

Figure 1.1 X-ray taken by Röntgen of his wife's hand and presented to the local physics society of Würzburg on December 28, 1895.

Physicians quickly began to exploit the medical applications of x-rays, which at the time were simple projections through tissues showing dense structures such as bones or foreign objects.[4] Thanks to this, skeletal trauma could be assessed in ways that had not previously be possible, and radiographs became an established tool in medicine. The potentiality increased as the x-rays beam become more powerful,[5] and soon radiologists began giving patients radio-opaque barium as swallow or an enema, taking films as the barium traversed the gastrointestinal tract. This technique, known as "fluoroscopy", allowed the first diagnosis of cancers of the esophagus, stomach and bowel, as well as ulcers, diverticulitis and appendicitis.[6] In the following years, the field of diagnostic radiography matured. By the beginning of World War I most hospitals had an x-ray department, and x-rays diagnosis became routine exams.[7] Different applications of this technique were developed, from mammography, which is a dedicated system that takes high-resolution images of the breast, to angiography in the 1950s, where the arterial injection of a radiodense contrast agent like iodine allows to detect, e.g., vascular narrowing of the carotid artery (which could lead to a stroke) or narrowing of the coronary arteries (which could lead to a heart attack).[8]

The 50s were also characterized by the introduction of a novel approach in the arsenal of diagnostic imaging tests: nuclear medicine. This imaging field is founded upon the understanding of radioactivity, which was discovered by *Antoine Henri Becquerel* in Paris in 1896. Inspired by Röntgen's findings on the x-rays, Becquerel decided to investigate whether fluorescent materials might emit the same type of radiation when exposed to sunlight. He performed the experiment on the salt of uranium $K_2UO_2(SO_4)_2 \times H_2O$, which was able to impress a photographic plate with its crystal structure. He then intended to repeat his experiment, but that day the sky over Paris was too cloudy for producing an effective excitement of fluorescence, so he stored uranium salts and photographic plates together in a drawer. Surprisingly, Becquerel observed that the plates resulted impressed by the salts as in his previous experiments, even if both had been shielded from sunlight and kept in darkness. He attributed the phenomenon to a sort of radiation emitted by uranium, with shared characteristics to x-rays, which could be deflected by a magnetic field, therefore composed by charged particles.[9]

Becquerel's discovery of spontaneous radioactivity (which he initially called "*uranic rays*") inspired several scientists to further research on these new phenomena. At the time, *Marie Curie Sklodowska* was a physics and mathematics graduate of the University of Paris, looking for a topic for her doctoral thesis research. She was fascinated by the work of Becquerel, and selected the uranic rays as main subject of her research. Madame Curie systematically investigated the emissions of various elements and compounds using an electrometer based on the piezoelectric effect (Figure 1.2), discovering that thorium emits the same rays as uranium, and that the quantity of emitted rays was directly related to the quantity and atomic properties of the element independently of its chemical form.[10] Also, she found that some particular substances (particularly pitchblende, an uranium oxide ore) presented radioactive emission levels far more higher than what was expected from their uranium content. Therefore, with her husband Pierre, they tried to extract a new element from the pitchblende ore, which should have been more "active" than uranium. In the publication of their results "*Sur une nouvelle substance fortement radio-active contenue dans la pechblende*",[11] it was coined the term *radioactivity*, and it was presented the discovery of the new element polonium (named for Marie's native country, Poland). Three months following this publication, Marie and Pierre Curie managed to isolate another radioactive element, 900 times more active than uranium, which they named radium. Because of their work on radioactivity, the Curies were awarded the Nobel Prize in physics in 1903.[12]

In the same years as the beginning of the studies on spontaneous radioactivity, at the Cavendish Laboratory in Cambridge, UK, *Ernest Rutherford* started his work to dissect the atom.[13] In 1899, in his publication "*Uranium radiation and the electrical conduction produced by it*"[14], he identified two different types of emissions in the radioactive decay described by Becquerel, calling them alpha (α) and beta (β) decay. Moreover, by studying how these rays are readily stopped in distinct materials, he developed a method that can still be used today to discriminate α and β particles emitted in radioactive decay. A few years later in 1903, from the collaboration with Frederick Soddy, Rutherford developed its theory of atomic disintegration. In their paper "*Radioactive changes*"[15] they stated that "(…) it is not possible to regard radioactivity as a consequence of changes that have already taken place. The rays emitted must be an accompaniment of the changes of the radiating system into the one next produced.", implying that the radioactive processes are to be attributed to the spontaneous disintegration of atoms. Furthermore, the Rutherford-Soddy collaboration gave birth to another essential concept in nuclear physics: by studying how radioactive samples decayed over time, they discovered that radioactive materials have a characteristic “half-live” ($t_{1/2}$), which is the time taken for half the nuclei in a radioactive sample to decay. For these contributions, Rutherford and Soddy were both awarded the Nobel Prize in Chemistry in 1908 and 1921, respectively.

Nevertheless, one of Rutherford’s greatest achievement is the development of its model of the atom. Between 1908 and 1913, together with his team he conducted a series of experiments, including the famous Rutherford scattering experiment: a beam of α particles emitted from polonium was directed towards a thin gold foil target (Figure 1.3a). From the path of the particles it was possible to determine that atoms are composed

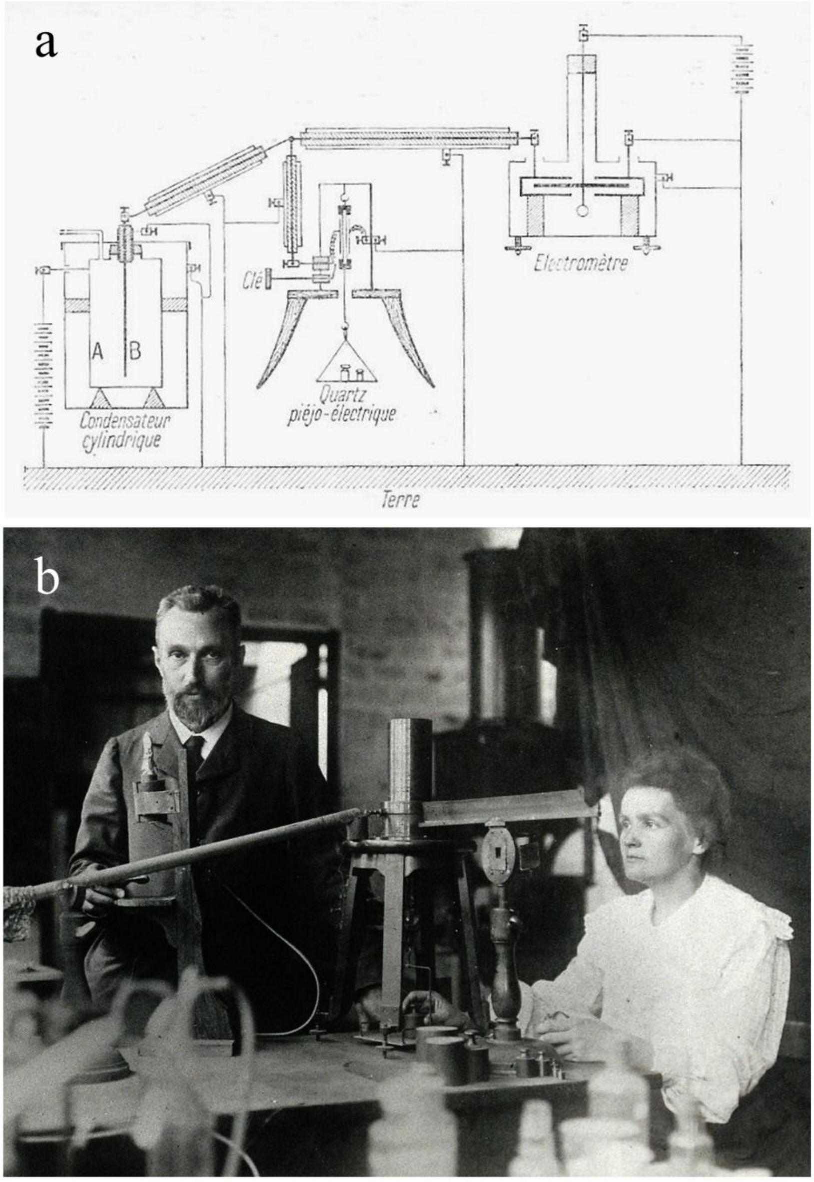

Figure 1.2 a) Schematic drawing of the device used in 1898 by Marie Curie to measure the radioactivity of various compounds: the radioactive material is pulverized in the cylindric condenser (*Condensateur cylindrique*, functioning as a capacitor). A known amount of current is generated by the piezo-electrical quartz (*Quartz piéjo-électrique*), then the current is transferred to the electrometer (*Electromètre*) and finally discharged to the capacitor A-B in the cylindric condenser. The time required for the complete discharge of the electrometer is proportional to the air conductivity in the capacitor, which is directly related to the radioactivity deposited in the condenser. b) Pierre and Marie Curie operating their piezoelectric electrometer in their laboratory at the Sorbonne, Paris.

mostly by empty space (99% of the particles passed straight through the foil), with the electrons orbiting around a small but concentrated positively charged nucleus (which deflected or even backscattered the rest of the particles), as shown in Figure 1.3b.[16]

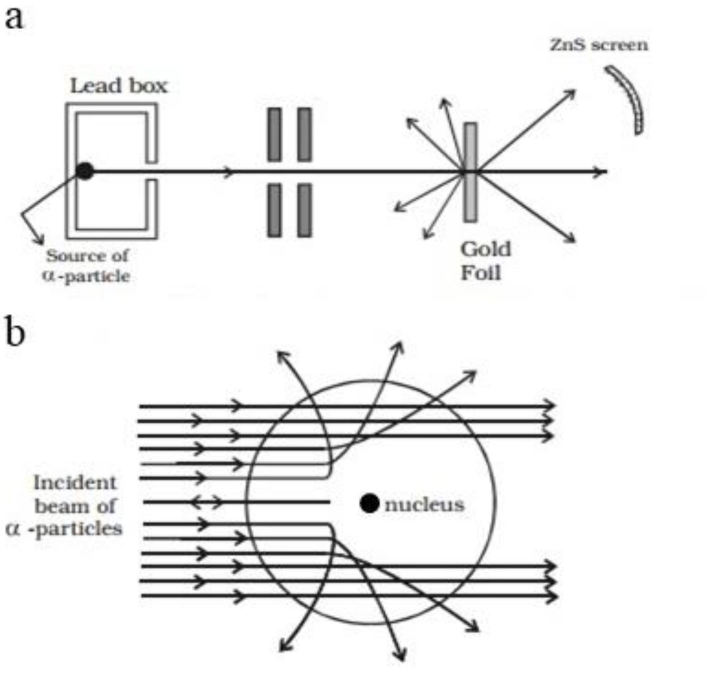

Figure 1.3 a) Rutherford apparatus for the study of the scattering of the α particles by a thin gold foil to investigate the structure of the atom. Polonium is the radioactive source of α particles. b) Rutherford's interpretation of the scattering path of the particles, which led to the formulation of his model of atom.

Rutherford went on also to be the first to recognize that an element could be transformed into a different element by artificial means. After bombarding nitrogen gas with α particles, he noticed that sometime they were stopped and a proton with high kinetic energy was released.[17] This was the first production of oxygen-17 via the $^{14}N(\alpha,p)^{17}O$ nuclear reaction.

$$^{14}_{7}N + ^{4}_{2}\alpha \rightarrow ^{17}_{8}O + ^{1}_{1}p$$

This result led the scientific community to investigate how different materials would react under the same circumstances. In 1930, *Walther Bothe* and *Herbert Becker* bombarded berillium, boron, fluorine and lithium with α particles emitted from polonium, reporting the emission of a radiation with great penetrating power,[18] which *Irène* and *Frédéric Joliot-Curie* (Marie and Pierre's daughter and son-in-law) erroneously postulated to be high-energy gamma (γ) rays, a type of highly penetrating radiation known at the time.[19, 20] In the meanwhile, *James Chadwick* at the Cavendish Laboratory in Cambridge was repeating the same experiment, bombarding ^{9}Be with α particles, and demonstrated that the interpretation of the experimental results was incompatible with energy and momentum conservation, if it has to be accepted the γ rays hypothesis. However, this contradiction disappeard if it was assumed that the radiation consisted of particles of mass 1 and charge 0, which he called neutrons.[21]

$$^{9}_{4}Be + ^{4}_{2}\alpha \rightarrow ^{12}_{6}C + ^{1}_{0}n$$

The discovery of this new particle changed completely the research landscape in the field of nuclear physics, and serveral scientists, including Chadwick, worked at the reshaping of the model of atom. By assuming that atomic nuclei consist of both neutrons and protons, they could enormoulsy simplify the atomic nucleus theory, giving birth to the atomic model that we all know today.

Although they were not able to recognize the neutron, Irène Curie and Frédéric Joliot gave their great contribution by proving that it was possible to artificially produce radionuclides.[22, 23] They discovered that, when irradiating certain non-radioactive light elements (i.e., boron, magnesium, aluminium) with the α rays emitted by polonium, the irradiated material emits positrons and remains radioactive during a reasonably long time after the exposure. This result led them to the conclusion that a new radioactive material had been artificially produced. For instance, they experimented the bombardment of aluminium with α particles reporting the formation of a silicon atom, and they suggested that the phenomenon takes palce in two steps. Initially, the α particle is captured by the aluminium nucleus with an istantaneous expulsion of a neutron, with the formation of a radioactive isotope of phosphorus.

$$^{27}_{13}Al + ^{4}_{2}\alpha \rightarrow ^{30}_{15}P + ^{1}_{0}n$$

Then, this new radioelement decays esponentially to silicon with a half-file of three minutes, releasing a positron.

$$^{30}_{15}P \rightarrow ^{30}_{14}Si + ^{0}_{1}e^{+}$$

In the same way they interpreted the production of radioactive elements when bombarding boron and magnesium. In the first case, an unstable nitrogen with a half-life of 11 minutes is produced, while in the second are produced unstable isotopes of silicon and aluminium.

The Joliot-Curies were awarded with the Nobel Prize in Chemistry in 1935, in recognition of their synthesis of new radioactive elements, discovery that laid the foundation for modern day nuclear medicine and radiopharmaceutical chemistry.

An additional and essential contribution in the development of new radioactive elements came from *Enrico Fermi*, who was the first to produce isotopes with neutrons in 1934.[24] He was trying to determine the possibility of using new particles, instead of α rays, to produce nuclear transformations. In contrast with α particles, neutrons are not spontaneously produced, therefore Fermi and his group used a radium-beryllium neutron source, where the α rays emitted from radium release neutrons from beryllium. With this method they were able to obtain more than 20 new radioactive isotopes, which decayed by β emission.

As a result of these latest discoveries, in a very short period a small family of a few dozens of radioactive elements in the hands of experimentalists expanded enormously. These isotopes found important applications as “tracers” in physics, chemistry and biology. However, even if the pioneering work of these scientists in nuclear physics paved the way for the production and use of synthetic radionuclides for medical purpose, the title of “father of nuclear medicine” is commonly attributed to *George de Hevesy*.[25] He was a Hungarian chemist, and was the first to describe the radiotracer principle that underpins the use of radionuclides to investigate the behaviour of stable atoms and molecules. In 1911, when working under Rutherford at the Cavendish Laboratory, de Hevesy developed the idea that a radioactive isotope, chemically inseparable from the corresponding stable compound, could be used as an indicator of the stable substance. He assumed that radiopharmaceuticals could participate in biological processes without altering or perturbing them, facilitating the imaging of normal and disease mechanisms. In 1923, he firstly applied this theory to the study of the adsorption and transport of lead in a plant of *Vicia faba*, using the radioactive isotope ^{212}Pb to trace its distribution in the roots, stems and leaves of the plant.[26] Then, looking for a less toxic radionuclide which could be used in biological research, he selected ^{32}P and performed a series of experiments where different phosphorus compounds were given to animals in order to study the distribution and metabolism of the substances. The experiment revealed new information about the skeleton metabolism, demonstrating that the bone formation is a dynamic process, where phosphorus atoms are continuously taken up and lost to be substituted with new ones.[27]

Despite this excellent results, de Hevesy research had the practical problem of obtaining enough activity of ^{32}P. This radionuclide was prepared by neutron bombardment of sulphur with Fermi’s neutron activation system, but the fluence of neutrons obtained in this way is very limited. Conveniently, in the same years at the University of California at Berkeley, *Ernest Lawrence* was investigating new methods to produce radionuclides by bombarding stable materials with high-energy particles. In 1934, he patented an invention called a cyclotron (Figure 1.4),[28] able to increase the speed, and therefore energy, of charged particles so that they can induce nuclear reactions. The energies developed were equivalent to enormous quantities of radium in a radium-beryllium source, therefore it became possible to produce radionuclides of nearly all elements in quantities sufficient for their application in medical and biological research.

Glenn Seaborg and *John Livingood* were able to synthesised at the cyclotron of Berkeley two longer-lived isotopes of ^{128}I ($t_{1/2} = 25$ min), by deuteron bombardment of tellurium-128 and obtaining ^{130}I ($t_{1/2} = 12$ h) and ^{131}I ($t_{1/2} = 8$ days).[29]

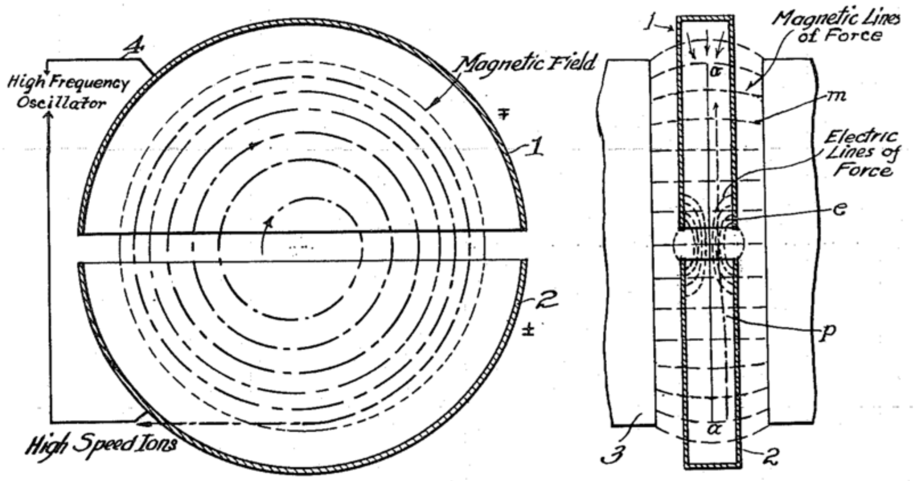

Figure 1.4 Ernest Lawrence design of the cyclotron, extracted from U.S. Patent No. 1,948,384. Electrodes 1 and 2 consist of two semicylindrical hollow metal plates, connected with each other as shown by 4 for maintaining the required alternating or oscillating electric potential difference. Magnets 3 produce a uniform magnetic field extended perpendicularly to the generated electric field. A charged particle (e.g., a proton or a deuteron) is accelerated by the electric field, and is subjected to the Lorentz force due to the magnetic field, which causes the spiral trajectory.

$$^{128}_{52}Te + ^{2}_{1}D \rightarrow ^{130}_{53}I + \gamma$$

$$^{128\,or\,130}_{52}Te + ^{2}_{1}D \rightarrow ^{129\,or\,131}_{53}I + ^{1}_{0}n$$

The consequent studies with ^{131}I allowed the *in vivo* tracking of the radionuclide over a long period of time,[30] and the development of a first nuclear treatment for for thyroid cancer.[31]

In the late 1930s, Lawrence's laboratory was producing ^{11}C ($t_{1/2} = 20$ min) by bombarding boron oxide with deuterons, which will be used years later to study the methabolism of carbohydrates.

$$^{10}_{5}B + ^{2}_{1}D \rightarrow ^{11}_{6}C + ^{1}_{0}n$$

The resulting $[^{11}C]CO_2$ was feeded to plants, which produced ^{11}C-labelled glucose via photosynthesis.[32] This radioactive derivative of glucose was then used for the investigation of the metabolism in lab rats.[33] ^{11}C was first used in humans by Tobias and his group to study the behavior of ^{11}C-labelled carbon monoxyde in man.[34]

The first reference to the production of ^{18}F can be found in an abstract of the "Minutes of the Pasadena Meeting", December 1936, reported by Lawrence's collaborator *Arthur H. Snell*.[35] He decribed the synthesys of the radioisotope ^{18}F ($t_{1/2}$ = 112 min) via deuteron bombardment of neon gas, followed by its radioactive decay to ^{18}O.

$$^{20}_{10}Ne + ^{2}_{1}D \rightarrow ^{18}_{9}F + ^{4}_{2}\alpha$$

This radionuclide found immediate application in the study of the absorption of fluoride by tooth enamel and bones.[36] However, despite these early advances, interest in this short-lived radionuclide increased only many years later, when it was employed for the development of 2-deoxy-2-[^{18}F]fluoro-D-glucose. Commonly abbreviated as [^{18}F] FDG, it is a radiolabeled form of glucose in which a ^{18}F takes the place of the hydroxyl group in position 2. This compound was originally developed with the specific purpose of measuring glucose metabolism in the human brain,[37] while in the late 1970s and early 1980s it found applications also in the imaging of myocardial and tumor metabolism.[38] The discovery of [^{18}F] FDG allowed the exploration of a wide range of diseases and conditions, including drug addiction,[39] eating disorders,[40] attention deficit hyperactivity disorder (ADHD),[41] Alzheimer's disease,[42] and epilepsy.[43]

Today, cyclotron-based synthesis of radionuclide is still the main production technique of radioactive elements for both research and diagnostic imaging. In addition, radionuclide generators can support the need of short-lived radionuclide for those hospitals or research centers which can't afford the presence of a cyclotron in their facilities. These devices provides short-lived radioactive substances from the decay of a longer-lived parent radionuclide. They are worth mentioning the $^{99}Mo/^{99m}Tc$ generator developed in 1958, and the $^{68}Ge/^{68}Ga$ generator. ^{99m}Tc ($t_{1/2}$ = 6 h) was discovered in Palermo, Italy, by Segré and Pierrer in 1937,[44] and is the daughter of ^{99}Mo ($t_{1/2}$ = 67 h) which can be produced by neutron activation of stable Mo. Likewise, ^{68}Ga ($t_{1/2}$ = 68 min) is the product of the decay of ^{68}Ge ($t_{1/2}$ = 271 days) via emission of positron, and in 1980 it became easily accessible with a simple elution of its generator for the synthesis of radiopharmaceuticals.[45]

The discovery of these radionuclide was only one of the steps required for the expansion of nuclear medicine, which would not have been possible without the development of the appropriate imaging instrumentation. Initially, detections were performed using Geiger-Müller counters, positioned on the target of interest to measure the uptake of the radionuclide. This method was soon abandoned in favour of scintillation detectors, as shown by *Hartmut Kallmann* in 1947.[46] He had the original idea of combining organic crystals of naphthalene to the face of a photomultiplier tube, which was then able to amplify and transform crystal scintillations into electrical pulses. The first detector of this kind especially designed for the detection and localization of radioactivity in biological systems was constructed by *Ben Cassen* in 1950,[47] and it was initially applied for the detection of ^{131}I uptake in the thyroid gland, quickly expanded to take nuclear images of other organs as well. Then, with the development of the rectilinear scanner it became possible the automated positioning of the scintillator on the target area, operation which required long time of analysis for the imaging of large organs.[48] In 1953, a multidetector instrument for the localization of brain tumors with positron emitting radionuclides was developed by *Gordon L. Brownell* and *William Sweet*, which consisted of two opposing sodium iodide NaI(Tl) detectors.[49, 50] Their paper "Localization of Brain Tumors with Positron Emitters" represent the first attempt to record positron data for the use in a medical application. However, it was only in the latter part of 1974 that *Mike Phelps* and *Ed Hoffman* built their first Positron Emission Tomography (PET) instrument for human studies, composed by 48 NaI(Tl) detectors displayed in a hexagonal array and able to combine a linear movement with a 60-degree rotation of the gantry (Figure 1.5a).[51] The images of blood flow, oxygen and glucose metabolism and ^{18}F bone scans obtained from this tomograph represent the first published human PET images (Figure 1.5b).

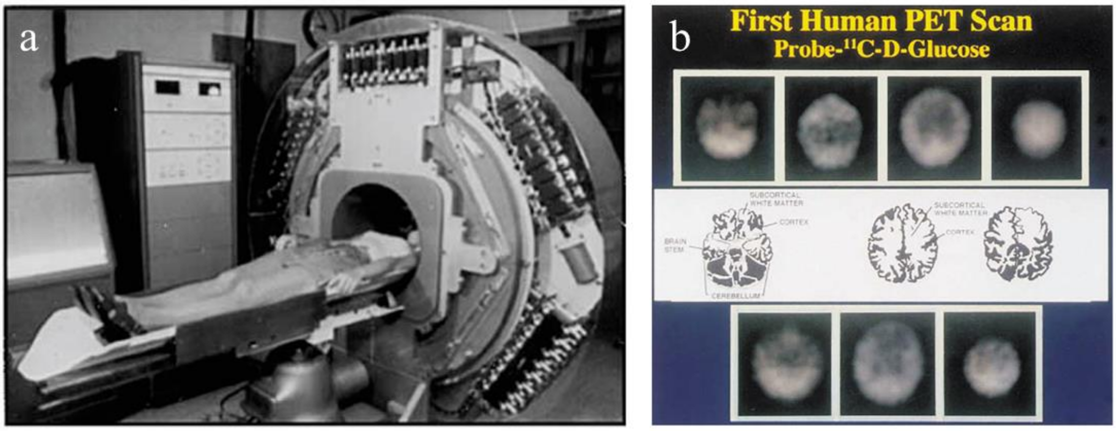

Figure 1.5 a) Phelps and Hoffman's first PET tomograph for human imaging (1953). b) The first published human PET images for the analysis of glucose metabolism

MOLECULAR IMAGING

Molecular imaging (MI) is defined as "*the visualization, characterization, and measurement of biological processes at the molecular and cellular levels in humans and other living systems*".[52]

Whereas morphological and functional imaging modalities, such as computed tomography (CT) or magnetic resonance imaging (MRI), can only provide information on biological structures or anatomy, and are usually used in medical practice on already enstablished pathological conditions (e.g. for identifying broken bone, diagnosis of cancer by its size and tissue density or determining kidney function), the use of MI techniques, such as positron emission tomography (PET) and single-photon emission computed tomography (SPECT), allows to detect a pathophysiological state, arising from a deregulated biochemical process, before any discernable anatomical changes occur.[53] This is made possible by the detection of molecular imaging agents, "*probes used to visualize, characterize, and measure biological processe in living systems*".[52]

These imaging agents, often referred to as tracers or radiotracers, are generally composed by a probe which provides the means for detection (considering PET, a positron-emitting radionuclide), and a pharmacophore responsible for the pharmacological behaviour of the tracer and its specific target engagement (Figure 1.6). The biological target can be a protein, enzyme or receptor which is overexpressed by the diseased tissue, and therefore distinctive and specific for that pathological process.

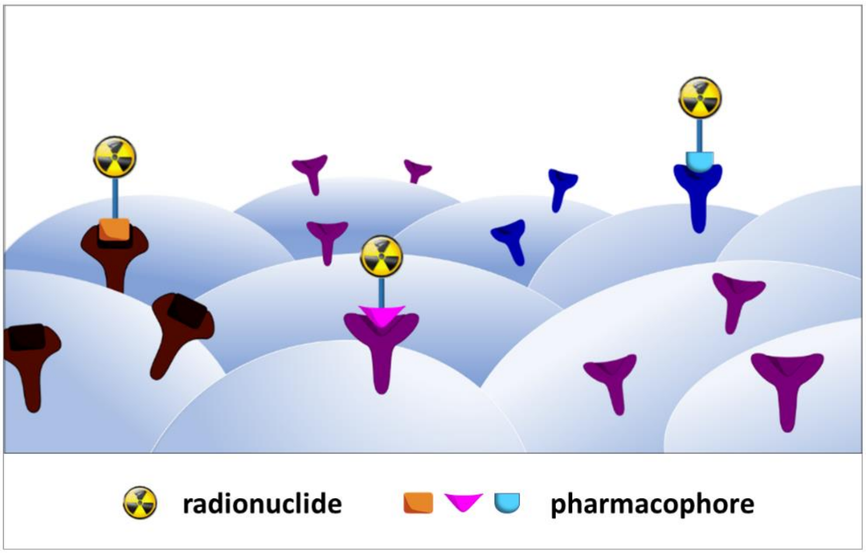

Figure 2.6 Schematic depiction of the concept of target-specific molecular imaging agents. The means for detection is provided by the radionuclide, while the target-specific engagement is mediated by the pharmacophore.

The development of specific taget imaging techinques revolutionized the medical imaging field, shifting the focus of the research from purely anatomical imaging towards modalities aimed at probing tissue phenotype and function. Taking cancer as an example, both the cellular expression of disease biomarkers and fluctuations in tissue metabolism and microenvironment have emerged as extremely promising targets for imaging.[54]

MI have undergone explosive growth during the past few decades, presenting today countless clinical applications, as well as supporting the drug discovery process.[55]

For instance, the application of MI, able to specifically detect a particular biological target, allows the assessment of target expression and the confirmation of target engagement in highly heterogenic diseases (Figure 1.7). In oncology, it is well known that not all cancers are the same, and the ability to stratify disease molecularly has improved cancer care by allowing for a personalized and targeted treatment approach. For example, ^{18}F-FDG (2-deoxy-2-^{18}F-fluoro-D-glucose) is used clinically for tumour detection, staging and detecting recurrence. However, because ^{18}F-FDG is an analogue of glucose and is taken up into all metabolically active cells through glucose transporters, it is likely taken up in all activated immune cells, presenting very low specificity for the cancer heterogeneity. Thus, of great interest is the development of personilized medicine approaches, which will not only provide a better detection of cancer, but also to predict the tumor response against a specific treatment, and provide more defined criteria for patient selection to identify those that would better respond to tretments.[56]

Identifying molecular heterogeneity becomes a central issue also in drug discovery, as clinical trials for new therapies may fail if not tested in groups with increased target expression. Also in early stage clinical trials, the use of molecular imaging agents can provide biological parameters of the tested drug, such as its target affinity or its pharmacokinetics.[53]

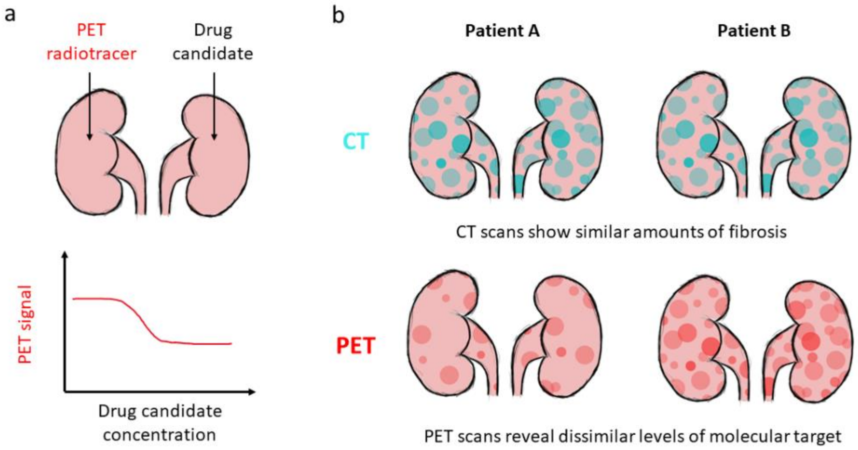

Figure 1.7 a) Depiction of the application of PET imaging in the determination of target engagement for a novel antifibrotic therapy. Radiotracer and tested drug compete for the same molecular target, thus the dose-dependent change in PET signal provides target concentration and affinity of the drug for the target. b) PET application for the determination of target expression. Unlike morphological techniques (e.g. CT), PET can discern two patients with similar amounts of renal fibrosis using a molecular probe that binds to a molecular target implicated in renal fibrosis pathogenesis. PET imaging differentiates high versus low expression of the molecular target, selecting patients for treatment with an inhibitor of the molecular target.

Moreover, MI agents can be used for the diagnosis and staging of different pathological processes (Figure 1.8). Diseases like fibrosis, to date, are detected when they are already enstablished or in a late stage by morphological imaging techniques, and the diagnosis often require tissue sampling, troubling for the patients. MI techniques can overcome these complications providing noninvasive early detection of the disease and its staiging.[57, 58]

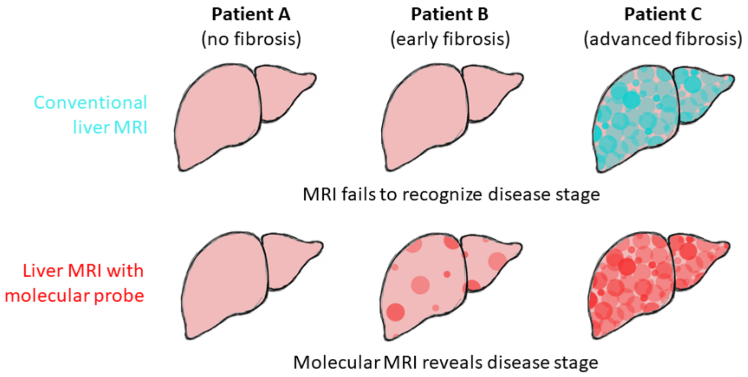

Figure 1.8 Depiction of the MI application in diagnosis and staging. In this scenario, patients at risk for liver fibrosis undergo conventional liver MRI and liver MRI with a molecular probe. The application of the MI approach enables earlier detection of fibrosis and noninvasive determination of disease stage.

This staging ability of MI can be also useful in the determination of treatment responses (Figure 1.9). Today, the assessment of the reactions to therapies of diseases like fibrosis and cancer rely on histological changes, organ functional assessment, and mortality.[59]

However, as disease progression may be slow, prolonged trial duration is needed to detect a possible initial response to the treatment. In order to limit the cost of the trial, surrogate endpoints for the determination of the treatment efficacy are needed, thereby reducing trial duration, but also increasing trial frailty. Because of the MI ability to

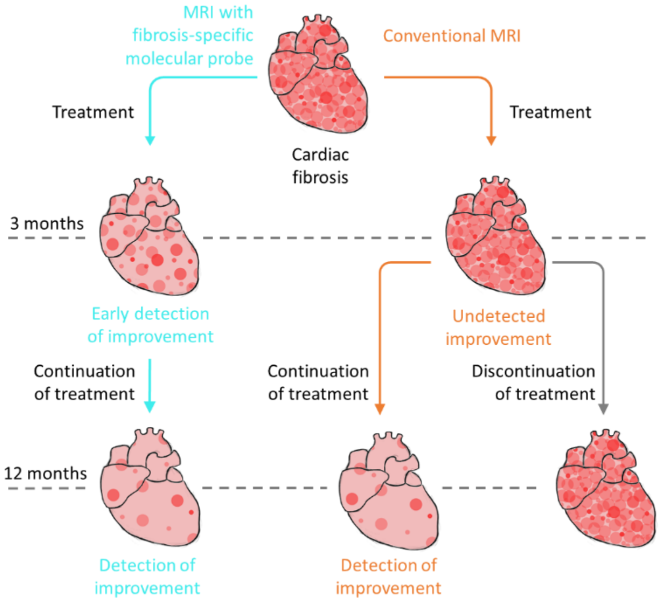

Figure 1.9 Depiction of MI application in the assessment of treatment response. In this scenario, patients with cardiac fibrosis undergo treatment with a novel therapy that reverses fibrosis. MRI using a fibrosis-specific molecular probe detects regression in fibrosis earlier than the standard MRI analysis.

noninvasively stage the disease progress with high sensitivity, this technique potentially allows the early detection of improvements in the patients, increasing the trial reliability.

Besides the molecular heterogeneity, various diseases are also clinically heterogenous in terms of disease progression. In idiopathic pulmonary fibrosis (IPF) there can be marked differences in pace of disease progression between patients.[60] Up to date, there are no clinically used methods to assess fibrotic activity or the pace at which an individual's disease is progressing at any one point in time. From a clinical perspective, the determination of disease activity would enable improved prognostication and tailoring of an individual patient's treatment plan. From a drug development perspective, the ability to determine disease activity would allow to select, for the clinical trial of novel therapies, certain subjects most at risk for disease progression and most likely to benefit from therapy, increasing the efficacy of the trial (Figure 1.10).[61] Indeed, this selection strategy may increase statistical power, thereby reducing the number of subjects needed to meet a prespecified endpoint and thereby decreasing overall trial costs.

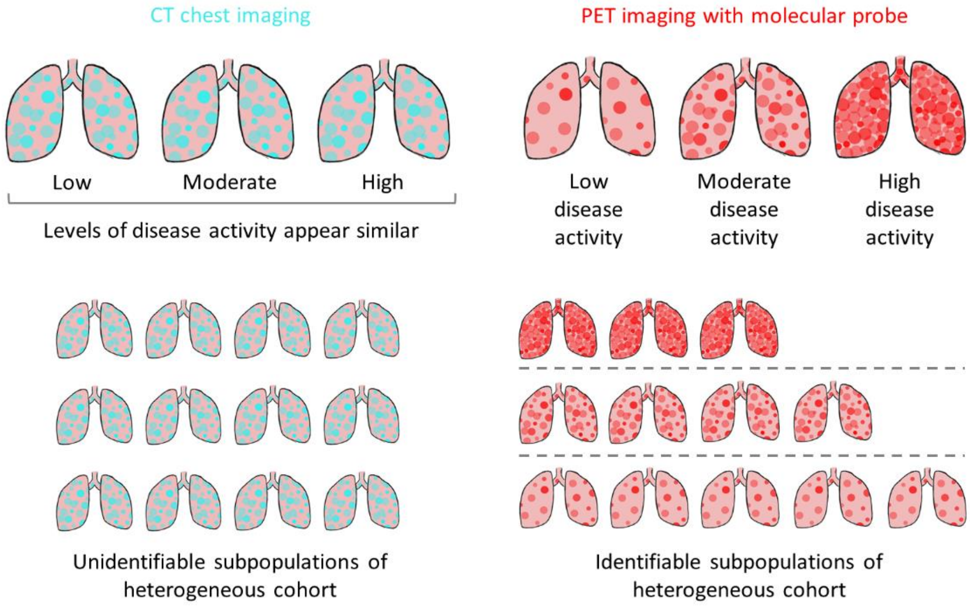

Figure 1.10 Depiction of PET application in cohort enrichment for clinical trials. In this scenario, PET imaging with a molecular probe is performed on IPF subjects for noninvasive detection of disease activity. Unlike conventional CT analysis, PET is able to differentiate subjects by degree of disease activity. This information can be used to select subjects most likely to meet prespecified primary endpoints during clinical trials.

Finally, MI can support the drug discovery process by providing a deeper understanding over the mechanism of action of the of the new drug candidate, determining for instance whether there is a correlation between its plasma level and the target engagement, and if the drug effect is caused by interaction with one or several biological targets.[53]

On these grounds, MI is an essential clinical tool increasingly involved in therapy and in the drug development process.

MULTIMODAL IMAGING

The rapid development of noninvasive imaging modalities has recently offered tremendous opportunities for disease diagnosis and therapeutic intervention. However, each one of these techniques presents its own peculiar strengths, as well as intrinsic drawbacks (Figure 1.11).

With its extremely high detection sensitivity, quantification capability, and unlimited depth penetration, PET is a well-established clinical tool, used to assist in early lesion detection, identification and whole-body localization of tumors, and individualized treatment optimization.[62-64] But this tool alone is often insufficient, due to the short live of radiotracers and its very low spatial resolution, which makes it difficult to obtain comprehensive information about disease sites, and cannot be overcome by improving imaging instrumentation alone. To compensate for this problem, the application of multimodal imaging strategies has been proposed.
Multimodal imaging is the simultaneous combination of imaging techniques, which combines the different advantages of each modalities, taking also in account the intrinsic limitations of which they are characterized. The choice of the imaging modalities to combine should avoid overlap of advantages, and compensate for the weaknesses to obtain synergistic imaging. Thus, PET have been combined with techniques with higher spatial resolution, such as MR or CT.[65] The multimodal

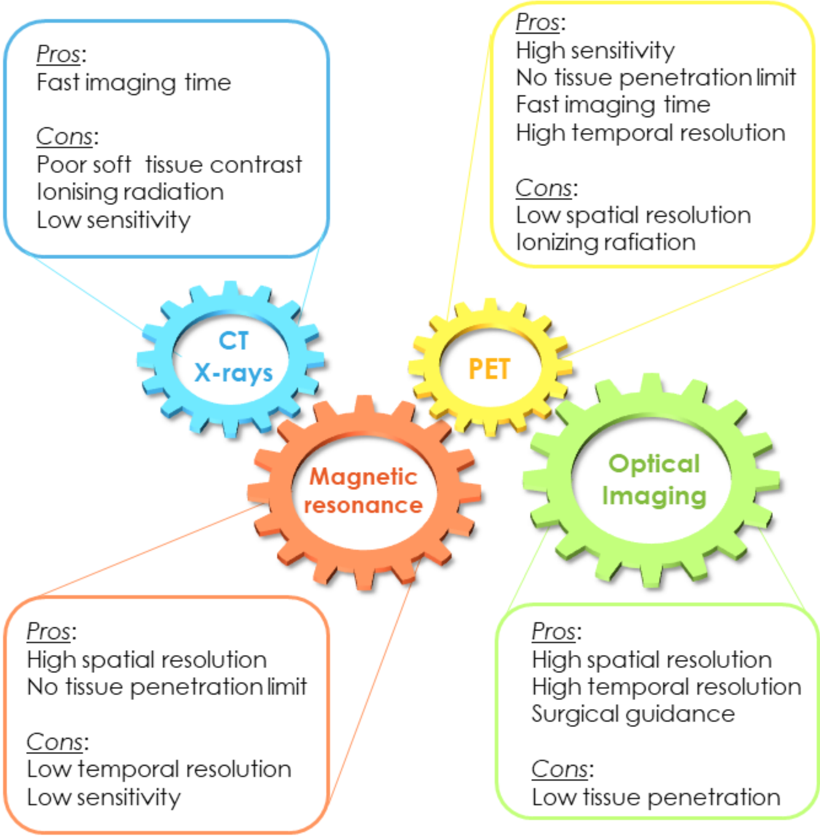

Figure 3.11 Features of the main imaging modalities used in multimodal imaging.

approach allows to widen the range of applicability of these techniques, which become possible to use also in previously unfavourable situations.
For instance, PET application in oncologic surgery is usually limited, and physicians would still have to rely on visual and tactile tissue assessment with relative difficulties in the accurate removal of the tumor. It is possible, however, to apply OI for surgical navigation.[66, 67] This technique uses non-ionizing radiations to illuminate endogenous or exogenous sources of contrast, and enables real-time, high resolution molecular image-guided surgery. Many optical imaging techniques rely on fluorescence as means of detection, using excitation light in the visible or near-infrared (NIR) region to excite a variety of fluorescent probes including small molecule dyes, biomolecule-dye conjugates and nanoparticles.[68-70] Although the high spatial resolution and the real-time imaging capability, the lack of penetration depth due to tissue scattering and absorption of light prevents its use for whole body imaging. Therefore, great interest derived from the possibility to combine PET and OI through a multimodal imaging approach.[71-73] The peculiar combination of PET/OI presents a very high potential, since it enables a preoperative total body scan by PET for the localisation of malignancies and tumor lesions, followed by intraoperative fluorescence-guided surgery by OI for the accurate detection and resection of tumor borders, small metastases and infected sentinel lymph nodes.[74-77]

However, this approach is only possible as long as tumor-specific multimodal imaging agents are available for the specific and sensitive visualization of the target malignancies by both modalities (Figure 1.12). Combined multimodal agents comprising both means for dual imaging detection is preferred to two different probes applied for PET and OI separately, since such agents can assure equal pharmacokinetic profiles and the visualization of the same structures by both

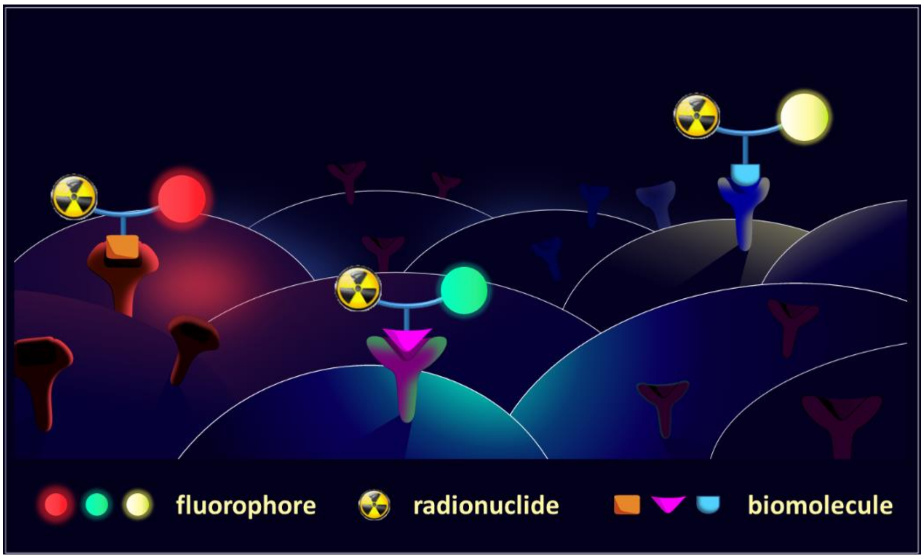

Figure 4.12 Schematic depiction of multimodal imaging agents for the target-specific imaging. The hybrid compounds present a positron emitter (PET) and a fluorescent dye (OI), both integrated in the structure of a target-specific biomolecule (e.g. peptide, antibody).

imaging modalities. For this purpose, efforts were made to develop hybrid multimodal imaging probes integrating in their structure a fluorescent dye, a positron emitter and a tumor-targeting vector, designed in a way that would have altered the physical and chemical properties of the building blocks as little as possible.[73, 78]
For the target-specific uptake of imaging agents in malignancies, peptide-based compounds present various advantages compared to other molecularly-targeted biomolecules (e.g. antibodies), such as straightforward chemical synthesis, fast pharmacokinetics, efficient tissue penetration, high target affinity and specific accumulation in target tissues.[79] However, due to their relatively small dimensions, the introduction of both probes for the imaging detection in the structure could alter their physical and biological properties, possibly compromising their ability to interact with the target. Therefore, it was required to develop multimodal imaging units (MIUs), composed by a positron emitter for PET detection and a fluorescent dye, which could be easily introduced into a target-specific carrier molecule without altering its binding profile.

A peptide-based bone structure for the MIU allows for a rapid solid-phase synthesis, and the efficient introduction of the imaging synthons. Besides, the building blocks which have to be integrated to obtain a fluorescent, positron-emitting imaging unit have to be chosen carefully:

- Considering the vast number of β^+ emitters which are suitable for medical imaging,[80, 81] physical characteristics such as the energy of the emitted positron or the half-life of the radionuclide have to be taken in consideration. In the same way, the production mode of these nuclides (generator or cyclotron) will influence their accessibility, and therefore it will affect the choice. Equally important is the chemistry of the β^+ emitter, being the radiolabeling reaction the last synthetic step for the preparation of the multimodal imaging agent. Thus, macrocyclic chelators (e.g. NODA-GA, DOTA) with their well-established coordination chemistry are usually used for the fast and selective incorporation of radioactive metal ions in biomolecules. These chelators can be introduced in the MIU either *via* click chemistry or by a simple acid-amide coupling.

- Moreover, the fluorescent dye and its conjugation chemistry have to be chosen. Also in this case, a number of dye molecules with very variable fluorescent characteristics exists.[82-90] Many of them can be introduced in the structure of biomolecules without changing their photophysical properties. Also the optical characteristics of the dye have to be taken in consideration, among them the absorption maximum, Stokes shift, emission maximum, extinction coefficient and quantum yield.

Then, the MIU has to be efficiently introduced in the structure of the targeting peptide vector. For this reason, the presence of chemical functions like maleimide-thiol or azide-alkine groups allows the fast and selective introduction of the imaging synthon in the peptide structure of the pharmacophore. However, the presence of the sterically hindered MIU can affect the pharmacological properties of the peptides. Thus, the introduction of a linker between the MIU and the peptides is usually required, since it acts as a pharmacological modifier affecting the pharmacokinetic profile of the peptide, preventing alterations in the binding properties caused by the steric effect of the imaging unit.

A previous successful attempt[91, 92] demonstrated that it was possible to insert a MIU composed by different small dye molecules and NODA-GA chelator ((1,4,7-triazacyclononane-4,7-diyl)diacetic acid-1-glutaric acid) in the structure of a PESIN-homodimer (Figure 1.13, PESIN = PEG_3-$BBN_{7–14}$, $BBN_{7–14}$ = truncated peptide sequence of the endogenous GRPR ligand bombesin, GRPR = gastrin releasing peptide receptor), without altering the binding properties of the resulting conjugates. GRPR attracted much attention in oncology and in nuclear medicine because of its high-density expression in major human cancers, such as prostate,[93-95] breast,[96-98] and small-cell lung cancer,[99] as well as in gastrinoma, gastrointestinal stromal tumors,[100, 101] and other cancer types.[102] Its endogenous ligand, bombesin, is a 14-peptide with sequence:

pGlu-Gln-Arg-Leu-Gly-Asn-Gln-Trp-Ala-Val-Gly-His-Leu-Met-NH_2

whose structure has been used for the development of a number of analogues targeting the GRPR, which were radiolabeled with different strategies obtaining radiotracers for the receptor.[103] Between these, PESIN, a truncated form of bombesin connected to a polyethylene glycol linker (PEG_3-$BBN_{7–14}$) has been applied as GRPR targeting vector in a variety of radiotracers, because of its high binding affinity for the receptor and the increased metabolic stability resulting

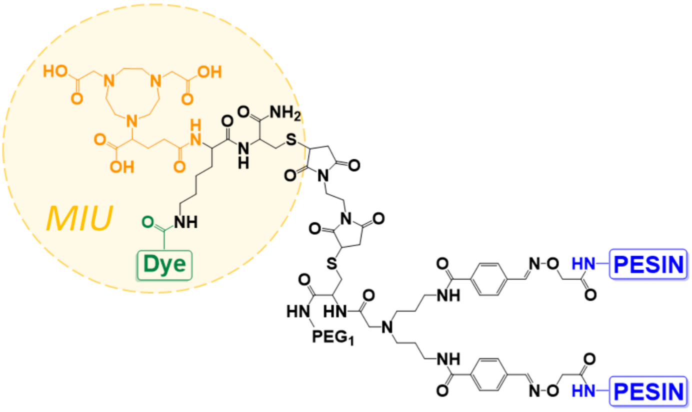

Figure 5.13 General structure of the PESIN-homodimer multimodal imaging agents prepared by Hübner et al., Presenting highlighted in the yellow circle the MIU comprising the NODA-GA chelator (orange) and the various fluorescent probes (green) .

from the presence of the PEG linker.[104] Thus, it was attempted to introduce a MIU in the structure of a PESIN homodimer, and it was observed that, even when conjugated, in the designed MIU neither the radiolabeling nor the photophysical properties were altered. However, even if the interaction of the synthesized bioconjugates with the target GRPR, as said before, was not considerably affected by the introduction of a chelator or bulky chelator and dye-comprising MIU, a strong correlation between the number of anionic charges carried by the fluorescent dye and the GRPR binding affinity of the imaging agents was found. To be more specific, it was suggested that the higher the number of negative charges in the selected dye was, the worse the affinity for the targeted receptor got (Figure 1.14). This concept was confirmed with various PESIN-homodimer conjugates presenting different dye units,[91, 92] as well as with a PESIN-homotetramer conjugate, a multimerized derivative characterized by a higher peptide valency.[105] In this latter case, it was interestingly observed that the adverse influence of the negatively charged synthons on the target affinity was partially compensated by the higher number of peptide units in the molecule, arguing a possible spatial shielding effect of the peptides on the charges (Figure 1.14).

Taken together, these results allowed to theorize that, at least for the GRP receptor: the increasing number of anionic charges in direct vicinity to the receptor-affine peptide unit has a negative influence on the target binding affinity, while the increment of peptidic binding motives in the imaging agent can partly compensate for this negative effect.

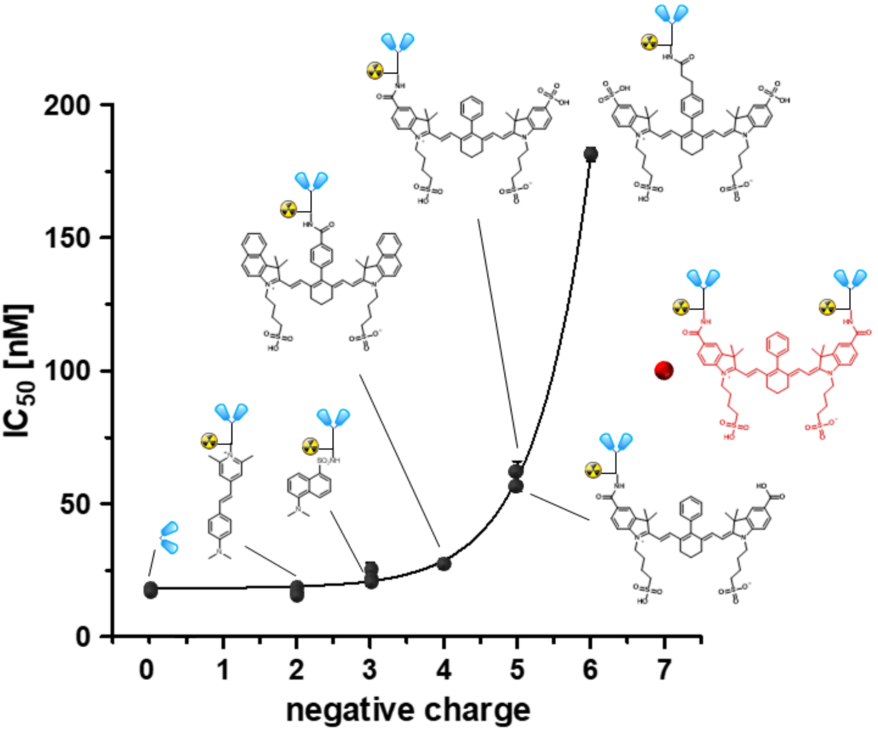

Figure 6.14 Depiction of the correlation between IC$_{50}$ values and overall molecular charge of the MIU-derivatized PESIN dimers (black data points and structures) and tetramer (red data point and structure).

IMAGING AND FIBROSIS

The scientific advances in medical imaging have revolutionized clinical practice and treatment of different pathologies. Many are the clinical applications of imaging, from early detection, to disease staging and prognostication.
In oncology, for example, ^{18}F-fluorodeoxyglucose PET-CT is standard of care for diagnosis, staging, and determination of treatment response for many cancers.[64]
In cardiology, SPECT imaging is used to assess cardiac perfusion and viability.[106]
In neurology, molecular imaging techniques may assist with earlier diagnosis of neurodegenerative conditions (e.g. Parkinson's disease).[107]

However, to date imaging is rarely applied to fibrotic diseases. Fibrosis is a progressive scarring process arising from tissue damage or inflammation that can result in both organ damage and failure.[108] It is a common pathological outcome of a variety of conditions, majorly characterized by the abnormal accumulation of extracellular matrix (ECM) components resulting in progressive architectural remodelling in almost all tissues and organs, leading to a disorder in the function of the affected tissues. Fibrosis is important in end-stage organ failure and death in a variety of chronic diseases that can develop in nearly every part of the body.[109, 110] Atrial fibrillation, atherosclerosis, hypertrophic cardiomyopathy, non-alcoholic steatohepatitis (NASH), diabetic nephropathy, idiopathic pulmonary fibrosis (IPF), inflammatory bowel disease, scleroderma, and pancreatic cancer are some examples of major illnesses with a fibroproliferative component.[111-113]
Although major advances in the understanding of these diseases have been made, there are currently no available treatments to stop the progression of fibrogenesis, but only treatments able to reduce its rate.[114, 115]
Clinical imaging techniques, such as computed tomography (CT), ultrasound, and magnetic resonance imaging (MRI), can detect established fibrosis in the lung, liver, and heart but are less sensitive at detecting early-stage disease, and cannot distinguish active disease (fibrogenesis) from stable scar. For example, IPF diagnosis is usually confirmed by histological identification of the usual interstitial pneumonia (UIP) pattern on surgical (and more rarely transbronchial) biopsies, together with high resolution computerized tomography scans of the chest for the identification of bilateral reticular abnormalities.[116]
As effective treatments become available, earlier detection strategies are needed to enable earlier interventions and the development of targeted therapies for a personalized medical approach to the disease. Moreover, biopsy is an imperfect strategy for understanding activated molecular pathways and is not without risks.

On these grounds, the development of a molecular imaging technique for the target of fibrotic processes is a clinical urgent need that could improve the management of patients and their survival rates. Therefore, the understanding of the fibrosis mechanisms is required for the identification of biomarkers to target with imaging probes.

Fibrosis consist of an abnormal tissue regeneration process that results in constant and severe tissue damage and cellular stress. Failure to fully control or eliminate inducing factors exacerbates inflammation and chronic wound-healing responses, which cause the replacement of normal tissue by scar tissue with deposition of fibrous tissue, leading eventually to organ failure (Figure 1.15).[117, 118]

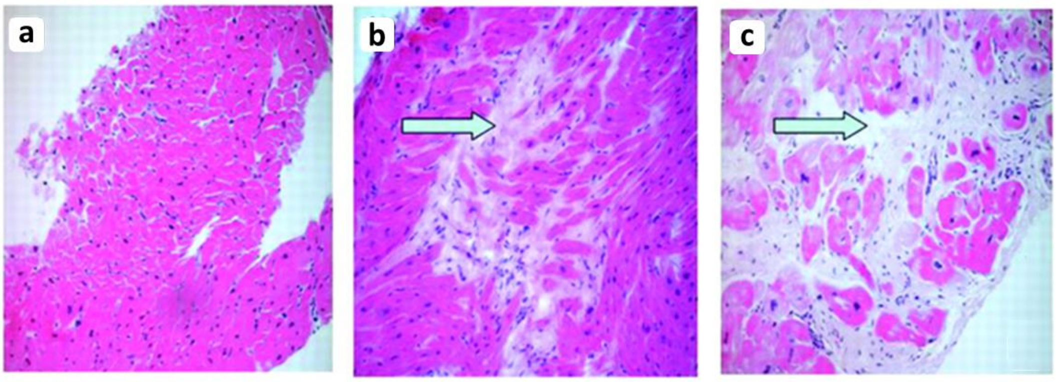

Figure 1.15 Typical histology (haematoxylin and eosin staining) from endomyocardial biopsies showing a) no, b) mild, and c) severe fibrosis. Biopsies were taken intraoperatively through the LV outflow tract from the endocardium of the basal LV septum. Arrows indicate fibrosis.

In *physiological* conditions, injured epithelial or endothelial cells release proinflammatory factors once an injury occurs. These factors trigger blood clots and the formation of a provisional extracellular matrix (ECM) by an antifibrinolytic-coagulation cascade. Then, an inflammatory and proliferative phase takes place, where leukocytes are recruited and start releasing chemokines and growth factors (e.g. interleukin (IL)-13 and TGF-β1, the transforming growth factor-β1). Injured epithelial and endothelial cells, as well as myofibroblasts, release matrix metalloproteinases (MMPs) that destroy basement membrane and release cytokines and chemokines to further recruit and activate neutrophils, macrophages, T cells, B cells, and eosinophils. Following this first inflammatory step, myofibroblasts generate more ECM, while endothelial cells form new blood vessels. Then, during a remodeling and maturation phase, activated myofibroblasts mediate the reduction in the amounts of connective tissue and capillaries, with wound contraction and scar formation. Finally, the injured tissue is regenerated, with the reorganization of fibres, blood vessel restoration, scar tissue elimination, and epithelial and/or endothelial cell regeneration to epithelium or endothelium (Figure 1.16).[119]

However, if a chronic tissue injury occurs, it can begins a sustained scarring response with an abnormal tissue regeneration process, characterized by sustained inflammation, myofibroblasts activation, excessive ECM accumulation, tissue necrosis and ultimately the disorganization of normal functional cells and eventual failure in multiple epithelial organs, such as lungs, liver, and kidney (Figure 1.16).[120-124]

Different can be the causes for the development of an abnormal fibrotic process. Aging is a crucial factor in the output of fibrosis in tissue, which commonly results in fibrosis in multiple organs.[125] Moreover, genetic factors contribute to tissue fibrosis, such as idiopathic pulmonary fibrosis (IPF) and cystic fibrosis (CF).[120, 126]

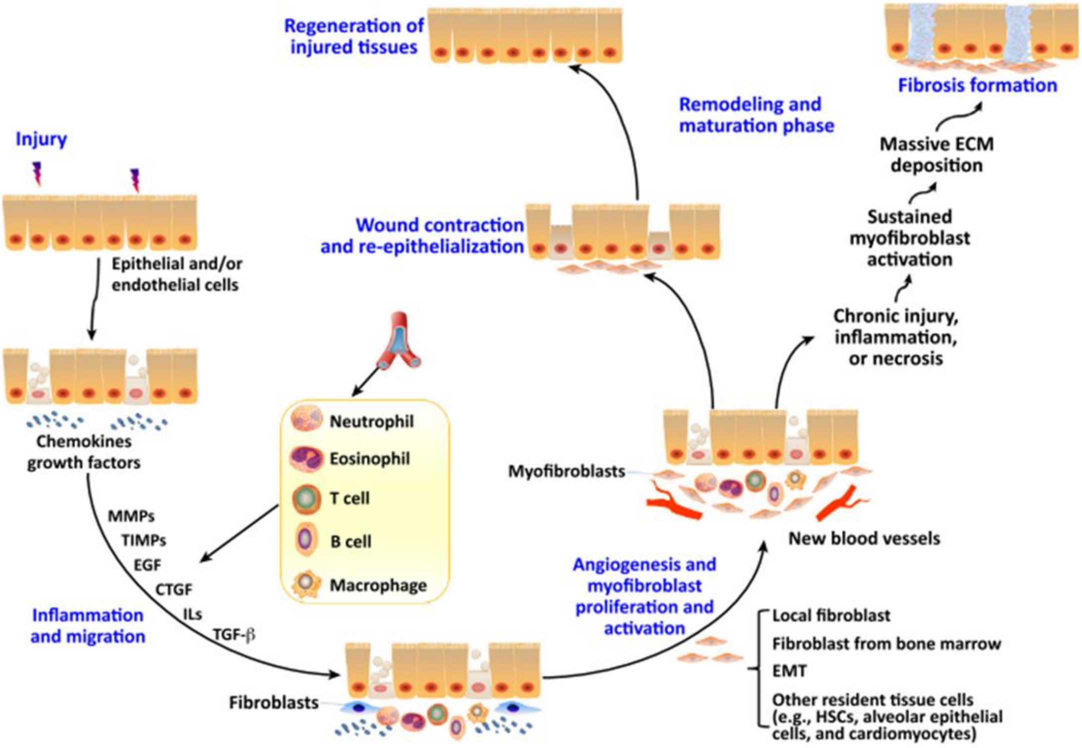

Figure 1.16 The general cellular mechanisms that can lead to the regeneration of the injured tissue in physiological conditions, or to the development of a fibrotic process.

To better understand the causes behind this pathology, the profibrotic cellular mechanisms have been intensively studied (Figure 1.17). Many biological pathways are involved in the activation of myofibroblasts, and the Wnt/β-catenin signaling is one of the most relevant.[119, 127]

Wnts are a highly conserved family of secreted glycoproteins that plays an essential role in organogenesis and tissue homeostasis. Wnt proteins transmit their signal by interacting with Frizzled (Fzd) receptors and low-density lipoprotein receptor-related protein co-receptors (LRP5/6). Upon binding to their receptors, Wnt proteins induce a cascade of intracellular downstream signaling events that culminates in the dephosphorylation and consequential stabilization of β-catenin.

The stabilized β-catenin then transmigrates into the nucleus of the cell and binds to T-cell factor/lymphoid enhancer-binding factor (TCF/LEF). There, the formed complex recruits a transcriptional co-activator, cAMP-response element-binding protein (CREB-binding protein or CBP) or E1A binding protein p300 (p300), to stimulate transcription of Wnt target genes (Figure 1.18).

In addition to this canonical pathway, certain Wnt proteins also exert their effects by activation of the planar cell polarity (PCP) pathway or the non-canonical

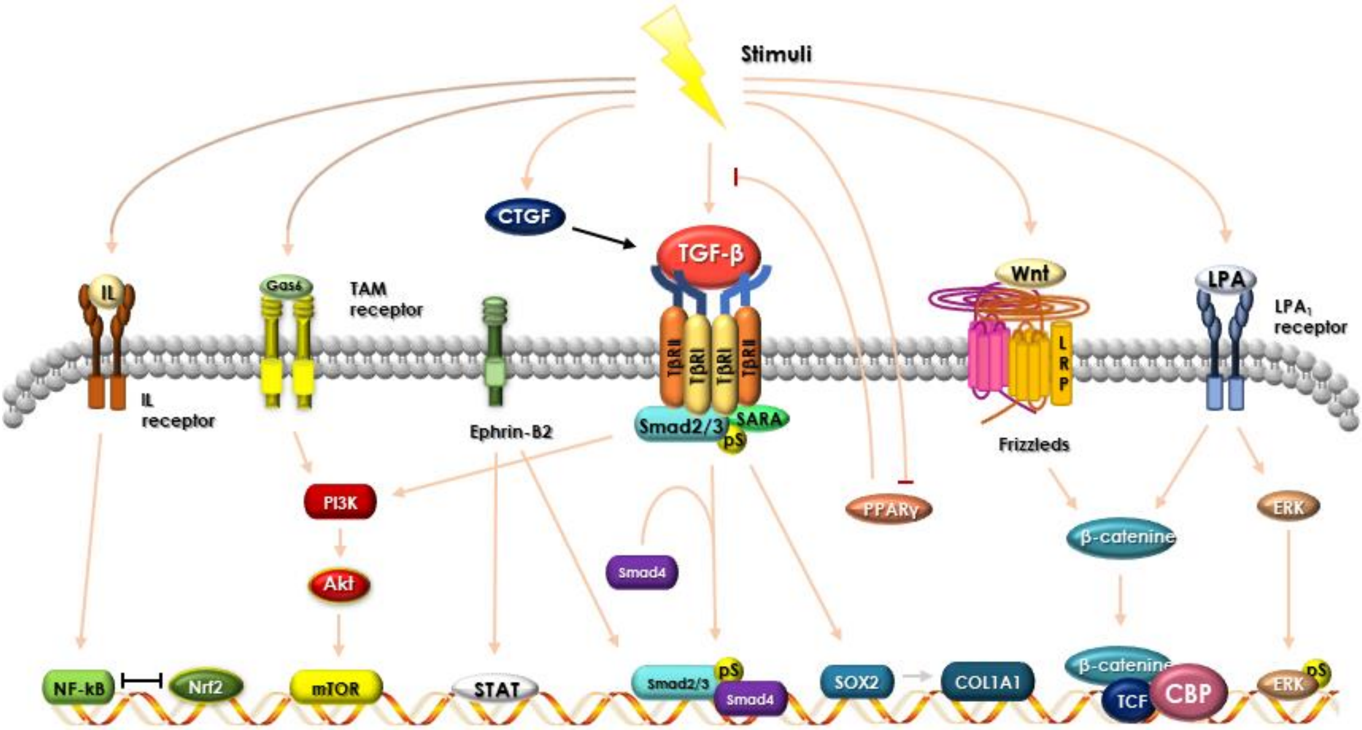

Figure 1.17 Fibrotic molecular mechanisms. TGF-β exerts a profibrotic effect through Smad-dependent and Smad-independent pathways. In the Smad-dependent pathway, TGF-β1 directly phosphorylates and activates the downstream mediator Smad2 and Smad3 through TGF-β receptor I, and then Smad2 and Smad3 bind Smad4, which forms a complex that moves into the nucleus and initiates gene transcription. Smad7, transcribed by Smad3, is a negative regulator of TGF-β/Smad signaling, and the imbalance between Smad3 and Smad7 can contribute to fibrosis. PI3K, ERK, and p38 MAPK are downstream mediators of the Smad-independent TGF-β pathway. PPARγ could inhibit TGF-β to reduce fibrosis, while CTGF, a matricellular protein, contributes to wound healing and virtually all fibrotic pathology. Additionally, Gas6 contributes to fibrosis through the TAM receptor, which further activates the PI3K/Akt pathway. Similarly, LPA triggers fibrosis through the LPA1 receptor that stimulates β-catenin to induce fibrogenesis. The activation of the hedgehog pathway induces the transcriptional activity of Gli to express target genes, which have an important role in interstitial fibrosis, undergoing myofibroblast transformation and proliferation. IL pathway stimulates NF-kB to activate TGF-β to induce fibrogenesis, while Nrf2 antagonizes NF-kB activity to protect against fibrosis.

calcium/calmodulin-dependent kinase pathway, resulting to be essential for the cellular homeostasis.

Consistent results[128-130] indicate that increased activation of canonical Wnt signaling might have an important role in fibrogenesis. Until now, pathologically activated canonical Wnts has been implicated in the pathogenesis of pulmonary, kidney and liver fibrosis. Wnt signaling has been shown to be activated in hepatic stellate cells (HSCs) upon liver injury, and it was demonstrated that its

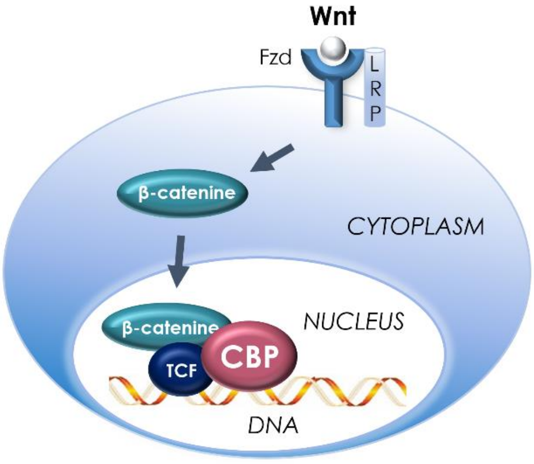

Figure 1.18 Depiction of the Wnt-pathway, showing the interaction of the nuclear β-catenin/TCF complex with the transcriptional coactivator CBP.

downregulation significantly inhibits HSCs activation and fibrogenesis, leading to a reduction in liver fibrosis.[130] The increased expression of many components of different Wnt pathways, including Wnt ligands, Frizzled receptors (Fzd), LRP5/6 co-receptor, and β-catenin have been documented during HSCs trans-differentiation.[131] Between these, one of the most interesting is the CREB binding protein.

CBP is a protein (Figure 1.19) that plays an essential role as transcriptional coactivator in human cells. It is structurally and functionally closely related to the E1A binding protein p300 (p300).[132, 133] They are ubiquitously expressed and presents two functions:

- Transcriptional coactivators (CoAs);
- Histone acetyltransferases (HATs).

Both proteins are constituted of nine domains, comprising the histone acetyltransferase (HAT) domain and bromodomain (BRD). These two domains have been recognized as promising targets for antitumoral treatments.[134]

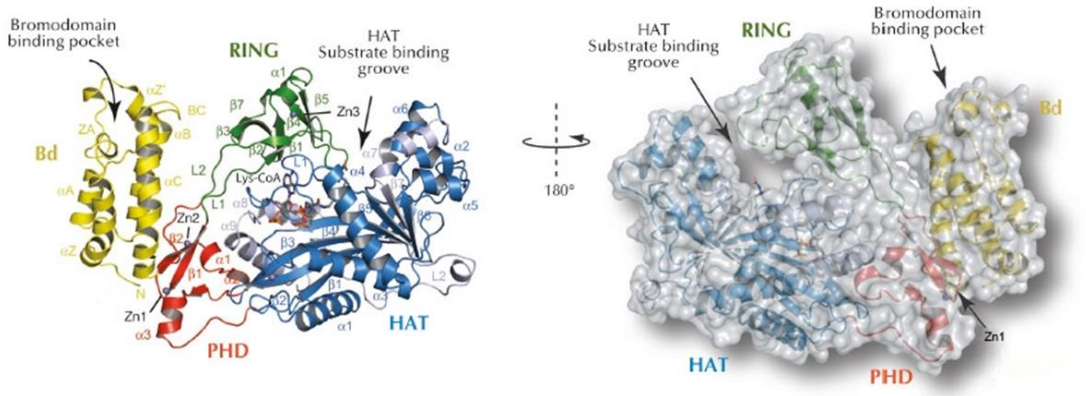

Figure 1.19 Crystal structure of CBP. The bromodomain (Bd) and histone acetyltransferase (HAT) domain are shown in yellow and blue, respectively.

Overexpression or mutation of this proteins are associated with several pathologies, such as malignant tumors, acquired immunodeficiency syndrome (AIDS), diabetes, neurodegenerative disorders and fibrosis.[135, 136]
CBP and p300 HAT domains are involved in the transfer of an acetyl group from acetyl coenzyme A (Acetyl-CoA) to histone lysine residues. This event causes the unfolding of the chromatin (that switches from heterochromatin state to euchromatin) leading to an increased accessibility of DNA for gene transcription in the acetylated section.

CBP and p300 BRDs are made up of 110 amino acids disposed in a characteristics four α-helices (αZ, αA, αB, αC) structure, connected by interhelical loops (Figure 1.20 b). This particular structure is called BRD fold. Two regions called ZA and BC loops form the hydrophobic binding pocket for acetyl-lysine (KAc). Indeed, BRD can recognize and bind acetyl-lysine of histone and non-histone proteins, recruiting cellular transcription machinery to a specific mark, and regulating in this way the expression of genes.

The X-ray crystal structure shows that the KAc recognition in BRD is mediated by a hydrogen bond with asparagine-1168 (N1168) and two other water mediated hydrogen bonds with Proline-1110 (P1110) and Tyrosine-1125 (Y1125) (Figure 1.20 c). Notably, there are five water molecules inside the deep pocket.[134]

The percentage of conservation between CBP and p300 is very high in almost every domain. Notably, there is a 96% conservation score for BRD, which means that finding a selective molecule for CBP over p300 probably requires an important structural optimization. The HAT domain has a percentage of conservation of 88% (Figure 1.20 a). There are 61 known BRDs encoded by human genome and they can be divided into sub-families based on structural similarity.[133] This enormous quantity of BRDs further complicate researches for selective inhibitors of CBP BRD.

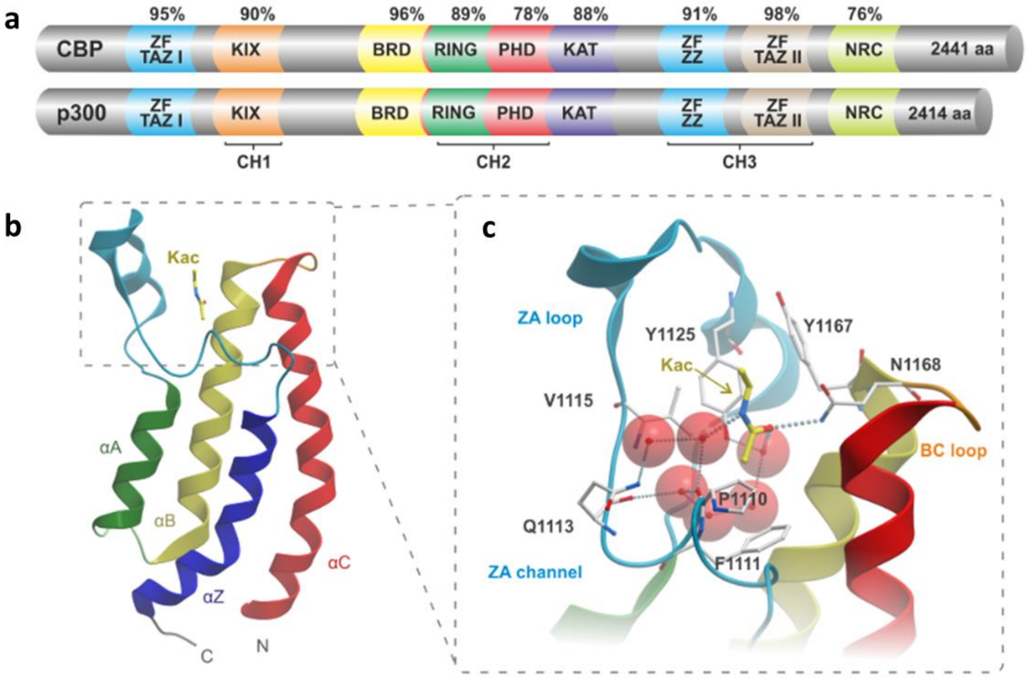

Figure 1.20 a) Percentual conservation and domain architecture of human CBP and p300. b) CBP BRD-fold depicting the four alpha-helices (αZ, αA, αB, αC) and, boxed, ZA and BC loops that form the acetyl-lysine (Kac) binding pocket. c) Kac in complex with CBP bromodomain.

In addition, it was shown that CBP is recruited by the tumor suppressor p53, upon DNA damage, to modify chromatin and aid transcriptional activation of p53 target genes. The recruitment process of the coactivator is mediated by the bromodomain of CBP, that binds to p53. An excessive activity of p53 has been linked to neurodegenerative disorders (e.g. Alzheimer, Parkinson's diseases and multiple sclerosis) and autoimmune diseases. In this scenario, small molecules capable of temporal and selective inhibition of p53 are of great interest.[132]

Finally, Zhou et al. reported a massive presence of CPB in hyperplastic AT2 cells in IPF tissues (Figure 1.21).[136] To better understand the biological role of this overexpressed protein, some selective inhibitors have been tested, and it has been demonstrated that the administration of a selective inhibitor of the CBP/β-catenin interaction ameliorates and reverses pulmonary fibrosis. Overexpressed level of CBP have been also detected in liver fibrosis.[137]

On these grounds, CBP seems to be an interesting biomarker of the fibrotic process, and thus a suitable target for the development of molecular imaging probes for the disease.

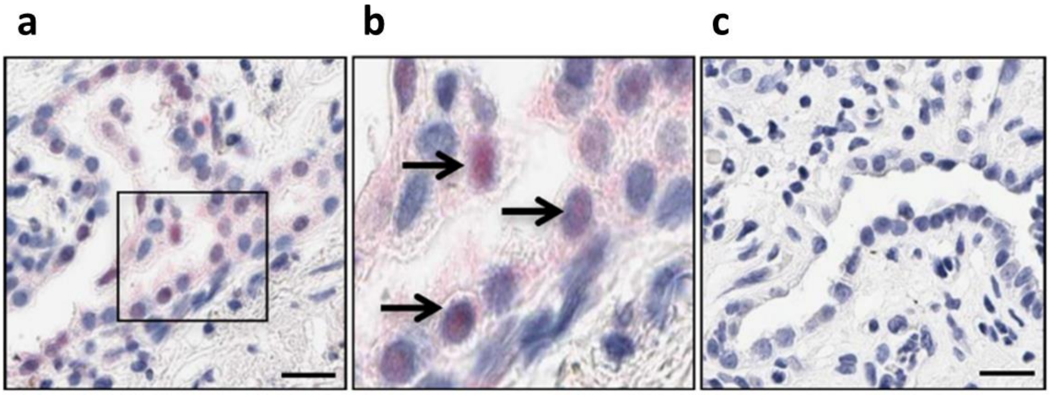

Figure 1.21 a – b) Expression of CBP (stained in pink) in hyperplastic AT2 in IPF, together with c) a healthy tissue as negative control.

LEAD COMPOUNDS FOR FIBROSIS IMAGING

In order to develop an imaging strategy for a specific disease, after having chosen the biological target it is necessary to identify a suitable lead compound, on which structure the imaging agent will be designed. Essential characteristics of this lead compound are high affinity and selectivity for the target.

Imaging agents, for instance PET tracers, are usually administered in submicrogram amounts, thus a high binding affinity of their pharmacophore is especially crucial as the radiotracer often has to compete with endogenous ligands for the binding site of the common target.

Equally important is a high selectivity for the target, which results in fewer specific interactions with other binding sites, such as other receptors, receptor subtypes, or transporters.

In the context of the fibrotic process, and in particular considering the CBP-mediated Wnt pathway, many high affinity ligands have been developed recently, to be used in the antifibrotic treatment. Between these, very promising results have been provided by ICG-001 and a series of benzimidazole derivatives.

ICG-001 (Figure 1.22) is a potent inhibitor of the CBP/β-catenin interaction (IC_{50} = 3 μM, Kd ≈ 1 nM), competing with β-catenin for its binding site.[138] It presents a very high selectivity for CBP, giving no interactions with the close analogue p300.

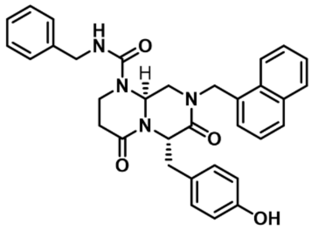

ICG-001

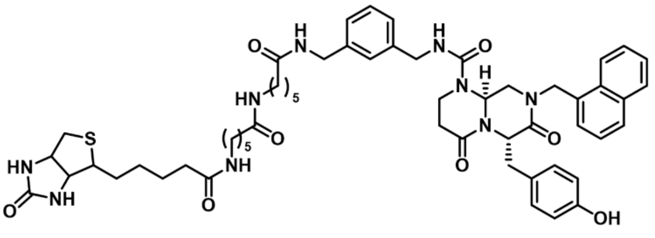

ICG-002

Figure 1.22 Chemical structures of the CBP inhibitor **ICG-001** and its biotinylated derivative **ICG-002**

Its antifibrotic activity was firstly observed in a screening test for inhibitors of the Wnt pathway. In order to define its biological target, a biotinylated derivative, *ICG-002* (Figure 1.22), was prepared. This compound was used in an affinity purification assay on cell lysates of different human colon carcinomas, and it was noted that CBP was the only protein still bonded to the beads after washing, demonstrating that CBP is the biological target of the molecule.[139]

ICG-001 has shown brilliant results in the treatment of pulmonary fibrosis bleomycin-inducted in mice. It is able to reverses the fibrosis and protects against lethality induced by bleomycin. Henderson et al.[129] studied the effects on fibrosis of delayed administration of ICG-001 after resolution of the early inflammatory response to bleomycin. In this studies, ICG-001 attenuates fibrosis (Figure 1.23 c – d) compared to the only bleomycin administration test (Figure 1.23 a – b). Results are very similar to the saline solution administration control (negative control, Figure 1.23 e – f).

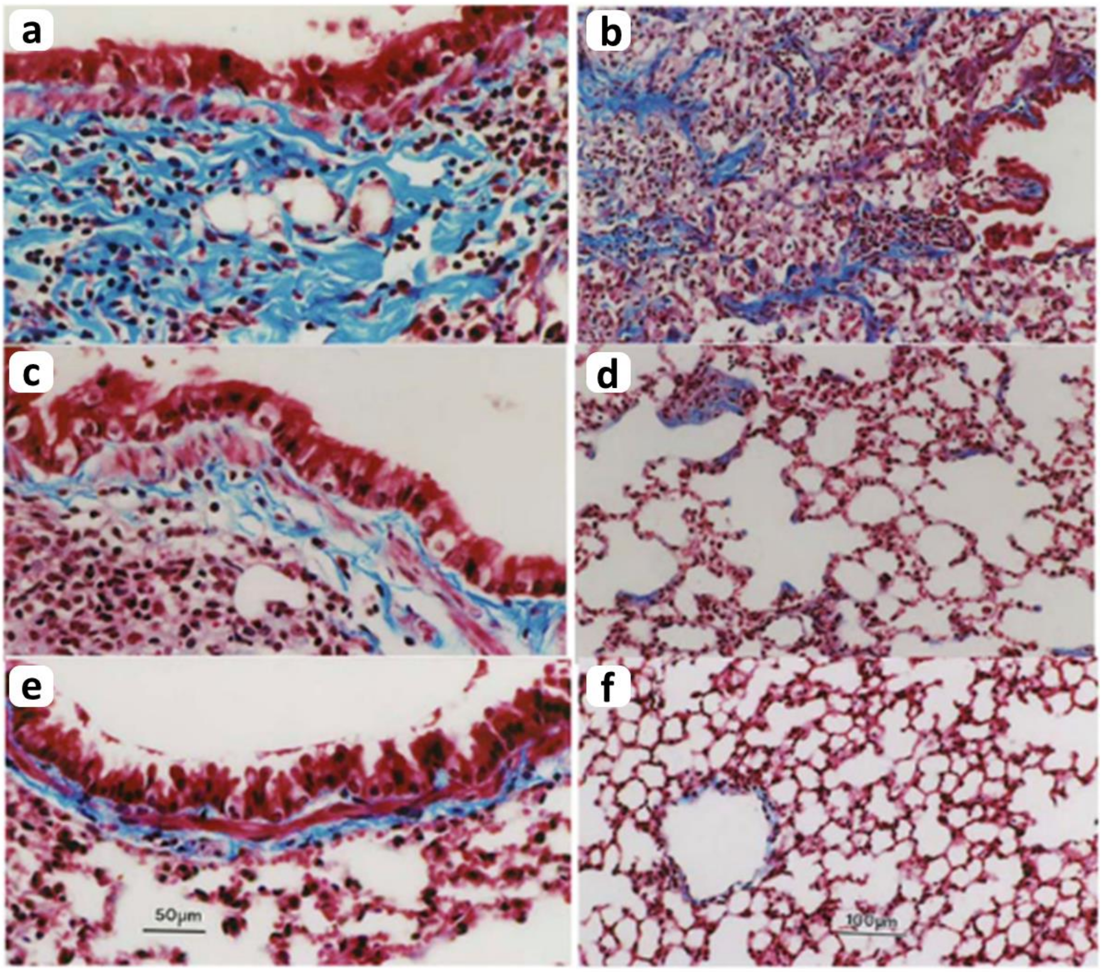

Figure 1.23 a – b) Bleomycin induced pulmonary fibrosis, positive control. c – d) Bleomycin induced pulmonary fibrosis treated with ICG-001. e – f) saline solution administration, negative control.

Moreover, ICG-001 and its derivates have shown promising results in animal models of hepatic fibrosis,[140, 141] making it potentially a suitable lead compound for the development of imaging agents targeting fibrotic processes.

Furthermore, a series of *benzimidazole derivatives* was developed as CBP inhibitors. This compounds were designed from the structure of 4-(1H-benzo[*d*]imidazol-5-yl)-3,5-dimethylisoxazole (Figure 1.24 a). This small molecule is a non-selective 3,5-dimethylisoxazole BRD inhibitor, with good pharmacokinetic characteristics such as low molecular weight (213 Da), reasonable lipophilic efficiency and ligand efficiency for CBP. Furthermore, it is possible to introduce different functions in its structure to improve ligand affinity and selectivity for CBP.[133]

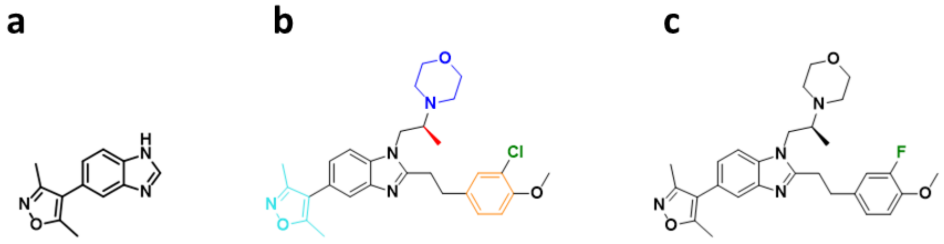

Figure 1.24 Chemical structures of a) 4-(1H-benzo[d]imidazol-5-yl)-3,5-dimethylisoxazole, b) SGC-CBP30, and c) Cmpd 63

Various compounds have been prepared from this backbone structure, among which SGC-CBP30 and its fluoro-analogue Cmpd 63 (Figure 1.24 b and c, respectively). This small molecules presents high affinity for the CBP-BRD (K*d* = 0.021 and 0.039 µM, respectively), and a very high selectivity over other BRDs (Figure 1.25).

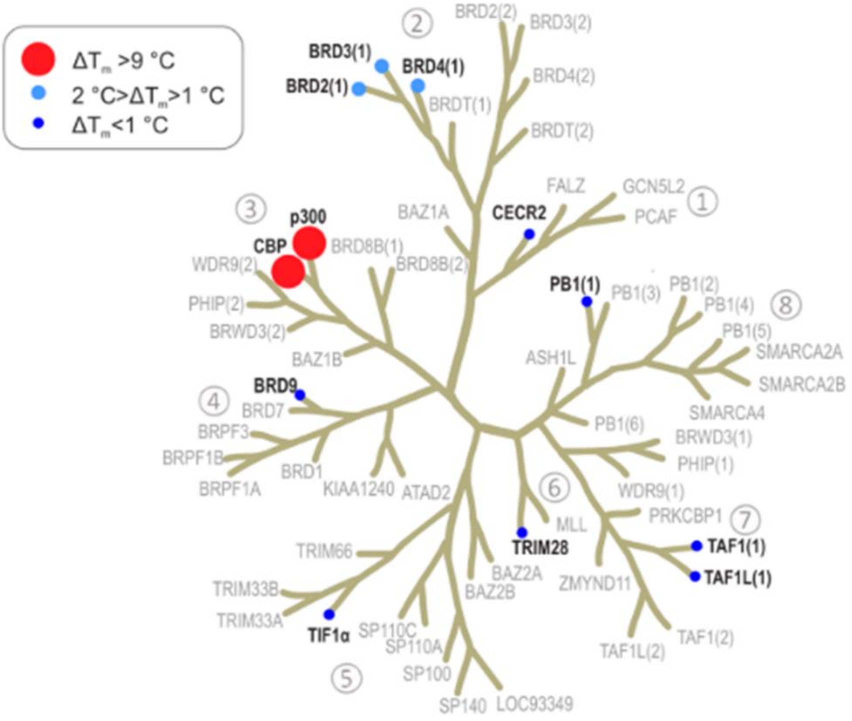

Figure 1.25 Selectivity assessment of SGC-CBP30 against human BRD families using DSF (ΔTm) binding assays. The 10 screened targets are in black on the phylogenetic tree of the human BRD family.

By analysing the crystal structure of the complex formed between SGC-CBP30 and CBP, it was possible to determine their peculiar interactions:

- The dimethylisoxazole group (light blue in Figure 1.24 b) mimics the key acetyl-lysine (KAc) binding in CBP BRD, forming a hydrogen bond to N1168 and a water-mediated hydrogen bond to Y1125;
- Morpholine (blue in Figure 1.24 b) is placed inside the ZA loop, between the targeted regions 1 and 2 (Figure 1.26 b);
- A π-cation interaction between the guanidino group of R1173 and the aryl ring (orange in Figure 1.24 b) is formed. It is possible to see the pocket for the aryl ring in Figure 1.26 b;
- The chlorine atom (green in Figure 1.24 b) sits in a hydrophobic pocket between V1174 and F1177 (Figure 1.26 b). This halogen group on the ring is the best in terms of selectivity between CBP/p300 BRD and the other BRDs, but a fluorine in place of chlorine does not significantly lower selectivity;
- The chiral methyl group (red in Figure 1.24 b) is placed below the aryl ring (orange in Figure 1.24 b), helping to lock the ring in position.

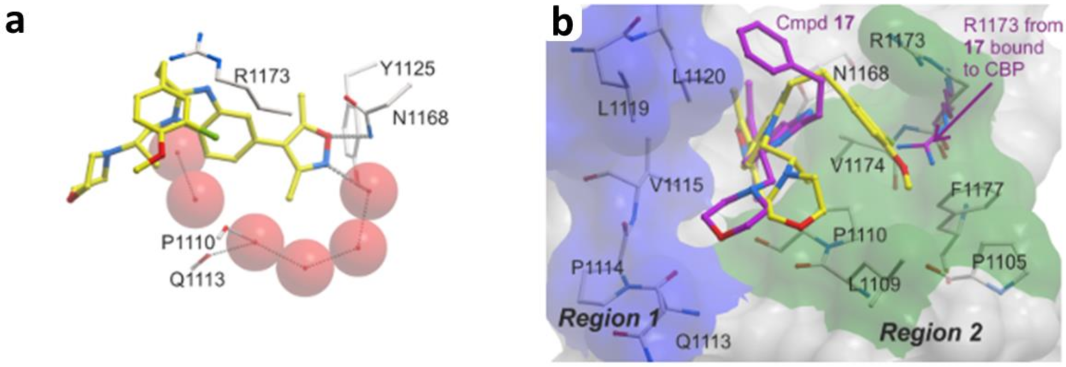

Figure 1.26 a) X-ray crystal structure between SGC-CBP30 and CBP-BRD, together with b) the surface view of the same crystal structure.

Because of their high affinity for the biological target, and their selectivity towards the CBP-BRD compared to other bromodomains of the same family, SCG-CBP30 and its fluoro-analogue Cmpd 63 presents suitable characteristics to be used as lead compound for the development of imaging agents targeting fibrotic processes.

PHARACEUTICAL RADIOCHEMISTRY

A radiopharmaceutical is a medicinal product that includes one radionuclide aiming to the imaging of biological processes, and the diagnosis or treatment of diseases in nuclear medicine. These chemicals have the ability to interact specifically with a biological target, thus they are accumulated in specific districts of the body. The detection of their radioactivity through the use of gamma cameras or similar gamma imaging instruments allows their constant localization throughout the body during their permanence in the biological system.

There are 3 steps for the synthesis of a radiopharmaceutical:

i. Production of the radionuclide;
ii. Radiosynthesis and pharmaceutical formulation;
iii. Quality control of the radiopharmaceutical.

After the synthesis there are three following steps to perform a PET exam:

iv. Intravenous administration to the patient or to the animal;
v. Acquisition of PET imaging;
vi. Reconstruction of acquired tomographic images.

PRODUCTION OF RADIONUCLIDES

The first step in the synthesis a radiopharmaceutical is the production of the radionuclide. This radioactive isotopes are produced *via* nuclear reactions, which are processes where two nuclear particles (i.e. two nuclei, or a nucleus and a subatomic particle such as proton, neutron, or high energy electron) collide to produce one or more new nuclides, or where an unstable atom spontaneously converts itself into a different nuclide without collision.

Nuclear reaction can be represented in equation as follow:

$$^{18}_{8}O + ^{1}_{1}p \rightarrow ^{18}_{9}F + ^{1}_{0}n$$

In this case the nucleus of oxygen-18 collides with a proton to produce fluorine-18 and a neutron. This collisions can actually result in a nuclear reaction only if the particle energies are high enough to overcome the repulsive barriers existing between the nuclei, and if the particles are close enough to introduce short-range strong forces. These high-energy particles are produced in particle accelerators or during nuclear decay processes.[142]
Based on the design of Ernest Lawrence (Figure 1.27), cyclotrons are devices able to accelerate charged particles through the combination of magnetic and electric fields. An ion source in the center of the cyclotron ionizes the particles, which are then accelerated by an electric field created between two *dees* (Figure 1.27). These two semicylindrical electrodes, separated by a gap and placed face to face in a vacuum chamber, produce a

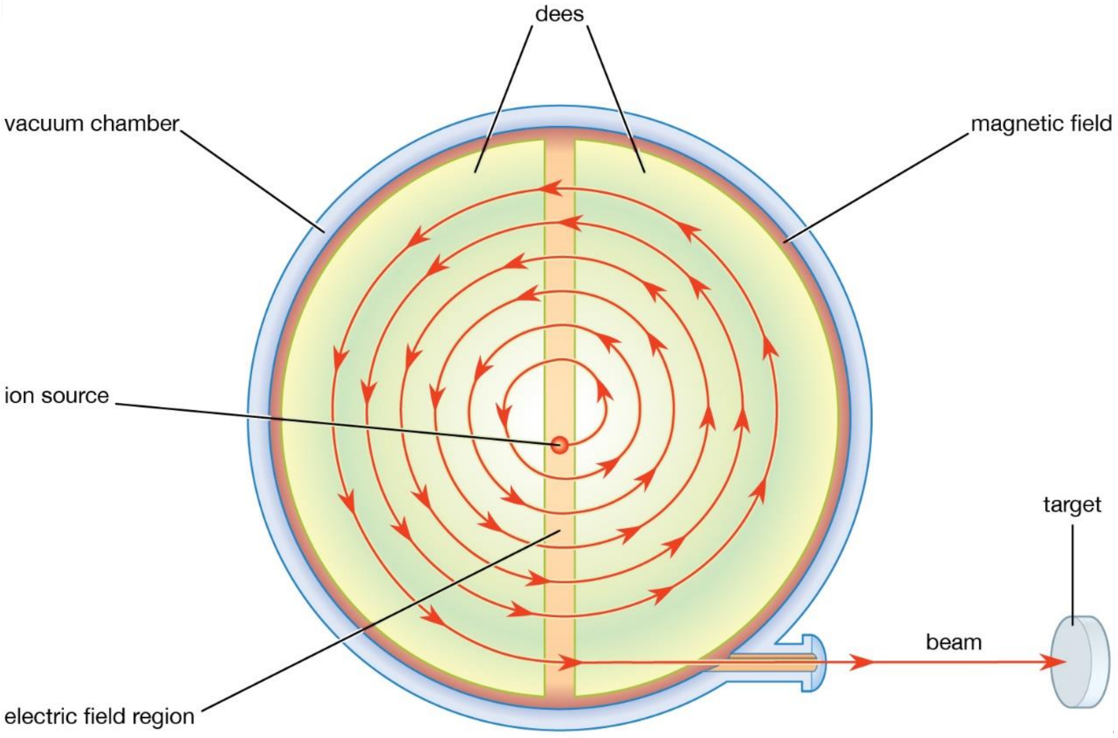

Figure 1.27 The scheme of a cyclotron.

linear electric field through the application of an high frequency alternating voltage, determining the linear acceleration of the charged particles. The dees are located between the poles of a large electromagnet, which applies a magnetic field perpendicular to the electrode plane. The moving particles, surrounded by the magnetic field, are subjected to the Lorentz force, which is perpendicular to their direction of motion and bends the path of particles in a circle. The frequency of the exchange of voltage in the dees is set in such a way that particles make one circuit during a single cycle of voltage. Each time after particles pass to the other dee electrode, the polarity of the radio frequency voltage reverses. In this way the electric field is in the correct direction to accelerate particles every time they cross the gap from one dee electrode to the other.
The increasing speed of particles causes them to move in a spiral path outward from the center to the rim of the dees. When the particles reach the rim, a small voltage on a metal plate deflects the beam, so that it exits the dees chamber. The accelerated particle beam then is able to hit the bombardment target. A high vacuumed atmosphere inside the cyclotron is essential because otherwise molecules and atoms of the air would stop the accelerated particles.[143]

In a different way, some radionuclides can be produced in specific generators from the decay of radioactive precursors. These long-lived unstable nuclei, defined “*parent nuclei*”, are usually immobilized on solid supports, and decays overtime in the desired radioactive “*daughter nuclide*”. The latter is then usually collected through ion chromatography elution and immediately used for the following radiolabeling reaction. An example is the ^{68}Ge/^{68}Ga generator, where the parent nuclide germanium-68, immobilized on a column, decays *via* electron capture with a $t_{1/2}$ of 271 days in the daughter nuclide gallium-68 (III) ($t_{1/2}$ = 68 min).

$$ {}^{68}_{32}Ge \rightarrow {}^{68}_{31}Ga^{3+} $$

Then, gallium-68 is eluted from the generator with a diluted aqueous solution of HCl (0.1 M), and the collected chloride salt [^{68}Ga]$GaCl_3$ is used on-site for the radiosyntheses.

DECAY OF RADIONUCLIDES

A radionuclide is an unstable atom which spontaneously transforms itself in a more stable species over time with a nuclear reaction. A commonly used parameter in this field of studies, as previously reported in chapter 1, is the half-life ($t_{1/2}$). Given a sample of a particular radionuclide, the half-life is the time required for exactly half of the entities to decay. This value is independent from outside influence factors, such as the physical state, chemical form, pressure and temperature.

Considering one-decay nuclear reactions:

$$\boldsymbol{N = N_0 * e^{-\lambda t}}$$

where N is the number of atoms at time t, N_0 the initial number of atoms and λ represent the decay constant. Half-life $t_{1/2}$ can then be calculated from the decay constant considering that: $N = N_0/2$ and $t = t_{1/2}$.

$$\boldsymbol{t_{1/2} = \frac{ln2}{\lambda}}$$

The radioactive decay law describes the behavior of a large number of nuclides, rather than individual atoms, and can be represented with the exponential decay curve reported in Figure 1.28.[144] The function is independent from the nature of the decay emission, and a complete decay of all nuclei is possible only if an infinite period of time is considered.
The decay process usually consists in a loss of energy by radiation emission. These radioactive emissions can be classified in three different type of decays: alpha (α), beta (β) and gamma (γ) decays. Each one of these transformations is defined by the different particle or radiation emitted, and by their penetration properties.

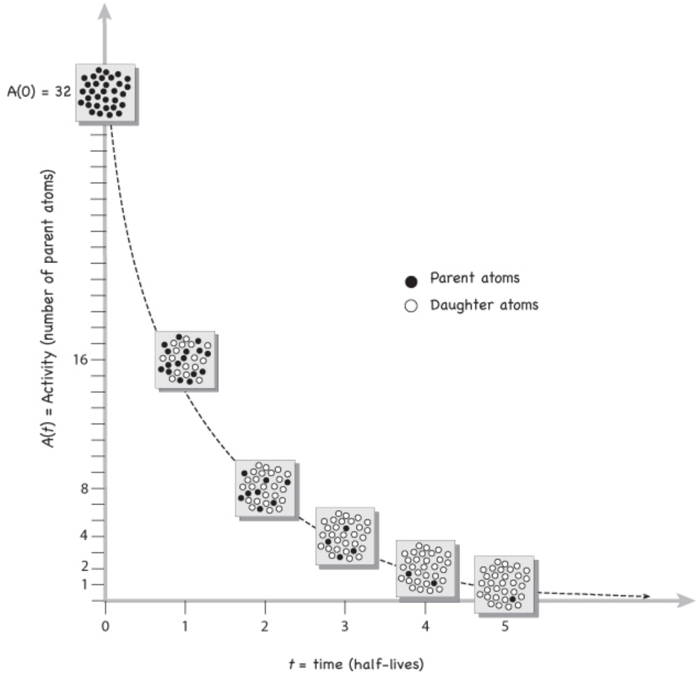

Figure 1.28 Radioactive decay curve of a generic radionuclide

Alpha decay: usually involves heavy nuclides and high energy. In this type of decay, an atomic nucleus emits an alpha particle (helium nucleus) and transmutes itself into a second more stable nucleus, with a reduced by four mass number ($A = A_0 - 4$) and a reduced by two atomic number ($Z = Z_0 - 2$) (Figure 1.29). Helium nuclei are highly charged and heavy particles, which generally present very low penetration depth and can be stopped by few centimetres of air or by the contact with the skin. In fact, they disperse their energy through electric collision and electric induction. Their LET (Linear Energy Transfer, the energy released by the radiation per unit of length) is very high and penetration range in tissues very low. That's why touching an alpha source is typically not harmful, but otherwise ingesting it can overtime led to potentially dangerous damages, like double-strand breaks to the DNA.

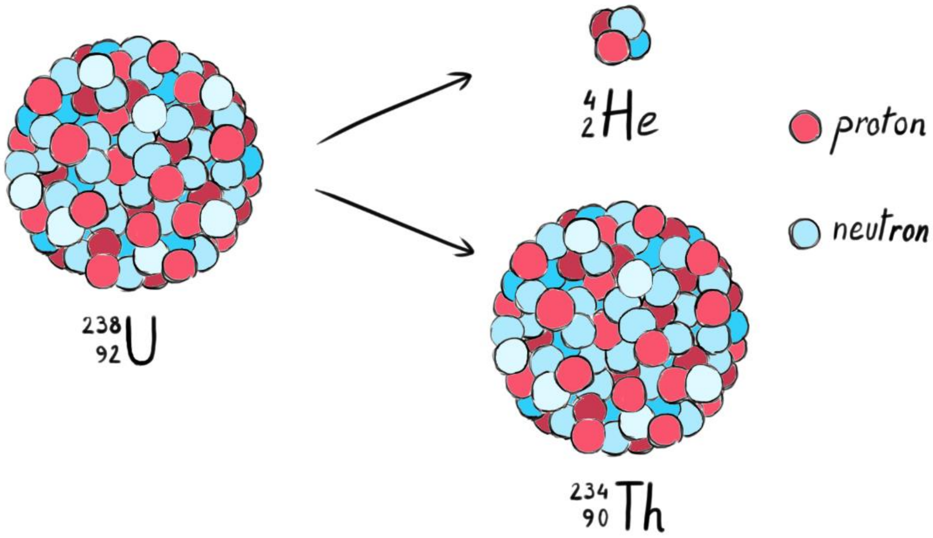

Figure 1.29 Schematic depiction of alpha decay.

An example of α-decaying atom is radon-226, which emits one α particle forming radon-222.

$$^{226}_{138}Ra \rightarrow ^{222}_{136}Ra + ^{4}_{2}He$$

Beta decay: The β-emission can take place in two different ways: beta-minus (β^-) and beta-plus (β^+) decay.

β^- decays are characterized by the emission of an electron and an antineutrino ($\bar{\nu}_e$) from the beta-emitting isotopes, which are generated by the transformation of a neutron into a positron. The resulting atom will present an increased by one atomic number ($Z = Z_0 + 1$) while the mass number remains unaltered ($A = A_0$) (Figure 1.30). β^- decay generally occurs because of the instability caused by an excess of neutrons in neutron-rich nuclei. β^- particles are high-energy electrons emitted during this type of decay which presents a higher penetration and a lower ionizing effect, compared to alpha particles. They are rapidly absorbed by the surrounding matter, and from this interaction x-rays are formed. A typical beta decay process involves carbon-14, often used in radioactive dating techniques.[145] The reaction forms nitrogen-14, an electron and an antineutrino:

$$ {}^{14}_{6}C \rightarrow {}^{14}_{7}N + {}^{0}_{-1}e^{-} + \bar{\nu}_e $$

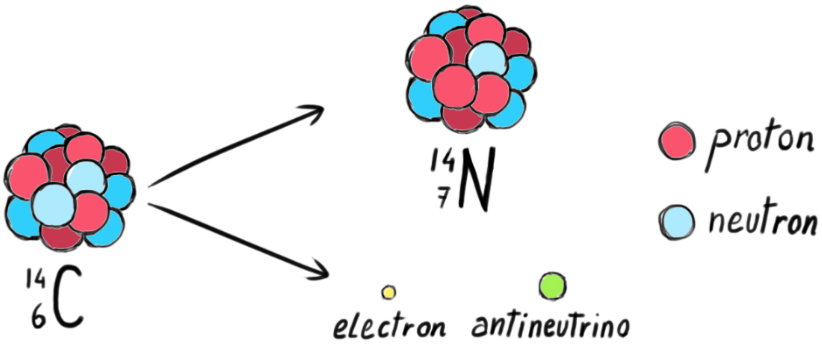

Figure 1.30 Schematic depiction of β^- decay.

On the other hand β^+ decay, commonly referred to as "*positron emission*", generally occurs in proton-rich nuclei, unstable for an excess of protons. In this case, a proton converts itself into a neutron, ejecting from the nucleus a positron and a neutrino (Figure 1.31). This β^+ particle travels for a short distance and is annihilated from the interaction with an electron. The annihilation of both electron and positron produces a pair of gamma photons at 511 keV, moving in opposite directions. This phenomenon is exploited in the imaging technique PET, which by measuring the angulation of the emitted gamma rays can localize the emitting radionuclide inside the patient. In this case the decay product presents a reduced by one atomic number ($Z = Z_0 - 1$), and the mass number remains unchanged ($A = A_0$) as for β^- decay. Different positron-emitters (e.g.^{18}F, ^{11}C, ^{13}N and ^{15}O) are used in nuclear medicine for diagnostic purposes in PET technology. An example of this kind of nuclear reaction is:

$$ {}^{18}_{9}F \rightarrow {}^{18}_{8}O + {}^{0}_{1}e^{+} + \nu_e $$

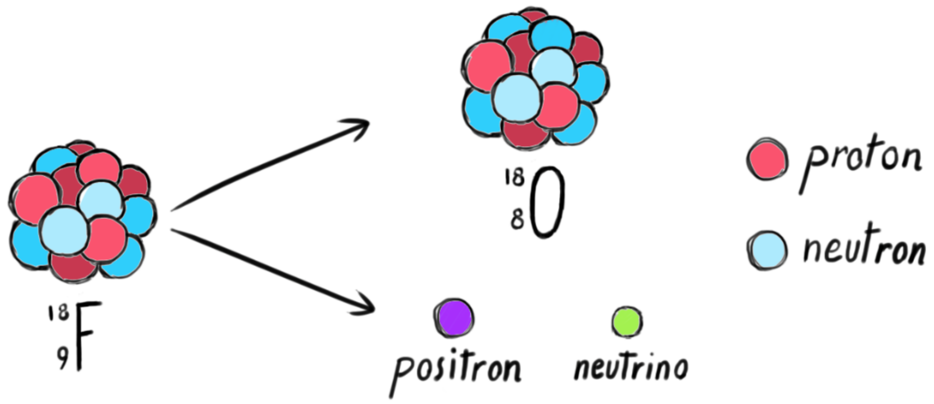

Figure 1.31 Schematic depiction of β$^+$ decay.

Electronic capture: It is an additional way for a nuclide to increase its neutron to proton ratio. An electron from an inner orbital is captured by the nucleus of the atom and combined with a proton to form a neutron. The energy is released with the emission of a neutrino (Figure 1.32). The species resulting from electron capture reactions present once again a reduced by one atomic number ($Z = Z_0 - 1$), and an identical mass number ($A = A_0$), as for β$^+$ decay. An example is Silver-106, which undergoes electronic capture to become Palladium-106:

$$^{106}_{47}Ag \rightarrow {}^{106}_{46}Pd + \nu_e$$

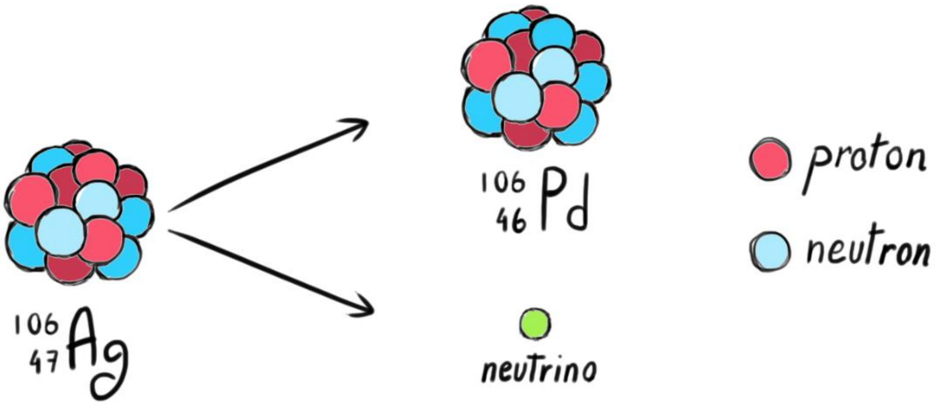

Figure 1.32 Schematic depiction of decay by electron capture.

Gamma decay: it is the decay of an unstable radionuclide to a lower energy state by emission of a gamma ray photon. There are no changes of atomic number ($Z = Z_0$) or atomic weight ($A = A_0$) in a simple γ-emission. γ-photons are highly penetrating particles, which require large amounts of shielding mass to reduce their energy to levels which are not harmful to living cells. In contrast to alpha particles, which can be stopped by paper or skin, and beta particles, which can be shielded by thin aluminum, γ-rays are best absorbed by materials with high atomic numbers and high density, such as lead shield. If not blocked, these particles are able to cross completely the tissues and cause dangerous effects like burns, genetic mutations and cancers.

POSITRON EMISSION TOMOGRAPHY

Positron Emission Tomography (PET) is a functional molecular imaging technique that uses radioactive substances, known as radiotracers, to visualize and measure changes in metabolic processes. It is an essential clinical tool for the diagnosis of several diseases. Different tracers can be used for various imaging purposes, depending on the target process to be investigated. The radiotracer is administrated to the patient right before the examination, then the scanner detects the spatial and temporal distribution of the radiotracer by detecting the emission of γ-rays. The events leading to this detection are:

1. Positrons are emitted by β^+ decay;
2. Positrons are slowed down, which is necessary for the annihilation reaction between these positrons and shell electrons of neighbouring atoms to occur. The distance covered by the positron (free path) depends on the energy of the β^+ decay but is typically one or a few millimetres;
3. The annihilation reaction produces two γ-rays (511 keV) which travel in almost exactly opposite directions (due to the conservation of energy and momentum laws);
4. The two gamma rays are detected by a scintillator in the scanning device, creating a burst of light that is detected by photomultiplier or photodiodes;
5. After the filtration of the collected raw data, sinograms are reconstructed into an image.[146]

In a coincidence counting system, the detection of one gamma ray by one detector results in the opening of an electronic time called "*window*", during which the detection of a second gamma ray in a different detector results in the counting of a coincidence event. The radioactive decay leading to the detection of such a coincidence event must have occurred along a straight line connecting the two detectors. Since the probability of absorption of the two gamma rays is independent from the position of the event along that imaginary line, PET is a quantitative imaging method allowing the measurement of regional concentrations of the radiotracer injected. In other words, from the measurement of the position in which the photons hit the detector, it is possible to reconstruct the hypothetical position in the body from which they were emitted, allowing the evaluation of the radioactivity of the sections of the body investigated. The resulting image represents the tissues in which radioactive molecules are more concentrated (Figure 1.33).

A radiotracer is a chemical entity, just like other medicinal molecules or xenobiotics in general, containing one radioactive atom in his structure. Radiochemical compounds are metabolized by the liver or by other metabolizing tissues, like the kidney. Different metabolites are produced during this process, and some of them may still contain the radioactive atom. These secondary products could have a different distribution, and this can lead to several errors in the interpretation of the image. There are three different PET analysis methods:

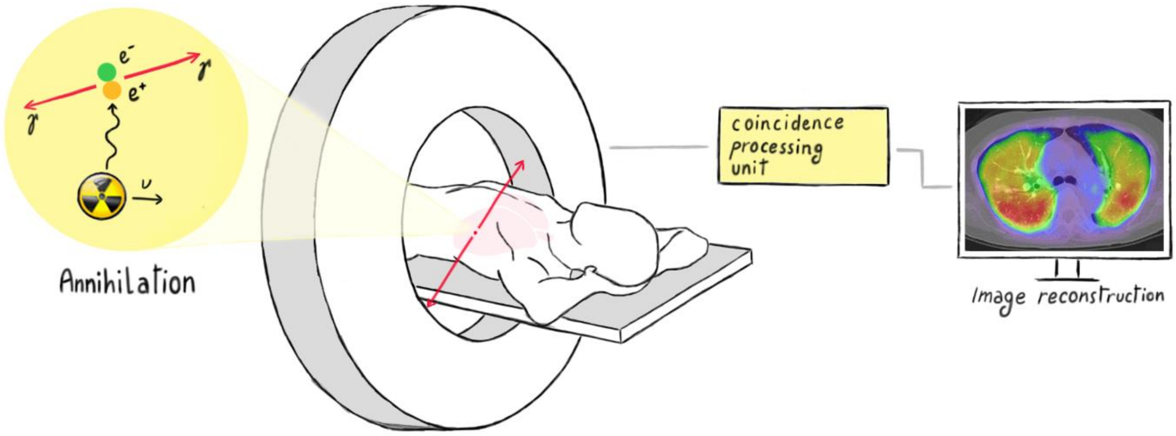

Figure 1.33 Operating PET scheme: a radiotracer decays via positron emission, then the annhilation between the positron and an electron produces two gamma rays, detected by a scintillator. The sinogram is processed and reconstructed in an image.

Qualitative method: the operator researches the accumulation of the radiochemical in the ROI (Region of Interest);

Semi-quantitative method: the accumulation of the radiotracer in ROI is assessed in relation to the background and normalized with the administered activity, using specific analysis programs. An important parameter to consider is the SUV (Standardized Uptake Value), that is the ratio between the uptake of the radiotracer in the site of interest and the weight of the patient multiplied by the administrated dose.

Quantitative method: it is a method to evaluate the kinetic accumulation of the radiotracer in the organ or in the tissue of interest with dynamic PET, blood sampling and programs able to provide quantitative parameters of the radiochemical compound, like concentration at the accumulation site.

In preclinical studies it is necessary to sacrifice animals to analyze the tissue metabolites doing an autoradiography to thin slice of tissue, to evaluate the repartition of the radiopharmaceutical in the organism. Mice and rats are mainly used for preclinical animal *in vivo* studies. This kind of analysis is useful to investigate some biological characteristics of radiotracers, like biodistribution over time, pharmacokinetics and uptake in tumor. A radiotracer is normally injected into the blood stream. For the analysis is used a dedicated animal PET instrument, called micro-PET.

It is important to consider the possible clinical utility of a potential radiotracer, since its final target is the human administration. For this reason it must present:

- High specificity and selectivity;
- High plasma clearance and low plasma protein binding;
- Neutral and hydrophilic characteristics to enhance elimination and reduce effective (radiation) dose;
- Low toxicity;
- Good *in vivo* stability;
- Sub-nanomolar or nanomolar affinity for the physiological target, to avoid any interference with normal biological function;
- Easy and quick production, with a reasonable radiochemical yield;
- Easily detectable during analysis;
- Reproducible pharmacokinetics;
- Limited or measurable metabolism;
- Half-life suitable with the biological process which is intended to study;
- β^+ decay process (other types of emission are not useful for image generation in PET and represent useless absorbed dose for patient).

Moreover, permeability through the blood-brain barrier (BBB) is necessary for radiotracers acting at the cerebral level. Molecules with a good lipophilicity and without charges are normally drugs capable to cross the BBB by passive diffusion.

Finally, molecular imaging methods such PET are increasingly involved in the development of new drug candidates.[53] PET can support the research and development of new drugs by giving fast access to in vivo data in the preclinical phases to verify the drug biodistribution and target engagement, and in the clinical phases to optimize the dosage and establish the efficacy of the drug.

Indeed, PET includes four principal roles in drug research:

i. to define if a biological target is associated with a specific disease;
ii. to examine the drug candidate’s biological parameters, which may include target engagement, nonspecific binding, passage across the BBB, and metabolism, allowing to conclude if the drug candidate is suitable to treat the disease of interest;
iii. to provide a deeper understanding of the drug mechanism of action, its biological interactions and properties. For example, to clarify if a drug effect is caused by interaction with one or several biological targets or whether there is a relationship between the plasma levels of a drug candidate and the target engagement;

iv. to determine the optimal dosing of a drug: in preclinical PET investigations, a broad range of plasma concentrations can be investigated in order to evaluate the drug-binding curves and to assign the behavioural or cognitive surrogate markers of efficacy. In clinical studies PET can help to identify an appropriate dose range using only a small group of healthy volunteers, therefore it can accelerate drug development, may minimize the risk of adverse events and reduce the required group size for clinical trials.

CHEMISTRY OF RADIOACTIVE NUCLEI (^{18}F, ^{11}C, ^{68}Ga)

Different are the radionuclides used nuclear medicine. This wide family can be initially divided between therapeutic and diagnostic nuclei: the first group composed mainly by α and β^- emitting radionuclides and associated with proteins and antibodies for the radio-immunotherapy and the treatment of cancer (e.g. ^{131}I and ^{32}P), while the second group is composed by single-photon emitting or positron emitting radionuclides, used for the imaging of pathological processes. In clinical PET, because of their suitable half-life, fluorine-18 (^{18}F) and carbon-11 (^{11}C) are two of the most used β^+ emitting radionuclides. In addition, non-conventional positron emitters, like ^{68}Ga can be used for their peculiar characteristics in PET imaging. The choice on the more appropriate radioactive atom to use for the design of a tracer should be based on the half-life of the radiochemical, the efficiency of the synthetic pathway, the position for the introduction of the radionuclide and the yield of the radiolabeling reaction.

Fluorine-18 (^{18}F) is a radionuclide with nine protons and nine neutrons. It presents some favorable properties for its application in PET imaging:

- It forms strong covalent bonds with carbon in place of an appropriate leaving group;
- Its half-life of 109.77 minutes is compatible with pharmacokinetic of the labeled compound and guarantees longer kinetic studies and low energy of the emitted positron, allowing better spatial resolution of the PET investigation;
- It can be introduced in a wide variety of organic molecule being a bioisostere of hydrogen atoms or hydroxyl groups. In fact, fluorine presents a Van der Waals radius completely similar to hydrogen one, and therefore the replacement would not involve any change in steric encumbrance in the labelled molecule. However, since fluorine is more electronegative than hydrogen, it is possible that the molecule acquires different biological properties. Nevertheless, fluorine could also replace a hydroxyl group without substantially modify the electronegative characteristics of the final molecule.[53]

To obtain Fluorine-18, [^{18}O]H_2O (water enriched with Oxygen-18) is bombarded with protons accelerated in a cyclotron. This type of production leads to [^{18}F]F^- in aqueous solution as product, that is not suitable for typical radiolabeling reactions (that usually require anhydrous environment). Therefore, [^{18}F]F^- is trapped on an anion-exchange separating cartridge, and then eluted with a ionic solution containing K^+, to form [^{18}F]KF. Potassium weakly binds [^{18}F]F^-, making [^{18}F]KF a very good reactive species for nucleophilic substitution. It is important to note that radiolabeling reactions are normally conducted in organic solvents, in which KF is not very soluble. To make it more soluble, a cryptand is usually employed. Cryptands are a family of synthetic polycyclic multidentate ligands for various cations. The most commonly used cryptand is 4,7,13,16,21,24-hexaoxa-1,10-diazabicyclo[8.8.8]hexacosane, also known as

Kryptofix®222 (K222) (Figure 1.34). It is a crown ether that complexes ions in its cavity and the resulting complex is lipophilic species, soluble in organic solvents. The most used eluting mixture is K_2CO_3 / Kryptofix®222.

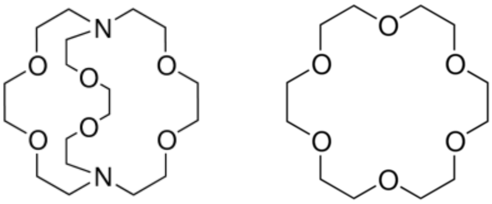

Figure 1.34 Structure of Kryptofix (K2.2.2) on the left, and structure of 18-crown-6 on the right.

Another mixture is K^+/18-crown-6 (1,4,7,10,13,16-hexaoxacyclooctadecane) with the addition of bicarbonate. This mixture produces less basic conditions and it can be used with products labile at alkaline pH. The elution solvent is then evaporated to have a completely anhydrous environment. It is important to note that in a radiosynthesis the limiting agent is the radioisotope. For this reason, in the reaction vessel there is a large excess of compound to be labeled. At the end of the synthesis all the non-reacted $[^{18}F]F^-$ should be removed to avoid interference with the radiolabeled compound during the imaging.

Carbon-11 (^{11}C) is a radionuclide with six protons and five neutrons. With a half-life of 20.334 min, ^{11}C is produced from proton bombardment *via* a $^{14}N(p,\alpha)\,^{11}C$ reaction. The target material is $[^{14}N]N_2$ containing trace quantities of oxygen, in order to obtain $[^{11}C]CO_2$. This radioactive carbonic anhydride is then transferred from the target to an automated module where it is trapped on molecular sieves at room temperature. There, it is converted into a reactive chemical species that facilitates incorporation into biologically active molecules. One of the most common transformation the reduction of the anhydride to the corresponding methyl iodide derivative (Figure 1.35).[147] $[^{11}C]CH_3I$ is a highly reactive species that can be used to introduce ^{11}C into biologically-active molecules via alkylation of ammino, hydroxy or mercapto groups. The $[^{11}C]CO_2$ trapped on molecular sieves is reduced by catalytic hydrogenation at 350°C. The $[^{11}C]CH_4$ produced is released from the solid support and it is purified and dried using a column filled with Ascarite (NaOH-coated silica, which traps impurities) and phosphorus pentoxide, which is a desiccant and dehydrating agent. Then, radioactive methane is trapped on a resin of Carboxen, and solidified at -75°C, removing the remaining gaseous impurities. $[^{11}C]CH_4$ is finally conveyed through a quartz serpentine containing solid I_2 at 720°C. In these conditions the radical iodination of methane takes place, generating methyl iodide. The produced $[^{11}C]CH_3I$ is then purified with two traps of Ascarite, and then it is trapped on a Porapak Q (Porous Polymer Adsorbent) column at room temperature. The reactive compound is released from the resin by heating at 190°C.

Another highly reactive form of carbon-11 is [^{11}C]methyltriflate. [^{11}C]CH_3OTf is obtained by passing gaseous [^{11}C]CH_3I over a column containing silver triflate (AgOTf) at 200°C. This triflate derivative is bulkier then methyl iodine, and it presents higher reactivity. In this way it is possible to have more selective reactions on less-hindered nucleophilic groups, and also to use lower amounts of compound to be labeled and a shorter reaction time.

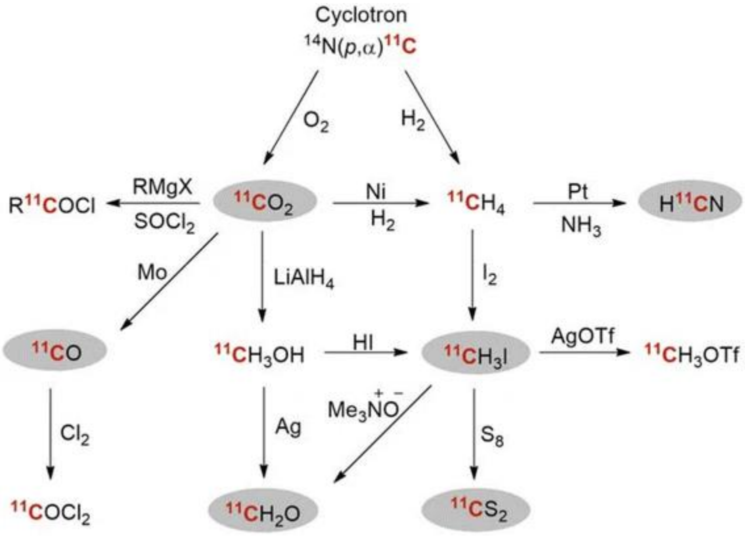

Figure 1.35 Synthetic strategies for the preparation of the different carbon-11 derivatives.

Gallium-68 (^{68}Ga) is a radionuclide with 31 protons and 37 neutrons. As previously reported, it presents an half-life of 68 minutes, and it is usually produced as ^{68}Ga (III) in ^{68}Ge/^{68}Ga generators. The labeling with this radionuclide is performed using suitable chelating agents (e.g. DOTA and NODA-GA, Figure 1.36), which are generally introduced in the structures of peptides and proteins for the imaging of cancers.

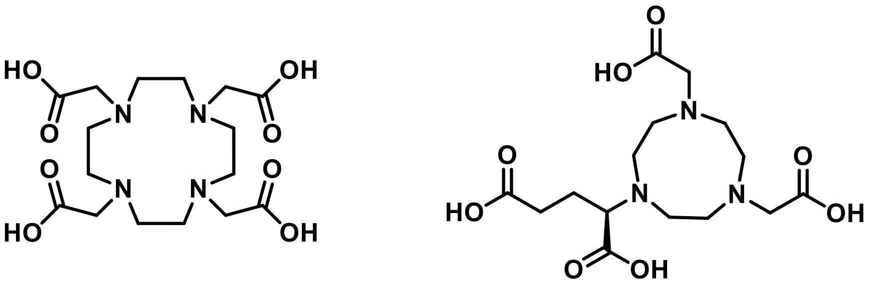

Figure 1.36 Chelating agents used for the introduction of metallic radionuclides in organic structures.

RADIOLABELING STRATEGIES

Based on the characteristics of the radionuclide, the choice of the radiolabeling strategy is a critical stage that can influence the outcome of the radiotracer production. On this decision it will also depend the design of the "*cold precursor*", which is the final synthetic step before the introduction of the radionuclide in the molecule. The necessity to perform the radiolabeling reaction as late as possible during the synthetic pathway is due to the short half-life of the clinically-used radionuclides and to maximize the radiochemical yield of the whole synthesis.

There are various labeling strategies for the introduction of the different radionuclides.

Labeling with *gallium-68* is usually mediated by chelating agents (Figure 1.36), which ensure high radiochemical yield using mild reaction conditions. As a drawback, the integration of this bulky chelators in the structure of small molecules or peptides can alter their biological properties and the ability to interact with their target. Thus, it is essential to evaluate the most suitable position for the conjugation of the chelator and the compound to be labeled.

Carbon-11 can be prepared as different species (Figure 1.35), and be introduced in chemical compounds forming different functional groups. For example, radioactive carbonic anhydride $[^{11}C]CO_2$ is obtained from the proton bombardment of ^{14}N if a small amount of oxygen is present in the cyclotron, and can be used for the formation of carboxylic acids, carbamates and ureas. On the other hand, if a small amount of hydrogen is present in the cyclotron target it is possible to obtain radioactive methane $[^{11}C]CH_4$, which can be used to produce reactive species as $[^{11}C]HCN$ or $[^{11}C]CH_3I$. radioactive methyl iodine is one of the most commonly used forms of carbon-11, and can be easily employed as methylating agent on nucleophilic groups of the cold precursor, such as amine, hydroxy and mercapto groups.[147]

Fluoride-18 is a bioisostere of both hydrogen and hydroxyl groups. Thus, it is possible to design ^{18}F-labeled radiotracers based on the structures of lead compounds already presenting a fluorine atom in their structures, or by chemically modifying the structure of the molecule of interest with substitutions between moieties with similar electronic (OH vs F) or sterical (H vs F) characteristics. The first group is referred to as *isotope tracers* (e.g. $[^{18}F]$Flumazenil, $[^{18}F]$Paroxetine), while the latter as *analogue tracers* (e.g. $[^{18}F]$FDG, $[^{18}F]$FDOPA) (Figure 1.37).[53] These different radioactive derivatives are obtained with different radioactive strategies, based on which form the radioactive fluorine is produced.

Fluorine-18 can be prepared in two chemical forms: positively charged (electrophile) or electron-rich (nucleophile). Electrophilic fluorine is produced by proton bombardment of oxygen-18 $[^{18}O]O_2$ forming $[^{18}F]F_2$ with the emission of a neutron. Similarly, nucleophilic

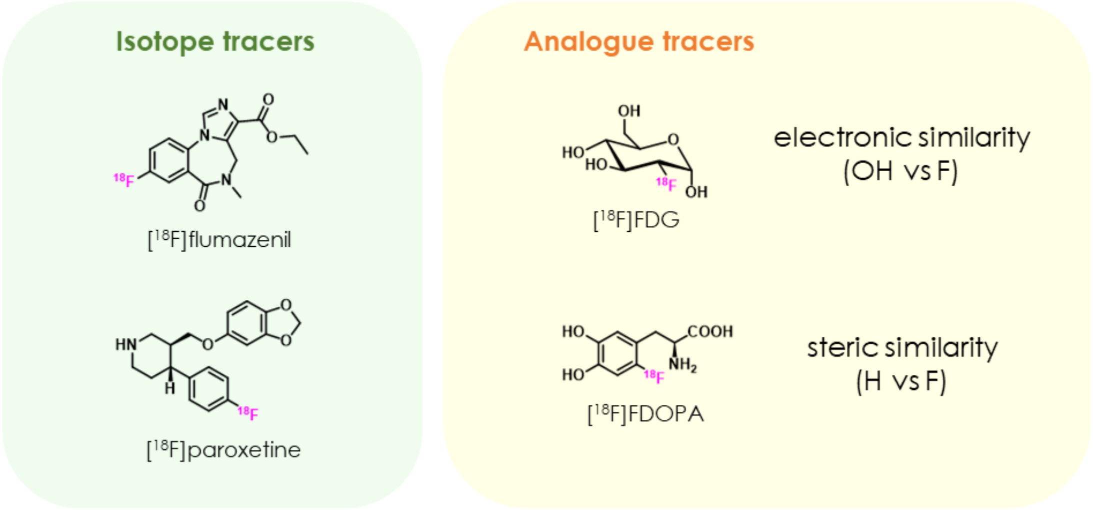

Figure 1.37 Example of structures of isotope tracers, already presenting a fluorine atom in the structure of their lead compound, and analogue tracers, with the different strategies for the introduction of fluorine in the designed structure of the tracer.

fluorine is obtained from the proton bombardment of enriched water [^{18}O]H_2O, forming radioactive fluoride ions [^{18}F]F^- in water solution. The nucleophilic form is usually preferred because of its easier handling and its higher selectivity in the radiolabeling reactions. Nucleophilic displacement which is usually used for *aliphatic fluorination reactions*, involves the SN_2 substitution of ^{18}F ion and alkyl substrate containing leaving groups such as halogens or sulfonic esters (Figure 1.38 a). These substitutions are usually done in a moderate temperature of 80 – 115 °C for 5 – 15 minutes. The efficiency of the nucleophilic displacement will be higher the more reactive is the leaving group. However, the high reactivity of these groups should be balanced with the stability of the compound, since it could lead to cold precursors unstable to the fluorination condition, causing potential side reactions such as elimination.

Aromatic fluorination reactions, on the other hand, are rarely performed with the same nucleophilic conditions as for the aliphatic substitution. In fact, aromatic SN are limited to electron deficient arenes, using nitro or quaternary trimethylammonium functions as leaving groups (Figure 1.38 b). Another way could be the use of diaryliodonium salts, which can mediate the nucleophilic fluorination without the need of electron withdrawing groups resulting in the [^{18}F]fluoroarene and the corresponding iodoarene (Figure 1.38 c).[148] Finally, [^{18}F]F^- can be introduced in an aromatic ring *via* cupper-mediated oxidative transmetallation reactions (Figure 1.38 d).[149] In this case, $Cu^{II}(OTf)_2$ mediates the reaction between the nucleophilic fluoride-18 and the arene substituted with suitable metal groups, such as boron acid/ester or organotin groups (Figure 1.39).

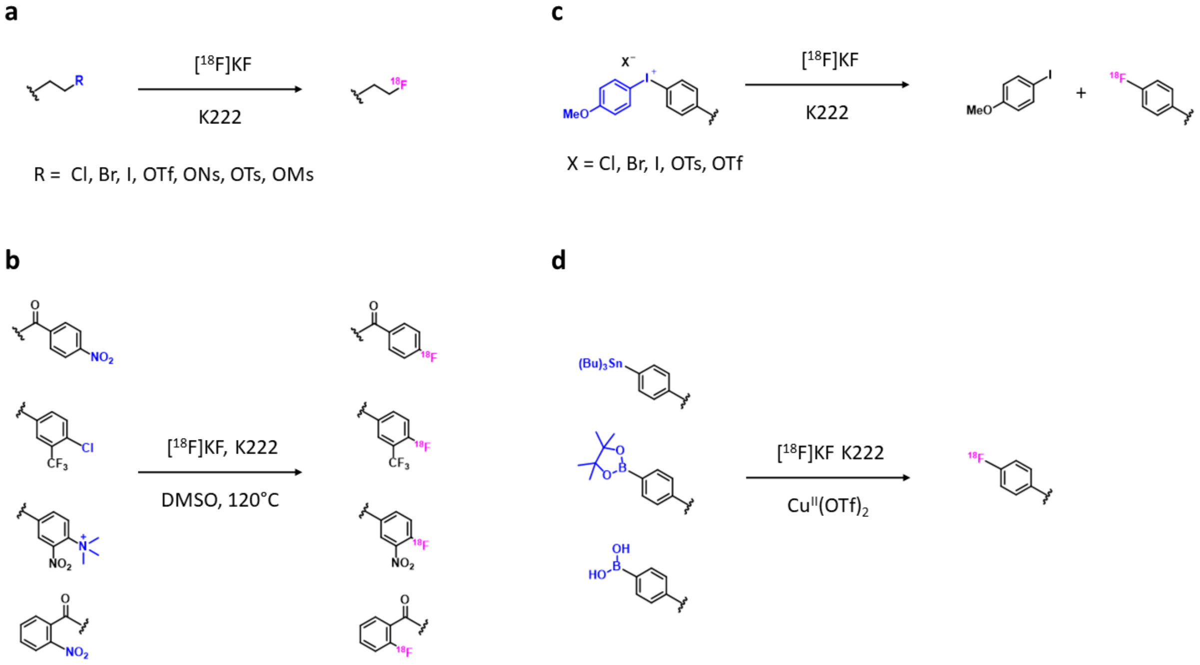

Figure 1.38 Main synthetic strategies for the radiolabeling with ^{18}F: a) aliphatic radiofluorination, b) aromatic radiofluorination SN-mediated, c) aromatic radiofluorination via diaryliodonium salt, and d) oxidative radiofluorination cupper-mediated.

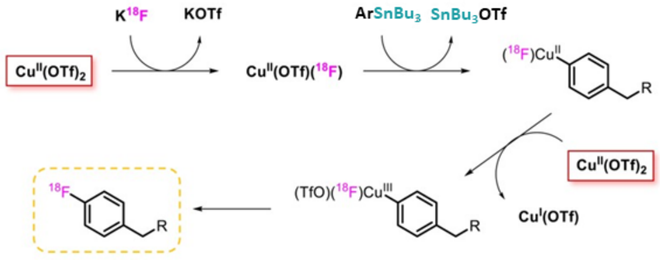

Figure 1.39 Mechanism of cupper (Cu^{II})-mediated oxidative transmetallation reactions.

CONCEPTS IN RADIOPHARMACEUTICAL CHEMISTRY

The following are a series of crucial parameters in a radiosynthesis process:

Radiochemical yield: it is defined as the ratio between the radionuclide activity employed for the radiosynthesis and the final activity of the desired compound. It is important to note that is possible to take two different reference times: normally is represented by the end of the bombardment (EOB), but it could also be represented by the end of radiopharmaceutical synthesis (EOS);

Specific activity: it is defined as the activity of a material divided by the mass of the material. Its characteristic unit of measurement is Bq/mg, where the Becquerel is defined as the number of radioactive transformations per second that occur in a particular radioactive isotope.

Molar activity: more relevant for medical applications than specific activity, it is defined as the activity of a radiolabeled compound divided by its molar amount. Its characteristic unit of measurement is Bq/mol or GBq/µmol.

Chemical purity: it is defined as the measurement of the number of impurities found in a chemical sample. It is important to confirm the chemical identity of the molecule and absence of other unwanted chemical substances.

Radionuclidic purity: it is defined as the ratio of the radioactivity of the desired radionuclide on the total radioactivity of the source. Radionuclidic purity is important because some radionuclidic impurities may increase the radiation dose received by the patient. Measurement of radionuclidic purity is usually performed using gamma-ray spectroscopy or half-life determination.

Radiochemical purity: it is defined as the percentage of radioactivity due to the desired labeled product respect to the total radioactivity. Radiochemical purity is important because the diagnostic image obtained could be obscured by radiochemical impurities which have different patterns of biodistribution. HPLC, GC, and TLC are used as methods to separate the different chemical species.

Apyrogeniticy: it is defined as the absence of endotoxins that can cause fever.

Sterility: it is defined as the absence of microorganisms in the preparation.

pH: the radiopharmaceutical must have pH included in the range of physiological acceptability (4.5 – 8.5) compatibly with the chemical stability of the product. Indeed, a too acid pH will cause pain during the administration of the radiochemical compound.

Stability: there are many factors to be considered, especially the half-life of the radionuclide, but also decomposition due to radiation (autoradiolysis) or oxidation.

CHAPTER TWO

Aim of the thesis

AIM OF THE PROJECT

In the field of molecular imaging, PET holds an essential role in both the diagnosis and treatment of diseases and in the discovery of new drug candidates. This project aims to apply this technique for the design and synthesis of new molecular imaging biomarkers targeting biological systems for which suitable radiotracers are not currently available.

This PhD project was developed following two main approaches of application of PET:

- *Monomodal approach*, for the development of radiolabeled small molecules suited for the PET imaging;
- *Multimodal approach*, for the labeling of peptides with both means for PET and optical imaging.

At first, the *monomodal approach* was focused on the development of PET tracers for the inflammatory processes involved in fibrosis, which is a final pathological feature of many chronic diseases.[121] Chronic tissue injury leads to a sustained scarring response with an abnormal tissue regeneration process, which gradually disrupts normal cellular functional units and eventually causes failure in multiple epithelial organs such as lungs, liver, and kidney. Failure to fully control or eliminate inducing factors exacerbates inflammation and chronic wound-healing responses, leading to the replacement of normal tissue by scar tissue, and ultimately organ failure. The ability to recognize early stages of fibrosis noninvasively is an urgent and clinical need that could improve the management of patients and increase the survival rate.

Among the many cellular and molecular mechanisms that contribute to progressive fibrosis,[119] one of the most promising targets for the development of an imaging strategy is the Wnt/β-catenin pathway. Wnts are glycoproteins that play an essential role in organogenesis and tissue homeostasis.[150] Upon binding to their receptors, Wnt proteins induce a cascade of intracellular events culminating in the stabilization of β-catenin and its translocation to the nucleus. The interaction between the nuclear β-catenin, the T cell factor (TCF) and coactivators, cyclic AMP response element-binding protein (CBP), or its closely related homolog p300, generates a transcriptionally active complex which regulates the expression of a range of genes involved in promoting proliferation and differentiation. So far, the pathologically activated Wnt/β-catenin pathway has been implicated in the pathogenesis of pulmonary, kidney, and liver fibrosis,[151-153] as well as in the initiation and progression of cancer.[154] CBP has been demonstrated to be overexpressed in both pulmonary and hepatic fibrosis,[136, 155] and it appears to be a potential target for the development of therapies for these diseases. In a screening for regulators of β-catenin/TCF mediated transcription in the Wnt pathway, the compound **ICG-001** (Figure 2.1 a), bearing the tetrahydro-1*H*-pyrazino[1,2-*a*]pyrimidine-4,7(6*H*,8*H*)-dione skeleton, a β-turn bicyclic peptidomimetic scaffold, proved to be one of the most potent inhibitors.[139] It is a competitor of β-catenin for the CBP binding site (IC_{50} = 3 μM, Kd ≈ 1 nM), and it is able to ameliorate both lung and liver fibrosis during *in vivo* experiments.[131, 153] In order to identify its biological target, a biotinylated derivative of this compound, **ICG-002** (Figure 2.1 a), was prepared and attached to streptavidin-agarose beads. These were used as stationary phase in an affinity purification assay of cell lysates of different human colon carcinoma cell lines. In this way, it was possible to identify CBP as the biological target of the molecule.

A further mechanism of inhibition of the CBP transcriptional activity is found in selective inhibitors of its bromodomain (BRD).[133] CBP-BRD is involved in the post-translational modification and recruitment of histones and non-histone proteins, and its interaction is crucial for the response mediated by the p53 gene to cellular stress. The inhibition of CBP-BRD has potential clinical applications: it can protect healthy tissues from p53-mediated damage caused by radio- and chemo-therapy, as well as can be applied for the treatment of neurodegenerative, autoimmune, and ischemic disorders related to hyperactive p53.[156] SGC-CBP30 and its fluoro derivative **Cmpd 63** (Figure 2.1 a) are potent, selective and cell-active CBP BRD inhibitors (K*d* = 0.021 and 0.039 µM, respectively) described by

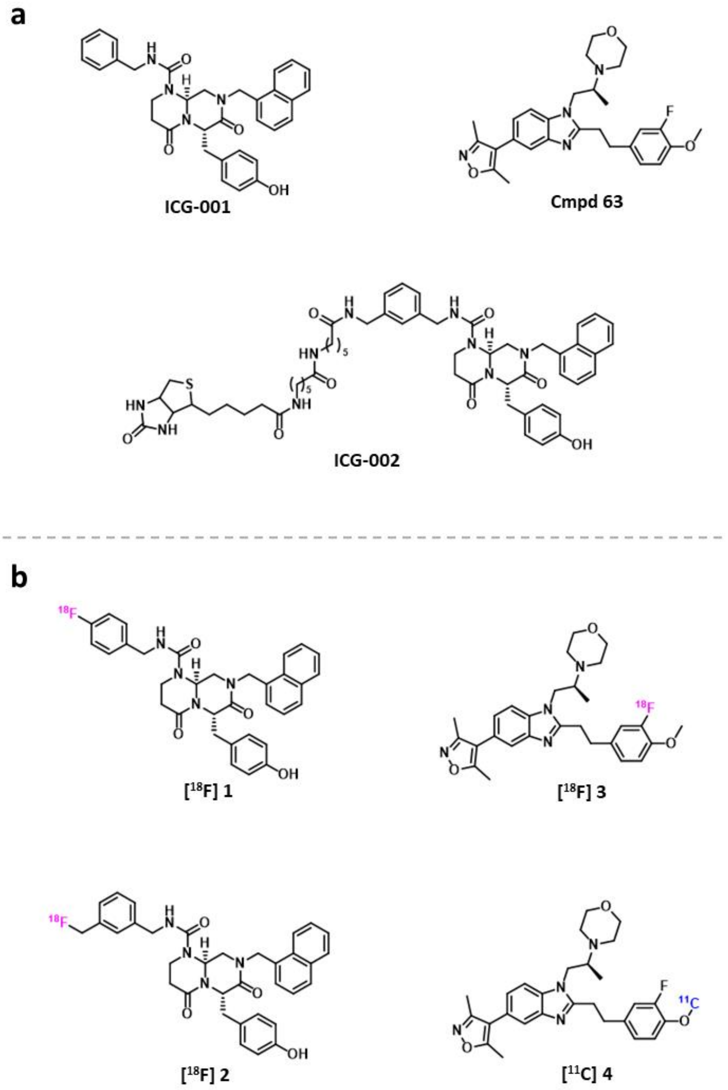

Figure 2.7. a) Structures of the lead compounds **ICG-001**, **ICG-002** and the SGC-CBP30 fluorinated derivative **Cmpd 63**, along with b) the labeled derivatives **1** – **4**.

Hay et al.[133] and they represent promising lead compounds for the development of clinical candidates.

The present research activity was focused on the development of novel biomarkers targeting pathways involved in the fibrotic process. To accomplish this, after choosing the biological targets, high-affinity ligands suitable to be converted in radiolabelled compounds were identified. Then, the cold precursors were designed and synthesized, and through their radiosynthesis, the final radiomarkers were obtained. Additionally, the reference compounds were prepared, which are used as standards to obtain both analytical and physiological data of the new entities. In particular, the CBP high-affinity ligands **ICG-001** and **ICG-002**, together with the fluorinated derivative of CBP BRD inhibitor SGC-CBP30, **Cmpd 63**, were chosen as lead compounds. The corresponding new PET radiotracers **[^{18}F] 1**, **[^{18}F] 2**, **[^{18}F] 3**, and **[^{11}C] 4** were designed and synthesized (Figure 2.1 b), then the derivatives which obtained the best radiolabeling results were tested *in vitro* on two different CBP-expressing cell lines.

Besides this first research activity, the application of a multimodal strategy allowed the development of dually labeled multimodal imaging agents targeting different tumor biomarkers.[157] This part of the project aimed to test and expand the theory correlating the total net charge of the conjugates with their binding affinity to the respective target. This correlation derived from the results of a series of PESIN homodimer and homotetramer conjugates, but its validity was still to be proven for the corresponding monomeric derivatives. Therefore, a first series of PESIN-monomer-based imaging agents characterized by a MIU containing (1,4,7-triazacyclononane-4,7-diyl)diacetic acid-1-glutaric acid (NODA-GA) as chelator and various fluorophores (**1 – 3 a**, Figure 2.2, Table 2.1) was synthesized. The chosen fluorescent dyes were a pyrylium salt, dansyl chloride, and a carboxylic derivative of indocyanine green (ICG), which were selected for their different ionic charge in aqueous solution (+1, 0, and -1, respectively). Moreover, to study the influence of the MIU on the chemical, biological and photophysical properties of the resulting conjugates, a reference compound (**4 a**) with the imaging unit bearing only the NODA-GA chelator but lacking the fluorescent dye was prepared. Finally, to verify if this concept could be applied to other receptor systems besides GRPR, two additional series of imaging agents, combining the previously described MIUs with two cyclic peptides were synthesized: the melanocyte stimulating hormone (α-MSH) derivative Nle-c(DHfRWK)[158] addressing the melanocortin-1 receptor (MC1R) (series **1 – 4 b**), and the cyclic peptide c(RGDfK)[159] targeting integrin $\alpha_v\beta_3$ (series **1 – 4 c**, Figure 2.2, Table 2.1). For all the synthesized conjugates the photophysical and chemical properties were determined, as well as the in vitro binding affinity to their respective receptor.

Along with the hybrid compounds of the first series, it was prepared a fluorescein-based monomeric PESIN derivative (**5 a**, Figure 2.2, Table 2.1), whose binding affinity resulting from the displacement assays apparently did not fit in the charge-cell binding correlation under test. To justify this aberrant behaviour, the spectroscopic properties of the fluorescein-based monomeric and dimeric PESIN derivatives (**5 a** and **7 a**) were analyzed.

Moreover, as a comparison set of equally charged conjugates, a series of tartrazine-based PESIN derivatives (**6 a** and **8 a**, Figure 2.2, Table 2.1) was designed and tested.

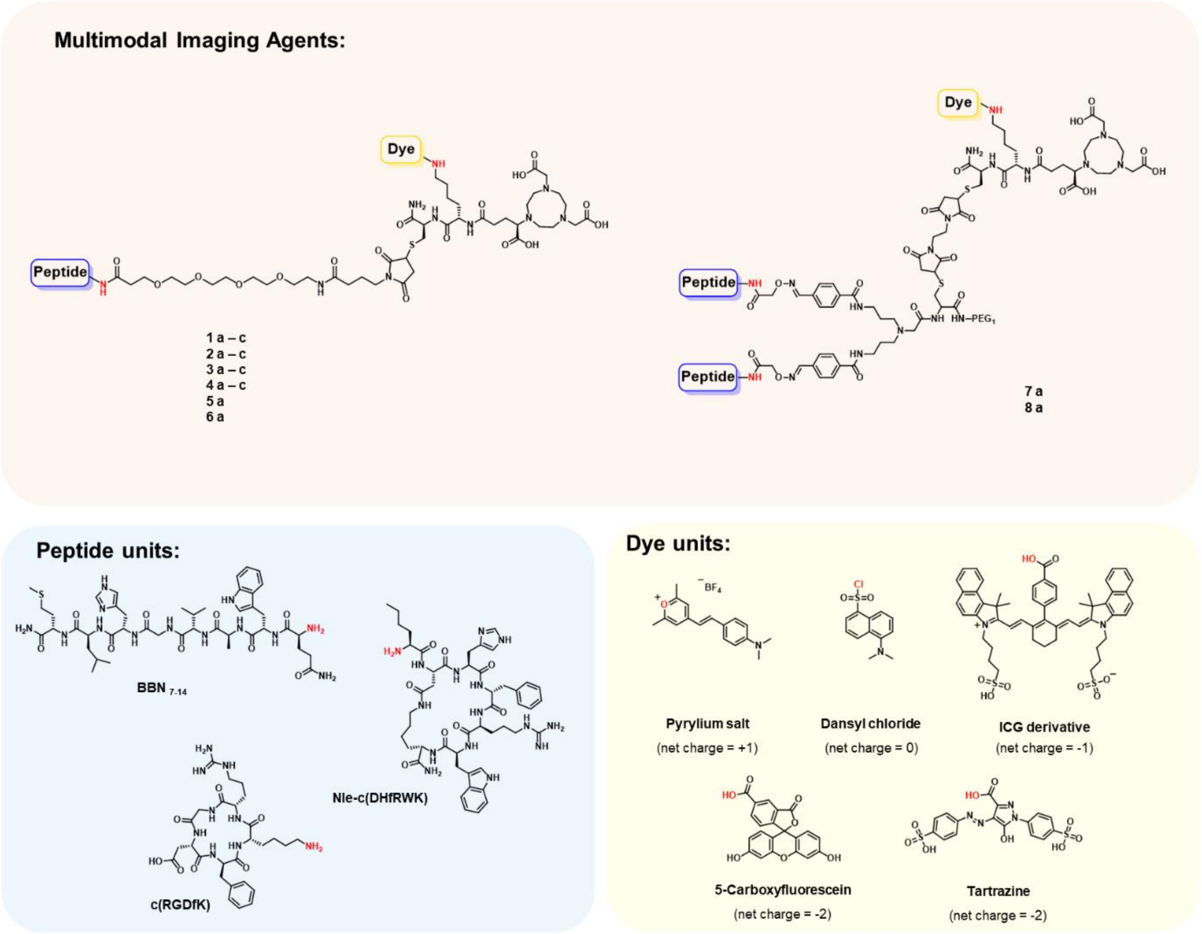

Figure 2.2 Structures of the synthesized multimodal imaging agents: each of the three series is characterized by a peptide unit between **BBN$_{7-14}$**, **Nle-c(DHfRWK)** and **c(RGDfK)**, for the target-specific uptake of the agent. In the same series, the conjugates differ for the fluorescent dye unit characterizing the MIU.

Table 2.1 Numbering of the synthesized compounds relative to the peptide and dye unit characterizing their structure

Peptide	Dye	Conjugate
BBN$_{7-14}$	Pyryllium salt	**1 a** (BBN$_{7-14}$-pyryllium-NODA-GA)
	Dansyl chrloride	**2 a** (BBN$_{7-14}$-dansyl-NODA-GA)
	ICG derivative	**3 a** (BBN$_{7-14}$-cyanine-NODA-GA)
	none	**4 a** (BBN$_{7-14}$-NODA-GA)
	5-Carboxyfluorescein	**5 a** (BBN$_{7-14}$-fluorescein-NODA-GA)
	Tartrazine	**6 a** (BBN$_{7-14}$-tartrazine-NODA-GA)
(Nle-c(DHfRWK)	Pyryllium salt	**1 b** (Nle-c(DHfRWK)-pyryllium-NODA-GA)
	Dansyl chrloride	**2 b** (Nle-c(DHfRWK)-dansyl-NODA-GA)
	ICG derivative	**3 b** (Nle-c(DHfRWK)-cyanine-NODA-GA)
	none	**4 b** (Nle-c(DHfRWK)-NODA-GA)
(c(RGDfK)	Pyryllium salt	**1 c** (c(RGDfK)-pyryllium-NODA-GA)
	Dansyl chrloride	**2 c** (c(RGDfK)-dansyl-NODA-GA)
	ICG derivative	**3 c** c(RGDfK)-cyanine-NODA-GA)
	none	**4 c** (c(RGDfK)-NODA-GA)
BBN$_{7-14}$-dimer	5-Carboxyfluorescein	**7 a** (BBN$_{7-14}$-fluorescein-NODA-GA)
	Tartrazine	**8 a** (BBN$_{7-14}$-tartrazine-NODA-GA)

CHAPTER THREE

Experimental section

MATERIALS AND INSTRUMENTS

All commercially available chemicals and solvents were at least of analytical grade and used, if not otherwise stated, without further purification. Products for the preparation of **[^{18}F] 1**, **[^{18}F] 2**, **[^{18}F] 3**, and **[^{11}C] 4** and their respective reference compounds were purchased by Merck (Milan, Italy). Fmoc-protected amino acids, Benzotriazole-1-yl-oxy-tris-pyrrolidino-phosphonium hexafluorophosphate (PyBOP), and the resins for the peptide synthesis (Rink Amide resin, Rink Amide AM resin LL, Fmoc-Asp-(NovaSyn® TGA)-OAll resin with loading 0.54, 0.34 and 0,18 mmol/g, respectively) were purchased form NovaBiochem (Darmstadt, Germany). 15-(9-Fluorenylmethyloxycarbonyl)amino-4,7,10,13-tetraoxa-pentadecanoic acid (PEG_3, Fmoc-NH-PEG_3-COOH), 8-(9-fluorenylmethyloxycarbonyl-amino)-3,6-dioxaoctanoic acid (PEG_1, Fmoc-NH-PEG_1-COOH), *N*-alpha-(9-fluorenylmethyloxycarbonyl)-S-(*t*Bu-thio)-*D*-cysteine (Fmoc-*D*-Cys(S-S-*t*Bu)-OH), {[*bis*(*t*-butyloxycarbonyl)amino]oxy}acetic acid monohydrate ($(Boc)_2$AOAc-OH x H_2O) and 2-(*bis*(3-(((9*H*-fluoren-9-yl)methoxy)carbonylamino)propyl)amino)acetic acid potassium hemisulfate (TrL, Fmoc-NH-Propyl)$_2$Gly-OH x $KHSO_4$) were obtained from Iris Biotech (Marktredwirz, Germany). *N*-succinimidyl-4-formylbenzoate (95 %) (SFB) and 4-maleimidobutyric acid were obtained from ABCR (Karlsruhe, Germany), and 4-(4,7-*bis*(2-(t-butoxy)-2-oxoethyl)-1,4,7-triazacyclononan-1-yl)-5-(*tert*-butoxy)-5-oxopentanoic acid ((*R*)-NODA-GA(*t*Bu)$_3$) from CheMatech (Dijon, France). *tris*(2-carboxyethyl)phosphine hydrochloride (TCEP) was purchased from Alfa Aesar (Kandel, Germany), and 1,2-*bis*(maleimido)ethane (BME), 2,4,6-trimethylpyrylium tetrafluoroborate, 4-dimethylaminobenzaldehyde, 4-carboxyphenylboronic acid and *tetrakis*(triphenylphosphine)palladium(0) ($Pd(PPh_3)_4$) were purchased from TCI (Eschborn, Germany). Morpholine, *N*,*N*-diisopropylethylamine (DIPEA), triisopropylsilane (TIS), 5-(dimethylamino)naphthalene-1-sulfonyl chloride (Dansyl-Chloride), 5(6)-carboxyfluorescein *N*-hydroxysuccinimide ester, ascorbic acid, tartazine and IR820 from Sigma-Aldrich (Taufkirchen, Germany). Dichloromethane (DCM), diethylether, dimethylformamide (DMF), 2-(1*H*-benzotriazol-1-yl)-1,1,3,3-tetramethyluronium hexafluoro-phosphate (HBTU), trifluoroacetic acid (TFA) and deionized water were purchased from Carl Roth (Karlsruhe, Germany), acetonitrile (MeCN) from Häberle Labortechnik (Lonsee-Ettlenschieß, Germany).

When specified, the syntheses were conducted under a nitrogen atmosphere and in anhydrous conditions, employing dry solvents. ^{1}H-NMR and ^{13}C-NMR have been registered with a Varian Mercury 300 instrument (300 MHz and 75 MHz respectively), chemical shifts (δ) are expressed as parts-per-million (ppm) and coupling constants (J) as hertz (Hz).

TLC analyses were performed on commercial silica gel 60 F254 aluminium sheets (Merck). As staining agents, a solution of ninhydrin (2 g in 100 mL EtOH + 3 mL acetic acid) was used to detect primary amines, and, while the Dragendorff reagent (solution of $K[BiI]_4$ in acetic acid and water) was used to detect secondary amines. Furthermore, a curcumin solution (turmeric powder suspended in EtOH/HCl 96:4) was employed to detect boronic esters and acids. Column chromatography was performed on silica gel Baker (0.063 - 0.200 mm). Eluents have been specified from time to time. For the radiosynthesis of compounds **[^{18}F] 1**, **[^{18}F] 2**, **[^{18}F] 3**, and **[^{11}C] 4**, semipreparative HPLC were performed on ThermoFisher Scientific™ BDS Hypersil C18 as stationary phase and NaH_2PO_4 0.05 M in H_2O:CH_3CN 60:40 as mobile phase. The method was performed with a flow rate of 5.0 mL/min. Analytical HPLC consists of a 515 pump, a 486 Tunable Absorbance UV detector and a NaI-radio-detector Flowcount FC 3200 (Eckert & Ziegler Radiopharma Inc. Hopkinton, MA, USA). The HPLC analyses of compounds were performed with ThermoScientific™ BDS Hypersil C18 (250 x 4.6 mm) column as stationary phase and NaH_2PO_4 0.05 M in H_2O:CH_3CN 50:50 as mobile phase. The method was performed with a flow rate of 1.0 mL/min. UV detection was measured at 254 nm.

During the preparation of the multimodal imaging agents, for HPLC chromatography, a Dionex UltiMate 3000 system was used together with Chromeleon Software (Version 6.80). For semipreparative analyses, a Chromolith (RP-18e, 100-10 mm, Merck, Germany) column was used. For radioanalytical use, a Dionex UltiMate 3000 system equipped with a Raytest GABI Star radioactivity detector was used together with a Chromolith Performance (RP-18e, 100–4.6 mm, Merck, Germany) column. All operations were performed with a flow rate of 4 mL/min using H_2O + 0.1% TFA and MeCN + 0.1% TFA as solvents. HR-ESI (high-resolution Electrospray Ionization) and MALDI (Matrix-Assisted Laser Desorption/Ionization) spectra were obtained with Finnigan MAT95Q and Bruker Daltronics Microflex spectrometers, respectively. γ-counting was performed using a 2480 Wizard gamma counter system from Perkin Elmer (Rodgau, Germany). For pH measurements, a SevenMulti from Mettler Toledo (Gießen, Germany) was used. The absorbance measurements were performed on a Genesys 50 UV/Vis spectrophotometer from ThermoFisher (Dreieich, Germany), while the emission spectra were recorded on a Tecan Infinite M200 Microplate reader together with a Nunc Micro-Well 96 solid plate from ThermoFisher. Confocal fluorescence microscopy was performed on a Leica TCS SP8 confocal microscope with lasers at λ = 405, 488, 552 and 638 nm. Overlays of microscopies were generated directly with the operating software or afterwards using FIJI software (V1.50e).

1 – 7 a conjugates were tested on Transfected Human Embryonic Kidney 293 cells stably expressing the GRP-Receptor (HEK-GRPR). HEK-GRPR cells were obtained from Dr. Martin Béhé, Paul Scherrer Institute, Villingen, Switzerland. **1 – 3 b** and **1 – 3 c** conjugates were tested on Murine Melanoma cells (B16F10) and Human Glioblastoma cells (U87MG), respectively, which were purchased from ATCC (Wesel, Germany). Confocal microscopy of BBN_{7-14} conjugates was performed using the human tumor cell line PC-3 (GRPR-positive), which was obtained from DSMZ (Braunschweig, Germany). [^{125}I]-Tyr^{4}-bombesin, [^{125}I]-NDP-MSH and [^{125}I]-echistatin were purchased from Perkin Elmer (Rodgau, Germany) in a molar activity of 81.4 GBq/µmol. Dulbecco's Modified Eagle's Medium (DMEM, high glucose, GlutaMax-I, 500 mL), Dulbecco's Modified Eagle's Medium (DMEM, 1X, 500 mL), geneticin (G418 Sulfate, 50 mg/mL), Opti-MEM I (GlutaMAX I), RPMI 1640 medium, L-Glutamine and PenStrep were obtained from Gibco (Schwerte, Germany), Eagle's Minimum Essential Medium (EMEM, 500 mL) from ATCC (Wesel, Germany), FCS (fetal calf serum) from Bio&SELL (Feucht, Germany) and Dulbecco's phosphate buffered saline (PBS), 1,10-phenantroline, *tris*(hydroxymethyl)aminomethane hydrochloride (Tris·HCl), manganese chloride ($MnCl_2$), 0.25% Trypsin with 0.02% EDTA solution in PBS and 4-(2-Hydroxyethyl)piperazine-1-ethanesulfonic acid (HEPES) from Sigma-Aldrich (Taufkirchen, Germany). Bovine serum albumin (BSA), sodium chloride (NaCl), calcium chloride ($CaCl_2$) and magnesium chloride ($MgCl_2$) were purchased from CarlRoth (Karlsruhe, Germany). The ^{68}Ge/^{68}Ga-Generator used was an IGG100 system, obtained from Eckert & Ziegler (Berlin, Germany) and eluted with HCl (0.1 M, 1.6 mL).

PREPARATION OF COMPOUNDS [^{18}F] 1, [^{18}F] 2, [^{18}F] 3, AND [^{11}C] 4

2,2-diethoxy-N-(naphthalen-1-ylmethyl)ethan-1-amine (5)

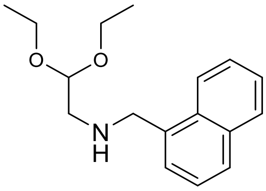

A mixture of 2,2-diethoxyethan-1-amine (5.00 g, 37.54 mmol) and 1-naphthaldehyde (5.86 g, 37.54 mmol) is heated in a steam bath for 30 min. Then, The cooled reaction is diluted with 25 mL of EtOH and $NaBH_4$ (1.42 g, 37.54 mmol) is added gradually. The reaction proceeds at room temperature for 24 h. The solvent is evaporated, and the residue dissolved in 37.5 mL of water and 75 mL of EtOAc. The separated organic phase is washed with water (2x25 mL), dried with Na_2SO_4 and evaporated to yield product **5** as a yellow oil (9.85 g, 96 %).

Rf: 0.11 (cyclohexane/EtOAc 8:2). Stained with Dragendorff reagent.

^{1}H-NMR (300MHz, $CDCl_3$) δ ppm 1.19 (t, J = 7.0 Hz, 6H, CH_3), 2,23 (br s, 1H, NH), 2.88 (d, J = 5.0 Hz, 2H, CH_2N), 3.47–3.73 (m, 4H, OCH_2), 4.29 (s, 2H, CH_2Ar), 4.62 (t, J = 5.6 Hz, 1H, CH), 7.40–8.15 (m, 7H, ArH).

^{13}C-NMR (75Mhz, $CDCl_3$) δ ppm 15.6, 51.7, 52.3, 62.5, 102.4, 123.9, 125.6, 125.8, 126.1, 126.2, 127.9, 128.9, 132.1, 134.1, 136.1.

(9H-fluoren-9-yl)methyl (S)-(3-(4-(tert-butoxy)phenyl)-1-((2,2-diethoxyethyl)(naphthalen-1-ylmethyl)amino)-1-oxopropan-2-yl)carbamate (6)

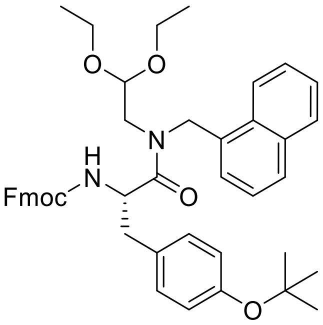

HATU (347.7 mg, 914.5 µmol) and DIPEA (159.3 µL, 914.5 µmol) are added to a solution of Fmoc-L-Tyr(*t*Bu)-OH (378.22 mg, 823.1 µmol) in 3 mL of DMF. The solution is stirred for 30 min at room temperature then **5** (250.00 mg, 914.5 µmol) is added and the reaction proceeds for 16 h. After the solvent evaporation, the residue is purified by column chromatography on silica gel (cyclohexane/EtOAc 9:1). **6** is obtained as a white foamy solid (325 mg, 50 %).

Rf: 0.31 (cyclohexane/EtOAc 8:2). Stained with ninhydrin (light yellow, green overheating).

^{1}H-NMR (300MHz, CDCl$_3$) δ ppm 1.06–1.35 (m, 6H, CH_3CH$_2$), 1.20 and 1.32 (two s, 9H, C(CH$_3$)$_3$), 2.77–3.05 (m, 4H, NCH_2CH, Tyr-CH$_2$), 3.16–3.76 (m, 5H, OCH_2CH$_3$, Fmoc-CH), 4.10–4.40 (m, 4H, Fmoc-CH$_2$, Tyr-CH, CHO), 4.72–5.18 (m, 2H, Napht-CH$_2$), 5.48–5.77 (m, 1H, NH), 6.65–8.17 (m, 19H, ArH).

^{13}C-NMR (75Mhz, CDCl$_3$) δ ppm 15.4, 28.9, 39.9, 47.2, 48.3, 50.0, 53.0, 63.7, 67.2, 78.5, 101.8, 120.1, 124.3, 124.4, 125.3, 125.4, 125.6, 126.2, 126.7, 127.3, 127.9, 128.2, 128.9, 130.0, 131.4, 132.0, 132.6, 134.1, 141.5, 144.1, 154.4, 155.7, 172.5.

(S)-2-amino-3-(4-(tert-butoxy)phenyl)-N-(2,2-diethoxyethyl)-N-(naphthalen-1-ylmethyl)propenamide (7)

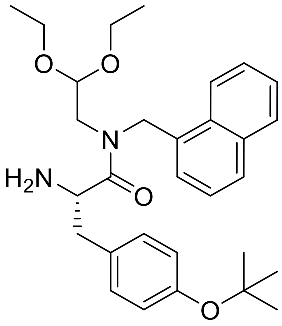

DEA (1.8 mL) is added dropwise to a stirring solution of **6** (300 mg, 419.6 µmol) in DCM (4.5 mL). The reaction proceeds for 4 h at room temperature, then the solvent is evaporated, and the residue is purified by filtration on a silica plug (cyclohexane/EtOAc 8:2 → 0:1). The product is obtained as a white foamy solid (200 mg, 96.7 %).

Rf: 0.09 (EtOAc). Stained with ninhydrin (strong yellow).

^{1}H-NMR (300MHz, $CDCl_3$) δ ppm 1.05–1.43 (m, 6H, CH_3CH_2), 1.22 and 1.33 (two s, 9H, $C(CH_3)_3$), 2.04 (br s, 2H, NH_2), 2.84–3.34 (m, 6H, NCH_2CH, Tyr-CH_2, 2×OCH_2CH_3), 3.43–3.79 (m, 3H, 2×OCH_2CH_3, Tyr-CH), 3.88–4.38 (m, 1H, CHO), 4.62–5.50 (m, 1H, Napht-CH_2), 6.64–8.12 (m, 11H, ArH).

^{13}C-NMR (75Mhz, $CDCl_3$) δ ppm 15.4, 29.1, 42.0, 48.8, 50.5, 53.5, 63.6, 78.4, 101.6, 122.2, 124.3, 125.4, 126.2, 126.7, 127.6, 128.0, 128.8, 129.2, 129.9, 132.4, 133.1, 134.0, 154.2, 176.5.

(9H-fluoren-9-yl)methyl (S)-(3-((3-(4-(tert-butoxy)phenyl)-1-((2,2-diethoxyethyl)(naphthalen-1-ylmethyl)amino)-1-oxopropan-2-yl)amino)-3-oxopropyl)carbamate (8)

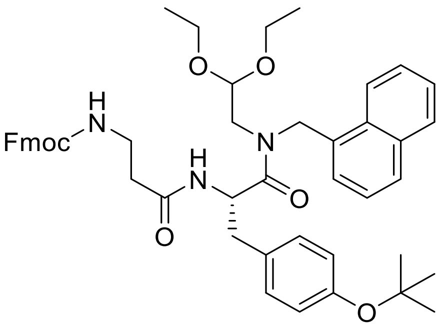

HATU (154.4 mg, 406.0 µmol) and DIPEA (70.7 µL, 406.0 µmol) are added to a solution of Fmoc-β-Ala-OH (113.7 mg, 365.4 µmol) in 1 mL of DMF and stirred for 30 min at room temperature. A solution of **7** (200 mg, 406.0 µmol) in 5 mL of DMF is added dropwise and the reaction stirred overnight at room temperature. After the solvent evaporation, the residue is purified by column chromatography on silica gel (cyclohexane/EtOAc 9:1). **8** is obtained as a white foamy solid (229 mg, 93 %).

Rf: 0.31 (cyclohexane/EtOAc 1:1). Stained with ninhydrin (light yellow, green overheating).

^{1}H-NMR (300MHz, $CDCl_3$) *δ* ppm 1.06–1.31 (m, 6H, CH_3CH_2), 1.19 and 1.43 (two s, 9H, $C(CH_3)_3$), 2.26–2.41 (m, 1H, Fmoc-NH), 2.84–3.76 (m, 12H, NCH_2CH, Tyr-CH_2, CH_2CO, OCH_2CH_3, Fmoc-CH_2), 4.13–4.35 (m, 4H, CH_2CH_2NH, Fmoc-CH, Tyr-CH), 4.82–4.98 (m, 1H, CHO), 5.22–5.51 (m, 2H, Napht-CH_2), 6.23–6.40 (m, 1H, Tyr-NH), 6.64–8.13 (m, 19H, ArH).

^{13}C-NMR (75Mhz, $CDCl_3$) *δ* ppm 15.4, 28.9, 36.1, 37.4, 39.4, 47.5, 48.5, 50.0, 51.3, 63.7, 66.8, 78.3, 101.6, 120.1, 124.3, 124.4, 125.3, 125.4, 125.5, 126.2, 126.6, 127.2, 128.0, 128.3, 128.9, 129.9, 131.6, 132.0, 132.5, 134.1, 141.5, 144.2, 154.6, 156.6, 170.7, 172.5.

(S)-2-(3-aminopropanamido)-3-(4-(tert-butoxy)phenyl)-N-(2,2-diethoxyethyl)-N-(naphthalen-1-ylmethyl)propenamide (9)

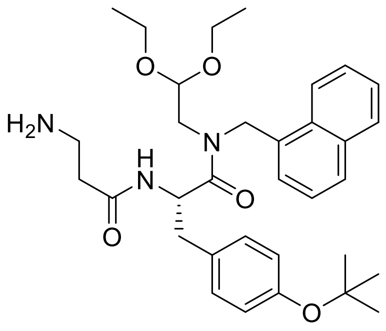

DEA (1.25 mL) is added dropwise to a stirring solution of **8** (190 mg, 241.7 µmol) in DCM (2.5 mL). The reaction proceeds for 6 h at room temperature, then the solvent is evaporated, and the residue is purified by filtration on a silica plug (cyclohexane/EtOAc/MeOH 8:2:0 → 0:1:0 → 0:8:2). The product is obtained as a white foamy solid (60 mg, 44 %).

Rf: 0.15 (EtOAc/MeOH 8:2). Stained with ninhydrin (green).

^{1}H-NMR (300MHz, $CDCl_3$) *δ* ppm 1.07–1.25 (m, 6H, CH_3CH_2), 1.19 and 1.28 (two s, 9H, $C(CH_3)_3$), 2.45–3.77 (m, 14H, NH_2, NCH_2CH, Tyr-CH_2, OCH_2CH_3, CH_2CO, CH_2NH_2), 4.41–5.63 (m, 4H, Tyr-CH, CHO, Napht-CH_2), 6.65–8.10 (m, 12H, ArH, Tyr-NH).

^{13}C-NMR (75Mhz, $CDCl_3$) *δ* ppm 15.4, 29.0, 38.7, 38.9, 39.1, 48.5, 50.0, 51.0, 63.9, 78.4, 102.0, 122.5, 124.3, 125.5, 126.1, 126.6, 127.9, 128.1, 128.8, 129.0, 129.9, 131.9, 132.6, 134.0, 154.4, 171.7, 172.7.

3-(hydroxymethyl)benzonitrile (18)

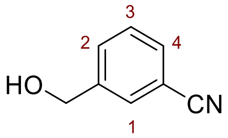

$BaCO_3$ (2.82 g, 14.28 mmol) is added to a solution of 3-(bromomethyl)benzonitrile (1.40 g, 7.14 mmol) in water (43 mL) then stirred at reflux for 3 h. The reaction is cooled down, then filtered. The filtrate is extracted with DCM (3x30 mL), and the reunited organic phases are dried with Na_2SO_4 and evaporated. The residue is purified by column chromatography on silica gel (cyclohexane/EtOAc 8:2). The product is obtained as a white solid (884 mg, 93 %).

Rf: 0.16 (EtOAc/MeOH 8:2).

^{1}H-NMR (300MHz, $CDCl_3$) δ ppm 2.20 (br s, 1H, OH), 4.75 (s, 2H, CH_2), 7.44–7.50 (m, 1H, H3), 7.54–7.63 (m, 2H, H2, H4), 7.67 (td, *J* = 1.1, 1.8 Hz, 1H, H1).

^{13}C-NMR (75Mhz, $CDCl_3$) δ ppm 63.9, 112.4, 118.9, 129.4, 130.2, 131.2, 131.3, 142.5.

(3-(aminomethyl)phenyl)methanol (19)

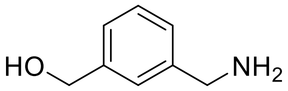

The reaction is carried out under argon atmosphere and in anhydrous conditions. **18** (177.5 mg, 808.4 µmol) is dissolved in 2 mL of dry THF. $LiAlH_4$ (46.0 mg, 1.21 mmol) is added at 0 °C, then the reaction is stirred at reflux (70 °C) for 2.5 h. The mixture is quenched with NaOH 15% aq. solution (5 mL) at 0 °C, filtered and the solvent evaporated. The residue is redissolved in water and extracted with EtOAc (3×5 mL). The combined organic layers are dried with Na_2SO_4 and evaporated to yield the desired product (185 mg, 91 %).

Rf: 0.53 (DCM/MeOH 9:1). Stained with ninhydrin (orange).

^{1}H-NMR (300MHz, $CDCl_3$) δ ppm 1.95 (br s, 3H, OH, NH_2), 3.86 (s, 2H, CH_2NH_2), 4.66 (s, 2H, CH_2OH), 7.18–7.35 (m, 4H).

^{13}C-NMR (75Mhz, $CDCl_3$) δ ppm 46.6, 65.2, 126.6, 127.0, 127.4, 129.6, 143.0, 143.6.

(3-(((tert-butyldimethylsilyl)oxy)methyl)phenyl)methanamine (20)

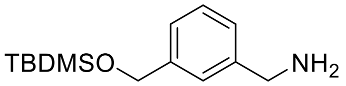

The reaction is carried out under argon atmosphere and in anhydrous conditions. Imidazole (83.37 mg, 1.22 mmol) and TBDMSCl (92.29 mg, 612.3 µmol) are added to a solution of **19** (84 mg, 612.3 µmol) in dry DCM (1.7 mL), then the solution is stirred overnight at room temperature. After completion the reaction is quenched with water (2 mL), the two phases are separated and the aqueous layer is extracted with DCM (3×3 mL). The collected organic layers are dried over Na_2SO_4 and the solvent evaporated to yield the product (55 mg, 34 %).

Rf: 0.67 (DCM/MeOH 95:5). Stained with ninhydrin.

^{1}H-NMR (300MHz, $CDCl_3$) δ ppm 0.09 (s, 6H, $SiCH_3$), 0.84 (s, 9H, $C(CH_3)_3$), 3.74 (s, 2H, CH_2NH_2),4.57 (s, 2H, CH_2O), 7.10-7.22 (m, 4H, ArH).

^{13}C-NMR (75Mhz, $CDCl_3$) δ ppm -4.1, 16.3, 24.0, 46.6, 65.2, 126.6, 127.0, 127.4, 129.6, 143.0, 143.6.

(S)-3-(4-(tert-butoxy)phenyl)-2-(3-(3-(3-(((tert-butyldimethylsilyl)oxy)methyl)benzyl)ureido)propanamido)-N-(2,2-diethoxyethyl)-N-(naphthalen-1-ylmethyl)propenamide (14)

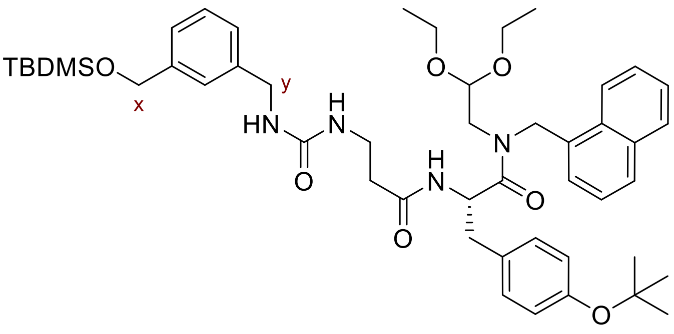

The reaction is carried out under argon atmosphere and in anhydrous conditions. A solution of carbonyldiimidazole (177.34 mg, 1.09 mmol) in dry THF (10 mL) is added dropwise in 10 min to a solution of **20** (250 mg, 994.3 µmol) in dry THF (10 mL). The reaction is stirred at room temperature for 9 h then a solution of **9** (560.50 mg, 994.3 µmol) in dry THF (10 mL) is added dropwise (in 10 min). The reaction is refluxed at 60 °C overnight. The cooled down reaction is quenched with water (20 mL), the organic solvent is evaporated, and the residual aqueous layer is extracted with DCM (10×3 mL). The reunited organic phases are dried with Na_2SO_4, the solvent is evaporated, and the residue is purified by column chromatography on silica gel (DCM/MeOH 98:02). The desired product is obtained as a white foamy solid (620 mg, 74 %).

Rf: 0.52 (DCM/MeOH 96:04). Stained with ninhydrin (light green).

^{1}H-NMR (300MHz, $CDCl_3$) δ ppm 0.08 (s, 6H, $SiCH_3$), 0.93 (s, 9H, $SiC(CH_3)_3$), 1.07–1.18 (m, 6H, CH_3CH_2), 1.16 and 1.23 (two s, 9H, $OC(CH_3)_3$), 2.24–2.38 (m, 2H, CH_2CH_2CO), 2.78–3.03 (m, 3H, Tyr-CH_2, 1×NCH_2CH), 3.17–3.73 (m, 7H, 1×NCH_2CH, OCH_2CH_3, $NHCH_2CH_2$), 4.34 (s, 2H, Hy), 4.70 (s, 2H, Hx), 4.85–5.45 (m, 4H, Tyr-CH, CHO, Napht-CH_2), 6.42–6.62 (m, 1H, Tyr-NH), 6.69–8.08 (m, 15H, ArH).

^{13}C-NMR (75Mhz, $CDCl_3$) δ ppm -4.12, 15.43, 16.22, 23.98, 29.01, 38.62, 38.73, 39.11, 46.66, 48.35, 50.09, 51.34, 63.92, 65.03, 78.43, 102.02, 122.57, 124.18, 125.35, 126.12, 126.44, 126.68, 127.06, 127.22, 127.92, 128.17, 128.84, 129.03, 129.45, 129.85, 131.94, 132.64, 134.05, 143.03, 143.79, 155.49, 159.55, 171.01, 172.91.

(6S)-6-(4-hydroxybenzyl)-N-(3-(hydroxymethyl)benzyl)-8-(naphthalen-1-ylmethyl)-4,7-dioxohexahydro-2H-pyrazino[1,2-a]pyrimidine-1(6H)-carboxamide (15)

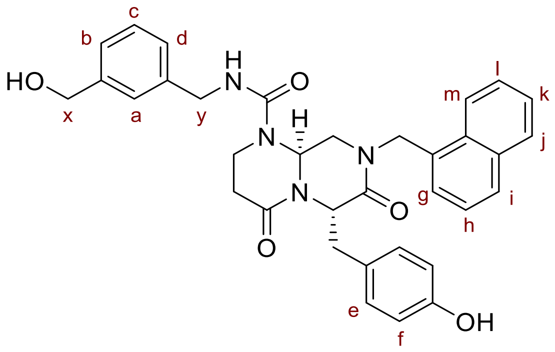

14 (600 mg, 713.3 µmol) is dissolved in a solution of formic acid/water (9:1, 6 mL) and stirred at room temperature overnight. A solution of LiOH·H_2O (77 mg, 1.83 mmol) in THF/water (1:1, 10 mL) is added and the mixture stirred for 10 min at room temperature (the solution turns from a yellow to a pink coloration), then HCl 2 M is added until pH = 1 and the aqueous mixture extracted with DCM (10×3 mL). The reunited organic phases are dried with Na_2SO_4, the solvent is evaporated, and the residue is purified by column chromatography on silica gel (DCM/MeOH 98:02). The desired product is obtained as a white foamy solid (240 mg, 58 %).

Rf: 0.26 (DCM/MeOH 96:4). Stained with ninhydrin (brown).

^{1}H-NMR (300MHz, $CDCl_3$) δ ppm 2.00–2.32 (m, 2H, CH_2CH_2CO), 2.83–3.86 (m, 6H, NCH_2CH_2, Tyr-CH_2, NCH_2CH), 4.06–4.20 (m, 2H, Hy), 4.63 (s, 2H, Hx), 4.92–5.16 (m, 4H, Tyr-CH, NH, Napht-CH_2), 5.32 (t, *J* = 5.2 Hz, 1H, NCH_2CH), 6.47 (d, *J* = 8.3 Hz, 2H, 2×Hf), 6.94 (d, *J* = 8.3 Hz, 2H, 2×He), 7.06 (d, *J* = 7.3 Hz, 1H, Hg), 7.16–7.30 (m, 4H, Ha, Hb, Hc, Hd), 7.36 (t, *J* = 7.6 Hz, 1H, Hh), 7.58–7.45 (m, 2H, Hk, Hl), 7.78–7.85 (m, 2H, Hi, Hj), 8.01 (d, *J* = 8.1 Hz, 1H, Hm).

^{13}C-NMR (75Mhz, $CDCl_3$) δ ppm 31.51, 35.84, 36.58, 44.64, 48.36, 57.06, 61.60, 65.60, 115.49, 123.46, 125.14, 126.28, 127.00, 127.37, 127.59, 127.62, 127.68, 127.71, 127.77, 128.84, 129.05, 129.18, 130.67, 130.74, 131.49, 133.88, 135.59, 139.16, 155.53, 161.00, 162.45, 166.24.

4-(((6S)-1-((3-(hydroxymethyl)benzyl)carbamoyl)-8-(naphthalen-1-ylmethyl)-4,7-dioxooctahydro-2H-pyrazino[1,2-a]pyrimidin-6-yl)methyl)phenyl acetate (16)

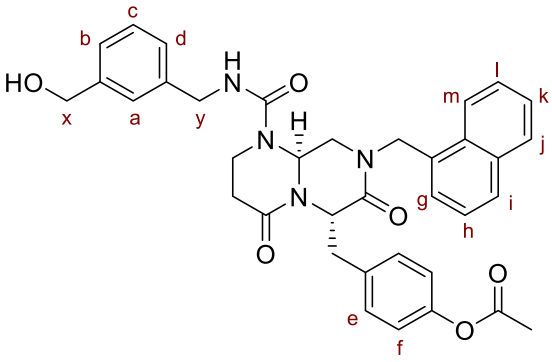

The reaction is carried out under argon atmosphere and anhydrous conditions. K_2CO_3 (114.64 mg, 829.5 µmol) is added to a solution of **15** (80 mg, 138.3 µmol) in dry acetone (5 mL) and cooled to 0 °C. Acetyl chloride (59 µL, 829.5 µmol) is added dropwise to the stirring mixture and the reaction stirred at 0 °C for 1 h. Ice cold water (10 mL) is added, and the reaction is extracted with EtOAc (3x15 mL). The reunited organic phases are dried with Na_2SO_4, the solvent is evaporated, and the residue is purified by column chromatography on silica gel (DCM/MeOH 98:02). The desired product is obtained as a white foamy solid (40 mg, 47 %).

Rf: 0.4 (DCM/MeOH 96:04). Stained with ninhydrin (brown).

^{1}H-NMR (300MHz, $CDCl_3$) δ ppm 2.03–2.31 (m, 2H, $CH_2C\mathit{H}_2CO$), 2.21 (s, 3H, $AcCH_3$), 2.38 (br s, 1H, OH), 2.86–3.14 (m, 3H, 1×$NC\mathit{H}_2CH_2$, Tyr-CH_2), 3.31 (d, *J* = 6 Hz, 2H, $NC\mathit{H}_2CH$), 3.72 (dd, J = 13.8, 4.8 Hz, 1H, 1×$NC\mathit{H}_2CH_2$), 4.25 (qd, *J* = 40.5, 14.7, 5.4 Hz, 2H, Hy), 4.58 (s, 2H, Hx), 4.83 (d, *J* = 14.7 Hz, 1H, 1×Napht-CH_2), 5.19–5.30 (m, 3H, 1×Napht-CH_2, Tyr-CH, NH), 5.37 (t, *J* = 6.0 Hz, 1H, $NCH_2C\mathit{H}$), 6.84 (d, *J* = 6.9 Hz, 2H, 2×Hf), 7.05 (d, *J* = 7.2 Hz, 1H, Hg), 7.17-7.26 (m, 6H, Ha, Hb, Hc, Hd, 2×He), 7.37 (t, *J* = 7.2 Hz, 1H, Hh), 7.47-7.56 (m, 2H, Hk, Hl), 7.77–7.84 (m, 2H, Hi, Hj), 8.01 (d, *J* = 7.8 Hz, 1H, Hm).

^{13}C-NMR (75Mhz, $CDCl_3$) δ ppm 21.05, 31.84, 35.98, 38.18, 44.41, 48.31, 48.35, 56.78, 62.34, 63.49, 121.73, 123.43, 125.14, 126.28, 127.06, 127.10, 127.60, 128.31, 128.92, 129.00, 129.32, 129.87, 130,73, 130.75, 131.45, 133.83, 133.85, 141.06, 142.03, 149.64, 155.33, 165.88, 165.90, 169.67.

4-(((6S)-1-((3-(((methylsulfonyl)oxy)methyl)benzyl)carbamoyl)-8-(naphthalen-1-ylmethyl)-4,7-dioxooctahydro-2H-pyrazino[1,2-a]pyrimidin-6-yl)methyl)phenyl acetate (17)

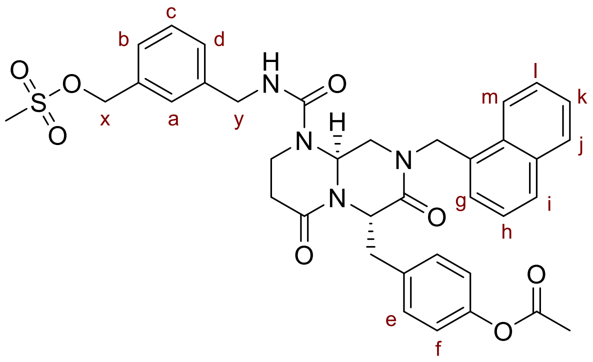

The reaction is carried out under argon atmosphere and in anhydrous conditions. A solution of **16** (27 mg, 43.5 µmol) in dry DCM (1 mL) is cooled to -30/-35 °C. TEA (12 µL, 87 µmol) is added dropwise to the stirring solution, followed by the dropwise addition of methanesulfonyl chloride (6.7µL, 87 µmol). The reaction is stirred at -30°C for 30 min then allowed to reach room temperature in 1 h. DCM (5 mL) is added to the stirring solution and the organic phase is washed with water (5 mL), NH_4Cl (5 mL) and $NaHCO_3$ (5 mL). Finally organic phase is dried over Na_2SO_4, the solvent is evaporated, and the residue is purified by column chromatography on silica gel (DCM/MeOH 98:02). The desired compound is obtained as a white foamy solid (28.5 mg, 94 %).

Rf: 0.50 (DCM/MeOH 95:5). Stained with ninhydrin (brown).

^{1}H-NMR (300MHz, $CDCl_3$) δ ppm 2.06–2.33 (m, 2H, CH_2CH_2CO), 2.21 (s, 3H, $AcCH_3$), 2.87 (s, 3H, $MsCH_3$), 2.88–3.19 (m, 3H, 1×NCH_2CH_2, Tyr-CH_2), 3.34 (d, *J* = 5.6 Hz, 2H, NCH_2CH), 3.75 (dd, *J* = 14.1, 4.8 Hz, 1H, 1×NCH_2CH_2), 4.26 (qd, *J* = 15.2, 5.6 Hz, 1H, Hy), 5.06 (dd, *J* = 75.0, 14.8 Hz, 2H, Napht-CH_2), 5.12 (s, 2H, Hx), 5.25–5.29 (m, 2H, Tyr-CH, NH), 5.40 (t, *J* = 6.0 Hz, 1H, NCH_2CH), 6.87 (d, *J* = 8.4 Hz, 2H, 2×Hf), 7.15 (d, *J* = 6.9 Hz, 1H, Hg), 7.20–7.30 (m, 6H, Ha, Hb, Hc, Hd, 2×He), 7.38 (t, *J* = 6.0 Hz, 1H, Hh), 7.47–7.56 (m, 2H, Hk, Hl), 7.78–7.85 (m, 2H, Hi, Hj), 8.03 (d, *J* = 7.9 Hz, 1H, Hm).

^{13}C NMR (75 MHz, $CDCl_3$) δ ppm 21.06, 29.64, 31.79, 36.05, 36.65, 38.14, 48.24, 44.38, 48.47, 53.46, 56.69, 62.10, 71.27, 121.67, 123.46, 125.14, 126.27, 126.98, 127.19, 127.59, 128.33, 128.82, 129.05, 129.09, 130.76, 131.45, 133.75, 133.88, 134.51, 139.98, 149.61, 155.44, 165.79, 165.95, 169.67,

ESI-MS (*m/z*) for $[M+H]^+$ (calculated): 699.6 (699.8); $[M+NH_3]^+$ (calculated): 716.3 (716.8).

3-(fluoromethyl)benzonitrile (25)

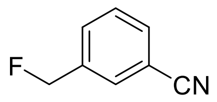

The reaction is carried out under argon atmosphere and in anhydrous conditions. 3-(chloromethyl)benzonitrile (1 g, 6.60 mmol), potassium fluoride (766.5 mg, 13.20 mmol) and 1,4,7,10,13,16-hexaoxacyclooctadecane (174.4 mg, 659.7 µmol) are dissolved in dry ACN (5 mL) and stirred in a reaction tube at 100 °C for 72 h. After completion, the reaction is cooled to room temperature and quenched with $NaHCO_3$ (pH ≥ 9), then extracted with DCM (3×10 mL). The reunited organic phases are dried with Na_2SO_4, the solvent is evaporated, and the residue is purified by column chromatography on silica gel (cyclohexane/EtOAc 8:2) affording the desired product as a yellow oil (743 mg, 83 %).

Rf: 0.24 (cyclohexane/EtOAc 8:2). Stained with $KMnO_4$ solution.

^{1}H-NMR (300MHz, $CDCl_3$) δ ppm 5.42 (d, J = 47.1 Hz, 1H, CH_2F) 7.49–7.67 (m, 4H, ArH).

^{13}C-NMR (75Mhz, $CDCl_3$) δ ppm 82.92 (d, J = 170.2 Hz, 1C, CH_2F), 113.07, 118.36, 129.59, 130.40, 131.13, 132.28, 137.91 (d, J = 18.0 Hz, 1C, CCH_2F).

(3-(fluoromethyl)phenyl)methanamine (26)

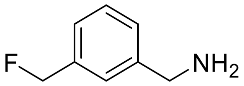

The reaction is carried out under argon atmosphere and in anhydrous conditions. 1M borane–tetrahydrofuran solution (5.92 mL, 5.92 mmol) is added dropwise at 0 °C to a stirring solution of **25** (200.0 mg, 1.48 mmol) in dry THF (2 mL). The reaction is heated 70 °C and stirred for 12 h. Then, the reaction is quenched with EtOH (5 mL) and the solvent is evaporated. The residue is redissolved in EtOAc (10 mL), which was then extracted with water (3 x 20 mL). The reunited aqueous layers are then basified with $NaHCO_3$ (pH = 8) and extracted with DCM. Finally, the reunited DCM layers are dried with Na_2SO_4, and the solvent is evaporated resulting in the product as a light yellow oil (50 mg, 25 %).

Rf: 0.20 (DCM/MeOH 8:2). Stained with ninhydrin (dark purple).

^{1}H-NMR (300MHz, CDCl3) δ ppm 1.60 (br s, 2H, NH_2) 3.89 (s, 2H, C*H*$_2$NH$_2$), 5.37 (d, J = 48.0 Hz, 2H, CH_2F), 7.20-7.43 (m, 4H, ArH).

^{13}C-NMR (75Mhz, $CDCl_3$) δ ppm 46.68, 82.91 (d, *J* = 170.2 Hz, 1C, CH_2F), 126.78, 127.12, 127.97, 129.53, 132.32, 141,32.

(S)-3-(4-(tert-butoxy)phenyl)-N-(2,2-diethoxyethyl)-2-(3-(3-(3-(fluoromethyl)benzyl)ureido)propanamido)-N-(naphthalen-1-ylmethyl)propenamide (23)

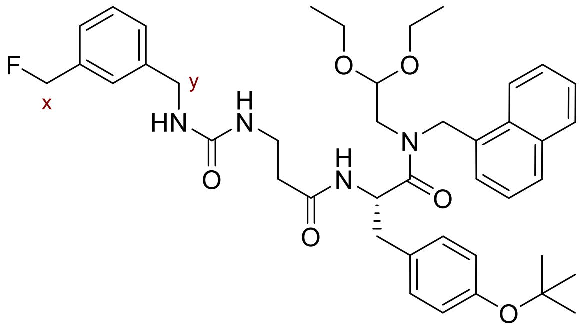

The reaction is carried out under argon atmosphere and in anhydrous conditions. A solution of carbonyldiimidazole (25.6 mg, 158.1 µmol) in dry THF (2 mL) is added dropwise in 10 min to a solution of **26** (20 mg, 143.7 µmol) in dry THF (2 mL), and the reaction is stirred at room temperature for 9 h. Then, a solution of **9** (81.0 mg, 143.7 µmol) in dry THF (2 mL) is added dropwise in 10 min to the stirring solution. The reaction is refluxed at 60 °C overnight. After completion, the cooled reaction is quenched with water (10 mL), and the aqueous layer is extracted with DCM (3×10 mL). The reunited organic phases are dried with Na_2SO_4, the solvent is evaporated, and the residue is purified by column chromatography on silica gel (DCM/MeOH 98:02). The desired product is obtained as a white foamy solid (85 mg, 81 %).

Rf: 0.59 (DCM/MeOH 95:5). Stained with ninhydrin (light green).

^{1}H-NMR (300MHz, $CDCl_3$) δ ppm 1.07–1.18 (m, 6H, CH_3CH_2), 1.16 and 1.23 (two s, 9H, $OC(CH_3)_3$), 2.41–3.79 (m, 12H, CH_2CH_2CO, Tyr-CH_2, NCH_2CH, OCH_2CH_3, $NHCH_2CH_2$), 4.34 (s, 2H, Hy), 4.85–5.45 (m, 5H, Tyr-CH, CHO, Napht-CH_2, 1×Hx), 5.46 (s, 1H, 1×Hx), 6.43–6.60 (m, 1H, Tyr-NH), 6.62–8.11 (m, 15H, ArH).

^{13}C-NMR (75Mhz, $CDCl_3$) δ ppm 15.41, 29.02, 38.64, 38.73, 39.11, 46.58, 48.31, 50.07, 51.21, 63.91, 78.41, 82.94 (d, *J* = 170.3 Hz, 1C, Cx), 102.03, 122.52, 124.19, 125.32, 126.10, 126.46, 126.68, 127.06, 127.32, 127.93, 128.27, 128.84, 129.01, 129.42, 129.75, 131.99, 132.54, 134.08, 143.01, 143.78, 155.39, 159.53, 171.01, 172.81.

(S)-N-(2,2-diethoxyethyl)-2-(3-(3-(3-(fluoromethyl)benzyl)ureido)propanamido)-3-(4-hydroxyphenyl)-N-(naphthalen-1-ylmethyl)propenamide (24)

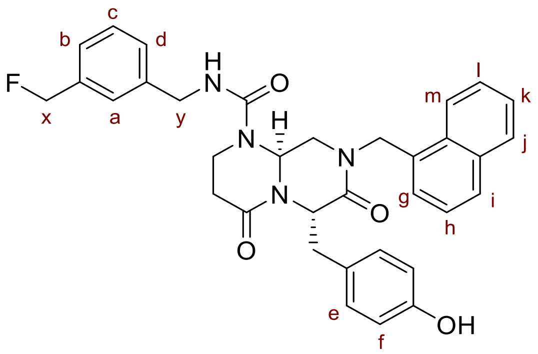

23 (82.0 mg, 112.5 µmol) is dissolved in formic acid (1 mL) and stirred overnight at room temperature. The solvent is evaporated, and the residue is purified by column chromatography on silica gel (DCM/MeOH 98:02). The desired is obtained as a white foamy solid (62 mg, 95 %).

Rf: 0.53 (DCM/MeOH 95:5). Stained with ninhydrin (brown, violet if overheated).

^{1}H-NMR (300MHz, $CDCl_3$) δ ppm 2.19–2.41 (m, 2H, CH_2CH_2CO), 2.96–3.17 (m, 3H, 1×NCH_2CH_2, Tyr-CH_2), 3.34 (ddd, J = 19.3, 14.1, 5.6 Hz, 2H, NCH_2CH), 3.75–3.83 (m, 1H, 1×NCH_2CH_2), 4.21–4.24 (m, 2H, Hy), 4.41–4.55 (m, 1H, NH), 4.95–5.04 (m, 1H, Tyr-CH), 5.11 (dd, J = 60.2, 14.6 Hz, 2H, Napht-CH_2), 5.35 (d, J = 47.8 Hz, 2H, Hx), 5.39 (t, J = 5.5 Hz, 1H, NCH_2CH), 6.57 (d, J = 8.2 Hz, 2H, 2×Hf), 7.05 (d, J = 8.1 Hz, 2H, 2×He), 7.14 (d, J = 7.2 Hz, 1H, Hg), 7.20 (s, 1H, Ha), 7.25–7.41 (m, 4H, Hb, Hc, Hd, Hh), 7.50–7.60 (m, 2H, Hk, Hl), 7.81–7.89 (m, 2H, Hi, Hj), 8.05 (d, J = 7.7 Hz, 1H, Hm).

^{13}C-NMR (75Mhz, $CDCl_3$) δ ppm 31.84, 35.87, 38.08, 44.32, 48.39, 56.78, 62.24, 82.94 (d, J = 170.3 Hz, 1C, Cx), 122.99, 123.43, 125.14, 126.19, 126.86, 126.90, 127.43, 127.54, 127.83, 127.91, 129.45, 129.93, 131.23, 131.25, 131.47, 132.77, 132.81, 139.40, 141.19, 146.53, 149.46, 155.31, 165.72, 165.74.

(*S*)-2-(3-(3-(4-bromobenzyl)ureido)propanamido)-3-(4-(*tert*-butoxy)phenyl)-*N*-(2,2-diethoxyethyl)-*N*-(naphthalen-1-ylmethyl)propenamide (10)

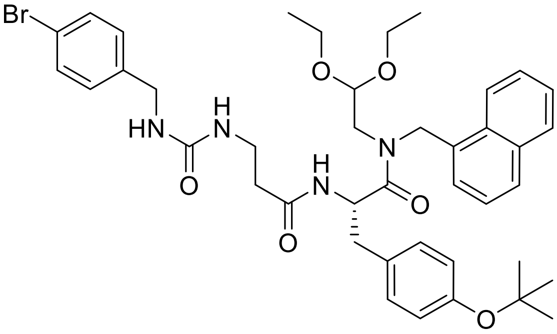

The reaction is carried out under argon atmosphere and in anhydrous conditions. **9** (50.0 mg, 88.70 µmol) is dissolved in dry THF (2 mL) and cooled in an ice bath. 4-Bromobenzyl isocyanate (18.8 mg, 88.70 µmol) is added dropwise to the stirring solution, then the reaction is stirred overnight at room temperature. After completion, the solvent is evaporated, and the residue is purified by column chromatography on silica gel (cyclohexane/EtOAc 2:8 → 0:1). The desired product is obtained as a white foamy solid (48 mg, 70 %).

Rf: 0.21 (EtOAc). Stained with ninhydrin (green).

^{1}H-NMR (300MHz, $CDCl_3$) δ ppm 1.07–1.18 (m, 6H, $C\mathit{H}_3CH_2$), 1.16 and 1.23 (two s, 9H, $OC(CH_3)_3$), 2.20–3.74 (m, 12H, $CH_2C\mathit{H}_2CO$, Tyr-CH_2, $NC\mathit{H}_2CH$, $OC\mathit{H}_2CH_3$, $NHC\mathit{H}_2CH_2$), 4.27–4.35 (m, 2H, $ArCH_2NH$), 4.64–5.47 (m, 4H, Tyr-CH, CHO, Napht-CH_2), 6.13–6.28 (m, 1H, Tyr-NH), 6.73–8.06 (m, 15H, ArH).

^{13}C-NMR (75Mhz, $CDCl_3$) δ ppm 15.36, 29.05, 38.61, 38.88, 39.11, 46.67, 48.37, 50.13, 51.37, 64.01, 78.45, 102.09, 119.47, 122.51, 124.16, 126.47, 126.73, 127.26, 127.91, 128.13, 128.67, 129.10, 129.40, 129.85, 131.14, 131.88, 132.67, 137.15, 143.80, 155.52, 159.56, 171.04, 172.93.

(6*S*,9a*S*)-*N*-(4-bromobenzyl)-6-(4-hydroxybenzyl)-8-(naphthalen-1-ylmethyl)-4,7-dioxohexahydro-2*H*-pyrazino[1,2-*a*]pyrimidine-1(6*H*)-carboxamide (11)

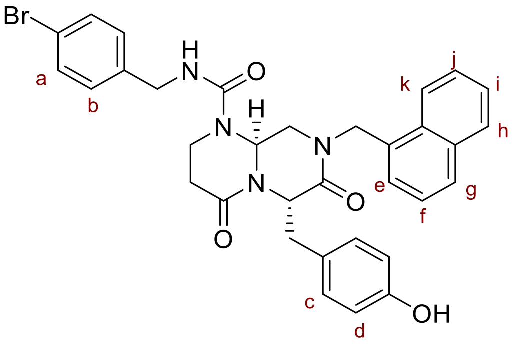

10 (116.0 mg, 149.5 µmol) is dissolved in formic acid (1 mL) and stirred overnight at room temperature. The solvent is evaporated, resulting in the desired product as a white foamy solid (93 mg, 99 %).

Rf: 0.37 (DCM/MeOH 95:5). Stained with ninhydrin (reddish/violet).

^{1}H-NMR (300MHz, $CDCl_3$) δ ppm 2.22–2.41 (m, 2H, CH_2CH_2CO), 2.96–3.18 (m, 3H, 1×NCH_2CH_2, Tyr-CH_2), 3.36 (ddd, *J* = 39.7, 13.9, 5.7 Hz, 2H, NCH_2CH), 3.76–3.82 (m, 1H, 1×NCH_2CH_2), 3.36 (ddd, *J* = 39.7, 13.9, 5.7 Hz, 2H, $ArCH_2NH$), 4.32–4.35 (m, 1H, NH), 4.95–4.99 (m, 1H, Tyr-CH), 5.11 (s, 2H, Napht-CH_2), 5.40 (t, *J* = 5.7 Hz, 1H, NCH_2CH), 6.59 (d, *J* = 8.5 Hz, 2H, 2×Hd), 6.97 (d, *J* = 8.4 Hz, 2H, 2×Hb), 7.07 (d, *J* = 8.5 Hz, 2H, 2×Hc), 7.27 (d, *J* = 7.2 Hz, 1H, He), 7.35–7.42 (m, 3H, 2×Ha, Hf), 7.50–7.60 (m, 2H, Hi, Hj), 7.82–7.89 (m, 2H, Hg, Hh), 8.07 (d, *J* = 8.0 Hz, 1H, Hk).

^{13}C-NMR (75Mhz, $CDCl_3$) δ ppm 31.53, 35.81, 37.90, 44.38, 48.33, 56.89, 62.03, 65.72, 119.51, 123.00, 123.43, 126.85, 127.45, 127.50, 127.81, 127.93, 129.21, 129.97, 131.12, 131.25, 131.29, 131.47, 132.71, 132.88, 137.21, 146.52, 149.49, 155.35, 165.70, 165.77.

4-(((6*S*,9a*S*)-1-((4-bromobenzyl)carbamoyl)-8-(naphthalen-1-ylmethyl)-4,7-dioxooctahydro-2*H*-pyrazino[1,2-*a*]pyrimidin-6-yl)methyl)phenyl acetate (12)

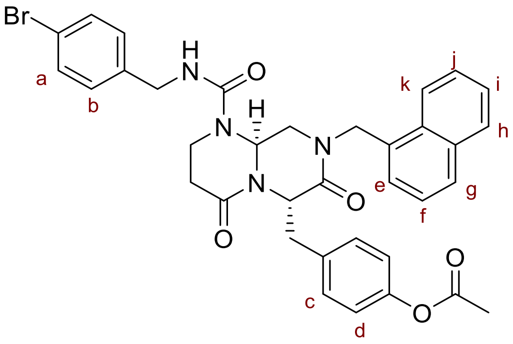

Acetic anhydride (146.4 mg, 1.43 mmol) is added dropwise to a stirring solution of **11** (90.0 mg, 143.4 µmol) in pyridine (1,5 mL), then the solution is stirred overnight at room temperature. The reaction is diluted with EtOAc (10 mL) and washed with 10% citric acid aq. solution (3×10 mL) and brine (10 mL). The organic phase is dried with Na_2SO_4, the solvent is evaporated, and the residue is purified by column chromatography on silica gel (DCM/MeOH 100:0 → 98:02). The desired product is obtained as a white foamy solid (91 mg, 95 %).

Rf: 0.56 (DCM/MeOH 96:4). Stained with ninhydrin (brown).

^{1}H-NMR (300MHz, $CDCl_3$) δ ppm 2.24 (s, 3H, $AcCH_3$), 2.27–2.48 (m, 2H, CH_2CH_2CO), 2.93–3.19 (m, 3H, 1×NCH_2CH_2, Tyr-CH_2), 3.32–3.56 (m, 2H, NCH_2CH), 3.86–3.93 (m, 1H, 1×NCH_2CH_2), 4.05–4.27 (m, 2H, $ArCH_2NH$), 4.40–4.46 (m, 1H, NH), 4.80–4.86 (m, 1H, Tyr-CH), 5.10 (s, 2H, Napht-CH_2), 5.43 (t, *J* = 5.4 Hz, 1H, NCH_2CH), 6.89 (d, *J* = 8.3 Hz, 2H, 2×Hb), 6.95 (d, *J* = 8.3 Hz, 2H, 2×Hd), 7.20–7.29 (m, 3H, 2×Hc, He), 7.36–7.41 (m, 3H, 2×Ha, Hf), 7.51–7.60 (m, 2H, Hi, Hj), 7.81–7.90 (m, 2H, Hg, Hh), 8.04–8.07 (m, 1H, Hk).

^{13}C-NMR (75Mhz, $CDCl_3$) δ ppm 21.04, 31.84, 35.98, 38.18, 44.41, 48.31, 48.35, 56.78, 62.34, 119.45, 121.73, 123.43, 127.10, 127.60, 128.31, 129.00, 129.13, 129.32, 129.87, 130,73, 130.75, 131.13, 131.45, 133.83, 137.20, 142.03, 149.64, 155.33, 165.88, 165.90, 169.67.

4-(((6*S*,9a*S*)-8-(naphthalen-1-ylmethyl)-4,7-dioxo-1-((4-(4,4,5,5-tetramethyl-1,3,2-dioxaborolan-2-yl)benzyl)carbamoyl)octahydro-2*H*-pyrazino[1,2-*a*]pyrimidin-6-yl)methyl)phenyl acetate (13)

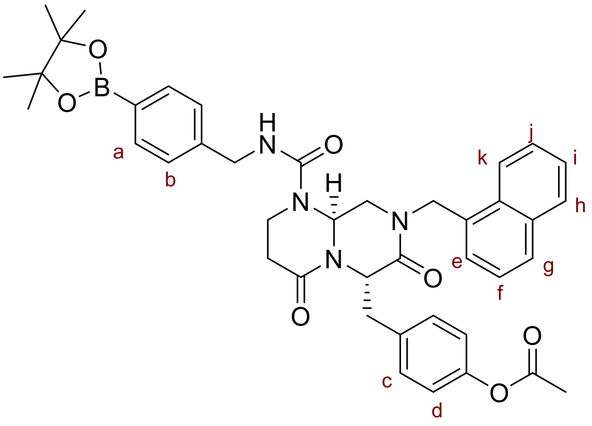

The reaction is carried out under argon atmosphere and in anhydrous conditions. **12** (200.0 mg, 298.7 µmol), B_2Pin_2 (91.0 mg, 358.4 µmol) and potassium acetate (88.0 mg, 896.1 µmol) are dissolved in dry dioxane (2 mL). Argon is purged in the reaction while it is stirred for 20 min. Then, $Pd(dppf)Cl_2$ is added to the stirring mixture, and the reaction is heated to 65/70°C for 20 h. After being filtered on a celite plug, the solvent of the reaction is evaporated, and the residue is purified by column chromatography on silica gel (DCM/MeOH 98:02). The desired product is obtained as a white foamy solid (98 mg, 46 %).

Rf: 0.49 (DCM/MeOH 97:3). Stained with curcumin solution (red).

^{1}H-NMR (300MHz, $CDCl_3$) δ ppm 1.24 (s, 12H, 12×pinacol-CH_3), 1.91 (s, 3H, AcCH_3), 2.24–2.44 (m, 2H, CH_2CH_2CO), 2.91–3.18 (m, 3H, 1×NCH_2CH_2, Tyr-CH_2), 3.37 (ddd, *J* = 61.8, 13.8, 5.4 Hz, 2H, NCH_2CH), 3.83–3.90 (m, 1H, 1×NCH_2CH_2), 4.03–4.25 (m, 3H, ArCH_2NH, NH), 4.78–4.82 (m, 1H, Tyr-CH), 5.01–5.20 (m, 2H, Napht-CH_2), 5.40 (t, *J* = 5.3 Hz, 1H, NCH_2C*H*), 6.58 (d, *J* = 8.4 Hz, 1H, 2×Hd), 6.83 (d, *J* = 8.1 Hz, 2H, 2×Hb), 7.08 (d, *J* = 8.3 Hz, 2H, 2×Hc), 7.35–7.40 (m, 1H, He), 7.52–7.58 (m, 2H, Hi, Hj), 7.62 (d, *J* = 8.2 Hz, 2H, 2×Hc), 7.82–7.90 (m, 2H, Hg, Hh), 8.08 (d, *J* = 7.8 Hz, 1H, Hk).

^{13}C-NMR (75Mhz, $CDCl_3$) δ ppm 21.04, 24.80, 31.85, 36.00, 38.19, 44.40, 48.29, 48.38, 56.77, 62.32, 88.23, 121.70, 123.44, 127.01, 127.15, 127.62, 128.33, 129.01, 129.29, 129.57, 129.88, 130,71, 130.79, 131.47, 133.32, 133.80, 137.88, 142.07, 149.67, 155.42, 165.81, 165.89, 169.65.

(*S*)-2-(3-(3-(4-fluorobenzyl)ureido)propanamido)-3-(4-(*tert*-butoxy)phenyl)-*N*-(2,2-diethoxyethyl)-*N*-(naphthalen-1-ylmethyl)propenamide (21)

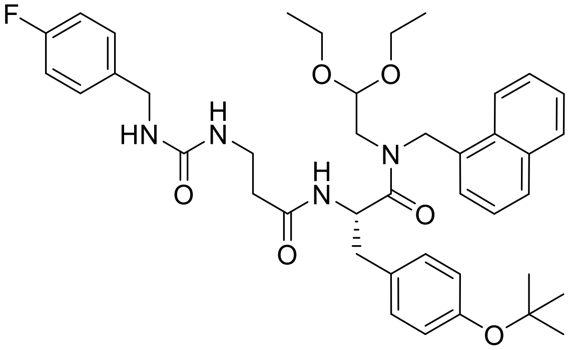

The reaction is carried out under argon atmosphere and in anhydrous conditions. **9** (700.0 mg, 1.24 mmol) is dissolved in dry THF (28 mL) and cooled in an ice bath. 4-Fluorobenzyl isocyanate (187.7 mg, 1.24 mmol) is added dropwise to the stirring solution, then the reaction is stirred overnight at room temperature. After completion, the solvent is evaporated, and the residue is purified by column chromatography on silica gel (cyclohexane/EtOAc 2:8 → 0:1). The desired product is obtained as a white foamy solid (624 mg, 70 %).

Rf: 0.21 (EtOAc). Stained with ninhydrin (green).

^{1}H-NMR (300MHz, CDCl$_3$) δ ppm 1.07–1.25 (m, 6H, CH_3CH$_2$), 1.21 and 1.28 (two s, 9H, OC(CH$_3$)$_3$), 2.20–3.72 (m, 12H, CH$_2$CH_2CO, Tyr-CH$_2$, NCH_2CH, OCH_2CH$_3$, NHCH_2CH$_2$), 4.23–4.29 (m, 2H, ArCH$_2$NH), 4.66–5.45 (m, 4H, Tyr-CH, CHO, Napht-CH$_2$), 6.28–6.47 (m, 1H, Tyr-NH), 6.71–8.05 (m, 15H, ArH).

^{13}C-NMR (75Mhz, CDCl$_3$) δ ppm 15.33, 29.11, 38.61, 38.81, 39.20, 46.33, 48.39, 50.17, 51.32, 64.13, 78.53, 102.15, 115.33, 122.56, 124.19, 126.41, 126.86, 127.25, 127.93, 128.15, 128.50, 128.73, 129.35, 129.84, 131.70, 132.53, 133.98, 143.84, 155.24, 159.57, 161.90 (d, *J* = 239.1 Hz, 1C, CF), 171.21, 172.97.

(6*S*,9a*S*)-*N*-(4-fluorobenzyl)-6-(4-hydroxybenzyl)-8-(naphthalen-1-ylmethyl)-4,7-dioxohexahydro-2*H*-pyrazino[1,2-*a*]pyrimidine-1(6*H*)-carboxamide (22)

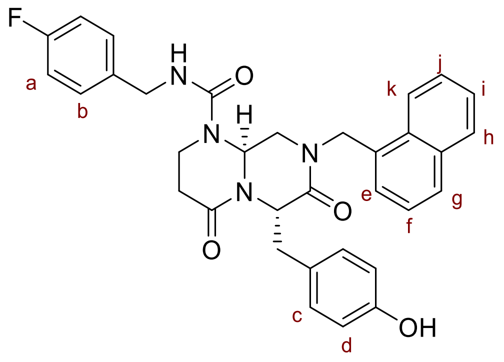

21 (116.0 mg, 149.5 µmol) is dissolved in formic acid (1 mL) and stirred overnight at room temperature. The solvent is evaporated, resulting in the desired product as a white foamy solid (93 mg, 99 %).

Rf: 0.37 (DCM/MeOH 95:5). Stained with ninhydrin (reddish/violet).

^{1}H-NMR (300MHz, CDCl$_3$) δ ppm 2.15–2.34 (m, 2H, CH$_2$C*H*$_2$CO), 2.96–3.16 (m, 3H, 1×NC*H*$_2$CH$_2$, Tyr-CH$_2$), 3.27–3.40 (m, 2H, NC*H*$_2$CH), 3.69–3.75 (m, 1H, 1×NC*H*$_2$CH$_2$), 4.20 (ddd, *J* = 37.6, 14.7, 5.5 Hz, 2H, ArC*H*$_2$NH), 4.46–4.55 (m, 1H, NH), 5.01–5.20 (m, 3H, Tyr-CH, Napht-CH$_2$), 5.40 (t, *J* = 5.9 Hz, 1H, NCH$_2$C*H*), 6.59 (d, *J* = 8.5 Hz, 2H, 2×Hd), 6.93–7.10 (m, 6H, 2×Ha, 2×Hb, 2×Hc), 7.26–7.29 (m, 1H, He), 7.36–7.40 (m, 1H, Hf), 7.49–7.99 (m, 2H, Hi, Hj), 7.81–7.88 (m, 2H, Hg, Hh), 8.06 (d, *J* = 8.0 Hz, 1H, Hk).

^{13}C-NMR (75Mhz, CDCl$_3$) δ ppm 31.46, 35.79, 36.63, 44.22, 48.23, 48.37, 57.05, 61.48, 115.35, 115.53, 115.63, 123.43, 125.13, 126.31, 127.03, 127.70, 128.87, 129.24, 129.26, 129.37, 130.55, 130.75, 131.47, 133.88, 134.10, 134.14, 155.40, 162.11 (d, J = 246.0 Hz, 1C, CF), 163.34, 166.09, 166.33.

4-(4-fluoro-3-nitrophenyl)-3,5-dimethylisoxazole (27)

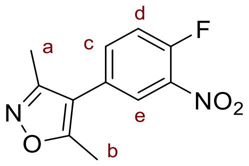

The reaction is carried out under argon atmosphere and in anhydrous conditions. Pd(dppf)Cl_2 (166.3 mg, 227.3 µmol) is added to a solution of 4-Bromo-1-fluoro-2-nitrobenzene (1.00 g, 4.55 mmol) and 3,5-dimethyl-4-(4,4,5,5-tetramethyl-1,3,2-dioxaborolan-2-yl)isoxazole (1.17 g, 5.23 mmol) in DME (10 mL). To the stirring mixture is then added saturated aq. $NaHCO_3$ solution (10 mL). The reaction is fluxed with argon for 2 min, then it is heated at 80 °C for 3 h. After completion, it is allowed to cool to room temperature and partitioned between ethyl acetate (20 mL) and water (20 mL). The organic layer is collected and dried with Na_2SO_4. The solid is filtered on a celite plug, then the filtrate is concentrated *in vacuo*. The residue is purified by column chromatography on silica gel (cyclohexane/EtOAc 9:1 → 7:3). After crystallization with Et_2O, the desired product is obtained as a beige solid (802.0 mg, 75.0%).

R_f: 0.26 (cyclohexane/EtOAc 9:1).

^{1}H-NMR (300MHz, $CDCl_3$) δ ppm 2.28 (s, 3H, 3×Ha), 2.43 (s, 3H, 3×Hb), 7.39 (dd, J = 10.1 Hz, 8.8 Hz, 1H, Hd), 7.52 (ddd, J = 8.4 Hz, 4.1 Hz, 2.2 Hz, 1H, Hc), 7.95 (dd, J = 6.9 Hz, 2.1 Hz, 1H, He).

^{13}C-NMR (75Mhz, $CDCl_3$) δ ppm 10.8, 11.8, 114.2, 119.3 (d, J = 21.5 Hz, 1C), 126.5 (d, J = 2.5 Hz, 1C), 127.9 (d, J = 5.0 Hz, 1C), 136.1 (d, J = 8.0 Hz, 1C), 137.8 (d, J = 6.5 Hz, 1C), 154.9 (d, J = 266.0 Hz, 1C), 158.2, 166.4.

(*S*)-*N*¹-(4-(3,5-dimethylisoxazol-4-yl)-2-nitrophenyl)propane-1,2-diamine (28)

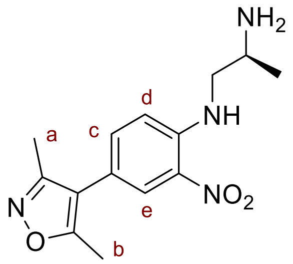

DIPEA (1.94 mL, 11.41 mmol) is added to a suspension of (S)-propane-1,2-diamine dihydrochloride (575.24 mg, 3.91 mmol) and **27** (770.0 mg, 3.26 mmol) in THF (3.1 mL). The mixture is stirred at room temperature for 16 h, then it was refluxed for 2 h. Next, K_2CO_3 (1.58 g, 11.41 mmol) and DMF (0.8 mL) are added at room temperature, and the mixture is stirred under reflux for 4 h, then cooled again to room temperature. The reaction is partitioned between EtOAc (20 mL) and water (20 mL), and the collected organic phase is washed with water (20 mL) and brine (20 mL), then dried over Na_2SO_4 and concentrated *in vacuo*. The residue is finally purified by filtration on a silica plug (cyclohexane/EtOAc/MeOH 3:7:0 → 2:5:3). The desired product is obtained as a red solid (658.0 mg, 69.5%).

R$_f$: 0.66 (DCM/MeOH/NH_4OH 90:9.9:0.1). Stained with ninhydrin (black).

^{1}H-NMR (300MHz, $CDCl_3$) δ ppm 1.36 (d, *J* = 5.8 Hz, 3H, CHC*H*$_3$), 2.25 (s, 3H, 3×Ha), 2.39 (s, 3H, 3×Hb), 3.37–3.60 (m, 3H, C*H*$_2$CH, CH$_2$C*H*), 6.96 (d, *J* = 8.9 Hz, 1H, Hd), 7.34 (dd, *J* = 8.8, 2.1 Hz 1H, Hc), 8.06 (d, *J* = 1.4 Hz, 1H, He), 8.43–8.45 (m, 1H, NH).

^{13}C-NMR (75Mhz, $CDCl_3$) δ ppm 10.7, 11.5, 22.1, 46.0, 50.9, 114.6, 114.8, 117.4, 127.0, 131.9, 136.7, 144.7, 158.5, 165.3.

(S)-4-(3,5-dimethylisoxazol-4-yl)-N-(2-morpholinopropyl)-2-nitroaniline (29)

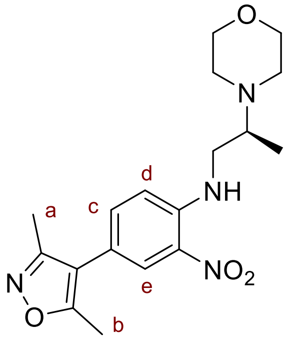

2-Bromoethyl ether (0.764 mL, 6.06 mmol) is added to a suspension of **28** (1.60 g, 5.51 mmol) and K_2CO_3 (2.29 g, 16.53 mmol) in DMF (55 mL). The mixture is stirred at 70 °C for 16 h then allowed to cool and partitioned between EtOAc (55 mL) and water (55 mL). The organic phase is collected, and the aqueous phase is extracted with more EtOAc (2x55 mL). The combined organic phases are washed with water (55 mL) and brine (55 mL), then dried over Na_2SO_4 and concentrated *in vacuo*. The residue is purified by column chromatography on silica gel (cyclohexane/acetone 8:2), resulting in the desired compound as a bright-orange solid (935 mg, 47.1 %).

Rf: 0,23 (cyclohexane/acetone 8:2). Stained with PMA (dark green).

^{1}H-NMR (300MHz, $CDCl_3$) δ ppm 1.11 (d, J = 6.4 Hz, 3H, $CHCH_3$); 2.24 (s, 3H, 3×Ha), 2.38 (s, 3H, 3×Hb), 2.43–2.75 (m, 4H, 4×CH_2CH_2N), 2.94–3.06 (m, 1H, CH_2CH), 3.08–3.16 (m, 1H, 1×CH_2CH), 3.27–3.35 (m, 1H, 1×CH_2CH), 3.68-3.84 (m, 4H, 4×OCH_2CH_2), 6.88 (d, J = 8.9 Hz, 1H, Hd), 7.32 (dd, J = 8.8, 2.1 Hz 1H, Hc), 8.07 (d, J = 2.2 Hz, 1H, He), 8.82–8.84 (m, 1H, NH).

^{13}C-NMR (75Mhz, $CDCl_3$) δ ppm 10.7, 11.3, 11.5, 45.3, 48.0 (s, 2C, 2×CH_2CH_2N), 57.4, 67.2(s, 2C, 2×OCH_2CH_2), 114.9, 114.9, 116.9, 127.0, 131.7, 136.6, 144.2, 158.6, 165.2.

methyl 3-(3-bromo-4-methoxyphenyl)propanoate (31)

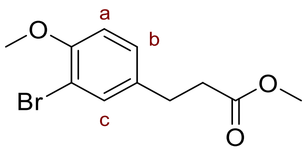

Bromine (250 µL, 4.89 mmol) is added slowly dropwise to a stirring solution of methyl 3-(4-methoxyphenyl)propanoate (1.00 g, 5.15 mmol) in DCM (8 mL) at 0 °C, and the mixture is stirred at that temperature for 2 h. Then the reaction is quenched with ice water, the organic phase is collected, and the aqueous fraction is extracted again with DCM (2×10 mL). The reunited organic phases are washed with saturated $NaHCO_3$ aq. solution (10 mL) and brine (10 mL), then dried with Na_2SO_4 and concentrated *in vacuo.* The desired product is obtained as a light-yellow oil (1.35 g, 95.7 %).

Rf: 0.81 (cyclohexane/EtOAc 7:3).

^{1}H-NMR (300MHz, $CDCl_3$) δ ppm 2.59 (t, *J* = 7.6 Hz, 2H, CH_2CH_2COO), 2.87 (t, *J* = 7.6 Hz, 2H, CH_2CH_2COO), 3.67 (s, 3H, $COOCH_3$), 3.87 (s, 3H, $ArOCH_3$), 6.82 (d, *J* = 8.4 Hz, 1H, Hb), 7.10 (dd, *J* = 8.4, 2.1 Hz, 1H, Ha), 7.38 (d, *J* = 2Hz, 1H, Hc).

^{13}C-NMR (75Mhz, $CDCl_3$) δ ppm 29.52, 35.52, 51.49, 56.08, 111.33, 111.81, 128.15, 132.92, 133.99, 154.20, 172.90.

methyl 3-(4-methoxy-3-(4,4,5,5-tetramethyl-1,3,2-dioxaborolan-2-yl)phenyl)propanoate (32)

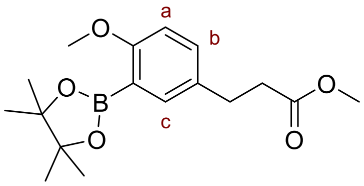

The reaction in carried out under argon atmosphere and in anhydrous conditions. **31** (400.0 mg, 1.46 mmol), B_2Pin_2 (482.0 mg, 1.90 mmol) and Pd(dppf)Cl_2 (432.2 mg, 4.39 mmol) are suspended in DME dry (4 mL). The mixture is stirred at reflux (110 °C) for 20 h. After completion, water (10 mL) and EtOAc (10 mL) are added. The organic layer is collected, while the aqueous phase is extracted with EtOAc (2×10 mL). Finally, the reunited organic phases are dried with Na_2SO_4 and concentrated *in vacuo*. The residue is purified by column chromatography on silica gel (cyclohexane/EtOAc 9:1), affording the desired product as a yellow oil (321 mg, 68%).

Rf: 0.4 (cyclohexane/EtOAc 8:2). Stained with curcumin solution (red).

^{1}H-NMR (300MHz, $CDCl_3$) δ ppm 1.35 (s, 12H, 12×pinacol-CH_3), 2.59 (t, J = 7.9 Hz, 2H, $CH_2C\mathit{H}_2COO$), 2.88 (t, J = 7.9 Hz, 2H, $C\mathit{H}_2CH_2COO$), 3.66 (s, 3H, $COOCH_3$), 3.80 (s, 3H, $ArOCH_3$), 6.78 (d, J = 8.5 Hz, 1H, Hb), 7.21 (dd, J = 8.4, 2.1 Hz, 1H, Ha), 7.49 (d, J = 1.9Hz, 1H, Hc).

^{13}C-NMR (75Mhz, $CDCl_3$) δ ppm 24.97 (s, 4C, 4×pinacol-$C\mathit{C}H_3$), 30.20, 36.25, 51.70, 56.12, 77.16, 83.61 (s, 2H, 2×pinacol-$\mathit{C}CH_3$), 110.79, 132.07, 132.36, 136.58, 162.95, 173.63.

3-(4-methoxy-3-(4,4,5,5-tetramethyl-1,3,2-dioxaborolan-2-yl)phenyl)propanoic acid (33)

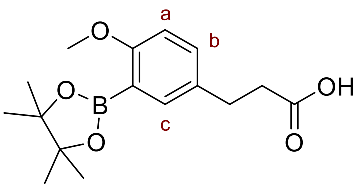

Cold NaOH 2 N (690 µL, 1.38 mmol) is slowly added to a solution of **32** (221.0 mg, 690.22 mmol) in MeOH (1.1 mL) and stirred for 2 h at room temperature. MeOH is removed under reduced pressure and the aqueous layer is extracted with DCM (2 mL). The aqueous phase is acidified with HCl 2 N (pH = 3), then extracted with DCM (4×5 mL). The organic phase is dried with Na_2SO_4 and concentrated *in vacuo*, resulting in the desired product as a yellow oil (105 mg, 50 %).

Rf: 0.25 (EtOAc). Stained with curcumin solution (red).

^{1}H-NMR (300MHz, $CDCl_3$) *δ* ppm 1.35 (s, 12H, 12×pinacol-CH_3), 2.64 (t, *J* = 7.8 Hz, 2H, CH_2CH_2COO), 2.89 (t, *J* = 7.7 Hz, 2H, CH_2CH_2COO), 3.80 (s, 3H, $ArOCH_3$), 6.79 (d, J= 8.4 Hz, 1H, Hb), 7.26-7.19 (m, 1H, Ha), 7.50 (s, 1H, Hb).

^{13}C-NMR (75Mhz, $CDCl_3$) *δ* ppm 24.97 (s, 4C, 4×pinacol-CCH_3), 29.66, 35.85, 56.25, 83.62 (s, 2H, 2×pinacol-CCH_3), 113.45, 133.22, 133.30, 145.93, 146.07, 153.82, 173.63.

(S)-(5-(2-(5-(3,5-dimethylisoxazol-4-yl)-1-(2-morpholinopropyl)-1H-benzo[d]imidazol-2-yl)ethyl)-2-methoxyphenyl)boronic acid (34)

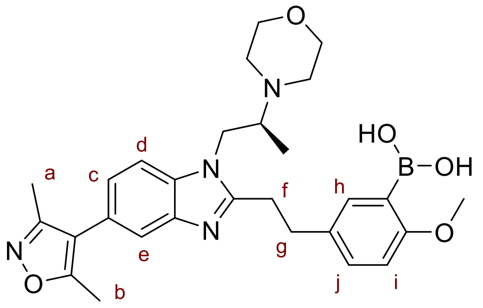

The reactions are carried out under argon atmosphere and in anhydrous conditions. **29** (125.0 mg, 346.8 µmol), NH_4HCO_2 (328.0 mg, 5.20 mmol) and activated-Zn (158.8 mg, 2.43 mmol) suspended in dry MeOH (1.9 mL) are heated in a CEM Discovery SP microwave synthesizer to 90 °C for 5 min (Standard method; 90 °C; 5 min hold time). 10 % aq. NH_3 (3.75 mL) is then added and the reaction is extracted with EtOAc (5 mL). The separated organic phase is dried with Na_2SO_4 and concentrated *in vacuo* to collect a yellow oil (**30**). Without further purifications, this oil is immediately dissolved in dry EtOAc (4.6 mL), then **33** (105.0 mg, 343.0 µmol), DIPEA (70.0 µL, 411.6 µmol) and T3P (50 wt.% in EtOAc, 445.0 µL, 696.2 µmol) are added to the solution. The reaction is microwaved at 150 °C for 20 min (Standard method; 150 °C; 20 min hold time). Next, NaOH 1M (1.6 mL) is added to the cooled mixture, and the collected organic phase is dried with Na_2SO_4 and concentrated *in vacuo*. The residue is finally purified by column chromatography on silica gel (cyclohexane/TEA/EtOH 7:2:1). The desired product was obtained as a light-yellow gum (45 mg, 20 %).

Rf: 0.16 (cyclohexane/TEA/EtOH 7:2:1). Stained with curcumin (red).

^{1}H-NMR (300MHz, $CDCl_3$) δ ppm 1.00 (d, J = 6.7 Hz, 3H, $CHCH_3$), 2.30 (s, 3H, 3×Ha), 2.43 (s, 3H, 3×Hb), 2.51–2.69 (m, 4H, 4×CH_2CH_2N), 2.99 (dd, J = 13.2, 6.5 Hz, 1H, CH_2CH), 3.12–3.32 (m, 4H, 2×Hf, 2×Hg), 3.60–3.74 (m, 4H, 4×OCH_2CH_2), 3.81–3.95 (m, 4H, OCH_3, 1×CH_2CH), 4.28–4.11 (m, 1H, 1×CH_2CH), 5.50 (br s, 2H, $B(OH)_2$), 6.84 (d, J= 8.5 Hz, 1H, Hi), 7.08–7.15 (m, 1H, Hc), 7.27–7.38 (m, 2H, Hd, Hj), 7.66 (s, 1H, He), 7.80 (d, J= 2.2 Hz, 1H, Hh).

^{13}C-NMR (75Mhz, $CDCl_3$) δ ppm 10.88, 11.57, 12.28, 29.91, 33.00, 46.62, 49.33, 55.64, 59.52, 66.98 (s, 2C, 2×OCH_2CH_2), 109.79, 110.12 (s, 2C, Ce, Ci), 117.05, 119.81, 123.46, 124.26, 132.70, 133.22, 134.49, 136.63, 142.63, 155.59, 158.98, 163.23, 165.01.

3-(3-fluoro-4-methoxyphenyl)propanoic acid (35)

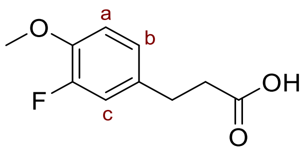

Malonic acid (371.3 mg, 3.57 mmol) and piperidine (41.4 mg, 0.49 mmol) are added to a solution of 3-fluoro-4-methoxybenzaldehyde (500.0 mg, 3.24 mmol) in pyridine (2 mL). The mixture is stirred at reflux (120 °C) for 14 h then poured into cold water. Then, the precipitate is filtered, and the solid residue is redissolved in acetic acid glacial (15 mL). Pd/C (345.2 mg, 324.4 µmol) is added to the solution, and the mixture stirred in a hydrogen atmosphere at room temperature for 2 hours. The reaction mixture is then filtered on a celite plug, and the filtrate is concentrated *in vacuo* to yield the desired product as a yellow oil (423 mg, 66 %).

Rf: 0.75 (EtOAc).

^{1}H-NMR (300MHz, $CDCl_3$) δ ppm 2.64 (t, *J* = 7.4 Hz, 2H, CH_2CH_2COO), 2.88 (t, *J* = 7.4 Hz, 2H, CH_2CH_2COO), 3.86 (s, 3H, OCH_3), 7.00–8.62 (m, 3H, Ha, Hb, Hc).

^{13}C-NMR (75Mhz, $CDCl_3$) δ ppm 29.62, 35.72, 56.26, 113.52, 116.10, 123.75, 133.20, 146.03, 150.60, 153.85.

(S)-4-(1-(5-(3,5-dimethylisoxazol-4-yl)-2-(3-fluoro-4-methoxyphenethyl)-1H-benzo[d]imidazol-1-yl)propan-2-yl)morpholine (36)

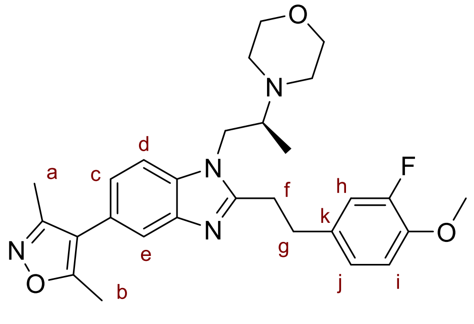

The reactions are carried out under argon atmosphere and in anhydrous conditions. **29** (215.0 mg, 596.5 µmol), NH_4HCO_2 (564.2 mg, 8.95 mmol) and activated-Zn (273.4 mg, 4.18 mmol) suspended in dry MeOH (3.30 mL) are heated in a CEM Discovery SP microwave synthesizer to 90 °C for 5 min (Standard method; 90 °C; 5 min hold time). 10 % aq. NH_3 (6.45 mL) is then added and the reaction is extracted with EtOAc (10 mL). The separated organic phase is dried with Na_2SO_4 and concentrated *in vacuo* to collect a yellow oil (**30**). This oil is immediately dissolved in dry EtOAc (6.75 mL), then **35** (100.0 mg, 504.6 µmol), DIPEA (103.0 µL, 605.6 µmol) and T3P (50 wt.% in EtOAc, 605.0 µL, 1,02 mmol) are added to the solution. The reaction is microwaved at 150 °C for 20 min (Standard method; 150 °C; 20 min hold time). Next, NaOH 1M (2.35 mL) is added to the cooled mixture, and the collected organic phase is dried with Na_2SO_4 and concentrated *in vacuo*. The residue is finally purified by column chromatography on silica gel (cyclohexane/TEA/EtOH 7:2:1). The desired product was obtained as a light-yellow gum (53 mg, 21.3%).

Rf: 0.33 (cyclohexane/TEA/EtOH 7:2:1).

^{1}H-NMR (300MHz, $CDCl_3$) δ ppm 0.99 (d, J = 6.7 Hz, 3H, $\mathrm{CHC}\mathit{H}_3$), 2.28 (s, 3H, 3×Ha), 2.41 (s, 3H, 3×Hb), 2.43–2.55 (m, 4H, 4×$\mathrm{CH_2C}\mathit{H}_2\mathrm{N}$), 2.94 (d, J = 6.8 Hz, 1H, $\mathrm{CH_2C}\mathit{H}$), 3.18–3.27 (m, 4H, 2×Hf, 2×Hg), 3.57–3.71 (m, 4H, 4×$\mathrm{OC}\mathit{H}_2\mathrm{CH_2}$), 3.79–3.92 (m, 4H, OCH_3, 1×$\mathrm{C}\mathit{H}_2\mathrm{CH}$), 4.10–4.17 (m, 1H, 1×$\mathrm{C}\mathit{H}_2\mathrm{CH}$), 6.70–7.00 (m, 3H, Hh, Hi, Hj), 7.10 (dd, J = 8.3, 1.4 Hz, 1H, Hc), 7.31 (d, J = 8.3 Hz, 1H, Hd), 7.61 (s, 1H, He).

^{13}C-NMR (75Mhz, $CDCl_3$) δ ppm 10.98, 11.68, 12.35, 29.79, 32.76, 46.92, 49.48, 56.45, 59.57, 67.23, 109.83, 113.74 (d, J = 2.2 Hz, 1C, Ci), 116.11, 117.16 (d, J = 17 Hz, 1C, Ch), 119.96, 123.46, 124.05 (d, J = 3.0 Hz, 1C, Cj), 124.30, 134.02 (d, J = 6.0 Hz, 1C, Ck), 134.77, 143.05, 146.26 (d, J = 10.5 Hz, 1C, *C*OMe), 152.41 (d, J = 245.0 Hz, 1C, CF), 155.31, 159.07, 165.09.

(*S*)-4-(2-(5-(3,5-dimethylisoxazol-4-yl)-1-(2-morpholinopropyl)-1*H*-benzo[*d*]imidazol-2-yl)ethyl)-2-fluorophenol (37)

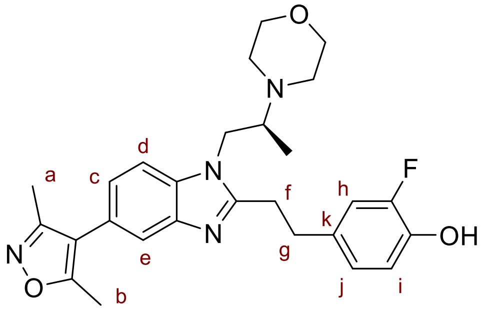

The reaction is carried out under nitrogen atmosphere and in anhydrous conditions. **36** (53.5 mg, 108.61 µmol) is dissolved in DCM dry (1.13 mL). The solution is cooled to -78°C, and BBr_3 (0.217 mL, 217.22 µmol) is added dropwise. The reaction is stirred at -78°C for 1 h, then for 3 h at room temperature. After completion, the reaction is quenched with water (2 mL) at 0°C, and neutralized to pH = 7 with $NaHCO_3$. The mixture is partitioned between DCM (10 mL) and water (10 mL), the organic phase is collected, and the aqueous layer extracted with more DCM (5×10 mL). The combined organic layers are dried over Na_2SO_4 and concentrated in *vacuo*. The residue is re-dissolved in EtOAc (4 mL), and this organic phase is extracted with NaOH 1M (5×1 mL). The combined aqueous phases are neutralized to pH = 7 with citric acid as a solid, then extracted with DCM (5×5 mL). The reunited organic phases are dried over Na_2SO_4 and concentrated in vacuo, resulting in the desired product as a white-yellowish solid (25.3 mg, 48.7%).

R_f = 0.19 (cyclohexane/TEA/MeOH 7:2:1).

^{1}H-NMR (300 MHz, $CDCl_3$) δ ppm 1.01 (d, J = 6.7 Hz, 3H, CHC*H*$_3$), 2.27 (s, 3H, 3×Ha), 2.40 (s, 3H, 3×Hb), 2.57–2.72 (m, 4H, 4×CH$_2$C*H*$_2$N), 2.99 (dd, *J* = 13.5, 6.8 Hz, 1H, CH$_2$C*H*), 3.14–3.19 (m, 4H, 2×Hf, 2×Hg), 3.57–3.71 (m, 4H, 4×OC*H*$_2$CH$_2$), 3.91 (dd, *J* = 14.5, 7.5 Hz, 1H, 1×C*H*$_2$CH), 4.22 (dd, *J* = 14.4, 5.8 Hz, 1H, 1×C*H*$_2$CH), 6.77–6.91 (m, 3H, Hh, Hi, Hj), 7.13 (dd, *J* = 8.3, 1.5 Hz, 1H, Hc), 7.35 (d, *J* = 8.3 Hz, 1H, Hd), 7.60 (d, *J* = 1.1 Hz, 1H, He).

^{13}C NMR (75 MHz, $CDCl_3$) δ ppm 10.83, 11.55, 12.14, 29.49, 33.44, 46.69, 49.35, 59.50, 66.85, 109.93, 115.50 (d, *J* = 4.3 Hz, 1C, Ci), 116.91, 117.90 (d, *J* = 2.5 Hz, 1C, Ch), 119.57, 122.71, 124.35 (d, *J* = 3.3 Hz, 1C, Cj), 126.45, 134.25 (d, *J* = 2.6 Hz, 1C, Ck), 135.72, 143.00, 146.47 (d, *J* = 4.4 Hz, 1C, COH), 153.79 (d, *J* = 131.2 Hz, 1C, CF), 155.20, 158.91, 165.09.

(6*S*,9a*S*)-*N*-(4-(fluoro-^{18}*F*)benzyl)-6-(4-hydroxybenzyl)-8-(naphthalen-1-ylmethyl)-4,7-dioxohexahydro-2*H*-pyrazino[1,2-*a*]pyrimidine-1(6*H*)-carboxamide ([^{18}F] 1)

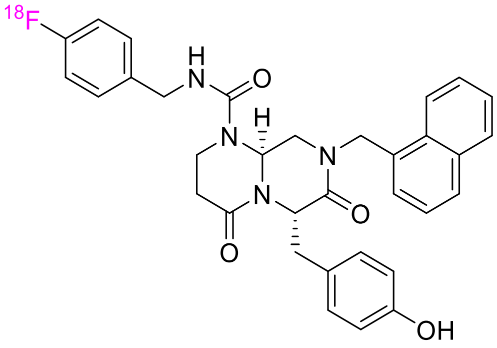

A solution of K_2CO_3 (0.1 mg/mL in water, 550 µL) and KOTf (5 mg) is added to vial number 1, while ACN (1 mL) is added in vial number 2. In vial number 3 it is put a solution of cold precursor **13** (3 mg), $Cu(OTf)_2$ (7.6 mg) and pyridine (41.6 µL) in dry DMF (1 mL). [^{18}F]F$^-$ derived from cyclotron is trapped on a preconditioned QMA light Sep-Pak cartridge and eluted with the solution contained in vial number 1 into the reactor. Then, ACN form vial number 2 is added, and the solvent in the reactor is evaporated with two heating cycles (60 °C × 5 min and 120 °C × 5 min). The solution in vial number 3 is then added in the reactor, and the reaction is stirred at 110°C for 20 min. Next, The reaction vessel is cooled down at 30 °C, diluted with DMF (1 mL) and a mixture of ACN/H_2O (45:55, 2.5 mL) and purified using BDS semipreparative HPLC column.

Radiochemical conversion (unoptimized): 2 %;

Radiochemical Purity: 99.9 %.

QUALITY CONTROL SETTINGS

HPLC column: BDS Hypersil C18 (250 x 4.6 mm);

Mobile phase: KH_2PO_4 (0.05 M)/ACN 50:50;

Flux: 1 mL/min;

Retention Time: 7.6 min.

(6*S*,9a*S*)-*N*-(3-((fluoro-^{18}*F*)methyl)benzyl)-6-(4-hydroxybenzyl)-8-(naphthalen-1-ylmethyl)-4,7-dioxohexahydro-2*H*-pyrazino[1,2-*a*]pyrimidine-1(6*H*)-carboxamide ([^{18}F] 2)

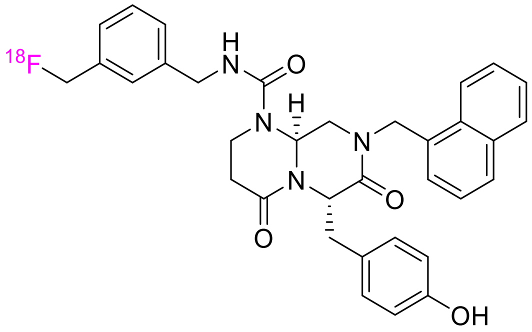

A mixture of Kryptofix® 222 (3 mg/mL in dry ACN) and K_2CO_3 (6.7 mg/mL in H_2O) is added to vial number 1, while ACN (1 mL) and a solution of cold precursor **17** (3 mg) in dry ACN (1 mL) are added in vial number 2 and 3, respectively. [^{18}F]F$^-$ (24 GBq) derived from cyclotron is trapped on a preconditioned QMA light Sep-Pak cartridge and eluted with the solution contained in vial number 1 into the reactor. Then, ACN form vial number 2 is added, and the solvent in the reactor is evaporated with two heating cycles (60 °C × 5 min and 120 °C × 5 min). The solution in vial number 3 is then added in the reactor, and the reaction is stirred at 100°C for 15 min. Next, NaOH 0.5 M (0.5 mL) is added from vial number 4 and the reaction stirred at 50 °C for 2 min. Citrate 0.5 M (pH = 5.4, 2 mL) from vial five and ACN (1 mL) from vial six are added, and the mixture in the reactor is injected into semipreparative HPLC (BDS Hypersil C18). **2** elutes after 12 min. Finally, the collected fraction is charged on a preconditioned tC18 separating cartridge, which is washed with H_2O (20 mL) from vial number 7, eluted with EtOH (1 mL) from vial number 8 and diluted with aqueous NaCl (5 mL) from vial number 9.

Recovered Radioactivity: 2.25 GBq;

Yield (not decay corrected): 9.2 %;

Yield (decay corrected): 13.4 %;

Radiochemical Purity: 99.9 %.

SEMIPREPARATIVE HPLC SETTINGS

HPLC column: BDS Hypersil C18;

Mobile phase: H_2O:ACN 70:30 for 7 min, then H_2O:ACN 30:70;

Flux: 5 mL/min;

Retention Time: 12 min.

QUALITY CONTROL SETTINGS

HPLC column: BDS Hypersil C18 (250 x 4.6 mm);

Mobile phase: NaH_2PO_4 (0.05 M)/ACN 50:50;

Flux: 1 mL/min;

Retention Time: 7.5 min.

(*S*)-4-(1-(5-(3,5-dimethylisoxazol-4-yl)-2-(3-(fluoro-^{18}*F*)-4-methoxyphenethyl)-1*H*-benzo[*d*]imidazol-1-yl)propan-2-yl)morpholine ([^{18}F] 3)

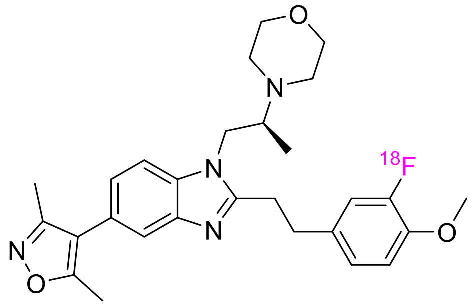

A mixture of K_2CO_3 (0.1 mg/mL in H_2O) and KOTf (5 mg) is added to vial number 1, while ACN (1 mL) is added in vial number 2. In vial number 3 it is put a solution of cold precursor **34** (3 mg), $Cu(OTf)_2$ (10.46 mg) and pyridine (58.5 µL) in dry DMF (1 mL). [^{18}F]F$^-$ (30 GBq) derived from cyclotron is trapped on a preconditioned QMA light Sep-Pak cartridge and eluted with the solution contained in vial number 1 into the reactor. Then, ACN form vial number 2 is added, and the solvent in the reactor is evaporated with two heating cycles (60 °C × 5 min and 120 °C × 5 min). The solution in vial number 3 is then added in the reactor, and the reaction is stirred at 100°C for 20 min. Next, The reaction vessel is cooled down at 40 °C, H_2O (3 mL) from vial number 5 is added and the diluted mixture is passed through a Sep-Pak Alumina N Plus separating cartridge. Other H_2O (1 mL) from vial number 4 is delivered to the reaction vessel and then channelled through the cartridge.

Recovered Radioactivity: 150 MBq;

Yield (not decay corrected): 0.5 %;

Yield (decay corrected): 0.8 %;

Radiochemical Purity: 50.0 %.

QUALITY CONTROL SETTINGS

HPLC column: BDS Hypersil C18 (250 x 4.6 mm);

Mobile phase: NaH_2PO_4 (0.05 M)/ACN 50:50;

Flux: 1 mL/min;

Retention Time: 9.6 min.

(*S*)-4-(1-(5-(3,5-dimethylisoxazol-4-yl)-2-(3-fluoro-4-(methoxy-^{11}*C*)phenethyl)-1*H*-benzo[*d*]imidazol-1-yl)propan-2-yl)morpholine ([^{11}C] 4)

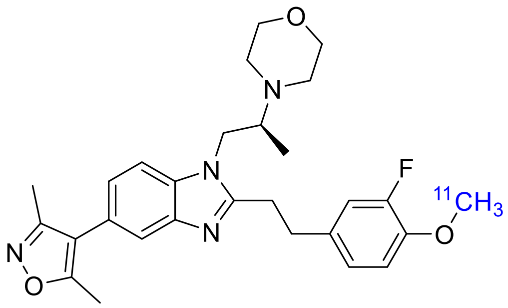

The solution of **37** (1 mg) and NaOH 1 M (2 µL) in 2-butanone (100 µL) is injected directly and slowly in the loop. [^{11}C]CH_3OTf (10 GBq) in helium passed through the loop and after 30 seconds of reaction at room temperature the content of the loop is injected into a semipreparative HPLC column for purification. At the end of the purification, **[^{11}C] 4** is gathered in the round bottom flask and diluted with 30 mL of water. **[^{11}C] 4** is filtered over a tC18 cartridge, then washed with purified water (10 mL), eluted with EtOH (0.7 mL), and diluted with physiological solution (3.0 mL). The injectable solution is collected in a two-neck container and then transferred in a suitable vial posed in the class A hot cell.

Recovered Radioactivity: 2.00 GBq;

Yield (not decay corrected): 19.8 %;

Yield (decay corrected): 56.3 %;

Radiochemical Purity: 99.5 %.

QUALITY CONTROL SETTINGS

HPLC column: BDS Hypersil C18 (250 x 4.6 mm);

Mobile phase: NaH_2PO_4 (0.05 M)/ACN 45:55;

Flux: 1 mL/min;

Retention Time: 8.6 min.

GENERAL SYNTHESIS OF PEPTIDES

Peptides were synthesized on Rink Amide resins by using N_α-Fmoc protecting groups and a standard HBTU activation strategy.[160] The resin was swollen in DCM for 30 min, washed with DMF, the Fmoc protecting group was cleaved with piperidine (50% in DMF, 2 min washing then 5 min). The resin was washed with DMF, then the respective protected amino acid was coupled by using the HBTU-pre-activated synthon in DMF (4 equiv. N_α-Fmoc amino acid, 3.9 equiv. HBTU, 4 equiv. DIPEA) which was allowed to react for 2 min before being added to the resin. The syringe was shaken for 1 h, then the reaction mixture was removed and the resin was washed with DMF. The same procedure was repeated for the following amino acids. Detailed syntheses of the three monomeric peptide units and PESIN peptide dimer can be found in the corresponding references.[161-163] Then the resin was washed thrice with DMF, dichloromethane and diethyl ether, and dried under reduced pressure. Finally, the peptides were cleaved from solid support by using a mixture of TFA:TIS (95:5 (v/v), 5 mL) for 1 h. The volatile components were removed under reduced pressure, the residues were dissolved in 1:1 MeCN:H_2O + 0.1% TFA and the products purified by semipreparative HPLC.

GENERAL SYNTHESIS OF MULTIMODAL IMAGING UNITS (MIUs) 38 – 43

Pyrylium salt and the **ICG derivative** fluorescent dye were synthesized following previously reported procedures.[91, 92] Rink amide resin-Cys(Trt)-Lys(alloc)-NODA-GA(*t*Bu)$_3$ was synthesized according to the standard Fmoc-based solid phase peptide synthesis protocol reported earlier, then the allyloxycarbonyl protecting group was removed still on solid support using tetrakis(triphenylphosphine)palladium(0). In the following step, 50 µmol Rink amide resin-Cys(Trt)-Lys-NODA-GA(*t*Bu)$_3$ was reacted with the respective dye. MIUs **38** and **39**: 4 eq. of the dyes **Pyrylium salt** and **Dansyl chloride** were reacted with the resin for 1 h without prior activation, 4 eq. of DIPEA were added after 30 minutes. MIU **40**: **ICG derivative** (1.5 eq.) was activated beforehand with HBTU (1.425 eq.) and DIPEA (1.5 eq.) as base, in DMF for 10 minutes, then reacted with the resin at 80°C for 3 hours. MIU **41**: 4 eq. of **5-carboxyfluorescein** were activated beforehand with HBTU (3.8 eq.) and DIPEA (4 eq.) as base, in DMF (4 mL) for 2 minutes, then reacted with the resin for 1 hour. MIU **42**: 2 eq. of **tartrazine** were activated beforehand with PyBOP (1.9 eq.) and DIPEA (2 eq.) as base, in DMF (3 mL) for 2 minutes, then reacted with the resin at 80°C for 4 hours. After the conjugation reaction was finished, the resin was filtered from the liquid components of the mixture and washed thrice with DMF, dichloromethane and diethyl ether. After drying, the dye conjugates were cleaved from solid support by using a mixture of TFA:TIS (95:5 (v/v), 5 mL) for 1–2 h. Then the volatile components were removed under reduced pressure, the residues were dissolved in 1:1 MeCN:H_2O + 0.1% TFA and the products purified by semipreparative HPLC. Similarly, Rink amide resin-Cys(Trt)-Gly-NODA-GA(*t*Bu)$_3$ **43** was prepared following the standard Fmoc-based solid phase peptide synthesis protocol, washed thrice with DMF, dichloromethane and diethyl ether, and cleaved from solid support by using a mixture of TFA:TIS (95:5 (v/v), 5mL) for 1 h. Once again, the dried residue was dissolved in 1:1 MeCN:H_2O + 0.1% TFA and purified by semipreparative HPLC.

Multimodal Imaging Units (MIUs):

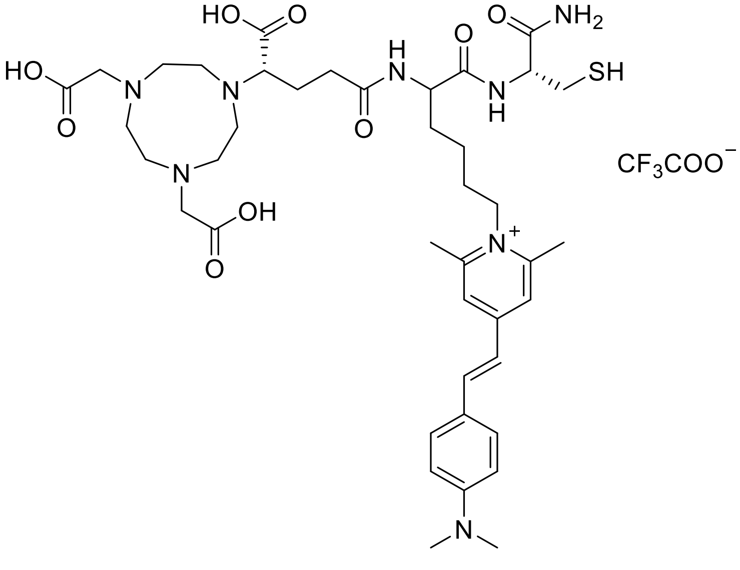

38 ($C_{41}H_{61}N_8O_9S$)(CF_3CO_2): HPLC gradient: 0 – 100 % MeCN + 0.1 % TFA in 12 min, R_t = 5.83 min, yield: 30 %, purity: 98 %, MALDI-MS (*m/z*) for $[M]^+$ (calculated): 841.25 (841.43); HR-ESI-MS (*m/z*) for $[M-2H+K+Na]^+$ (calculated): 901.3257 (901.3655).

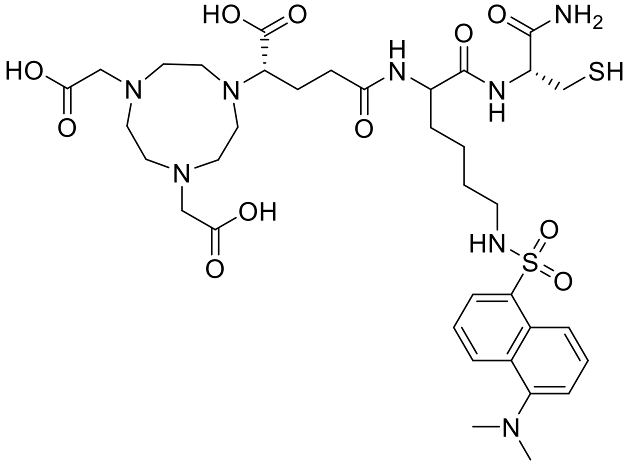

39 ($C_{36}H_{54}N_8O_{11}S_2$): HPLC gradient: 0 – 100 % MeCN + 0.1 % TFA in 12 min, R_t = 5.25 min, yield: 35 %, purity: 85 %, MALDI-MS (*m/z*) for $[M+H]^+$ (calculated): 839.48 (839.34); $[M+Na]^+$ (calculated): 861.49 (861.33); $[M+K]^+$ (calculated): 877.50 (877.30); HR-ESI-MS (*m/z*) $[M-H+K+Na]^+$ (calculated): 899.2405 (899.3353).

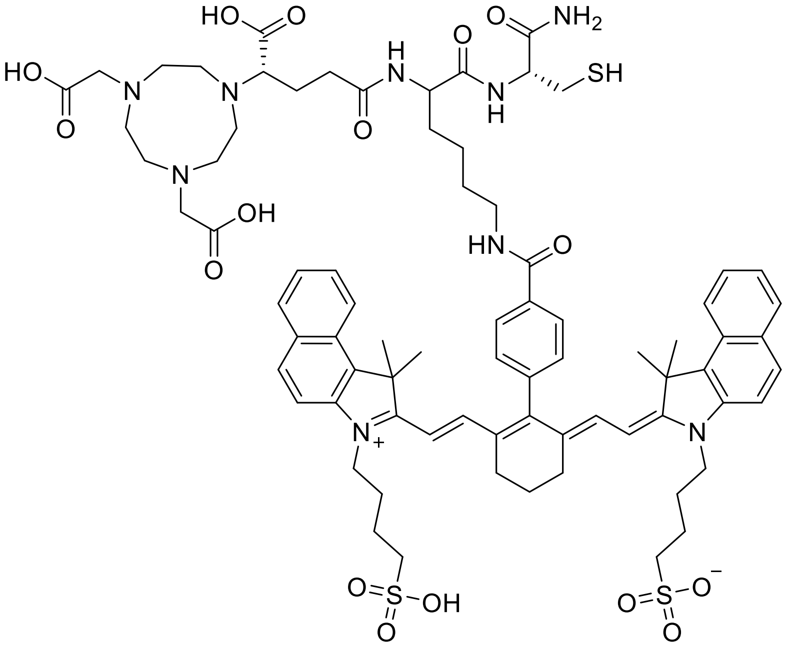

40 ($C_{77}H_{97}N_9O_{16}S_3$): HPLC gradient: 0 – 100 % MeCN + 0.1 % TFA in 5 min, Rt = 2.80 min, yield: 30 %, purity: 95 %, MALDI-MS (*m/z*) for $[M+H]^+$ (calculated): 1500.49 (1500.62); $[M+Na]^+$ (calculated): 1522.48 (1522.61); $[M+K]^+$ (calculated): 1538.49 (1538.59); $[M+2Na]^+$ (calculated): 1545.38 (1545.60); HR-ESI-MS (*m/z*) for $[M+2K+Na]^{2+}$ (calculated): 779.7598 (779.8108).

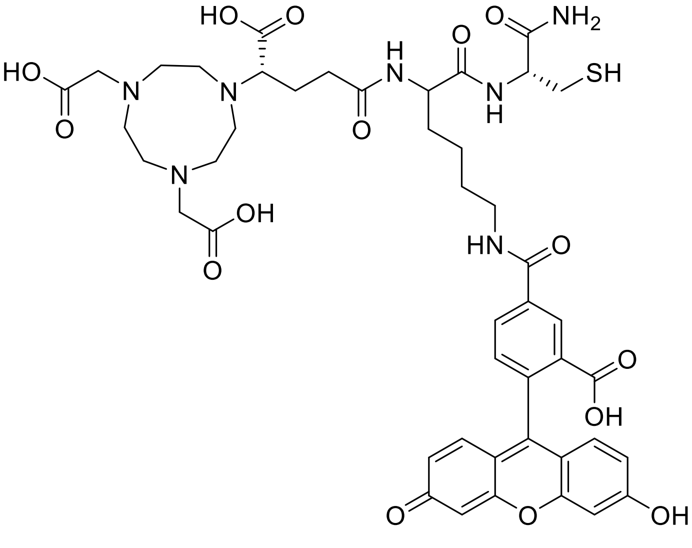

41 ($C_{45}H_{53}N_9O_7S$): HPLC gradient (analytical): 0 – 100 % MeCN + 0.1 % TFA in 12 min, R_t = 5.80 min, yield: 30 %, purity: 97 %, MALDI-MS (m/z) for $[M+H]^+$ (calculated): 964.26 (964.34); $[M+Na]^+$ (calculated): 986.28 (986.32); $[M+K]^+$ (calculated): 1002.25 (1002.30); HR-ESI-MS (m/z) for $[M+H+Na]^{2+}$ (calculated): 493.2250 (493.2509).

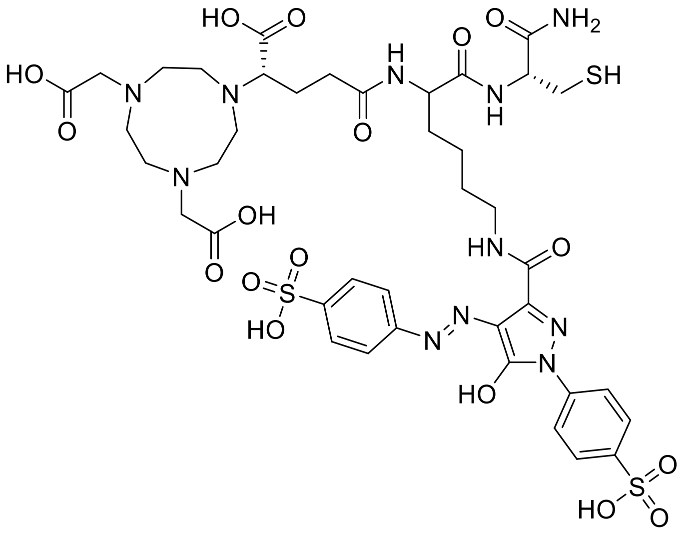

42 ($C_{40}H_{53}N_{11}O_{17}S_3$): HPLC gradient (analytical): 0 – 55 % MeCN + 0.1 % TFA in 15 min, R_t = 6.28 min, yield: 10 %, purity: 98 %, MALDI-MS (m/z) for $[M+H]^+$ (calculated): 1057.44 (1057.10); $[M+Na]^+$ (calculated): 1079.41 (1079.09); $[M+K]^+$ (calculated): 1095.33 (1095.20); HR-ESI-MS (m/z) for $[M+2Na]^{2+}$ (calculated): 553.0879 (553.1298).

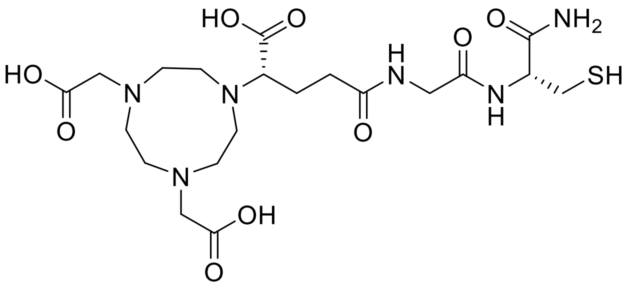

43 ($C_{20}H_{34}N_6O_9S$): HPLC gradient: 0 – 100 % MeCN + 0.1 % TFA in 8 min, Rt = 2.80 min, yield: 30 %, purity: 95 %, MALDI-MS (*m/z*) for $[M+H]^+$ (calculated): 535.10 (535.59).

GENERAL SYNTHESIS OF PEPTIDE-MIU-CONJUGATES 1 a – c, 2 a – c, 3 a – c, 4 a – c, 5 – 8 a

1.45 µmol of the respective peptide (1 eq.) and 1.60 µmol of the respective MIU (1.1 eq.) were dissolved in 200 µL of 1:1 MeCN:H_2O + 0.1 % TFA and the pH was adjusted to 7.0 with phosphate buffer (0.5M, pH = 7.2). After 5 minutes of reaction at 25 °C, the HPLC purification of the products was performed.

Peptide-MIU conjugates:

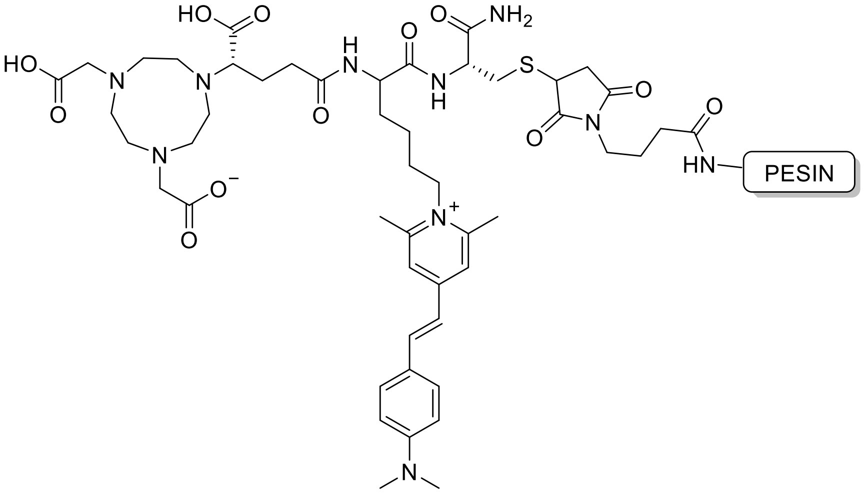

1 a ($C_{103}H_{153}N_{23}O_{26}S_2$): HPLC gradient: 0 – 100 % MeCN + 0.1 % TFA in 8 min, R_t = 6.02 min, yield: 76 %, purity: 99 %, MALDI-MS (m/z) for $[M]^+$ (calculated): 2193.09 (2193.61); HR-ESI-MS (*m/z*) for $[M+H]^{2+}$ (calculated): 1097.54822 (1097.305).

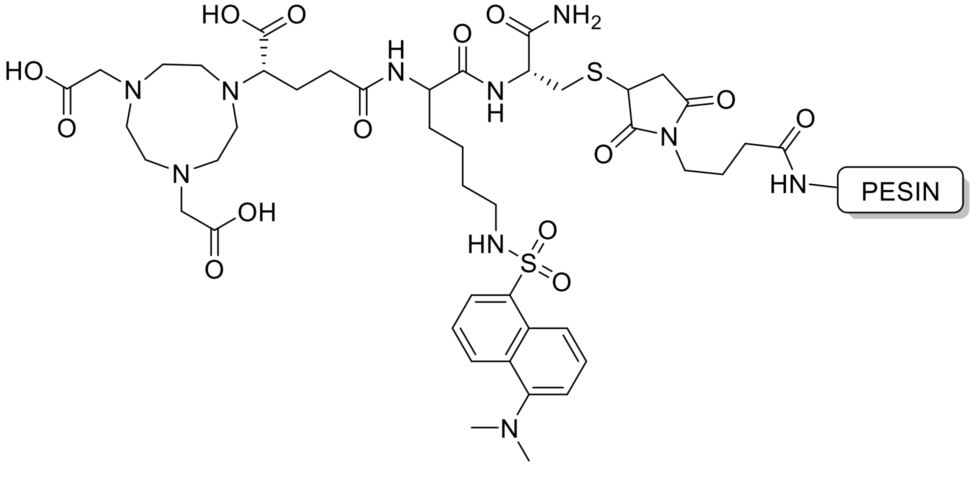

2 a ($C_{98}H_{147}N_{23}O_{28}S_3$): HPLC gradient: 0 – 100 % MeCN + 0.1 % TFA in 12 min, R_t = 5.81 min, yield: 30 %, purity: 98 %, MALDI-MS (m/z) for $[M-H]^+$ (calculated): 2190.27 (2190.57); HR-ESI-MS (*m/z*) for $[M+2H]^{2+}$ (calculated): 1096.50559 (1096.285).

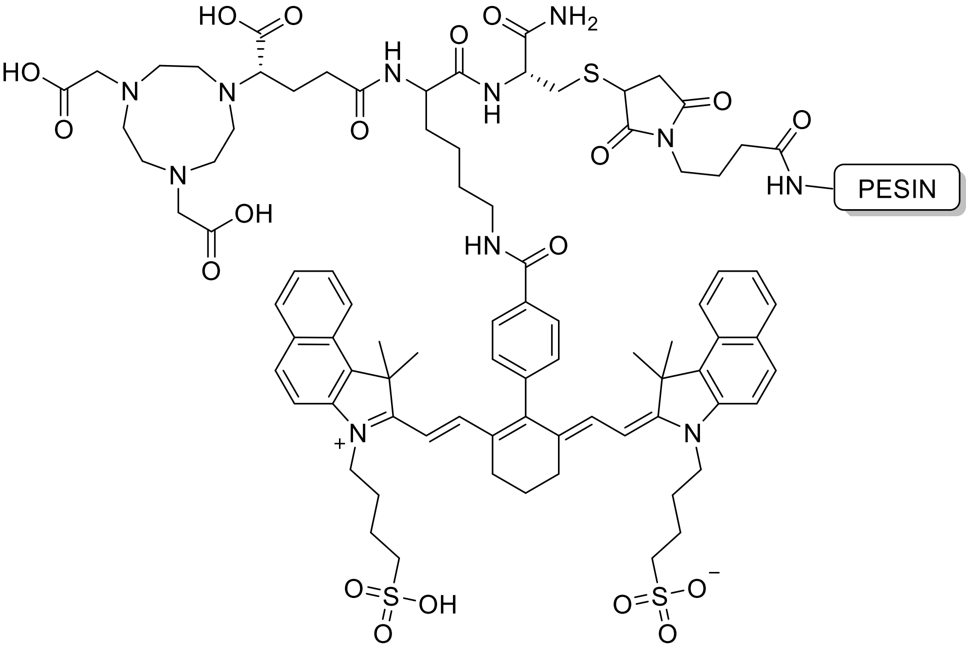

3 a ($C_{139}H_{188}N_{24}O_{33}S_4$): HPLC gradient: 0 – 100 % MeCN + 0.1 % TFA in 5 min, R_t = 4.55 min, yield: 36 %, purity: 99 %, MALDI-MS (m/z) for $[M-2H]^+$ (calculated): 2851.70 (2851.42).

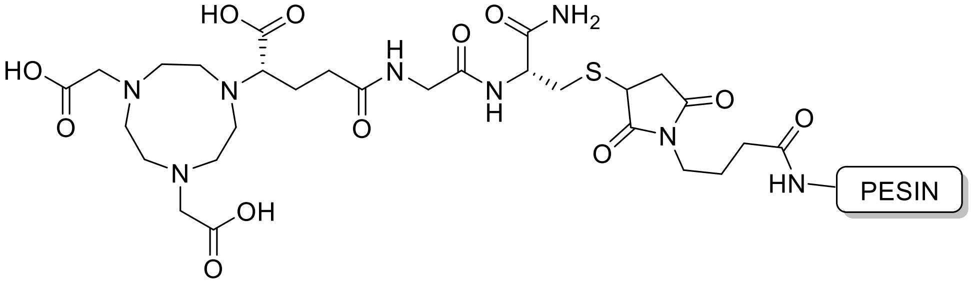

4 a ($C_{82}H_{125}N_{21}O_{26}S_2$): HPLC gradient: 0 – 100 % MeCN + 0.1 % TFA in 8 min, R_t = 4.52 min, yield: 54 %, purity: 99 %, MALDI-MS (m/z) for $[M-2H]^+$ (calculated): 1885.70 (1885.14); HR-ESI-MS (*m/z*) for $[M+H]^{2+}$ (calculated): 943.94170 (944.07).

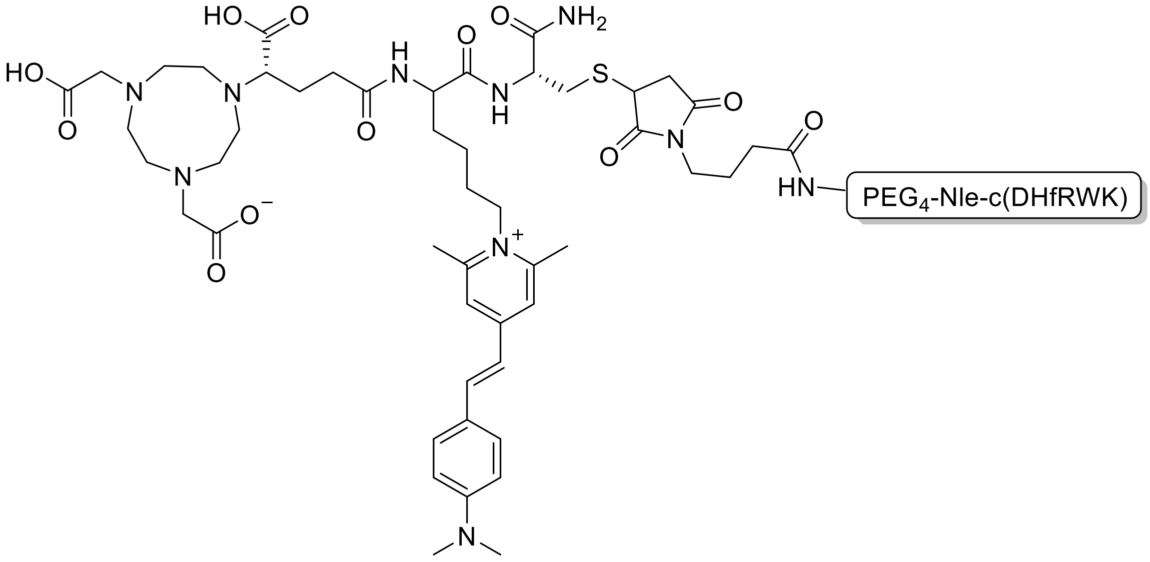

1 b ($C_{108}H_{155}N_{25}O_{25}S$): HPLC gradient: 0 – 100 % MeCN + 0.1 % TFA in 5 min, R_t = 3.87 min, yield: 70 %, purity: 99 %, MALDI-MS (m/z) for $[M-H]^+$ (calculated): 2234.38 (2234.65); HR-ESI-MS (*m/z*) for $[M+2H]^{3+}$ (calculated): 746.05278 (745.883).

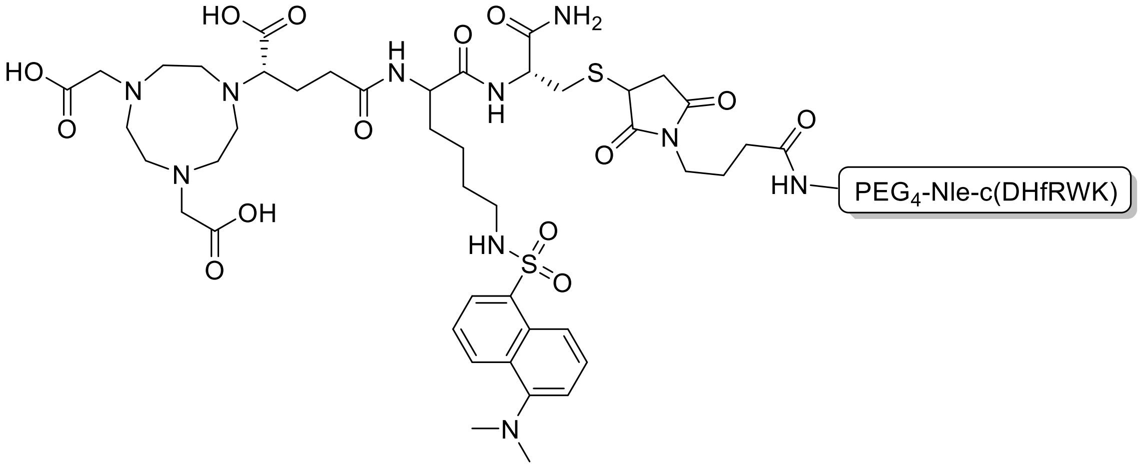

2 b ($C_{103}H_{149}N_{25}O_{27}S_2$): HPLC gradient: 0 – 100 % MeCN + 0.1 % TFA in 5 min, R_t = 3.78 min, yield: 47 %, purity: 98 %, MALDI-MS (m/z) for $[M-H]^+$ (calculated): 2232.15 (2232.59); HR-ESI-MS (*m/z*) for $[M+H]^{2+}$ (calculated): 1117.53224 (1117.295).

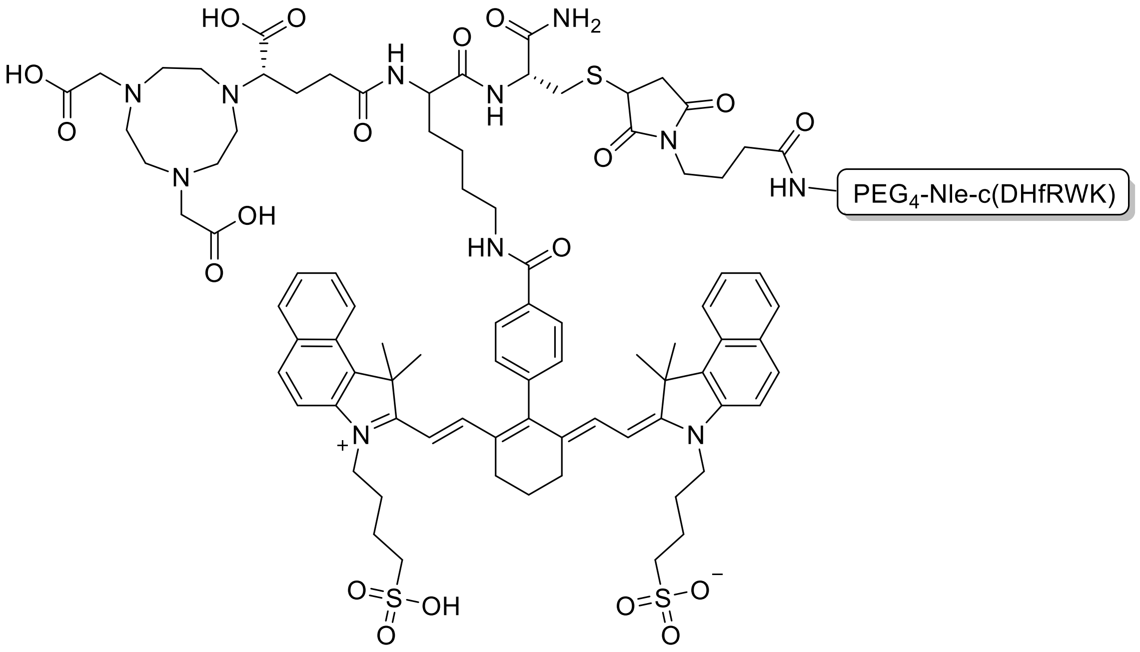

3 b ($C_{144}H_{192}N_{26}O_{32}S_3$): HPLC gradient: 0 – 100 % MeCN + 0.1 % TFA in 5 min, R_t = 4.53 min, yield: 82 %, purity: 99 %, MALDI-MS (m/z) for $[M]^+$ (calculated): 2895.18 (2895.45).

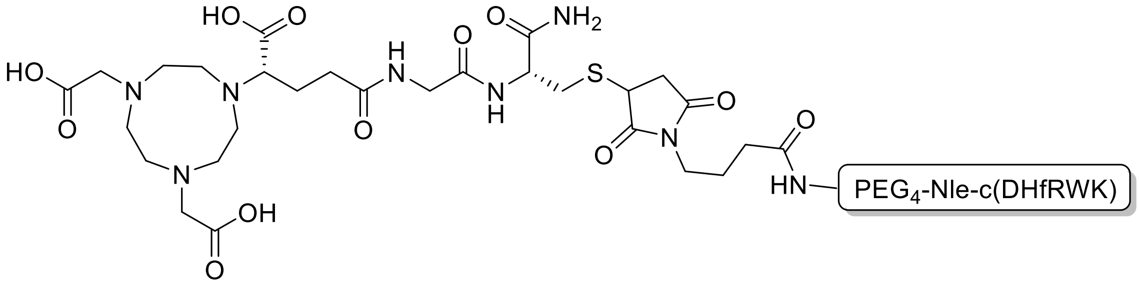

4 b ($C_{87}H_{129}N_{23}O_{25}S$): HPLC gradient: 0 – 75 % MeCN + 0.1 % TFA in 10 min, R_t = 5.96 min, yield: 52 %, purity: 98 %, MALDI-MS (m/z) for $[M-H]^+$ (calculated): 1928.49 (1928.19); HR-ESI-MS (*m/z*) for $[M+H]^{2+}$ (calculated): 965.47125 (965.095).

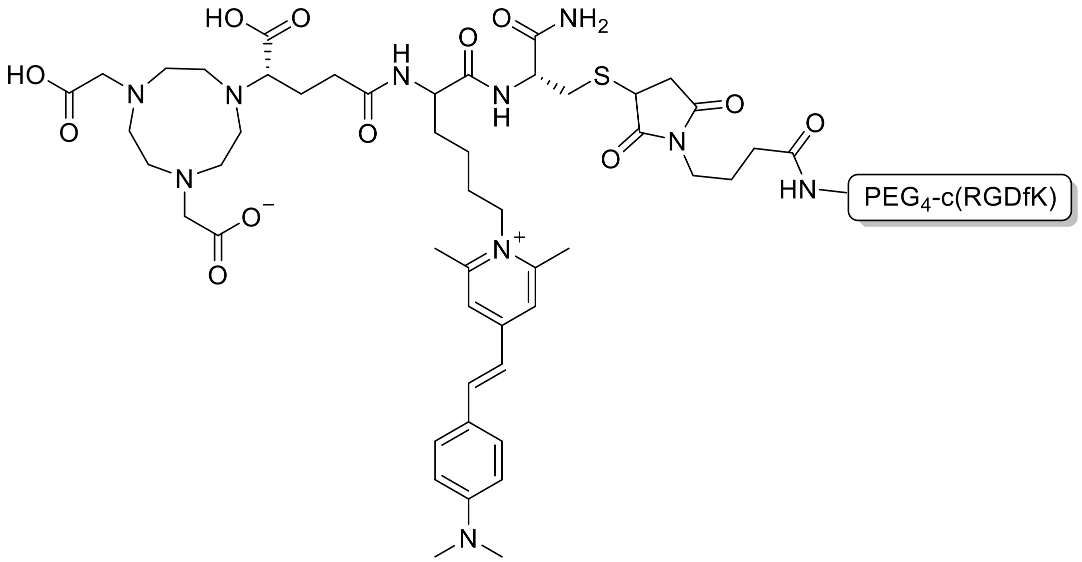

1 c ($C_{87}H_{129}N_{19}O_{24}S$): HPLC gradient: 0 – 100 % MeCN + 0.1 % TFA in 8 min, R_t = 4.48 min, yield: 38 %, purity: 99 %, MALDI-MS (m/z) for $[M-2H]^+$ (calculated): 1854.76 (1855.17); HR-ESI-MS (*m/z*) for $[M]^{2+}$ (calculated): 929.46754 (929.085).

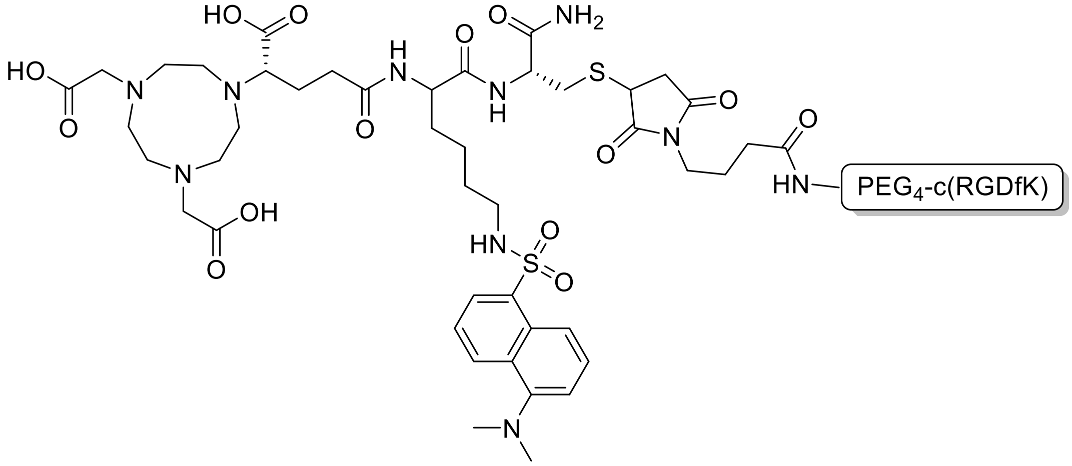

2 c ($C_{82}H_{123}N_{19}O_{26}S_2$): HPLC gradient: 0 – 100 % MeCN + 0.1 % TFA in 5 min, R_t = 3.50 min, yield: 49 %, purity: 99 %, MALDI-MS (m/z) for $[M-2H]^+$ (calculated): 1853.62 (1853.11); HR-ESI-MS (*m/z*) for $[M+Na+K]^{2+}$ (calculated): 958.88036 (958.555).

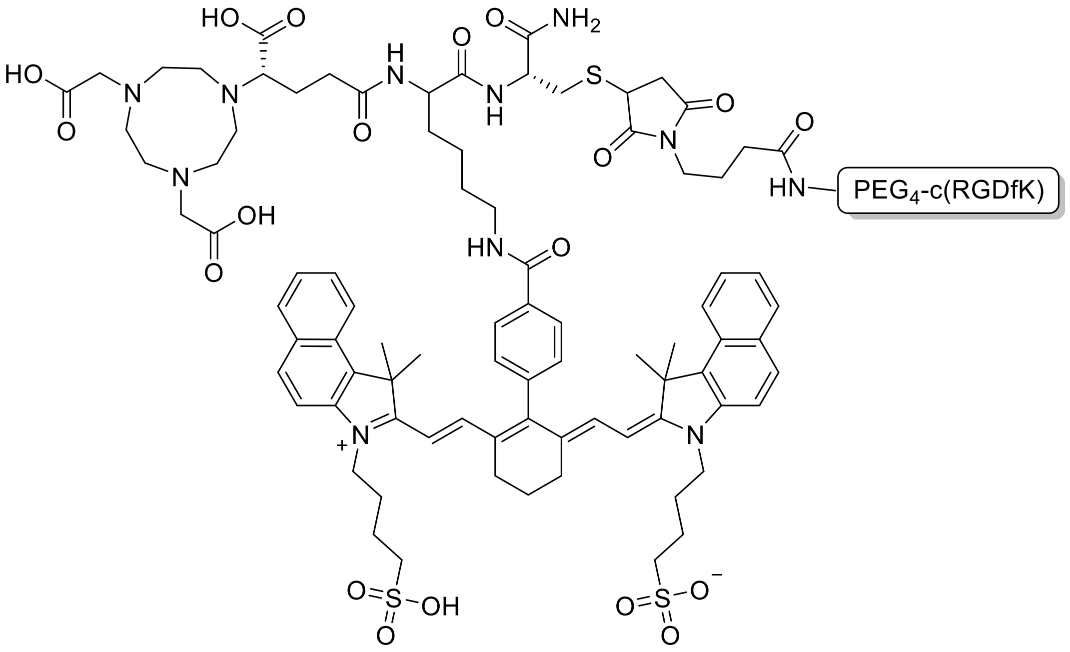

3 c ($C_{123}H_{166}N_{20}O_{31}S_3$): HPLC gradient: 0 – 100 % MeCN + 0.1 % TFA in 8 min, R_t = 5.80 min, yield: 33 %, purity: 99 %, MALDI-MS (m/z) for $[M-2H]^+$ (calculated): 2514.05 (2514.97); HR-ESI-MS (*m/z*) for $[M+Na]^{2+}$ (calculated): 1270.05862 (1269.985).

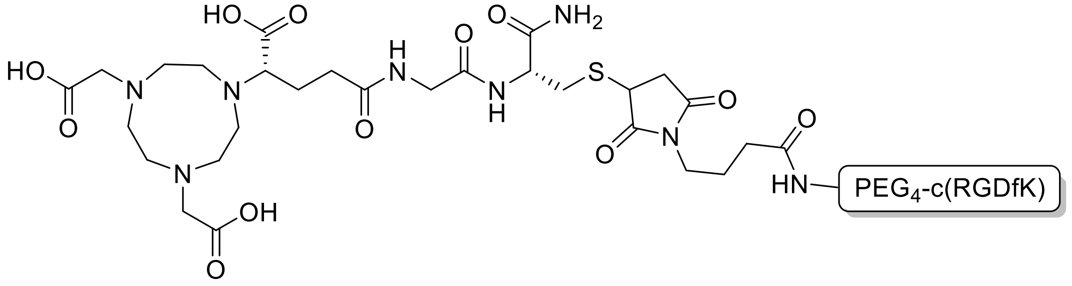

4 c ($C_{66}H_{103}N_{17}O_{24}S$): HPLC gradient: 0 – 100 % MeCN + 0.1 % TFA in 8 min, R_t = 3.96 min, yield: 23 %, purity: 97 %, MALDI-MS (m/z) for $[M-H]^+$ (calculated): 1549.56 (1549.71); HR-ESI-MS (*m/z*) for $[M+Na+K]^{2+}$ (calculated): 806.81736 (806,855).

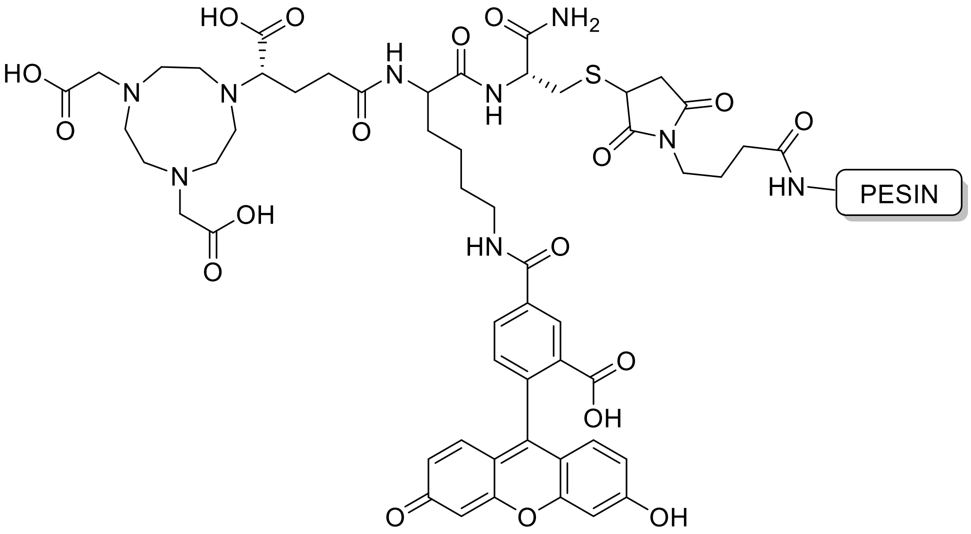

5 a ($C_{107}H_{144}N_{22}O_{32}S_2$): HPLC gradient: 0 – 100 % MeCN + 0.1 % TFA in 12 min, R_t = 6.00 min, yield: 67 %, purity: 98 %, MALDI-MS (m/z) for $[M+H]^+$ (calculated): 2315.62 (2315.68); $[M+Na]^+$ (calculated): 2338.05 (2338.06); HR-ESI-MS (*m/z*) for $[M+3Na]^{3+}$ (calculated): 796.5123 (796.5423).

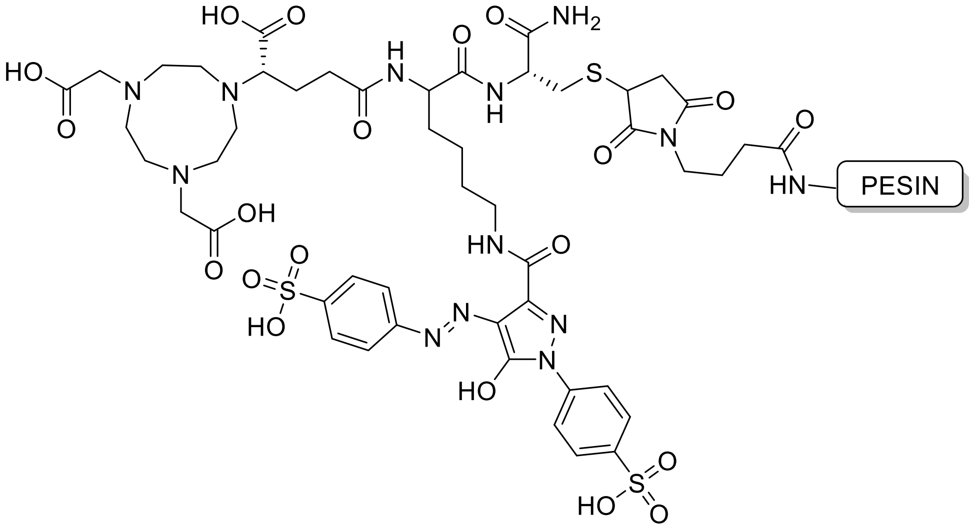

6 a ($C_{102}H_{146}N_{26}O_{34}S_4$): HPLC gradient: 0 – 100 % MeCN + 0.1 % TFA in 8 min, R_t = 4.47 min, yield: 42 %, purity: 99 %, MALDI-MS (m/z) for $[M+H]^+$ (calculated): 2409.56 (2409.68); $[M+Na]^+$ (calculated): 2432.56 (2432.68); $[M+K]^+$ (calculated): 2448.14 (2448.68); HR-ESI-MS (*m/z*) for $[M+Na+K]^{2+}$ (calculated): 1235.4218 (1235.3841).

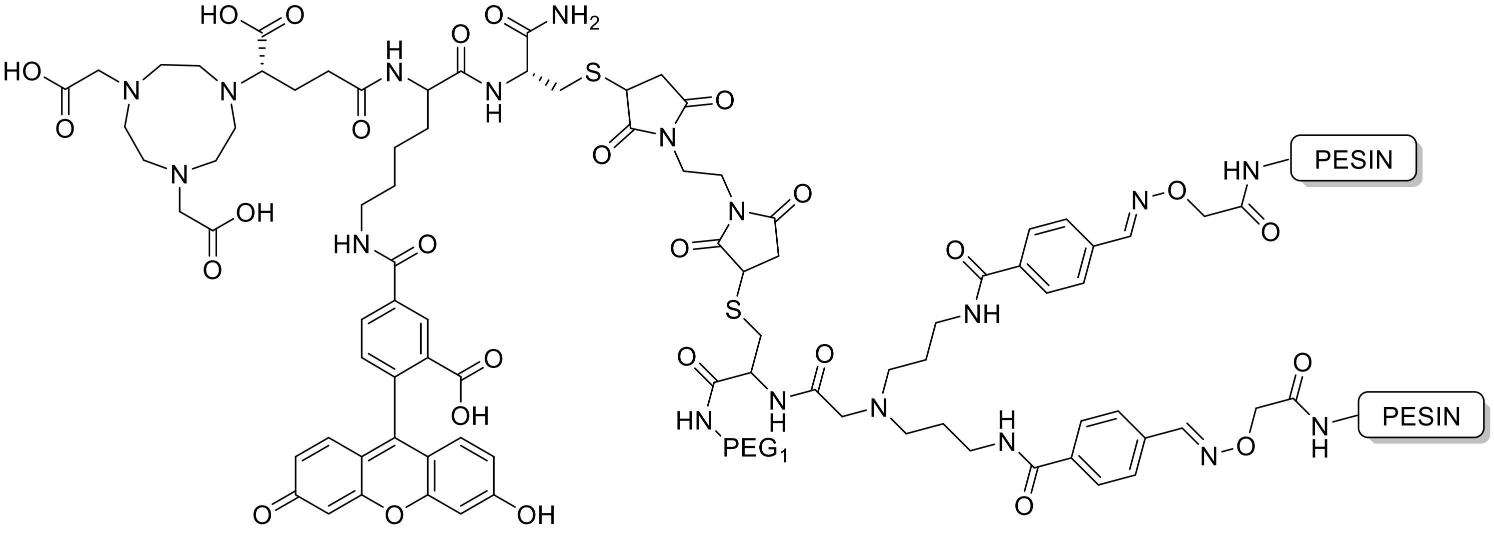

7 a ($C_{200}H_{279}N_{45}O_{58}S_4$): HPLC gradient: 0 – 100 % MeCN + 0.1 % TFA in 12 min, R_t = 6.50 min, yield: 30 %, purity: 99 %, MALDI-MS (m/z) for $[M+H]^+$ (calculated): 4368.06 (4367.92); $[M+Na]^+$ (calculated): 4390.68 (4389.90); $[M+K]^+$ (calculated): 4406.18 (4405.89); HR-ESI-MS (m/z) for $[M+H+3Na]^{4+}$ (calculated): 1109.2219 (1109.2230).

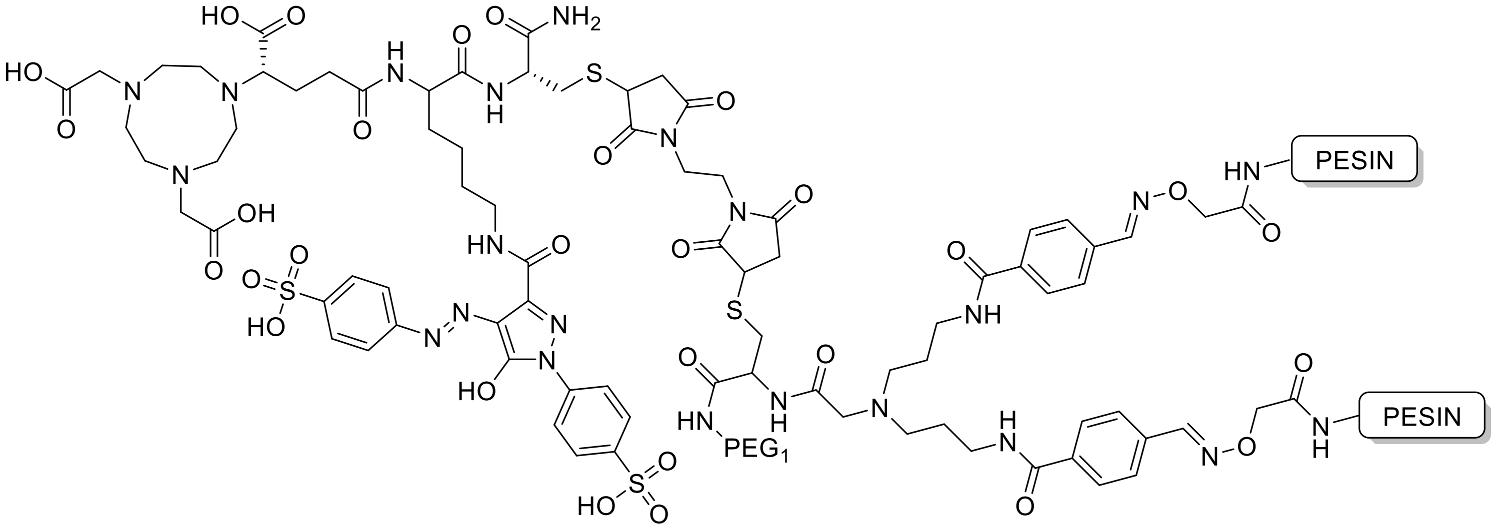

8 a ($C_{107}H_{144}N_{22}O_{32}S_2$): HPLC gradient: 0 – 100 % MeCN + 0.1 % TFA in 12 min, R_t = 6.00 min, yield: 76 %, purity: 98 %, MALDI-MS (m/z) for $[M+H]^+$ (calculated): 4463.73 (4463.02); $[M+Na]^+$ (calculated): 4486.18 (4486.00); $[M+K]^+$ (calculated): 4502.11 (4502.12); HR-ESI-MS (*m/z*) for $[M+H+2Na]^{3+}$ (calculated): 1502.9456 (1502,9998).

Radiochemistry

A solution of the peptide-MIU-conjugates in H_2O (Tracepur quality, 1mM) was added to 90 - 120 MBq of [^{68}Ga]$GaCl_3$ in a solution obtained by fractioned elution of an IGG ^{68}Ge/^{68}Ga generator system with HCl (0.1 M, 1.6 mL) and subsequent titration to pH 3.5 – 4.2 by addition of sodium acetate solution (1.25 M, 50 – 75 µL). All labeling experiments were performed by addition of 1 mg ascorbic acid to suppress radiolysis-induced product fragmentation. In the labelling experiments of the MIUs, 1 mg TCEP x HCl was also added. After 10 minutes of reaction at 45°C, the mixtures were analyzed by analytical radio-HPLC. The radiolabeled products were found to be 95 – 99 % pure and obtained in non-optimized molar activities of 90 - 120 GBq/µmol.

Log$_D$ determination

The water/1-octanol partition coefficient (log$_D$) was determined by adding 5 µL of the respectively ^{68}Ga-labeled compound (0.8 – 1.2 MBq) to a mixture of phosphate buffer (0.05 M, pH 7.4, 795 µL) and 1-octanol (800 µL). The mixtures were intensively shaken for 5 minutes on a vibrating plate. After subsequent centrifugation at 13,000 rpm for 5 min, 125 µL were taken from each phase and measured in a γ-counter. The log$_D$ values were calculated from three or four independent experiments, each performed in triplicate.

Cell Culture

All cell lines were cultivated at 37°C in a humidified incubator at 5% CO_2. HEK-GRPR cells were cultured in Dulbecco’s Modified Eagle’s Medium (DMEM, high glucose, GlutaMax-I, 500 mL) supplemented with 10 % FCS, 1.5 % geneticin and 1 % PenStrep. B16F10 cells were cultured in Dulbecco’s Modified Eagle’s Medium (DMEM, 1X, 500 mL) and the U87MG cells in Eagle’s Minimum Essential Medium (EMEM), each medium supplemented with 10% FCS and 1% PenStrep. The medium was exchanged every two or three days and cells were split at 70-90% confluence using 0.25/0.02% Trypsin/EDTA (*w*/*v*) in PBS. A medium change was performed 24 h before an experiment.

In vitro competitive binding assays

To determine the binding affinity to the respective receptor, competitive displacement studies were performed on GRPR-expressing HEK, MC1R-expressing B16F10 and on integrin $\alpha_v\beta_3$-expressing U87MG cells. Each compound was evaluated at least three times, each experiment being performed in triplicate. As radioligands, [^{125}I]-Tyr^4-bombesin, [^{125}I]-NDP-MSH and [^{125}I]-echistatin (81.4 GBq/ µmol) were used as competitors. A Millipore Multiscreen punch kit and Millipore 96 well filter plates (pore size 1.2 µm) were used. The plates were incubated with PBS/BSA (1%) solution (each well 200 µL) at 25 °C for one hour before use. After preparing the respective binding buffers (Opti-MEM I – GlutaMAX I without additional supplements; DMEM with 25 mM HEPES, 0.3 mM 1,10-phenanthroline and 0.2% BSA; EMEM with 20 mM Tris·HCl, 150 mM NaCl, 2 mM $CaCl_2$, 1 mM $MgCl_2$, 1 mM $MnCl_2$ and 0.1% BSA), the dilution series of the BBN$_{7-14}$ (0.1 - 250 nM for **1 a, 2 a** and **4 a**, 0.25 – 500 nM for **3 a** and **7 a**, 0.5 – 1000 nM for **5 a**, **6 a**, and **8 a**), Nle-c(DHfRWK) (0,005 – 100 nM for **1 b** – **4 b**), c(RGDfK) conjugates (50 – 100000 nM for **1 c** – **4 c**) and the reference compounds (0,1 – 250 nM for endogenous BBN, 0,0025 – 5 nM for NDP-MSH, 10 – 25000 nM for c(RGDyK)) were prepared in the respective binding buffer. The solution of the respective radioligand was prepared by adding 55 – 75 kBq of the respective ^{125}I-labeled competitor to 7 mL of binding buffer. The respective cells were harvested and re-suspended in the binding buffer to give a cell concentration of 2 × 10^6/mL. After the BSA solution was filtered using the Millipore Multiscreen vacuum manifold, 50 µL of a cell suspension containing 10^5 cells were seeded in each well. Subsequently, 25 µL of the ^{125}I-labeled competitor solution (0.01 kBq/µL) and 25 µL of the respective compound to be tested were added. The compound to be tested was added in eleven increasing concentrations, while the 12th well contained no test compound to ensure the 100% binding of the ^{125}I-labeled competitor. After incubation of the plate for another hour at 25 °C, the solution was filtrated, and the cells were washed three times with cold PBS (1 × 200 µL, 2 × 100 µL). Using a Millipore MultiScreen disposable punch and a Millipore MultiScreen punch kit, the filters of the well plate were collected in γ-counter tubes separately and measured by γ-counting. The determination of the half-maximal inhibitory concentration (IC_{50}) values was performed by fitting the obtained data via nonlinear regression using GraphPad Prism (v5.01).

Confocal Fluorescence Microscopy

Since the HEK-GRPR cells do not exhibit any adhered characteristics to glass plates, the GRPR positive human tumor cell line PC-3 was used for the confocal fluorescence microscopy experiments of the BBN_{7-14} series instead. PC-3 cells were cultured at 37 °C in RPMI 1640 medium supplemented with 10% FCS, 1% L-Glutamine and 1% PenStrep in a humidified atmosphere containing 5% CO_2. B16F10 and U87MG cell lines were cultured as previously described for the competitive binding assays. Fluorescence microscopy was performed on a Leica TCS SP8 confocal microscope with laser excitation wavelengths of 405 and 638 nm. Overlays of microscopies were generated directly with the operating software or afterwards using FIJI software (v1.50e). Each cell line (4 x 10^4) was seeded two days prior to the measurements in 24-well culture plates, each well was equipped with cover slips for microscopy. Medium was exchanged after 24h. After 2 days, the medium was removed and the cells were washed carefully with PBS. Then, 500 µL of a 10 µM solution of the peptide-MIU-conjugates in antibiotic-free medium were added, with or without the peptide blockade (BBN, NDP-MSH, c(RGDyK) 200 µM) followed by incubation for 4h. After washing of each cover slip with PBS thrice, they were consequently put reversed on object slides which were before prepared with a drop (10µL) of DAPI antifade solution and then the respective cover slide was sealed and fixed with clear coat on the object slides.

pH and sodium titrations of compounds 5 a and 7 a

For the pH titration in pure water, a solution of compounds **5 a** and **7 a** in deionized water (10 µM, 5 mL) was basified with 100 µL of ammonia solution (0.1 M) to pH ≈ 10. The basic solution was then treated with consecutive additions of 2 µL HCl solution (0.1 M) to pH = 2. After each addition the absorption spectra were recorded. The pH titration in presence of sodium was performed as previously described for the titration in pure water, and in addition NaCl was added in concentration of 0.1 M in both the 10 µM solution of compounds **5 a** and **7 a** and the 0.1 M titrating solutions of ammonia and HCl.

For the sodium titration, the pH of a solution of compounds **5 a** and **7 a** in deionized water (10 µM, 5 mL) was adjusted to pH = 8.23 using ammonia and HCl solutions (0.1 M). The resulting solution was then treated with 20 consecutive additions of 150 µL NaCl solution (2 M). After each addition the pH was corrected to the value of 8.23 and the absorption spectra were recorded.

DFT calculations

DFT calculations were all conducted as implemented in Spartan'20 (1.0.0)[164] using B3LYP[165-167] exchange correlation functionals and 6-31G* polarization basis set were assigned for all elements. Characterization of each optimized structure as local minimum on the potential energy surface was carried out by harmonic frequency analysis based on the second derivative. Start geometries for the structure optimization were taken from the library implemented in Spartan. The structures (Monoanionic phenolate and monoanionic carboxylate) were subsequently optimized in Spartan and the local minima determined, then the proton was exchanged by a sodium atom and the structure was minimized again and after the local minima determined. The ready conjugated biomolecules (monomer and dimer) were constructed from a DFT minimized structure of BBN_{7-14} and DFT minimized structure of the MIU and then the energy was minimized only by the molecular mechanics minimization implemented in Spartan. All attempts to calculate the energy minimum by DFT failed because of the size of this molecules.

CHAPTER FOUR

Results and Discussion

SYNTHESES OF [^{18}F] 1, [^{18}F] 2, [^{18}F] 3, AND [^{11}C] 4

The synthetic approach applied for the synthesis of the labeled compounds was designed in a fashion that left as the last step of the synthesis of the radiolabelling reaction. As a general rule, this strategy should be applied when working with short-living radionuclides, to optimize the radiochemical yield and to reduce as much as possible the exposure of the operator to radioactive material.

The syntheses were designed based on the final radiolabeling reactions, which will require different cold precursors. To obtain the labeled compounds, different cold precursors were prepared, but only a few of them could be effectively reacted with the radionuclide. Here are reported the successful attempts that led to the desired compounds **[^{18}F] 1**, **[^{18}F] 2**, **[^{18}F] 3**, and **[^{11}C] 4**. Furthermore, the radiosynthesis required the preparation of reference compounds for the correct identification of the labeled products in HPLC.

Compounds **[^{18}F] 1** and **[^{18}F] 2** are radioactive analogues of the cyclic pseudopeptide **ICG-001**. The planned synthetic route, reported in scheme 4.1, involves the introduction of fluorine in two different positions of the aromatic ring: directly on the phenyl group in *para* position (compound **[^{18}F] 1**), or in *meta* position *via* a methylene bridge (compound **[^{18}F] 2**). This last substitution is inspired by the structure of the guanylate derivative ICG-002, and it was introduced to evaluate the differences in efficacy between aromatic or aliphatic radiolabeling reactions. Both syntheses start from the condensation of 1-naphthaldehyde with 2,2-diethoxyethanamine, followed by reduction of the Schiff base intermediate resulting in (2,2-diethoxyethyl)-naphthalen-1-ylmethyl-amine **5**. Then, this amine is coupled with aminoacids using a classical liquid-phase Fmoc based strategy. Initially, it is coupled with Fmoc-L-Tyr(*t*-Bu)-OH. The coupling reaction is performed with (1-[Bis(dimethylamino)methylene]-1*H*-1,2,3-triazolo[4,5-*b*]pyridinium 3-oxid hexafluorophosphate (HATU) as coupling agent and diisopropylethylamine (DIPEA) as base in dimethylformamide (DMF). The removal of the Fmoc group is performed in dichloromethane (DCM) with diethylamine (DEA). The resulting amine **7** is then coupled with Fmoc-β-Ala-OH, again in presence of HATU and DIPEA in DMF. The cleavage of the Fmoc protection gives in intermediate **9**. From this amine, a divergent synthetic strategy will result in the desired radiolabeled derivatives. Firstly, **9** is reacted with 4-bromobenzyl isocyanate. The resulting urea **10** is cyclized upon treatment with formic acid to afford the brominated ICG-001 derivative **11**. The phenol group was protected *via* acetylation resulting in compound **12**. From this brominated derivative, the boronated cold precursor is prepared *via* a Miyaura borylation with bis(pinacolato)diboron, KOAc, and Pd(dppf)Cl_2 as catalyst in dioxane to give the boronic ester derivative **13.**

Likewise, to prepare compound **2**, **9** is reacted with the *in situ*-formed isocyanate obtained from the reaction between compound **20** and carbonyldiimidazole, resulting in the urea intermediate **14**. The following cyclization gives the ICG-001 methanol

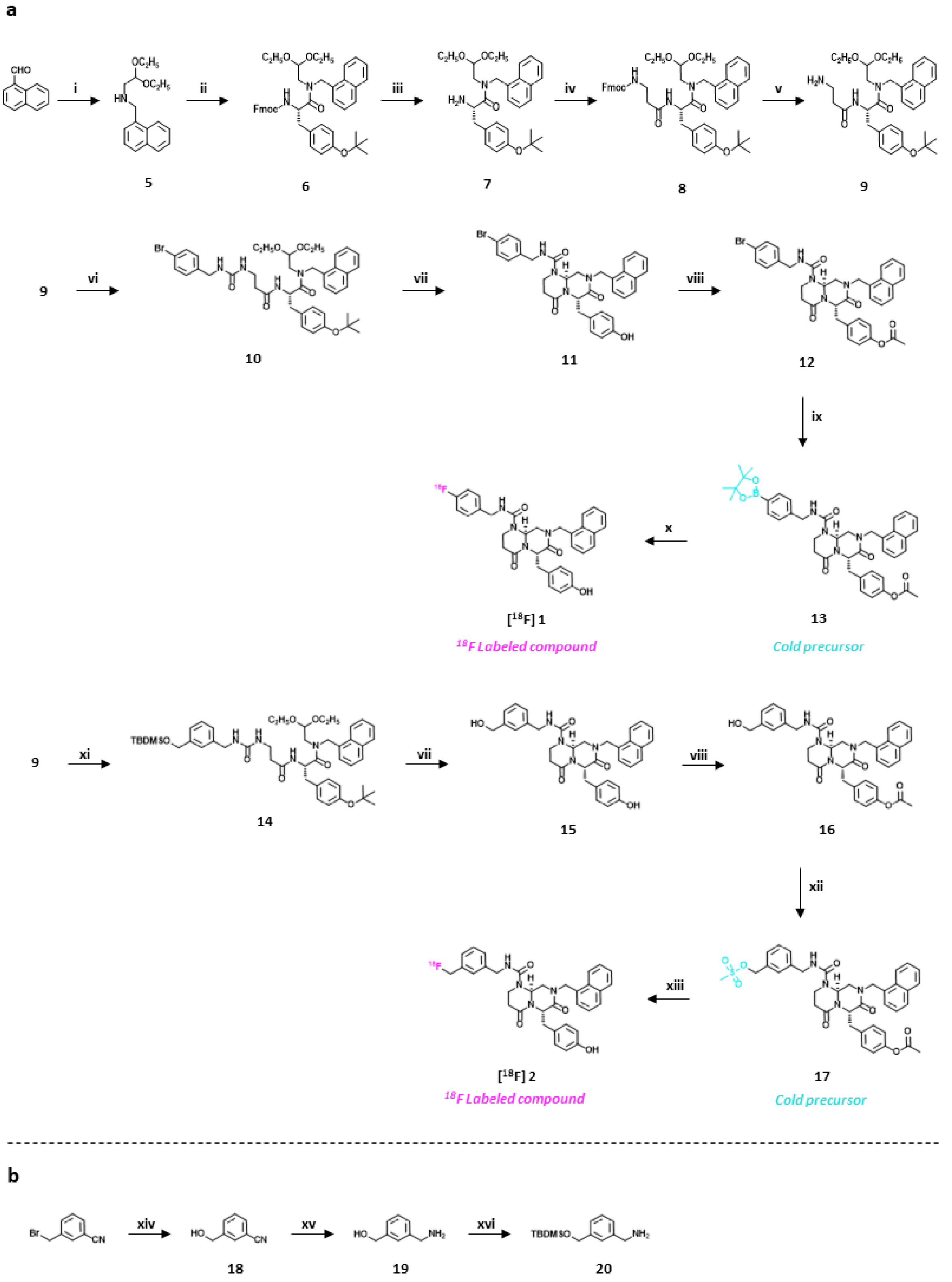

Scheme 4.8 Synthetic route to a) **1** and **2**, and b) intermediate **20** for the urea formation. *Reagents and conditions*: i) $NaBH_4$, EtOH; ii) Fmoc-L-Tyr-(t-Bu)-OH, HATU, DIPEA, DMF; iii) DEA, DCM; iv) Fmoc-ß-Ala-OH, HATU, DIPEA,DMF; v) DEA, DCM; vi) $BrC_6H_5CH_2NCO$, DCM; vii) HCOOH; viii) Ac_2O, Py; ix) bis(pinacolato)diboron, $Pd(dppf)Cl_2$, KOAc, dioxane; x) $[^{18}F]KF$, $Cu(OTf)_2$, Py, DMF; xi) carbonyldiimidazole, THF; xii) MsCl, TEA, DCM; xiii) $[^{18}F]KF$, K_2CO_3, K_{222}, NaOH, CAN; xiv) $BaCO_3$, H_2O; xv) $LiAlH_4$, THF; xvi) TBDMSCl, imidazole, DCM.

derovative **15**. Then, the protection *via* acetylation of the phenol group and the mesylation of the primary alcohol resulted in the cold precursor **17**.

Finally, the radiolabelling reactions of these compounds were performed following two different approaches. **[^{18}F] 1** was obtained *via* an oxidative fluorination, using nucleophilic radioactive fluoride and copper(II) triflate. In this reaction, copper plays the dual role of transition metal mediator for aryl-F coupling, as well as the oxidant to access the Cu(III) intermediate, requiring excess copper(II) triflate. The mechanism involves transmetallation of a Cu(II)(OTf)(F) complex and subsequent oxidation by another equivalent of copper(II) triflate to generate the highly reactive Cu(III) species (scheme 4.2).[149] On the other hand, **17** was labeled *via* nucleophilic substitution using radioactive fluoride, Kriptofix®222 (K_{222}), and NaOH.

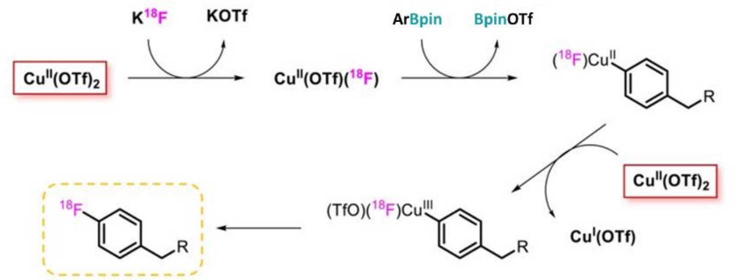

Scheme 4.2 Mechanism of oxidative fluorination of borylated arenes employing nucleophilic fluoride and copper(II) triflate.

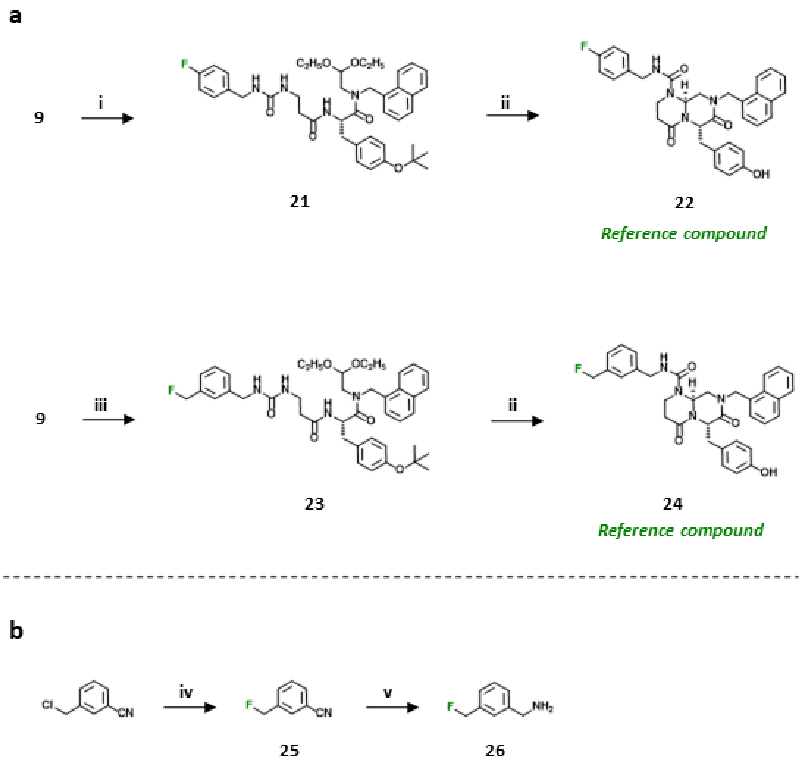

Scheme 4.3 Synthetic route to a) reference compounds of **1** and **2**, and b) intermediate **26**. *Reagents and conditions*: i) $FC_6H_5CH_2NCO$, DCM; ii) HCOOH; iii) **26**, carbonyldiimidazole, THF; iv) KF, 1,4,7,10,13,16-hexaoxacyclooctadecane, ACN; v) BH_3, THF.

Reference compounds are prepared following a similar synthetic route, reported in Scheme 4.3. **9** is reacted with 4-Fluoro-benzyl isocyanate and (3-(fluoromethyl)phenyl)methanamine for the synthesis of compounds **22** and **24**, respectively. The urea intermediates obtained (**21** and **23**) are finally cyclized upon treatment with formic acid to afford the target reference compounds **22** and **24**, which will be used for the radiosynthesis of **[^{18}F] 1** and **[^{18}F] 2**, respectively.

The second lead compound targeting the fibrotic process, **SGC-CBP30**, is a highly potent and selective ligand for the bromodomain module of CBP. Its fluorinated analogue **Cmpd 63**, although it presents a slightly weaker affinity to its target (K_d = 0.039 μM), is a suitable candidate for the development of a radiomarker for fibrosis.[133] From its structure, two imaging agents were designed, compounds **[^{18}F] 3** and **[^{11}C] 4**, labeled respectively with ^{18}F and ^{11}C. The synthesis of **[^{18}F] 3** (scheme 4.4) starts with the Suzuki reaction of 4-bromo-1-fluoro-2-nitrobenzene with the pinacol ester of 3,5-dimethyl-4-isoxazole boronic acid. Compound **28** is formed through an S$_N$Ar reaction of compound **27** with (*S*)-1,2-diaminopropane and the following reaction with 2-bromoethyl ether results in the morpholine derivate **29**. This nitro derivative is submitted to a dithionite-mediated nitro reduction to give a diamino intermediate **30** which is not isolated but directly condensed in dehydrating conditions with compound **33** in the presence of propylphosphonic anhydride (T3P). The carboxylic acid intermediate **33** is in turn obtained by bromination of 3-(4-methoxyphenyl)propanoic acid and subsequent Miyaura

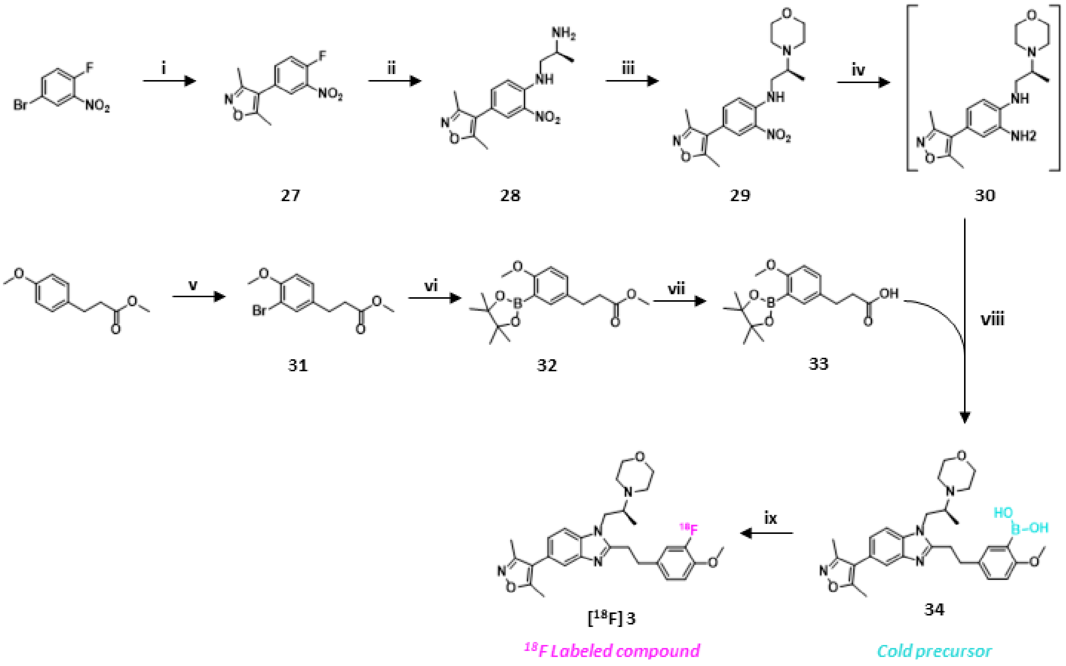

Scheme 4.4 *Reagents and conditions*: i) 3,5-dimethoxyisoxazole-4-boronic acid pinacol ester, Pd(dppf)Cl_2, $NaHCO_3$, DME/H_2O; ii) (*S*)-1,2-diaminopropane dihydrochloride, K_2CO_3, DMF; iii) 2-bromoethyl ether, K_2CO_3, DMF; iv) $Na_2S_2O_4$, H_2O, EtOH; v) Br_2, DCM; vi) B_2pin_2, Pd(dppf)Cl_2, KOAc, dioxane; vii) NaOH, MeOH/H_2O; viii) T3P, DIPEA, EtOAc; ix) K^{18}F, Cu(OTf)$_2$, Py, DMF.

borylation with bis(pinacolato)diboron, KOAc, and Pd(dppf)Cl_2 as catalyst in dioxane**.** The methyl ester group of the resulting compound **33** is then hydrolysed and condensed with intermediate **30**, giving the benzimidazole boronated derivative **34**, cold precursor of **$[^{18}F]$ 3**. The radiolabeling reaction, similarly to the reaction which resulted in **$[^{18}F]$ 1**, is performed *via* oxidative fluorination using nucleophilic radioactive fluoride with copper(II) triflate and pyridine in DMF.

Finally, the syntheses of the reference (**36**) and the labeled compound **$[^{11}C]$ 4** are overlapped (scheme 4.5). Compound **30** is condensed with **35**, which is prepared from the reductive condensation of 3-fluoro-*p*-anisaldehyde and malonic acid in pyridine. The resulting reference compound **41** is then demethylated using BBr_3, giving the cold precursor **42** which was eventually labeled *via* ^{11}C methylation using $[^{11}C]CH_3OTf$ and NaOH in 2-butanone as solvent.

Further details and the optimized results of the radiolabeling reactions are reported in the next paragraph.

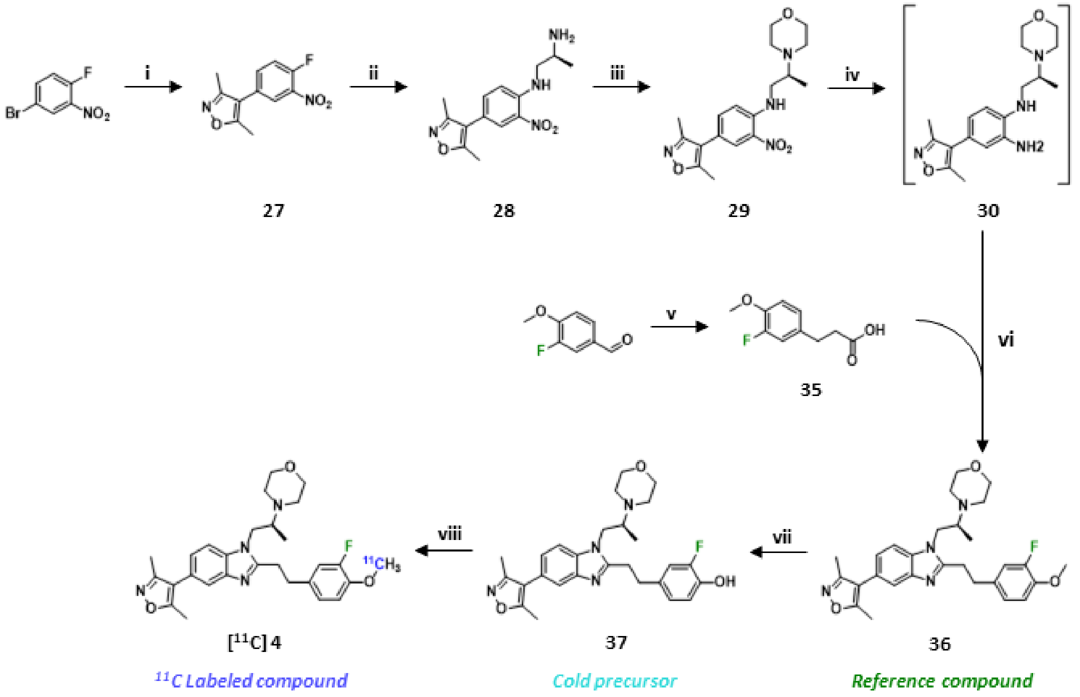

Scheme 4.5 Synthetic route to the reference and labelled compound **4**. *Reagents and conditions*: i) 3,5-dimethoxyisoxazole-4-boronic acid pinacol ester, Pd(dppf)Cl_2, $NaHCO_3$, DME/H_2O; ii) (S)-1,2-diamonopropane dihydrochloride, K_2CO_3, DMF; iii) 2-bromoethyl ether, K_2CO_3, DMF; iv) $Na_2S_2O_4$, H_2O, EtOH; v) malonic acid, Py, Pd/c; vi) T3P, DIPEA, EtOAc; vii) BBr_3, DCM; viii) $[^{11}C]CH_3OTf$, NaOH, 2-butanone.

GENERAL RADIOSYNTHETIC PROCEDURES FOR [^{18}F] 1, [^{18}F] 2, [^{18}F] 3, AND [^{11}C] 4

The previously synthesized cold precursors **13**, **17**, **34,** and **37** are reacted with the corresponding radionuclide to give the labeled compounds **[^{18}F] 1**, **[^{18}F] 2**, **[^{18}F] 3**, and **[^{11}C] 4**. All the radiosyntheses are conducted with an automated synthesis module, that assures high quality and reproducibility of the reaction and safety for the operator. In these experiments, TRACERlab® FX$_{FN}$ and TRACERlab® FX N Pro (Figure 4.1 a) from GE Healthcare (Milan, Italy) were employed for the automated synthesis of ^{18}F and ^{11}C labeled tracers. These instruments operate the handling of the radionuclides from the post-production in the cyclotron of [^{18}O]H$_2$O[^{18}F]F$^-$ and [^{11}C]CO$_2$, passing through their purification and transformation in the radiolabeling agents [^{18}F]KF and [^{11}C]CH$_3$I/CH$_3$OTf, to the effective radiolabeling reaction with the cold precursors and purification of the prepared tracers.

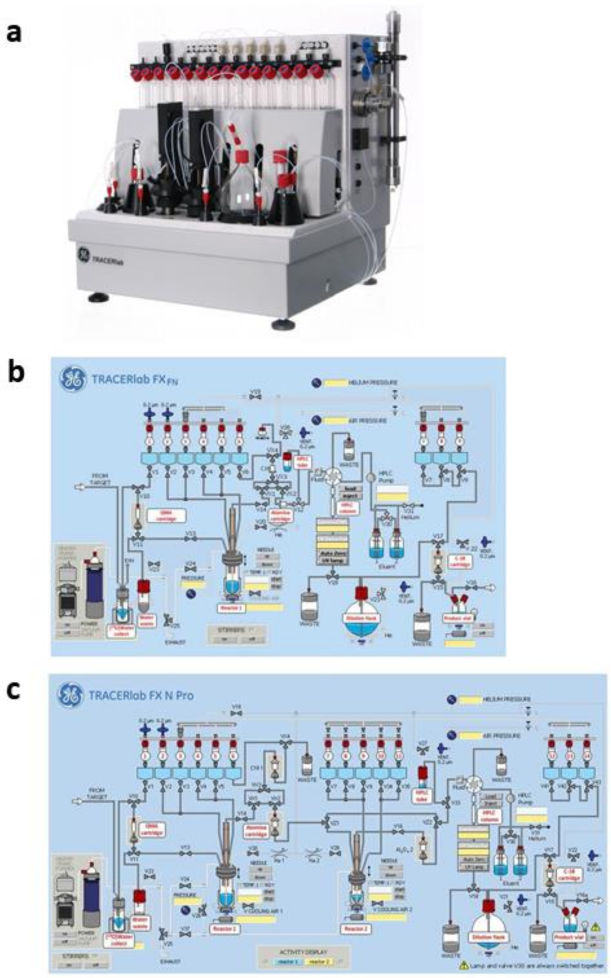

Figure 4.1 a) Picture of the TRACERlab® FX N Pro, and the schematic representation of both b) TRACERlab® FX$_{FN}$ and c) TRACERlab® FX N Pro.

In order to minimize the exposure to radiation of the operator, these modules are placed in shielded cells, composed of 10 cm lead shields on each side, which are able to absorb most of the radioactivity produced in the module during the synthesis. A "window" in the front panel, made of leaded glass, ensures the same shielding effect and the visual control of the module, while a negative pressure inside the cell prevents the dispersion of contaminated air in the laboratory during the procedure. From the synoptic panel (Figure 4.1 b and c) it is possible to control the different components of the module, such as the valves connecting vials with the reactor, stirring and heating parameters, vacuum pumps, and HPLC purification columns.

As a general procedure for radiofluorination reactions, following the cyclotron bombardment, $[^{18}F]F^-$ in aqueous solution is automatically transferred to the module, avoiding radioactive exposure to the operator. Then, separation of $[^{18}F]F^-$ from water-18 is performed by trapping the radionuclide on an ion-exchange cartridge (QMA-light Sep-Pak, preconditioned with K_2CO_3 aqueous solution). $[^{18}F]F^-$ is eluted from the cartridge using K_2CO_3 aqueous solution with a cryptand (typically K_2CO_3 + Kryptofix®222), or a water solution of K_2CO_3 and KOTf. The water is then azeotropically evaporated (60 °C × 5 min, 120 °C × 5 min), and the dissolved cold precursor in the reaction solvent is added. Following the completion of the radiolabeling reaction, the crude is separated from the potentially unreacted $[^{18}F]F^-$ using a separating cartridge (e.g. C18, tC18, alumina), and the final radiolabeled product is purified *via* HPLC. Finally, the radiotracer is trapped on a Sep-Pak extraction cartridge for the removal of organic solvents and the following formulation in a suitable solvent, to make the radiopharmaceutical compatible with intravenous administration. The final product is transferred from the shielded cell to the Quality Control room (QC) into a shielded hollow cylinder called "safety box". The cleaning procedure can be performed in an automated or manual way.

Considering the carbon-11 radiolabeling, the radionuclide is initially produced by proton bombardment in the cyclotron. Then, $[^{11}C]CO_2$ is transferred to the automated module, and trapped on molecular sieves at room temperature. There, it is reduced to $[^{11}C]CH_4$ by catalytic hydrogenation on nickel catalyst at 350°C. Radioactive methane is purified using an Ascarite and phosphorous pentoxide column, then it is trapped on a resin of Carboxen at -75°C. $[^{11}C]CH_4$ is converted into $[^{11}C]CH_3I$ by radical iodination at 720°C with solid I_2. Liquid $[^{11}C]CH_3I$ is purified from the reaction side products with two traps of Ascarite, and then trapped at room temperature on Porapak Q resin. $[^{11}C]CH_3I$ is released from the resin with a heating cycle at 190°C. If needed, $[^{11}C]CH_3OTf$ can be obtained from $[^{11}C]CH_3I$ by reacting the latter with silver triflate at 200 °C. The methylating agent is then channelled in the reactor containing the solved cold precursor and the base needed for deprotonation. Following the completion of the reaction, the ^{11}C-labeled final product is purified and formulated as previously described in the radiofluorination procedure.

The identities of the synthesized radiotracers were determined by comparing their retention time with the one of the corresponding reference compounds, analysed with the same chromatographic conditions.

RADIOSYNTHESIS RESULTS FOR [^{18}F] 1, [^{18}F] 2, [^{18}F] 3, AND [^{11}C] 4

The best radiolabeling conditions found for the synthesis of compounds **[^{18}F] 1**, **[^{18}F] 2**, **[^{18}F] 3**, and **[^{11}C] 4** are summarized in table 4.1.

Table 4.1 Summary of the parameters and radiochemical yields of the final radiolabeling reactions, performed on the respective cold precursors.

Labeled compound	Reagents	Solvent	Temperature (°C)	Reaction time (min)	Radiochemical yield [a]/purity (%)
[^{18}F] 1 [b]	Cu(OTf)$_2$ + Py	DMF	110	20	2.0 [d] / 99.0
[^{18}F] 2 [b]	K$_{222}$ + K$_2$CO$_3$	ACN	100	15	13.4 / 99.9
[^{18}F] 3 [b]	Cu(OTf)$_2$ + Py	DMF	110	20	0.8 / 50.0
[^{11}C] 4 [c]	NaOH	2-butanone	25	0.5	56.3 / 99.5

[a] Radiochemical yield corrected for the decay. Cold precursors were radiolabeled with [b] [^{18}F]KF or [c] [^{11}C]CH$_3$OTf. [d] Unoptimized radiochemical conversion.

RADIOLABELING OF [¹⁸F] 1

In detail, compound **[^{18}F] 1** was obtained as shown in scheme 4.6. [^{18}F]KF is reacted with the cold precursor **13** via oxidative fluorination mediated by cupper triflate and pyridine, which form *in situ* a pyridinium sulfonate cupper salt $Cu(OTf)_2(Py)_4$.[168] The reaction is conducted for 20 minutes at 110 °C, then cooled to room temperature and purified using BDS Hypersil semipreparative HPLC column, leading to the desired product with a radiochemical purity of 99.9 % and a maximum radiochemical conversion of 2.0 %, which was not possible to be reproduced (Figure 4.2).

$$H_2{}^{18}O[^{18}F]^- \xrightarrow[CH_3CN]{KOTf,\ K_2CO_3} \begin{matrix}5'\ 60°C\\5'\ 120°C\end{matrix} \xrightarrow[DMF]{13} 5'\ 100°C \xrightarrow[20'\quad 110°C]{\begin{matrix}Cu(OTf)_2\\Py,\ DMF\end{matrix}} [^{18}F]\ 1$$

Scheme 4.6 Radiolabeling conditions for the synthesis of compound **[^{18}F] 1**.

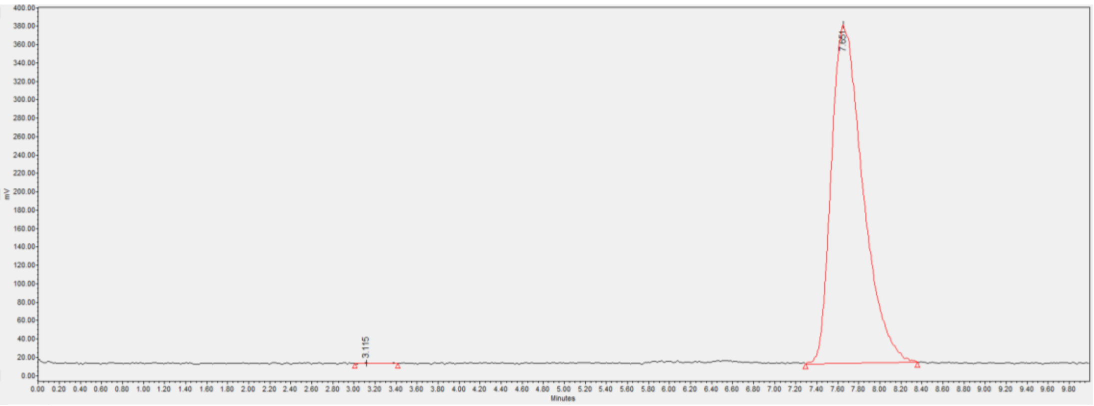

Figure 4.2 Radiochromatogram of **[^{18}F] 1** obtained with semipreparative BDS Hypersil C18 column and KH_2PO_4 (0.05 M)/ACN (50:50) as eluent. The identity of the radiocompound was determined by comparing its retention time (R_t = 7.6 min) with the one of the reference compound **23** in the same chromatographic conditions (R_t = 7.4 min, difference due to the consecutive in-line position of the UV- and radio-detectors).

This relatively low yield has to be attributed to the low stability of the cold precursor **13** to the reaction conditions. Following the radiolabeling, HPLC analysis demonstrates that

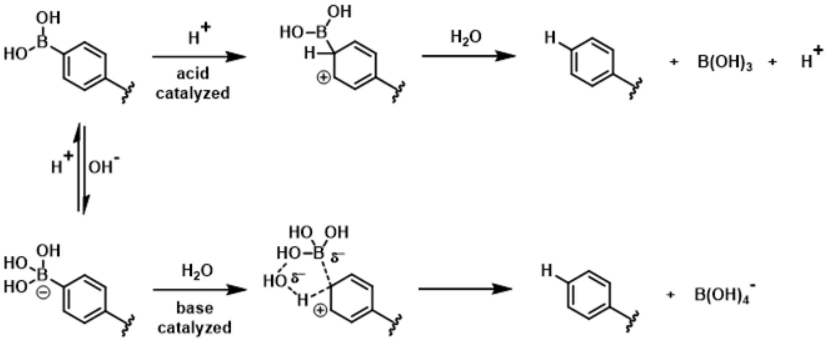

Scheme 4.7 Protodeboronation mechanism of a generic aryl boronic acid, both acid- and base-mediated

13 is almost completely degraded in side products, possibly due to thermolysis or protondeboronation (scheme 4.7).[169]

RADIOLABELING OF [^{18}F] 2

The optimized radiosynthesis of compound **[^{18}F] 2** was performed as reported in scheme 4.8. [^{18}F]F$^-$ is introduced in the structure of **17** *via* aliphatic nucleophilic substitution on the mesyl group of the cold precursor. Initial attempts afforded the desired compound with very poor yield. A study by Zhao et al.[170] found an inverse correlation between yields of their aliphatic nucleophilic radiofluorinations and K_2CO_3 and Kryptofix®222 concentrations.

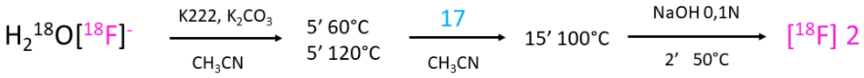

Scheme 4.8 Radiolabeling conditions for the synthesis of compound **[^{18}F] 2**.

Thus, the content of K_2CO_3 was increasingly reduced, keeping Kryptofix®222 in medium/high concentration to assure a good Fluorine-18 recovery from the separating cartridge (QMA-light Sep-Pak). This allowed to increase the radiochemical yield (3%), however there was still an important level of degradation, suggesting that the reaction temperature (120 °C) was too high. Therefore, it was performed a heating stability test on **17**, so to determine the optimal reaction temperature (table 4.2):

Table 4.2 Heating stability results. The test was performed by heating cold precursor **17** dissolved in ACN in the reactor at different temperatures for 15 minutes, followed by HPLC chromatography.

Temperature (°C)	Residue of precursor **17**[a]
Room temperature	34.0 %
80	34.0 %
100	32.0 %
110	9.5 %
120	0.3 %

[a] The precursor used for this test is not 100 % pure, 34 % is to be considered as the maximum purity

The results of this test showed that the maximal temperature which could be reached during the radiolabeling reaction without altering the structure of the cold precursor is 100 °C. By setting the temperature to this level, it was then possible to obtain the result reported in figure 4.3.

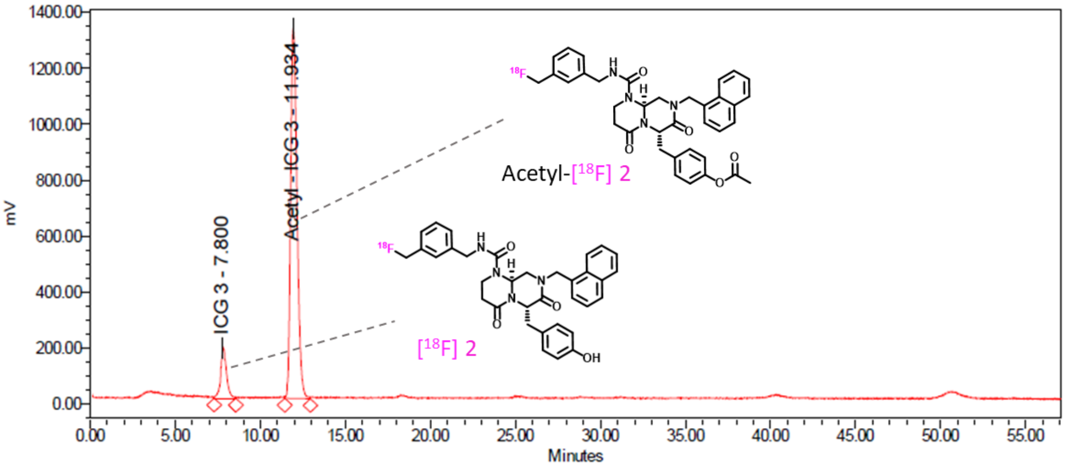

Figure 4.3 Radiochromatogram obtained with analytical BDS Hypersil C18 column and NaH_2PO_4 0,05 M/ACN (50:50) as eluent. **2** represents 11 % of the total radioactivity, while the still acetylated compound **Acetyl-2** 89 %.

Besides the desired compound, by lowering the temperature it was obtained a side product with R*t* = 11.9 min, which was supposed to be the acetylated derivative **Acetyl-[^{18}F] 2** (Figure 4.3). To confirm this hypothesis, a final hydrolytic step was introduced in the synthetic pathway. Thus, after the 15 minutes reaction, NaOH 0.5 M (0.5 mL) is added to the reactor, and stirred for 2 minutes at 50 °C. After the hydrolysis, citric acid (0.5 M, 2 ml) is used to acidify the reaction to pH = 5.4. Citric acid was added to restore a pH compatible with the intravenous administration. The reaction converted all the side product in the desired compound **[^{18}F] 2**, validating the initial hypothesis, and giving a 90% radiochemical purity, as shown in figure 4.4.

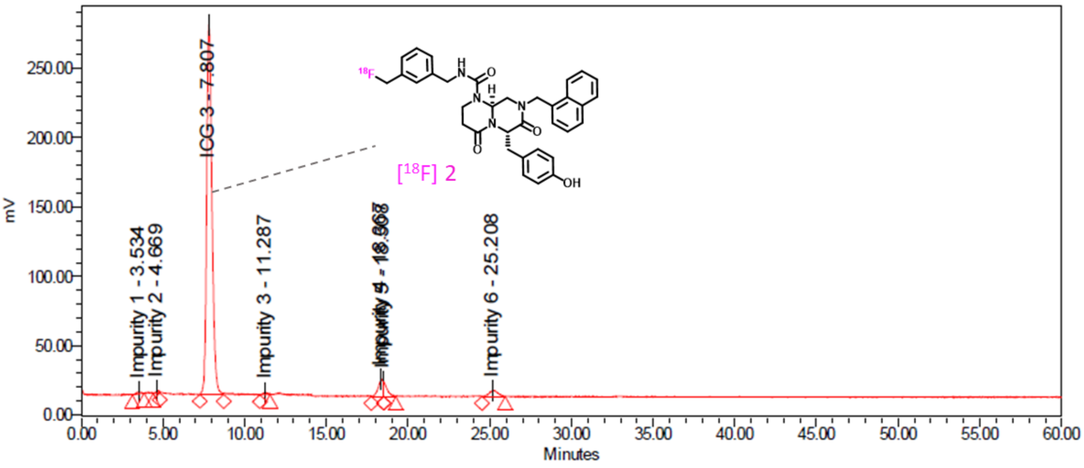

Figure 4.4 Radiochromatogram obtained with analytical BDS Hypersil C18 column and NaH_2PO_4 0,05 M/ACN (50:50) as eluent. Compound **2** represents 90.0 % of the total radioactivity.

Moreover, it was noted that after the reaction step the reactor was opened at 85 °C, fluxing helium and under vacuum. This procedure led to the complete evaporation of the solvent, because of the low boiling point of acetonitrile (82 °C). To prevent this from happening, the reactor is maintained closed until 50 °C is reached. This change leads to a

145% increase in terms of radiochemical yield (from 6.4% to 15.6%). Furthermore, to increase the radiochemical purity over 95%, a semipreparative HPLC was introduced (Figure 4.5). The column is eluted with H_2O/ACN 70:30 for 7 minutes, then with H_2O/ACN 30:70, resulting in the desired compound **[^{18}F] 2** with a radiochemical purity of 99.9 %.

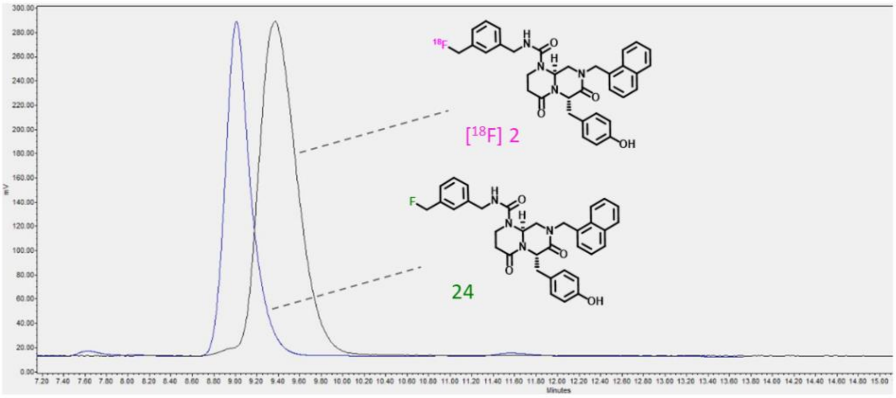

Figure 4.5 Overlapped chromatograms of compound **2** (blue, R_t = 9.3 min) and the reference compound **24** (grey, R_t = 9.5 min), both obtained with semipreparative BDS Hypersil C18 column and NaH_2PO_4 0,05 M/ACN (50:50) as eluent. The different elution time is caused by consecutive in-line position of the UV- and radio-detectors.

*RADIOLABELING OF **[^{18}F] 3***

The radiosynthesis of compound **[^{18}F] 3** followed the strategy used to obtain compound **[^{18}F] 1**, as reported in scheme 4.9. [^{18}F]F$^-$ is introduced in the structure of **34** via oxidative radiofluorination cupper mediated. Various attempts were performed, modifying the different parameters which characterize the reaction (table 4.3). From the stability test conducted on the cold precursor, 110 °C was selected as the optimal temperature for the reaction. It was also noted that the presence of air during the reaction improved the overall yield, compared to the radiolabeling performed under inert conditions. Moreover, the variation of reaction time, from 10 to 20 minutes, had very little impact on the final result. On the other hand, the use of the preformed pyridinium sulfonate cupper salt $Cu(OTf)_2(Py)_4$, instead of forming it *in situ*, seemed to have a negative influence on the radiochemical yield of the reaction. Finally, it was also tested the procedure proposed by Zischler et al.[171], who demonstrated that the presence of ethanol in the reaction mixture could enhance cupper-mediated radiofluorinations. Unfortunately, in the present experiment the combination of DMF and EtOH didn't afford any improvement.

$$H_2{}^{18}O[^{18}F]^- \xrightarrow[CH_3CN]{KOTf,\ K_2CO_3} \begin{matrix} 5'\ 60°C \\ 5'\ 120°C \end{matrix} \xrightarrow[DMF]{34} 5'\ 100°C \xrightarrow[20'\quad 110°C]{\begin{matrix} Cu(OTf)_2 \\ Py,\ DMF \end{matrix}} [^{18}F]\ 3$$

Scheme 4.9 Radiolabeling conditions for the synthesis of compound **[^{18}F] 3**.

Table 4.3 Summary of the reaction conditions used in the various attempts for the synthesis of compound **[^{18}F] 3**.

Solvent	Fluoride eluent	Reagent	Temperature (°C)	Reaction time (min)	Radiochemical yield [a]/purity (%)
DMF	TBA-HCO_3	$Cu(OTf)_2(Py)_4$	110	10	-
DMF	K_2CO_3 + KOTf	$Cu(OTf)_2$ + Py	110	10	0.50 / 50.0
DMF	K_2CO_3 + KOTf	$Cu(OTf)_2$ + Py	110	20	0.51 / 50.0
DMF	K_2CO_3 + KOTf	$Cu(OTf)_2(Py)_4$	110	10	0.03 / 32.0
DMF/EtOH	K_2CO_3 + KOTf + K_{222}	$Cu(OTf)_2(Py)_4$	110	10	-

[a] Radiochemical yield not corrected for the decay.

Summing up, the best conditions for the radiosynthesis of **[^{18}F] 3** required the elution of [^{18}F]F$^-$ with a mixture of K_2CO_3/KOTf, DMF as solvent of the reaction with the addition of $Cu(OTf)_2$ and pyridine. The reaction is carried out at 110 °C for 20 min, then purified using a Sep-Pak Alumina N Plus cartridge. Compound **[^{18}F] 3** could be obtained with a radiochemical yield of only 0.51 %, and radiochemical purity of 50.0 % (Figure 4.6). The reason for this unsatisfactory result has to be attributed to the very low stability of the cold precursor to the labelling conditions: as shown in figure 4.7, the addition of the radiolabeling mixture causes the complete degradation of **34** (Figure 4.7 b). Future attempts should consider the modification of the elution mixture of radioactive fluoride, in order to reduce its impact on the cold precursor during the reaction.

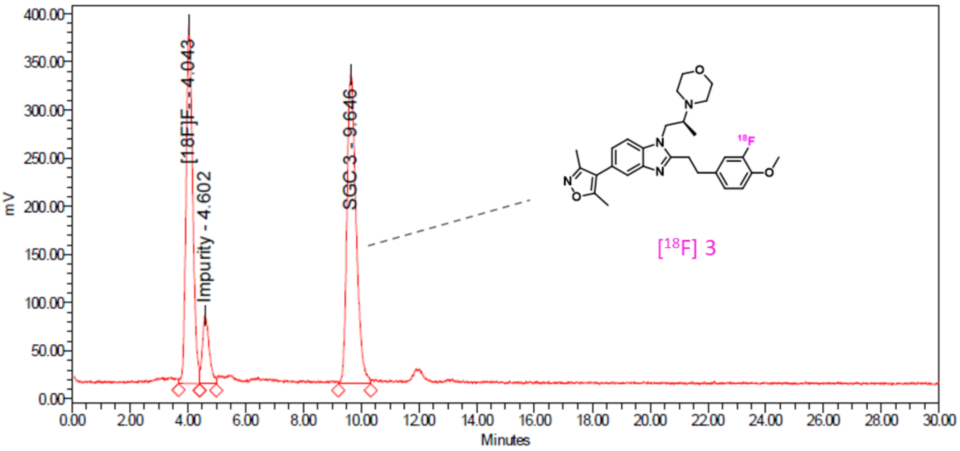

Figure 4.6 Radiochromatogram obtained with analytical BDS Hypersil C18 column and NaH_2PO_4 0,05 M/ACN (50:50) as eluent. Compound **[^{18}F] 3** (R_t = 9.6 min) represents 50.0 % of the total radioactivity.

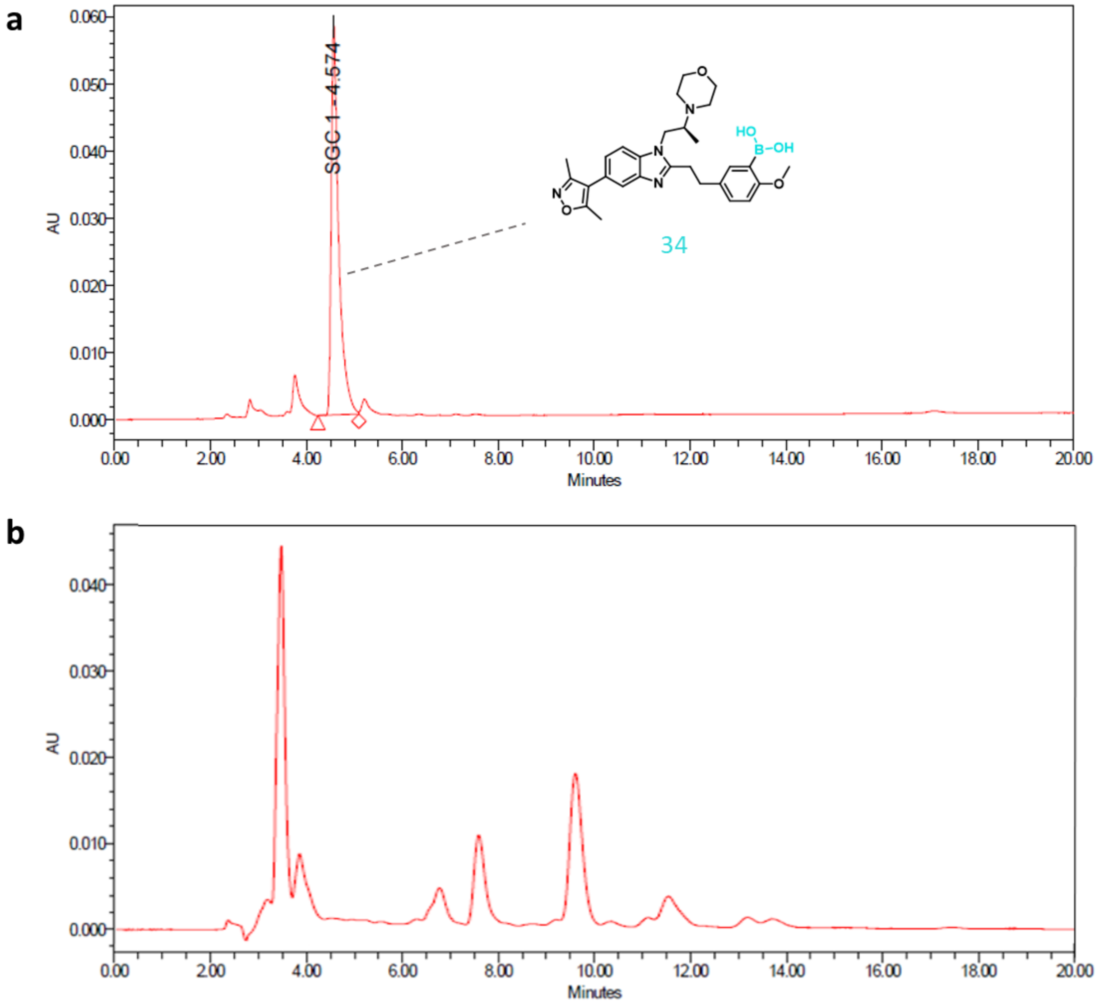

Figure 4.7 Chromatograms of a) cold precursor **34** before the radiolabeling, and b) the reaction mixture post-radiolabeling. Both chromatograms are obtained with analytical BDS Hypersil C18 column and NaH_2PO_4 0,05 M/ACN (50:50) as eluent. Complete degradation of the cold precursor is observed during the reaction.

RADIOLABELING OF [^{11}C] 4

Unlike the previous synthesis, compound **[^{11}C] 4** was designed following a carbon-11-based strategy, where the phenol group of cold precursor **37** is labeled with a radioactive methylating agent. Although ^{11}C presents a reduced half-life compared to ^{18}F, the shorter reaction time and the milder conditions of this kind of reaction make this radiolabeling strategy a suitable substitute for radiofluorinations. Different radiolabeling conditions were tested (table 4.4).

Table 4.4 Summary of the reaction conditions used in the various attempts for the synthesis of compound **[^{11}C] 4**.

Solvent	Precursor (mg)	Reagent	Base [a]	Reaction time (sec)	Radiochemical yield [b]/ purity (%)
2-butanone	0.5	[^{11}C]CH_3OTf	NaOH	90	33.0 / 51.6
2-butanone	0.5	[^{11}C]CH_3OTf	TBAOH	90	20.7 / >99
2-butanone	0.5	[^{11}C]CH_3I	TBAOH	90	2.2 / 28.3
2-butanone	1	[^{11}C]CH_3OTf	NaOH	90	41.8 / >99
2-butanone	1	[^{11}C]CH_3OTf	NaOH	30	58.0 / 99.5

[a] NaOH 1 M, TBAOH 54.0-56-0 % solution in H_2O. [b] Radiochemical yield corrected for the decay.

Initially, compound **37** was labelled using a standard radiomethylation protocol, with [^{11}C]CH_3OTf as methylating agent, NaOH as deprotonating base and 2-butanone as solvent, for 90 seconds at room temperature. By comparing the retention time of the reference compound **36** (R_t = 9.8 min, measured with analytical BDS Hypersil C18 column and NaH_2PO_4 0,05 M/ACN 50:50 as eluent) and the peaks resulting from the HPLC, it was possible to identify compound **[^{11}C] 4**, which was initially obtained with 33.0 % of radiochemical yield and 51.6 % of radiochemical purity (Figure 4.8). The purity level was

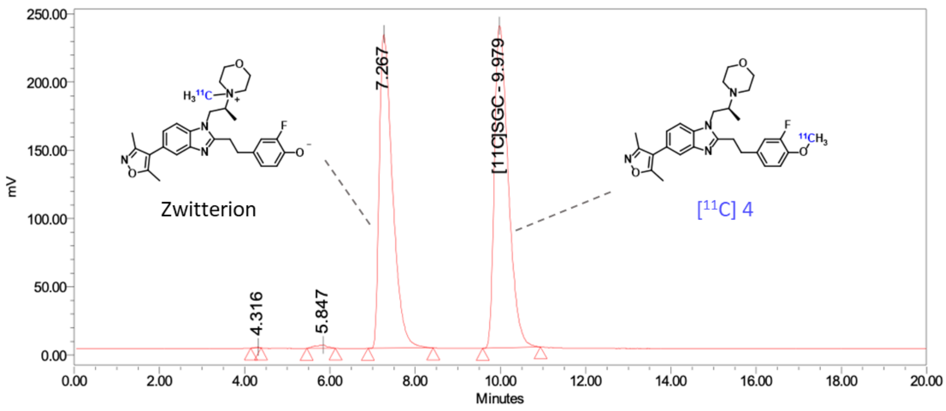

Figure 4.8 Radiochromatogram obtained with analytical BDS Hypersil C18 column and NaH_2PO_4 0,05 M/ACN (50:50) as eluent. Compound **[^{11}C] 4** (R_t = 9.9 min) represents 51.6 % of the total radioactivity.

reduced by the presence of a side-product with a lower retention time, which we assumed to be the zwitterionic form of the phenolate, ^{11}C-methylated on the morpholine function of the precursor (Figure 4.8). In support of this hypothesis, the introduction of TBAOH, which is a weaker base compared to NaOH, reduced the formation of **[^{11}C] 4** in favour of the N-methylmorpholine side product, since it decreased the deprotonation of the fenol group facilitating the nucleophilic substitution on the tertiary amine of morpholine. Moreover, the combination of TBAOH and [^{11}C]CH_3I as methylating agent enhanced again the formation of the side product (Figure 4.9), highlighting [^{11}C]CH_3OTf and NaOH as the best combination for this radiolabeling reaction.

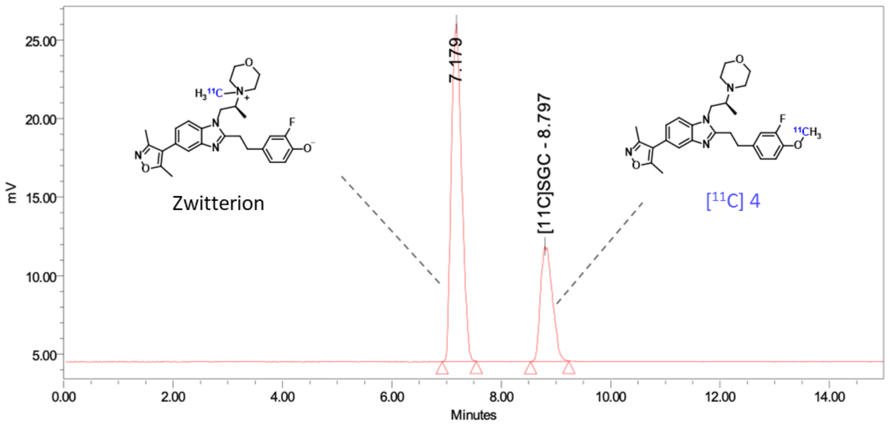

Figure 4.9 Radiochromatogram obtained with analytical BDS Hypersil C18 column and NaH_2PO_4 0,05 M/ACN (45:55) as eluent. Compound **4** (R_t = 8.8 min) represents 28.3 % of the total radioactivity.

The reaction conditions were further optimized by doubling the quantity of reacting cold precursor from 0.5 to 1.0 mg, and by decreasing the reactiont time from 90 to 30 seconds. In this way it was possible to increase the radiochemical yield to 58.0 %, obtaining **[^{11}C] 4** with a radiochemical purity of 99.5 % (Figure 4.10).

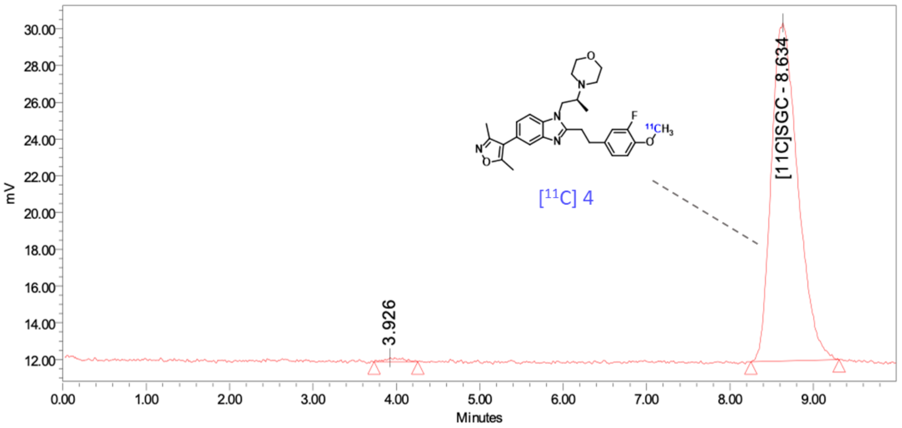

Figure 4.10 Radiochromatogram of **[^{11}C] 4** obtained with analytical BDS Hypersil C18 column and NaH_2PO_4 0,05 M/ACN (45:55) as eluent.

IN VITRO EVALUATION OF [^{18}F] 2 AND [^{11}C] 4

Since only compounds **[^{18}F] 2** and **[^{11}C] 4** could be obtained with satisfactory yields and purity, they were selected to further study their biological properties with *in vitro* assays. Initially, their cellular uptake was tested. two CBP-expressing cell lines were chosen as in vitro models: adenocarcinomic human alveolar basal epithelial (A549) and triple-negative breast cancer (MDA-MD-231) cells. As shown in figure 4.11 a - b, compound **[^{18}F] 2** presents a very low uptake level in both the tested cell lines, which does not raise overtime. In addition, the test was repeted adding increasing concentrations of cold reference compound **24**, and it was not possible to find a correlation between the cellular uptake of the labeled compound and the reference concentration (Figure 4.11 c - d).

Figure 4.11 Results of the uptake assays of compounds **[^{18}F] 2** and **[^{11}C] 4** on different tumor cell lines. a – b) Uptake assay of **[^{18}F] 2** tested without competitor at different time, c – d) uptake levels of **[^{18}F] 2** tested with increasing concentrations of the cold reference compound **24** as competitor at 15 min, e – f) uptake assay of **[^{11}C] 4** tested without competitor at different time, g – h) uptake levels of **[^{11}C] 4** tested with increasing concentrations of the cold reference compound **36** as competitor at 30 min. Assays on compound **[^{11}C] 4** were performed in triplicate, error bars represent SD. * $p < 0.05$ vs control, ** $p < 0.01$ vs control.

These results shows that **24**, used in this test as a blocking agent, is not able to reduce the cellular uptake of **[^{18}F] 2** in both tested cell lines, suggesting that the labeled compound is probably subjected to non-specific interactions inside the cell. This behaviour can be explained by the higher lipophilicity of compound **[^{18}F] 2** compared to the lead compound **ICG-001**, which can negatively influence the biological parameters of the molecule. Because of this, the possibility to used **[^{18}F] 2** as imaging agent for the fibrotic process is yet to be proven.

On the other hand, also compound **[^{11}C] 4** was tested on the two CBP-expressing cell lines. It presents the same low uptake level as **[^{18}F] 2** (Figure 4.11 e - f), however, its cellular concentration dropped when increasing concentrations of its reference compound **36** were applied in the competition assays (Figure 4.11 g - h). The partial success of the blocking experiments suggests specific interactions with its biological target in both cell lines, thus compound **[^{11}C] 4** presents interesting characteristics for its potential application in the imaging of the fibrotic process. Further tests may demonstrate that a high binding affinity may compensate for the overall low uptake in the cells, and a high selectivity towards a targeted tissue may demonstrates the potential of compound **[^{11}C] 4** as imaging agent. From todays results it is possible to conclude that this compound is the most promising one of the series, and it will require additional tests to be considered a suitable radiotracers of fibrosis.

SYNTHESES OF MULTIMODAL IMAGING AGENTS

Recent studies[91, 92, 105] revealed that, when aiming to synthesize peptide dually labelled imaging probes suited for both positron emission tomography and optical imaging (PET/OI), the choice of the fluorescent dye for the optical detection can have a significant influence on the *in vitro* binding profile of the multimodal imaging agent. At first, this was observed in dually labelled PESIN derivatives for the selective gastrin releasing peptide receptor (GRPR) imaging (PESIN = PEG_3-$BBN_{7\text{-}14}$, $BBN_{7\text{-}14}$ = truncated peptide sequence of the endogenous GRPR ligand bombesin, Figure 4.12), which receptor affinities resulted to be negatively affected by the total negative charge of the ready biomolecule expressed by the respective fluorescent dye. Therefore, it was suggested the following charge-cell binding correlation: The higher the number of anionic charges carried by the conjugate, introduced by the selected dye, the worse the resulting GRPR binding affinity of the multimodal imaging agent. This concept was confirmed using various PESIN-homodimer[91, 92] and -homotetramer[105] conjugates presenting different dye units. By comparing the binding profiles of these series, it was also observed that the GRP receptor affinities of the conjugates with a higher number of peptidic binding motives per molecule was less affected by the negative influence of the anionic charges then their corresponding conjugates with a lower peptide valency. From this evidence, a second hypothesis emerged: The adverse influence of negatively charged fluorescent dyes on the GRPR binding affinities of PESIN-based imaging agents can be mitigated by a higher valency of peptide multimerization. Both these correlations represent critical aspect to be taken in consideration during the design of tailored hybrid multimodal imaging agents with specific needs and applications.

To test and extend this concept of charge-cell binding correlation, hybrid multimodal imaging agents characterized by different peptide monomers and ionic charges have been prepared. Is was employed a convergent synthetic strategy aiming to combine the multimodal imaging unit with the corresponding biomolecule for target-specific accumulation. The reported modular synthesis strategy allows not only to prepare these complex conjugates, but also to adapt the compounds to specific requirements by easily exchanging the individual parts which compose the molecule, such as the radioactive agent, dye and peptide. At first, three peptides (Figure 4.12) were chosen for the specific targeting of different tumor biomarkers. As a comparison to the previous studies reporting the charge-cell binding concept, monomeric bombesin derivative $\mathbf{BBN_{7\text{-}14}}$ to address the gastrin-releasing peptide receptor (GRPR) was selected. In addition, two novel peptides were identified to extend the concept to different receptors: the hormone α-MSH derivative **Nle-c(DHfRWK)** and **c(RGDfK)**, each peptide addressing respectively its target receptor MC1 and integrin $\alpha_v\beta_3$. Then, the tumor-targeting vector was appropriately designed by introducing a maleimide-function into the monomeric peptide structures for the efficient coupling with the MIUs.

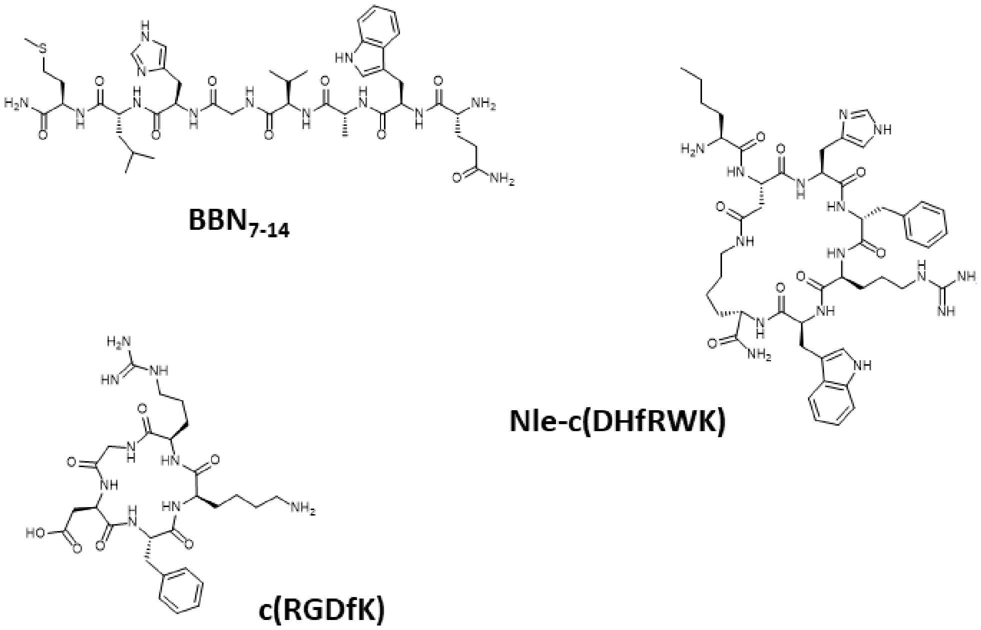

Figure 4.12 Selected peptides for the preparation of the tumor-targeting vectors.

The synthetic pathway to the peptide moieties is reported in Scheme 4.13. The three **peptides a – c** were completely built on solid support using standard Fmoc-based solid phase-assisted synthesis protocols, as reported in previous procedures.[161-163]

Cyclization of peptides was performed while still attached to the resin, after deprotection of the respective protecting groups (Mtt and O-2-PhiPr-PG for **peptide b** under mildly acidic conditions, All-PG for **peptide c** by treatment with phenylsilane ($PhSiH_3$) and tetrakis(triphenylphosphine) palladium(0) ($Pd(PPH_3)_4$)). Following the final Fmoc-deprotection of **peptides a – b** and the Mtt-deprotection of **peptide c**, the monomeric **peptide units a – c** were prepared by introducing a linker composed by a polyethylene glycol spacer (PEG_3) and 4-Maleimidobutyric acid: the length of the spacer resulted to be optimal for both the stability and the biological properties of the conjugates,[104] and the maleimide-function allows to introduce the MIUs in the peptide structure via an efficient and chemoselective thiol-based Michael click reaction.

Moreover, during this project it was necessary to prepare homodimer derivatives of PESIN, to justify the aberrant behaviour of one of the synthesized multimodal imaging agents. For this reason, it was then prepared a maleimide-modified **PESIN-dimer peptide unit**, following the synthetic strategy previously described by Hübner et al. (Scheme 4.14).[91]

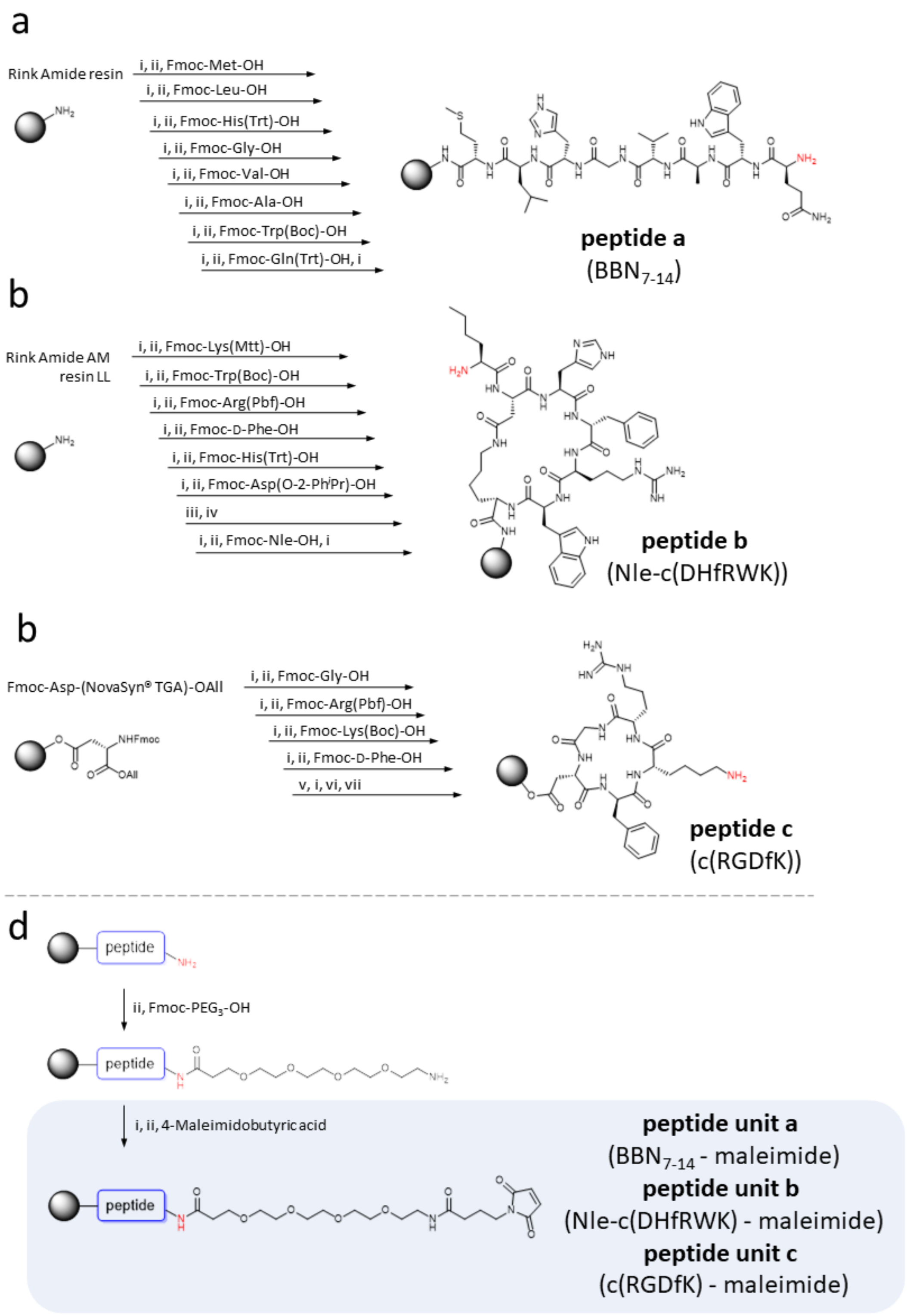

Scheme 4.13 Solid-phase synthesis of **peptide units a – c**: a) Synthesis of resin-BBN$_{7\text{-}14}$ **peptide a**; b) Synthesis of resin-Nle-c(DHfRWK) **peptide b**; c) Synthesis of resin-c(RGDfK) **peptide c**. The amine function which was functionalized with the linker is marked in red; d) Peptide functionalisation for the preparation of maleimide-modified **peptide units a – c**. Reaction conditions: i) deprotection of Fmoc-PG: piperidine/DMF (1/1, v/v), 1 + 5 min; ii) activation of amino acids: 4.0 equiv. DIPEA, 3.9 equiv. HBTU in DMF, 2 min, coupling, 60 min; iii) deprotection of Mtt- and O-2-Ph^{i}Pr-PG: TFA/CH_2Cl_2 (1/99, v/v), 90 min; iv) cyclization: 4.0 equiv. DIPEA, 3.9 equiv. PyBOP in DMF, 20 h; v) deprotection of All-PG: 24.0 equiv. $PhSiH_3$, 0.25 equiv. $Pd(PPh_3)_4$ in CH_2Cl_2, 3 × 30 min; vi) cyclization: 4.0 equiv. DIPEA, 3.9 equiv. HBTU in DMF, 16 h; vii) deprotection of Mtt-PG: TFA/CH_2Cl_2 (1/99, v/v), 3 x 30 min.

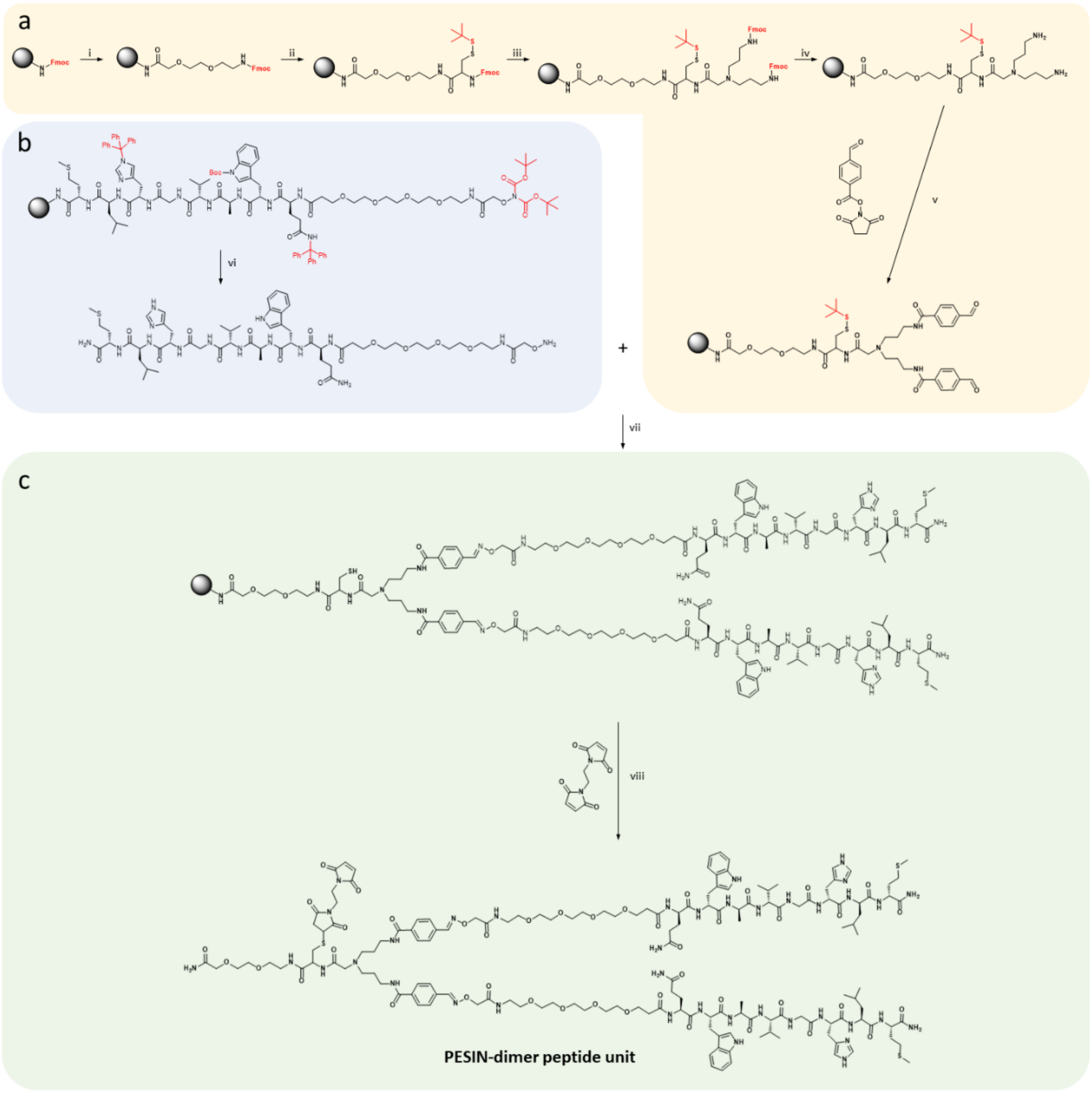

Scheme 4.14 Schematic depiction of the synthesis of the maleimide-modified **PESIN-dimer peptide unit**. a) (yellow background): Synthesis of the orthogonally functionalized branched dendron; b) (blue background): Synthesis of aminooxy-PESIN; c) (blue background): Synthesis of the PESIN-dimer peptide unit. *Reaction conditions*: i) swelling 45 min; piperine/DMF (1:1), 5 min; 4 equiv. activated amino acid for 30 min (activation: 3.9 equiv. HBTU, 4 equiv. DIPEA, 2 min). ii) Piperine/DMF (1:1), 5 min; 4 equiv. activated amino acid for 30 min (activation: 3.9 equiv. HBTU, 4 equiv. DIPEA, 2 min). iii) Piperine/DMF (1:1), 5 min. iv) TFA/TIS (95:5 v/v); 60–120 min; HPLC. v) 2 equiv. Succinimidyl-*p*-formyl-benzoate; pH 7.0–7.2; 30 min at 45 °C; HPLC. vi) TFA/TIS (95:5 v/v); 60–120 min; HPLC vii) a) 2.25 equiv. PESIN; pH 4.0–4.2; 60 min at 45 °C, b) 10 equiv. TCEP=(tris(2-carboxyethyl)phosphine)); pH 4.0–4.2; 120–240 min at 45 °C; HPLC. viii) 3 equiv. 1,2-*bis*(maleimido)ethane; pH 7.0–7.2; 5 min; HPLC.

The molecular design of the MIUs was based on the structure of the previously reported PESIN-homodimers conjugates, in which the imaging synthon was composed by (1,4,7-triazacyclononane-4,7-diyl)diacetic acid-1-glutaric acid (NODA-GA) as chelating agent for ^{68}Ga-labeling, by a variety of fluorescent small dye molecules for the optical detection and a thiol functional group for the efficient conjugation with the peptide vector.[91, 92] In the current study, a pyryllium dye,[172] Dansyl chloride, a cyanine dye based on the structure of indocyanine green (ICG)[173] and 5-carboxyfluorescein (Scheme 4.15 a) were chosen for their biological and optical properties, as well as for their different ionic charge, whose influence on the conjugates peptide moieties should be studied. In addition, tartrazine was chosen as equally-charged dye to study the complex behaviour of the fluorescein derivatives. The synthesis of the MIUs **38** – **42** can be performed completely on solid support by employing an orthogonal protecting group strategy, as reported in Scheme 4.15 b. Firstly, the NODA-GA modified di-peptide Cys(Trt)-Lys(alloc)-NODA-GA(tBu)$_3$ was prepared, followed by the deprotection of the N$_\varepsilon$-alloc protecting group of lysine by palladium catalysis. The free N$_\varepsilon$-amino group of lysine was then reacted with the corresponding dyes: the pyryllium dye and Dansyl chloride were reacted directly,

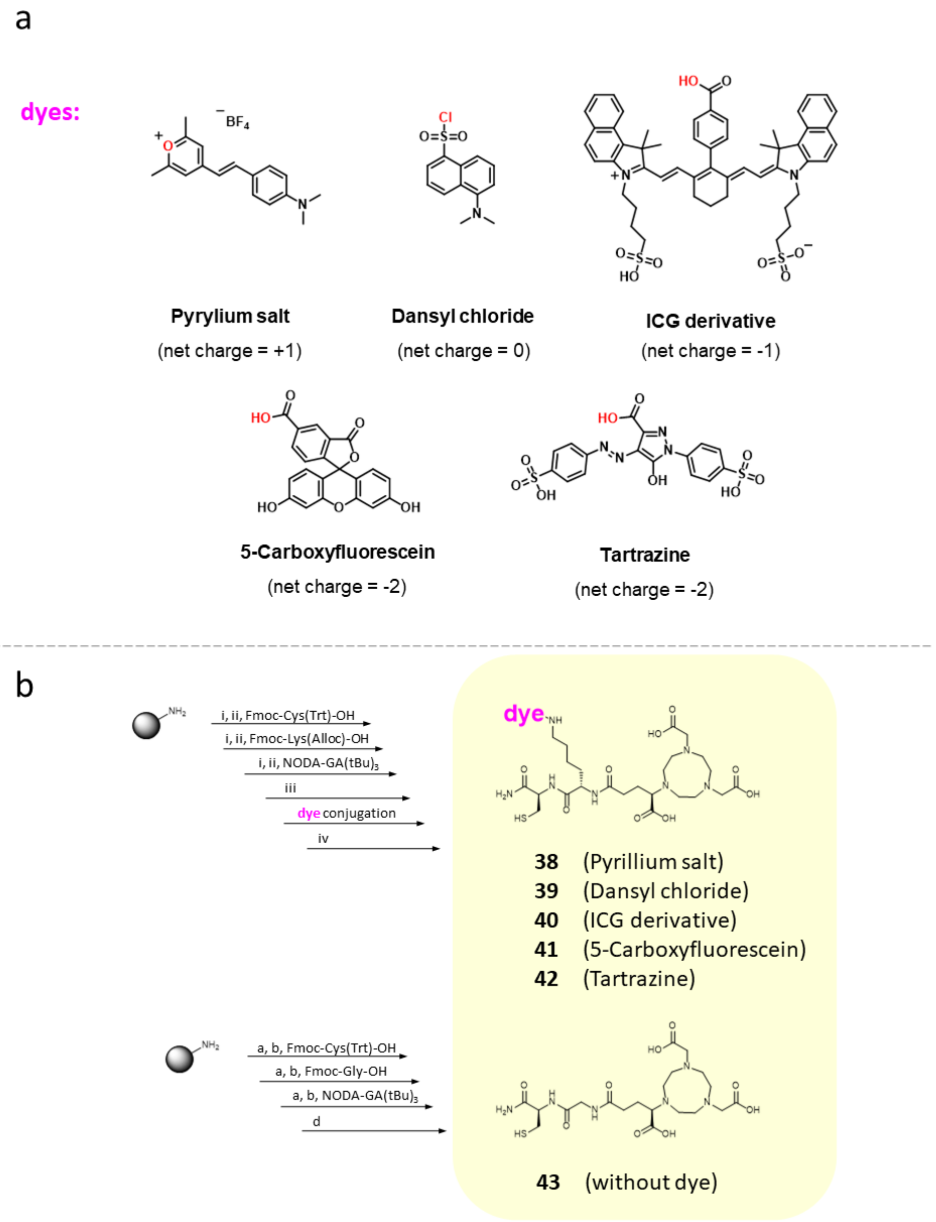

Scheme 4.15 a) Selected fluorescent dyes for the preparation of the MIUs. The functional group of the respective dye which was reacted with the N$_\varepsilon$-amine of lysine to obtain the MIUs is marked red. b) Solid-phase synthesis of the MIUs **38** – **43**. Reaction conditions: i) deprotection of Fmoc-PG: piperidine/DMF (1/1, v/v), 1 + 5 min; ii) activation of amino acids: 4.0 equiv. DIPEA, 3.9 equiv. HBTU in DMF, 2 min, coupling, 60 min; iii) deprotection of Alloc-PG: 20.0 equiv. morpholine, 2.0 equiv. Pd(PPh$_3$)$_4$ in CH$_2$Cl$_2$, 2 h; iv) cleavage from resin and deprotection of remaining protective groups: TFA/TIS (95/5, v/v), 1 h.

while the cyanine dye (prepared following the reported procedure),[161] 5-carboxyfluorescein and tartrazine were activated beforehand with a coupling agent. After cleavage from solid support and deprotection, the MIUs **38** – **42** (whose total charges considering also the three negative charges of the NODA-GA chelator are -2, -3, -4, -5, and -5, respectively) were obtained in high purity and reasonable yields. Finally, it was necessary to synthesize an appropriate reference compound to compare the influence of the MIU on the chemical, biological and photophysical properties of the resulting conjugates. For this purpose, the imaging unit **43** (net charge = -3) bearing only the NODA-GA chelator but lacking the fluorescent dye was prepared. To assemble the multimodal imaging agents **1 a – c**, **2 a – c**, **3 a – c**, **4 a – c** and **5 – 8 a**, the thiol groups of MIUs **38** – **43** were reacted with the maleimide function of the corresponding peptide unit. The reaction was carried out under mild conditions via the bioorthogonal Michael click reaction,[174] resulting in the formation of the final conjugates in only 5 minutes (Scheme 4.16). The non-optimized reaction yields obtained after the cleavage from the resin and the purification of the conjugates are reported in Table 4.5. With these results it has been shown once again that the designed MIUs can be chemoselectively introduced in maleimide-comprising biomolecules with high efficiency, yielding the modified multimodal imaging agents in acceptable yields. Moreover, the high flexibility and adaptability of the developed convergent synthetic strategy is demonstrated, since its

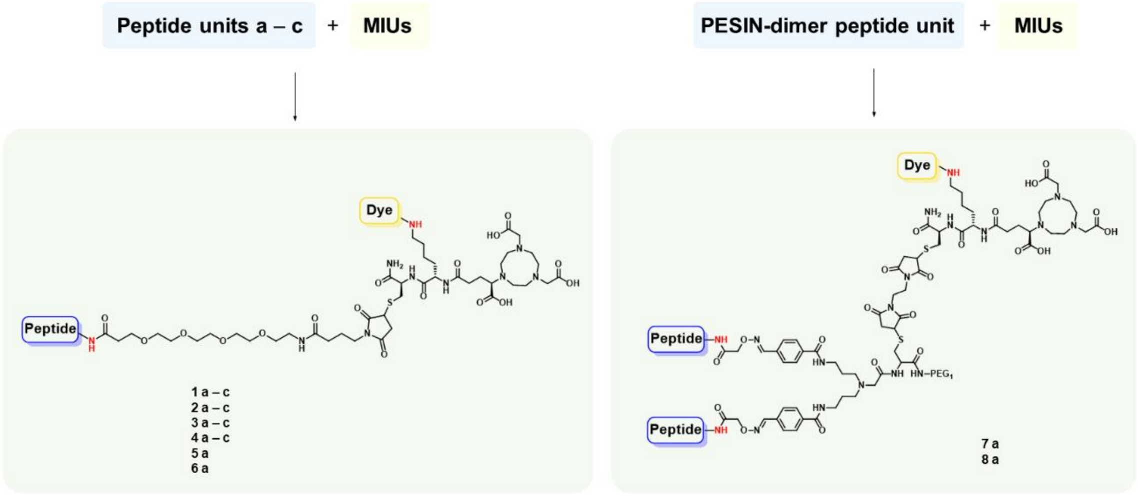

Scheme 4.16 Conjugation reaction of the maleimide-modified monomeric and dimeric peptide units with the corresponding MIUs. *Reaction conditions*: conjugation of the building blocks: H_2O/CH_3CN (1/1, v/v), 5 min, pH = 7; cleavage from resin: TFA/TIS (95/5, v/v), 1 h.

modular approach enables both the tailored design of multimodal imaging units with different imaging properties by simply exchanging their constitutive building blocks (e.g. chelator derivative or fluorescent dye), as well as the efficient introduction of these units in the structure of peptidic vectors (monomeric as in the present work, but also homodimeric or heterobi/multivalent) or antibodies to address the selected target receptors.

Table 4.5 Non-optimized conjugation yields of the purified hybrid imaging agents **1 a – c**, **2 a – c**, **3 a – c**, **4 a – c** and **5 – 8 a** obtained by conjugation of the MIUs **38** – **43** to the **peptide units a – c** and the **PESIN-dimer peptide unit**.

Peptide unit	MIU	Conjugate	Yield %
a (BBN_{7-14}-maleimide)	38 (thio-pyryllium-NODA-GA)	1 a(BBN_{7-14}-pyryllium-NODA-GA)	76
	39 (thio-dansyl-NODA-GA)	2 a (BBN_{7-14}-dansyl-NODA-GA)	30
	40 (thio-cyanine-NODA-GA)	3 a (BBN_{7-14}-cyanine-NODA-GA)	36
	43 (thio-NODA-GA)	4 a (BBN_{7-14}-NODA-GA)	54
	41 (thio-fluorescein-NODA-GA)	5 a (BBN_{7-14}-fluorescein-NODA-GA)	44
	42 (thio-tartrazine-GA)	6 a (BBN_{7-14}-tartrazine-NODA-GA)	35
b (Nle-c(DHfRWK)-maleimide)	38 (thio-pyryllium-NODA-GA)	1 b (Nle-c(DHfRWK)-pyryllium-NODA-GA)	70
	39 (thio-dansyl-NODA-GA)	2 b (Nle-c(DHfRWK)-dansyl-NODA-GA)	47
	40 (thio-cyanine-NODA-GA)	3 b (Nle-c(DHfRWK)-cyanine-NODA-GA)	82
	43 (thio -NODA-GA)	4 b (Nle-c(DHfRWK)-NODA-GA)	52
c (c(RGDfK)-maleimide)	38 (thio-pyryllium-NODA-GA)	1 c (c(RGDfK)-pyryllium-NODA-GA)	38
	39 (thio-dansyl-NODA-GA)	2 c (c(RGDfK)-dansyl-NODA-GA)	49
	40 (thio-cyanine-NODA-GA)	3 c c(RGDfK)-cyanine-NODA-GA)	33
	43 (thio -NODA-GA)	4 c (c(RGDfK)-NODA-GA)	23
PESIN-dimer	41 (thio-fluorescein-NODA-GA)	7 a (BBN_{7-14}-fluorescein-NODA-GA)	15
	42 (thio-tartrazine-GA)	8 a (BBN_{7-14}-tartrazine-NODA-GA)	21

PHOTOPHYSICAL PROPERTIES OF 1 a – c, 2 a – c, 3 a – c, 4 a – c

Following the successful synthesis of the target compounds, their photophysical properties were determined. INITIALLY, only the compounds presenting a total of -2, -3, and -4 negative charges were tested. Here, a possible negative influence of the conjugation of the different MIUs to the corresponding peptidic structures on the absorbance coefficients, or the absorption or emission wavelengths should be investigated. In Table 4.6 the results of the novel MIU-peptide conjugates are reported, as well as the values of the MIUs **38** – **40** which could be found in literature.[91, 92] A significant loss or shift of fluorescence properties of the final compounds compared to their imaging units before conjugation was not observed. This is in line with the observation for the PESIN homodimer-MIU conjugates described in literature: also with these compounds, the introduction of the imaging unit in the structure of the peptidic vector did not altered the optical properties of its components.[91, 92]

Table 4.6 Summary of the photophysical properties of the MIUs **38 - 40** and the corresponding hybrid bioconjugates **1 a – c**, **2 a – c** and **3 a – c**. (Values were determined in PBS at a concentration of 1 × 10^{-5} $molL^{-1}$).

Compound	$\lambda_{max(abs)}$ [nm]	Log ε [M^{-1} cm^{-1}]	$\lambda_{max(em)}$[a] [nm]	Stokes shift [nm]
38 [c]	440	4.16	600	160
1 a	448	4.27	601	153
1 b	450	4.16	597	147
1 c	450	4.29	607	157
39 [c]	-	-	550	-
2 a	-	-	549	-
2 b	-	-	545	-
2 c	-	-	543	-
40 [b, c]	720/790	4.80/4.61	800	10
3 a[b]	724/800	4.79/4.60	809	9
3 b[b]	726/802	4.78/4.57	807	5
3 c[b]	722/798	4.65/4.54	811	13

[a] excitation wavelength λ_{ex} = 400 nm. [b] excitation wavelength λ_{ex} = 650 nm. [c] values of MIUs reported in literature.[91, 92]

Due to the preserved fluorescence characteristics of **1** – **3 a**, **1** – **3 b** and **1** – **3 c**, their binding to the respective receptor was further analysed performing confocal microscopy experiments. The three conjugate series were applied for the fluorescent staining of the corresponding cell line (GRPR-expressing PC-3, MC1R-expressing B16F10 and integrin $\alpha_v\beta_3$-expressing U87MG cells, respectively) in the presence of the nuclear marker DAPI. Receptor-mediated binding for all the compounds was confirmed by detection of fluorescence at the expected wavelength (Figure 4.13). Nonspecific binding could be excluded by blocking experiments, where the blocking agent was applied in 50-fold excess, reducing the membrane-associated fluorescence to background levels and thus demonstrating the specific accumulation of the multimodal imaging agents in the cells.

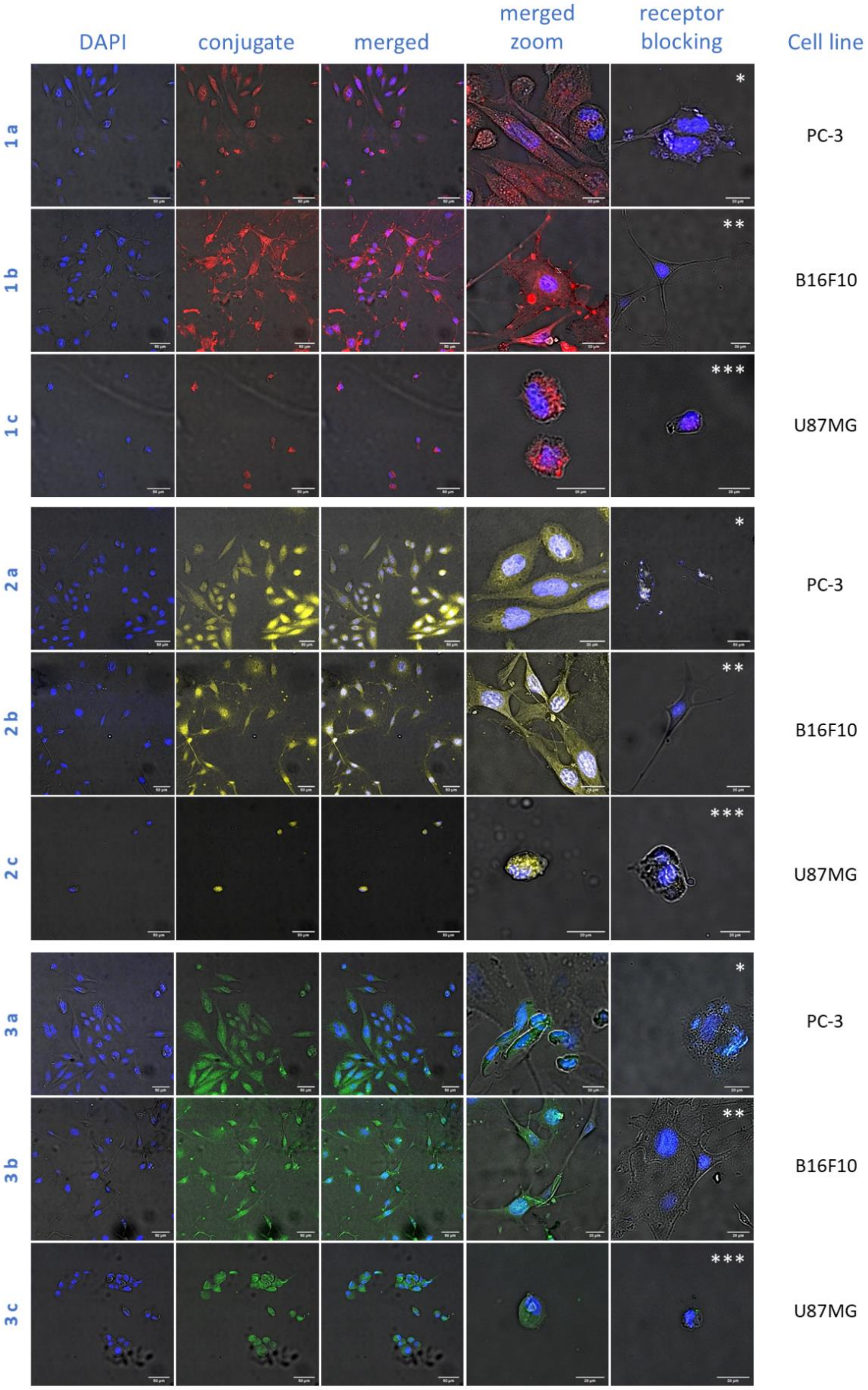

Figure 4.13 Receptor-specific staining of GRPR-positive PC-3, MC1R-positive B16F10 and integrin $\alpha_v\beta_3$-positive U87MG tumor cells using 10 mM solutions of the hybrid multimodal bioconjugates **1 a** – **c** (red signal, detector window 705–751 nm), **2 a** – **c** (yellow signal, detector window 705–800 nm) and **3 a** – **c** (green signal, detector window 705–800 nm). The cell nuclei were stained with DAPI (detector window 440–490 nm). Receptor blocking experiments were performed applying a 50-fold excess of * BBN, ** NDP-MSH and *** c(RGDyK), respectively.

RADIOLABELING PROPERTIES OF 1 a – c, 2 a – c, 3 a – c, 4 a – c

The radiolabeling efficiency of the synthesized conjugates **1 a** – **c**, **2 a** – **c**, **3 a** – **c**, **4 a** – **c** with $^{68}Ga^{3+}$ ($t_{1/2}$= 68 min) was investigated in order to verify their radiochemical suitability for combined hybrid multimodal imaging using PET and OI. Radiolabeling of all the compounds with ^{68}Ga was performed in aqueous solution at 45 °C for 10 min using standard acetate buffer conditions at pH 3.9 – 4.0.[175] The addition of ascorbic acid to the reaction mixture showed to be mandatory in order to avoid the relatively fast degradation of the fluorescent dyes that were susceptible to the radiolysis-induced formation of ions and radicals within minutes.[176] Under these conditions, the labeled bioconjugates **[^{68}Ga]Ga-1 a** - **c**, **[^{68}Ga]Ga-2 a** – **c**, **[^{68}Ga]Ga-3 a** – **c** and **[^{68}Ga]Ga-4 a** – **c** were obtained in high radiochemical yields (RCYs) of ≥95% and high non-optimized molar activities of 90 – 120 GBq/µmol. Most of the compounds exhibited high radiochemical purities (RCPs) of ≥95%, except from **[^{68}Ga]Ga-3 a** – **c** (carrying the indocyanine-based dye) which were obtained in lower RCPs of ≥85% (Figure 4.14). As this effect was not observed for the earlier-reported PESIN homodimer and tetramer of MIU **40**,[91, 92] and occurs in case of all three peptide conjugates, it is thus no result of dye- or peptide-related decomposition, but might be caused by the formation of aggregates of the peptide monomer conjugates due to the large size of the π-system of the dye as peptide monomers should be less able to hinder this aggregate formation compared to peptide multimers.

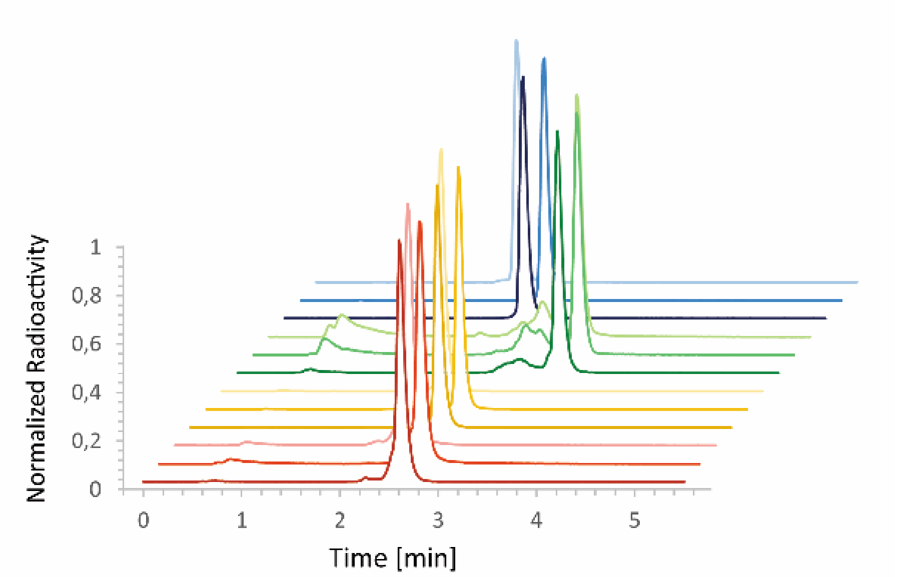

Figure 4.14 Radio-HPLC chromatograms of the synthesized imaging agents, from front to back: **[^{68}Ga]Ga-1 a**, **[^{68}Ga]Ga-1 b**, **[^{68}Ga]Ga-1 c**, **[^{68}Ga]Ga-2 a**, **[^{68}Ga]Ga-2 b**, **[^{68}Ga]Ga-2 c**, **[^{68}Ga]Ga-3 a**, **[^{68}Ga]Ga-3 b**, **[^{68}Ga]Ga-3 c**, **[^{68}Ga]Ga-4 a**, **[^{68}Ga]Ga-4 b**, **[^{68}Ga]Ga-4 c**.

In the following, the lipophilicity of the labeled conjugates was investigated to get a first idea of the potential excretion pathway of the agents during an *in vivo* application. The $\log_D$ values were determined by partition experiments between *n*-octanol and aqueous solution at pH 7.4. By comparing the obtained data with the results for the MIUs **38** – **40** and **43**, only a minor reduction in hydrophilicity was observed being caused by the introduction of the peptide monomers (Table 4.7). Compounds **[^{68}Ga]Ga-4 a** – **c**, which lack the dye in their imaging synthon, presented the lowest lipophilicity of the tested compounds, with $\log_D$ values of −3.78 ± 0.04, −3.36 ± 0.02 and −4.06 ± 0.10, respectively. In general, the $\log_D$s of the bioconjugates seem to be mainly dependent on the structural composition of the hybrid imaging units, especially on their charge and the size of their π-conjugated systems (Figure 4.15). It can be deduced that the major factor influencing the compounds hydrophilicity/lipophilicity is the applied MIU, and within these systems, the main influence is exerted by the selected fluorescent dye.

Table 4.7 Summary of the $\log_D$ values of the MIUs **38 – 40** and **43** and the corresponding hybrid bioconjugates **1 a – c**, **2 a – c**, **3 a – c** and **4 a – c**; values are given as mean ± SD.

Compound	$\log_D$	overall charge
38 [a]	-2.04 ± 0.11	-2
1 a	-2.38 ± 0.02	-2
1 b	-2.03 ± 0.06	-2
1 c	-2.51 ± 0.09	-2
39 [a]	-1.39 ± 0.04	-3
2 a	-1.44 ± 0.01	-3
2 b	-1.66 ± 0.03	-3
2 c	-2.17 ± 0.14	-3
40 [a]	-1.29 ± 0.11	-4
3 a	-1.45 ± 0.06	-4
3 b	-1.42 ± 0.13	-4
3 c	-1.97 ± 0.18	-4
43 [a]	-3.35 ± 0.15	-3
4 a	-3.78 ± 0.04	-3
4 b	-3.36 ± 0.02	-3
4 c	-4.06 ± 0.10	-3

[a] Values of MIUs reported in literature.[91, 92]

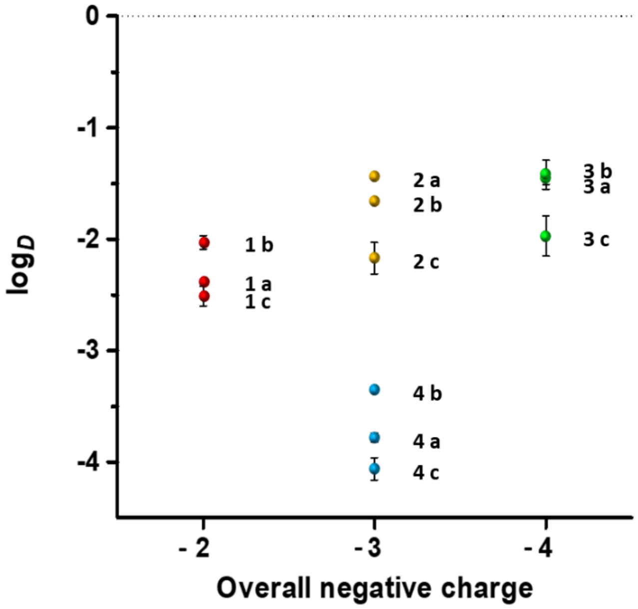

Figure 4.15 Plot of lipophilicity vs. overall negative charge of the novel radiolabeled MIU-monomer conjugates **1 a – c**, **2 a – c**, **3 a – c** and **4 a – c**.

COMPETITIVE BINDING ASSAYS OF 1 a – c, 2 a – c, 3 a – c, 4 a – c

Finally, this project aim was directed to explore different aspects of the charge-binding affinity correlation previously described,[91, 92] and therefore competitive binding assays for the synthesized multimodal imaging agents were performed.

The first question that was addressed was whether the introduction of the imaging unit in PESIN monomers would have resulted in the same effect observed on the binding properties of the homodimer equivalents. Thus, conjugates **1** – **4 a**, which present BBN_{7-14} monomer (**peptide a**) as functional peptide, were tested on stably GRPR-transfected HEK-293 cells, using $[^{125}I]$-Tyr^4-bombesin as a competitor and endogenous bombesin (BBN) as an internal standard with a known high affinity for this receptor type. All the conjugates of this first series showed IC_{50} values in the range of 10.01 ± 0.67 nM to 58.27 ± 3.66 nM (Table 4.8, Figure 4.16 a and d), while endogenous bombesin (BBN) showed an IC_{50} of 2.01 ± 0.17 nM. By comparing these data with the reported results of the homodimer-analogues,[91, 92] it can be deduced that: i) in the instance of PESIN monomers, the conjugation with the imaging unit also led to a decreased GRPR binding affinity compared to the endogenous reference BBN; ii) the compound carrying the uncharged dye (**2 a**, net charge = -3) and the one lacking the fluorescent dye (**4 a**, net charge = -3) presented similar, slightly increased IC_{50} values (15.09 ± 1.04 nM and 19.13 ± 1.44 nM, respectively) compared to the conjugate containing the pyridinium dye (**1 a**, 10.01 ± 0.67 nM, net charge = -2); iii) the cyanine-based conjugate **3 a**, carrying a negative charge within the fluorescent dye for an overall charge of -4, presented a considerably decreased GRPR affinity (IC_{50} value of 58.27 ± 3.66 nM); iv) compared to their homodimer-analogues, **1 a**, **2 a** and **4 a** showed a slight increment in the binding affinities (IC50 values of the corresponding homodimers were 16.47 ± 0.25 nM, 26.20 ± 0.89 nM and 21.48 ± 1.22 nM, respectively), whereas **3 a** more than doubled its IC50 value, decreasing the affinity to

Table 4.8 Summary of the affinity data (IC_{50} values) measured on the respective cell line of the hybrid bioconjugates **1 a – c**, **2 a – c**, **3 a – c** and **4 a – c**; values are given as mean ± SD.

Compound	IC50 [nM]	overall charge
1 a	10.01 ± 0.67[a]	-2
1 b	1.00 ± 0.10[b]	-2
1 c	2338.00 ± 116.83[c]	-2
2 a	15.09 ± 1.04[a]	-3
2 b	1.58 ± 0.04[b]	-3
2 c	3893.50 ± 295.89[c]	-3
3 a	58.27 ± 3.66[a]	-4
3 b	5.73 ± 0.50[b]	-4
3 c	7425.75 ± 207.44[c]	-4
4 a	19.13 ± 1.44[a]	-3
4 b	3.98 ± 0.07[b]	-3
4 c	4560.67 ± 436.66[c]	-3

Competitive displacement studies performed on: [a] GRPR-expressing HEK, [b] MC1R-expressing B16F10 and [c] integrin $\alpha_v\beta_3$-expressing U87MG cell line.

the receptor (IC50 values of the corresponding homodimer was 27.39 ± 2.01 nM).

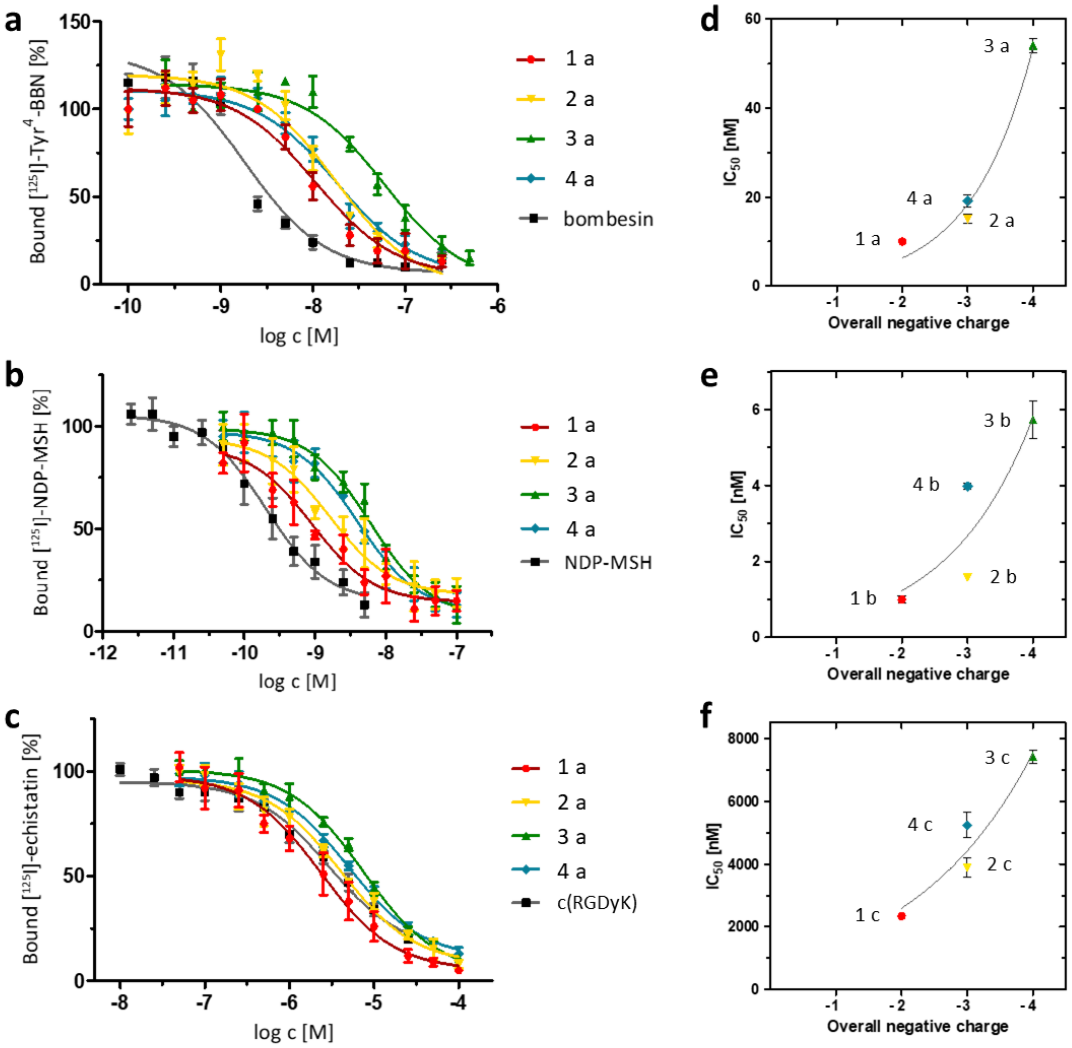

Figure 4.16 Results of the competitive displacement assays. Depiction of the determined binding curves of a) **1 – 4 a** and the reference bombesin, tested on stably GRPR-transfected HEK-293 cells, using [^{125}I]-Tyr^4-bombesin as a competitor, b) **1 – 4 b** and the reference NDP-MSH, tested on MC1R-positive B16F10 cells, using [^{125}I]-NDP-MSH as a competitor, c) **1 – 4 c** and the reference c(RGDyK), tested on $\alpha_v\beta_3$-expressing U87MG cells, using [^{125}I]-echistatin as a competitor; correlation between IC_{50} values and number of negative charges of d) **1 – 4 a**, e) **1 – 4 b** and f) **1 – 4 c;** error bars represent SD.

Taken together, these data are in accordance with previous findings obtained for PESIN-homodimer. By introducing the MIUs in the monomer structure, it was observed only a minor reduction of binding affinity of the conjugates, which were still able to interact with the GRPR. However, a negative influence of the increasing in the number of negative charges of the conjugated dye on the binding affinities of the peptides was confirmed. Moreover, the MIU-monomer conjugates are more affected from this negative influence than their PESIN-homodimer equivalents, as it is shown in Figure 4.17. On this regard, the opposite tendency with hybrid multimodal imaging agents characterized by higher peptide valency was observed: in the reported study,[105] it was possible to partially compensate for the adverse effect of the negative charge on the GRPR binding affinity by increasing the number of peptidic binding motives in the imaging agent, a PESIN-homotetramer conjugate. From this, it was possible to deduce that besides the overall negative charge, the structural composition and the number of peptide units in the molecule are also of relevance in the GRPR interaction. In the present study, an under-compensating effect caused by the reduction in the peptide valency, passing from the homodimers to the corresponding monomers was observed. It is possible to presume that the single PESIN copy is less prone to shield the negative charges brought into the molecule by the NODA-GA chelator and the dye, hence the series of synthesized multimodal imaging PESIN-monomers **1 – 4 a** is more susceptible to their negative effect on the GRPR binding affinity. This observation confirms the suggested compensation-effect on the charge influence on GRPR binding affinity provided by the peptide multimerization.

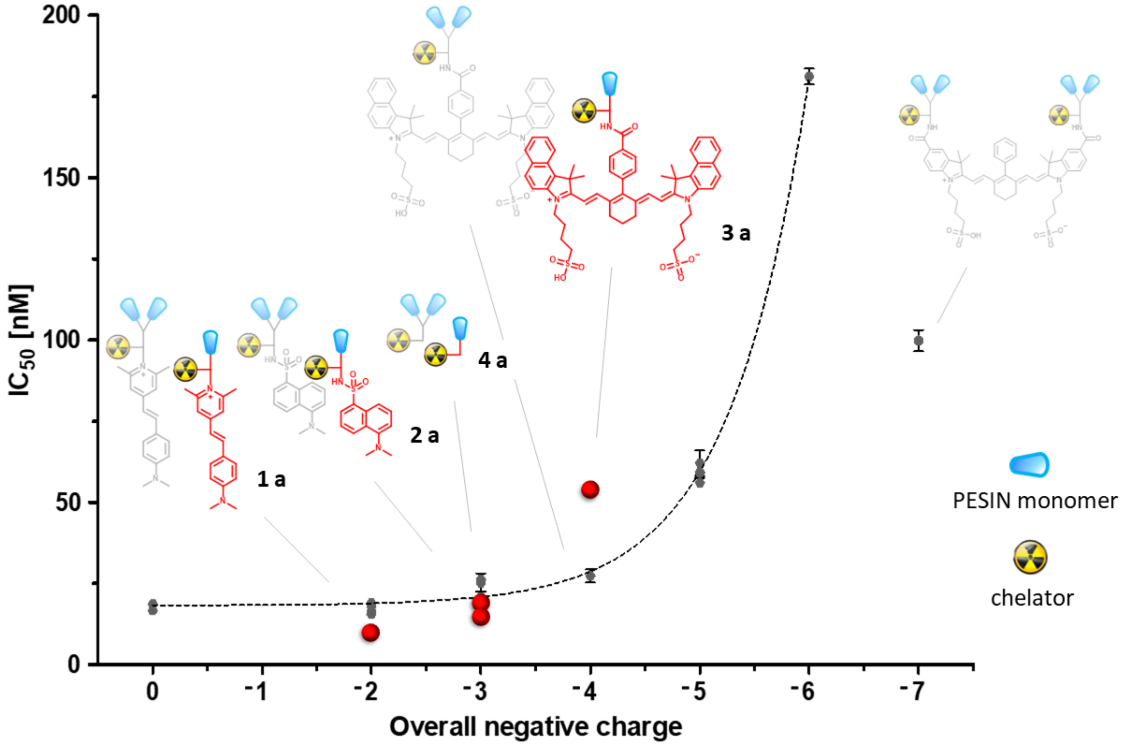

Figure 4.17 Depiction of the results of the competitive displacements assays on GRPR-transfected HEK-293 cells for in vitro determination of GRPR affinities of the new hybrid multimodal imaging agents **1 – 4 a**. Graphical classification of the new data (red data points and structures) in the context of the literature values (grey data points and structures). Shown is the correlation between IC$_{50}$ values and overall molecular charge of the MIU-derivatized PESIN dimers (black data points).

Besides this first results, an additional focus of the present study was the possibility to observe the same charge-binding affinity correlation applied to other receptors, apart from GRPR. To address the issue, competitive binding assays were performed also on the conjugate series targeting MC1R and integrin $\alpha_v\beta_3$.

Conjugates **1 – 4 b**, composed by Nle-c(DHfRWK) monomer (**peptide b**) as functional peptide, were tested on MC1R-expressing B16F10 cells, using [^{125}I]-NDP-MSH as competitor and NDP-MSH as internal standard with known affinity for this receptor type. The compounds of this series showed IC_{50} values in the range of 1.00 ± 0.10 nM to 5.73 ± 0.50 nM (Table 4.8, Figure 4.16 b and e), while the reference compound showed an IC_{50} value of 0.25 ± 0.02 nM. From the resulting data it can be observed that: i) the conjugate containing the uncharged dye (**2 b**, IC_{50} = 1.58 ± 0.04 nM, net charge = -3) presented again a similar IC_{50} value compared to the compound carrying the positively charged dye (**1 b**, IC_{50} = 1.00 ± 0.10 nM, net charge = -2); ii) compound **4 b** (IC_{50} = 3.98 ± 0.07 nM, net charge = -3) showed a higher IC_{50} value compared to **2 b**; iii) furthermore, the worst result in the MC1R binding affinity was shown by the cyanine-based conjugate **3 b** (IC_{50} = 5.73 ± 0.50 nM, net charge = -4), presenting the negatively charged dye. Taken together, these results show once again a clear trend correlating the charge carried by the fluorescent dye and the binding affinity of the imaging agent. The higher the overall negative charge of the conjugates was, the worse the MC1R binding affinity got. The difference between the IC_{50} values of **2 b** and **4 b** might be associated to the reduction in lipophilicity which occurred by removing the fluorescent dye from the MIU structure, observed during the $\log_D$ measurements (Figure 4.15). This effect was observed on a smaller scale also in the other series of monomer conjugates, but not in the multimerized forms of the PESIN-based compounds,[91, 92] suggesting that this influence may be suppressed with higher peptide valency.

Finally, conjugates **1 – 4 c**, composed by c(RGDfK) monomer (**peptide c**) as functional peptide, were tested on integrin $\alpha_v\beta_3$-expressing U87MG cells, using [^{125}I]-echistatin as competitor and c(RGDyK) as internal standard with known affinity for this receptor type. The compounds of this final series showed IC_{50} values in the range of 2338.00 ± 116.83 nM to 7425.75 ± 207.44 nM (Table 4.8, Figure 4.16 c and f), while the reference compound showed an IC_{50} value of 2936.60 ± 208.22 nM. From the assay results it was possible to observe that: i) compound **1 c**, carrying the positively charged dye (net charge = -2), presented the highest $\alpha_v\beta_3$ binding affinity (IC_{50} = 2338.00 ± 116.83 nM); ii) the compound carrying the uncharged dye (**2 c**) and the one lacking the fluorescent dye (**4 c**), both characterized by an overall negative charge of -3, presented similar IC_{50} values (3893.50 ± 295.89 nM and 4560.67 ± 436.66 nM, respectively); once again, the compound carrying the negatively charged dye (**3 c**, net charge = -4) presented the worst $\alpha_v\beta_3$ binding affinity. Thus, even with integrin $\alpha_v\beta_3$ it was possible to observe the same, clear correlation between the overall negative charge of the synthesized imaging agents and their receptor affinity, which seems independent from the nature of the corresponding receptor.

COMPETITIVE BINDING ASSAYS OF 5 – 8 a

In this paragraph will be discussed the abnormal behaviour of the fluorescein-based monomeric PESIN derivative **5 a**.[177]

Initially, it was designed and synthesized a fluorescein-based multimodal imaging agent, in order to complete the series of PESIN-derivatives with a -5 charged compound. Fluorescein and its derivatives can exist in aqueous solution in a number of prototropic forms: cationic, neutral, monoanionic and dianionic (Figure 4.18). In particular, there are three different tautomers for the neutral species – a quinoid, a zwitterion and a neutral species – and a further two for the monoanion, with ionized carboxyl or hydroxyl groups.[178]

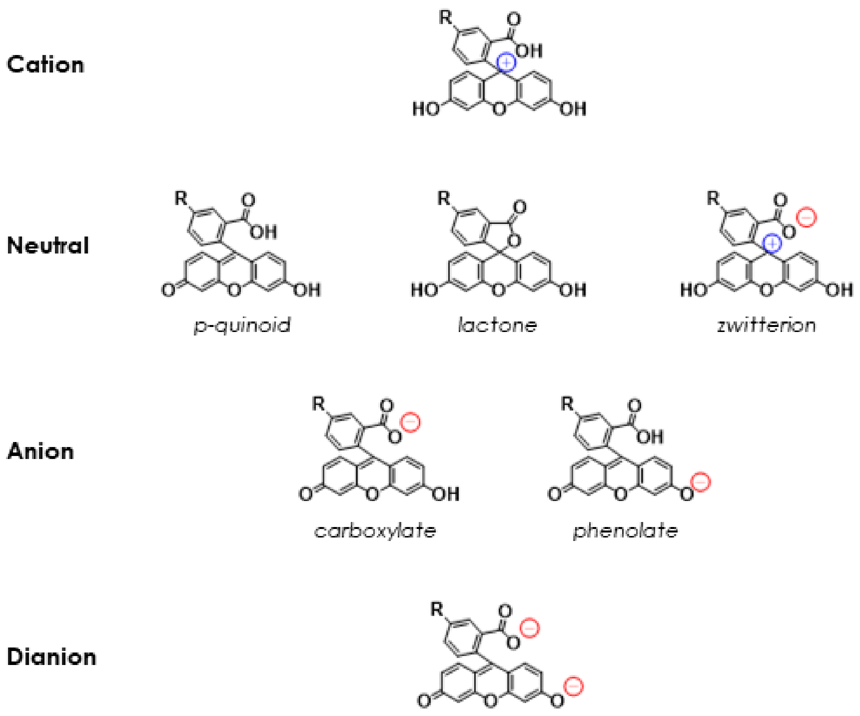

Figure 4.18 Proteolytic structures of a fluorescein derivative at different pH values of solution.

In previous studies,[91] the more stable conformation in the assays conditions, thus the most abundant, was considered to be the dianionic form. Indeed, the fluorescein-based PESIN-homodimer derivative **7 a** presents a binding affinity to the GRP receptor of 62.07 ± 3.87 nM, in line with the affinity of other -5 charged derivatives of the same dimeric series.

However, when tested on stably GRPR-transfected HEK-293 cells, the corresponding monomeric derivative **5 a** showed an unexpected binding affinity of 60.33 ± 3.53 nM, which is very similar to the IC_{50} value showed by the -4 charged compound **3 a**, from the same monomeric derivative series (Figure 4.19).

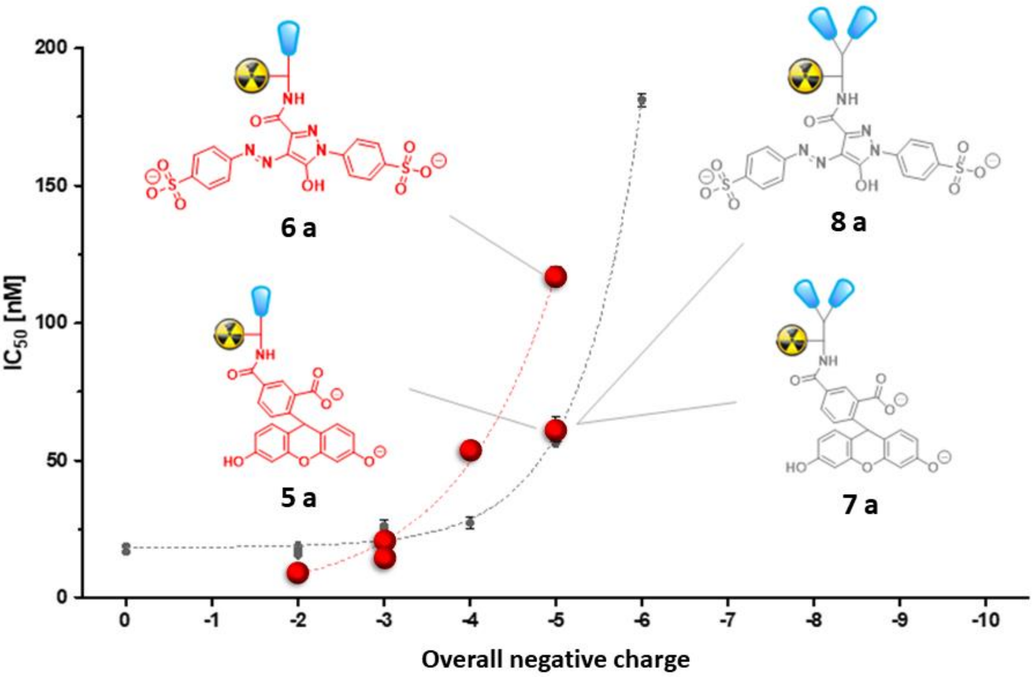

Figure 4.19 Depiction of the results of the competitive displacements assays on GRPR-transfected HEK-293 cells for in vitro determination of GRPR affinities of the new hybrid multimodal imaging agents **5** – **8 a**. Graphical classification of the monomeric series data (red data points and structures) in the context of the literature values (grey data points and structures). Shown is the correlation between IC_{50} values and overall molecular charge of the MIU-derivatized PESIN dimers (black data points) and of the MIU-derivatized PESIN monomers (red data points).

To evaluate whether the charge-cell binding correlation could still be applied in the description of the binding affinity profile of the monomeric series, two additional compounds have been prepared: the tartrazine-based PESIN monomer **6 a** and dimer **8 a**. Tartrazine is a non-fluorescent dye, commonly used as pharmaceutical and food colorant (Figure 4.20).[179, 180] It was chosen because it is easy to be introduce in the structure of the MIU by coupling on the carboxylic moiety, and since it presents two sulfonic functions, the formed tartrazine based MIU will present a total net charge of -5 in the assay condition. The binding affinities of the synthesized conjugates **6 a** and **8 a** were tested, and a depiction of the results is reported in Figure 4.19. As shown, compound **8 a** presents an IC_{50} value of 58.44 ± 1.47 nM, which is comparable to other dimeric PESIN conjugates carrying two negative charges within the dye moiety (whose total net charge, considering also the three

Figure 4.20 Tartrazine used as yellow colorant in a popular Italian non-alcoholic beverage.

negatively charged chelator, is -5),[91, 105] including the fluorescein-based PESIN dimer **7 a**. Besides, compound **6 a** showed an IC_{50} value of 117.00 ± 3.71 nM, which is almost doubled compared to the corresponding -4 charged PESIN monomer derivative **3 a** (IC_{50} = 58.27 ± 3.66 nM). The results of the tartrazine-based monomeric and dimeric series demonstrate once again a clear correlation between the number of negative charges carried by the multimodal imaging agent and its binding affinity to the molecular target.

However, the binding profile of the fluorescein-based monomeric conjugate **5 a** diverged significantly form the one of **6 a**, although both compounds should be characterized by two negative charges in their dye moiety. With a total net charge of -5. This apparently aberrant behaviour is justified by a previously undescribed mechanism of interaction of sodium ions with fluorescein, which will be discussed in detail in the next paragraph.

RADIOLABELING AND PHOTOPHYSICAL PROPERTIES OF 5 – 8 a

Also with this last series, the radiolabeling efficiency of the synthesized conjugates **5 – 8 a**, with $^{68}Ga^{3+}$ ($t_{1/2}$= 68 min) was investigated. Radiolabeling of all the compounds with ^{68}Ga was performed in aqueous solution at 45 °C for 10 min using standard acetate buffer conditions at pH 3.9 – 4.0.[175] The addition of ascorbic acid to the reaction mixture was again necessary to avoid the dye degradation.[176] Under these conditions, the labeled compounds **[^{68}Ga]Ga-5 a**, **[^{68}Ga]Ga-6 a**, **[^{68}Ga]Ga-7 a** and **[^{68}Ga]Ga-8 a** were obtained in high radiochemical yields (RCYs) of ≥95% and high non-optimized molar activities of 90 – 120 GBq/µmol (Figure 4.21).

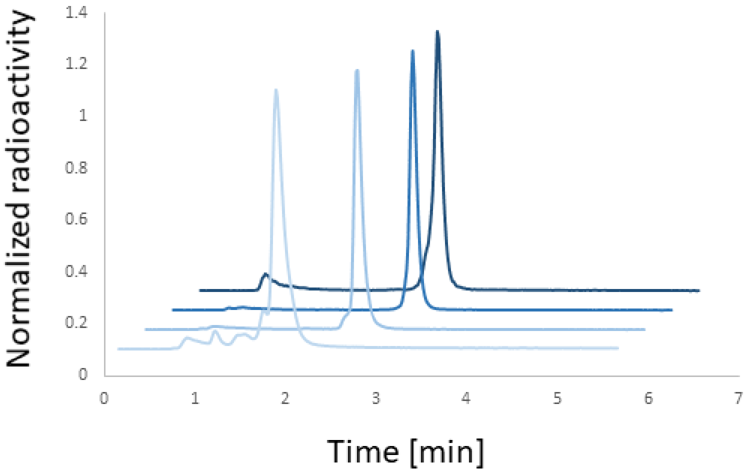

Figure 4.21 Radio-HPLC chromatograms of the synthesized imaging agents, from front to back: **[^{68}Ga]Ga-5 a**, **[^{68}Ga]Ga-6 a**, **[^{68}Ga]Ga-7 a**, **[^{68}Ga]Ga-8 a**.

Then, the $\log_D$ values of the labeled conjugates were determined by partition experiments between *n*-octanol and aqueous solution at pH 7.4. In Table 4.9 are reported the results of the lipophilicity assay, together with the preliminary optical evaluation.

Table 4.9. Summary of the $\log_D$ values and the GRPR affinity data (IC_{50} values, given as mean ± SD) of the hybrid conjugates **5 – 8 a**, as well as their photophysical properties determined in pure water at a concentration of 1 × 10^{-5} mol L^{-1}.

Compound	IC_{50}[a] [nM]	$\log_D$	$\lambda_{max(abs)}$[b] [nm]	Log ε [M^{-1} cm^{-1}]	$\lambda_{max(em)}$[c] [nm]	Stokes shift [nm]
5 a	60.33 ± 3.53	-3.27 ± 0.02	496	4.72	523	27
6 a	117.00 ± 3.71	-3.58 ± 0.02	432	4.09	-	-
7 a	62.07 ± 3.87	-2.54 ± 0.06	498	4.59	525	27
8 a	58.44 ± 1.47	-2.23 ± 0.06	440	4.17	-	-

[a] competitive displacement studies performed on GRPR-expressing HEK cell line. [b] spectra recorded in deionized water at pH = 8.23. [c] excitation wavelength λ_{ex} = 400 nm.

To explain the reason behind the abnormal binding affinity of compound **5 a**, an in-depth study of the photophysical characteristics of the fluorescein derivatives was performed.

Fluorescein is a well-known fluorescent dye, broadly used as fluorescent probe in biological and biochemical applications.[181, 182] As mentioned above, this compound can exists in water solutions in different prototropic conformations (Figure 4.18). As a result, the spectroscopic properties of fluorescein, such as absorption and fluorescence, are strongly pH dependent, and it was determined that to each proteolytic form a specific absorption spectrum is associated, with characteristics shapes and absorption peaks (Figure 4.22).[183, 184] In particular, titration experiments were performed, where the optical properties of fluorescein were evaluated at different pH levels.[183] It was demonstrated that:

- the dianionic conformation has its main absorption peak at 490 nm, with a shoulder around 475 nm;
- the anionic conformation has somewhat weaker absorption in the visible region with peaks at 472 and 453nm of roughly the same molar absorptivity;
- the neutral species has by far lowest absorption in the visible region, with a maximum at 434 nm;
- the cation has maximum absorption at 437 nm.

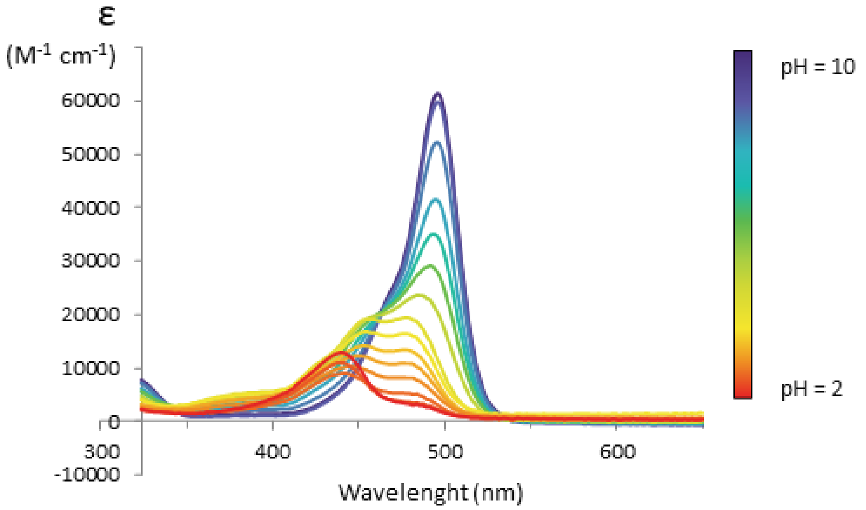

Figure 4.22 Absorption spectra of compound **5 a** (10 µM) in pure water, recorded at pH: 9.8, 9.2, 8.0, 7.5, 7.0, 6.7, 6.2, 5.3, 4.6, 4.2, 3.9, 3.5, 3.0, 2.3, 2.0.

Therefore, in principle, it is possible to determine in which proteolytic conformation fluorescein or its derivative exist in specific conditions by analysing the absorption spectra. This aspect may be useful in the present study, since, in the same conditions, the dimeric PESIN derivative of fluorescein **7 a** presents the binding profile of the dianionic species, while the monomeric derivative **5 a** behaved as the monoanionic species. However, from the initial analysis in pure water it was not possible to identify any difference between the two conjugates, which both presented a main absorbance peak at 496/498 nm (Table 4.9), with a shoulder around 475 nm, in line with the description of the dianionic conformation of fluorescein. Also, the titration experiments performed in pure water on compound **5 a** (Figure 4.22) and **7 a** showed the same peak shift as reported for the fluorescent dye.

Thus, it was speculated that the presence of sodium ions in the assay medium (OPTIMEM, total concentration of sodium salts = 0.1 M)[185] could have an effect on the total number of negative charges presented by the conjugates. Interactions of fluorescein derivatives with metal ions have been reported in literature, exploited for their application as fluorescent chemosensor for the detection of both cations and anions.[186-189] Figure 4.23 a – b shows absorption spectra of compounds **5 a** and **7 a** recorded in the pH range 2 – 9 in 0.1 M NaCl solution. Unlike the fluorescein analysis methods reported in literature, this titration was performed without the use of buffer solutions, instead only hydrochloric acid and ammonia solutions were used to reach the desired pH level. The results of the titration experiment performed in the presence of sodium were compared to the titrations performed in pure water (Figure 4.23 c – d), to highlight the influence of this metal ion on the proteolytic equilibria. This comparison demonstrated that, while compound **7 a** doesn't present any significant variation, the presence of sodium in the titration experiment of **5 a** has a clear impact on the mono-dianionic equilibrium. As shown in Figure 4.23 c, the addition of the metal ion alters the molar absorptivity (ε) variation in the pH range 5 – 10, indicating a decreasing in the value of the anion-dianion proteolytic constant. This alteration is due to the stabilization of the dianionic conformation of fluorescein, determined by the interaction between the fluorescent dye and sodium ions. Furthermore, to exclude the increase of ionic strength as a potential cause of this variation, a sodium titration at the fixed pH of the assay medium (pH = 8.23) was performed, revealing that the increment in the NaCl concentration doesn't result in a significant variation of absorptivity for either compound **5 a** or **7 a** (Figure 4.23 e – f).

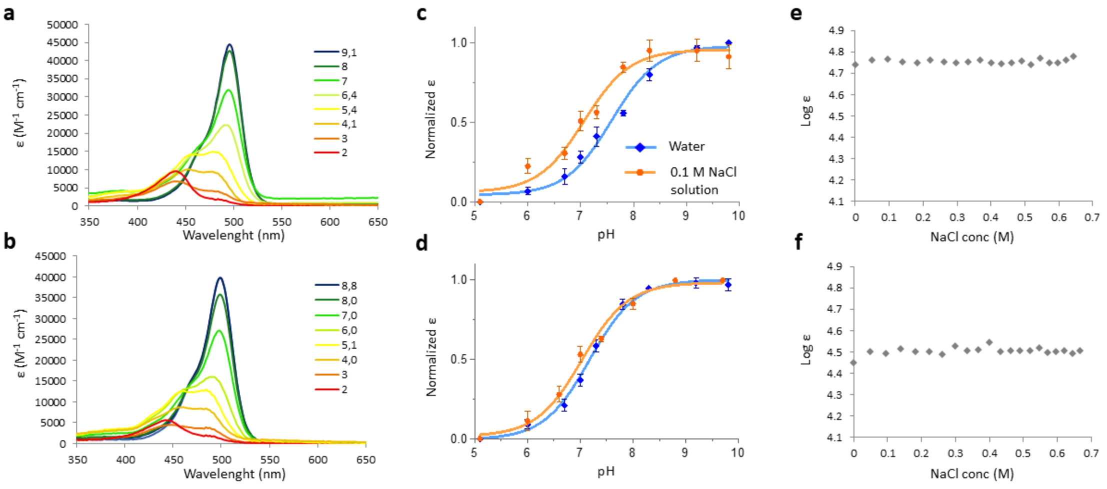

Figure 4.23 Absorption spectra of a) **5 a** and b) **7 a** 10 µM in 0.1 M NaCl solution, recorded ad different pH; normalized variation of molar absorptivity in relation to pH of c) **5 a** and d) **7 a** in pure water (blue) and in 0.1 M NaCl solution (orange); molar absorptivity in relation to NaCl concentration of e) **5 a** and **7 a** recorded at pH = 8.23.

Taken together, these results confirm the influence exerted by sodium salts on the conformation of fluorescein, and they can indirectly explain the unexpected binding affinity profile of the PESIN-monomer derivative. It is hypothesized that fluorescein can interact with one sodium ion *via* a chelating-like mechanism. This interaction is responsible for the stabilization of the dianionic conformation of the dye, as shown in the titration experiments, while it can also reduce the expressed overall negative charge of the conjugate 5 a from -5 to -4, as shown from the competitive binding assay.

To determine the biding pose of the sodium ion in the structure of fluorescein, DFT calculations were performed (Figure 4.24). In detail, from the energy minimized structures of both fluorescein phenolate and carboxylate sodium salts, it was observed that the metal salt ends up in the nearly same position in both simulations, between the carboxylate and the phenolate functions. This suggests a possible affinity between these functional groups and the sodium cation, making the described pose the most suitable to represent the chelation mechanism of fluorescein with the metal ion (Figure 4.25).

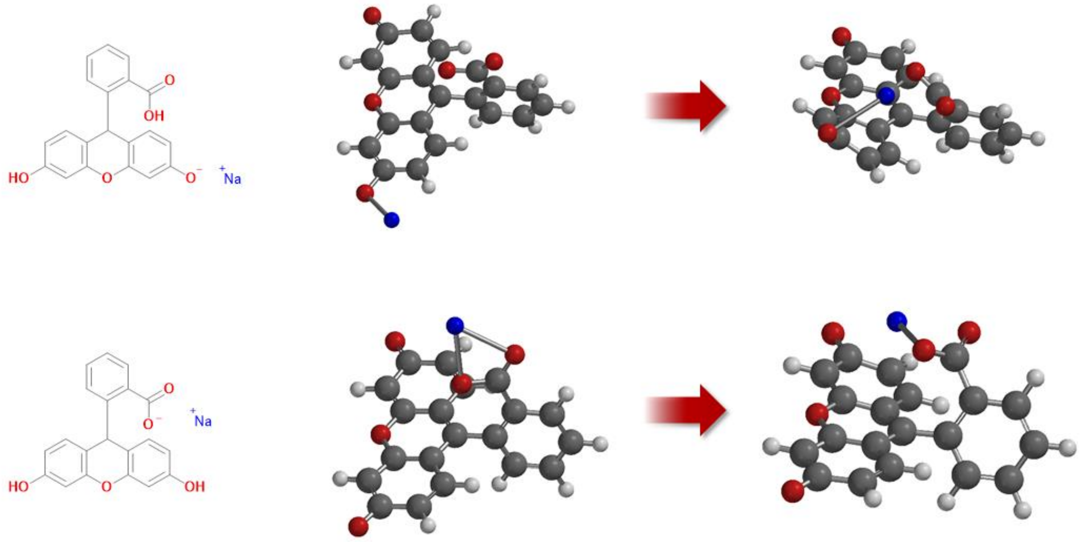

Figure 4.24 Starting points and DFT minimized energy structures of fluorescein phenolate (top) and carboxylate (bottom) sodium salts

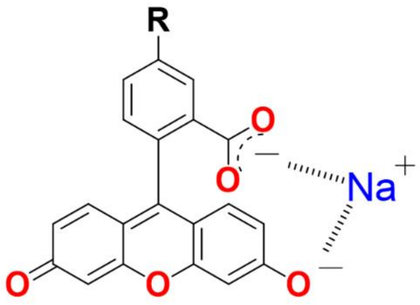

Figure 4.25 Proposed binding mode between the dianionic conformation of the fluorescein dye moiety and sodium.

Finally, although this suggested mechanism has been described, and its effects on the spectroscopic and binding properties of **5 a** have been observed, the same doesn't apply to the dimeric PESIN derivative **7 a**. In this latter case, in fact, the presence of sodium doesn't alter either the photophysical characteristics or the GRPR affinity profile of the conjugate. To explain this difference, molecular mechanic calculations were performed, determining the minimized energy structures of both conjugates (Figure 4.26).

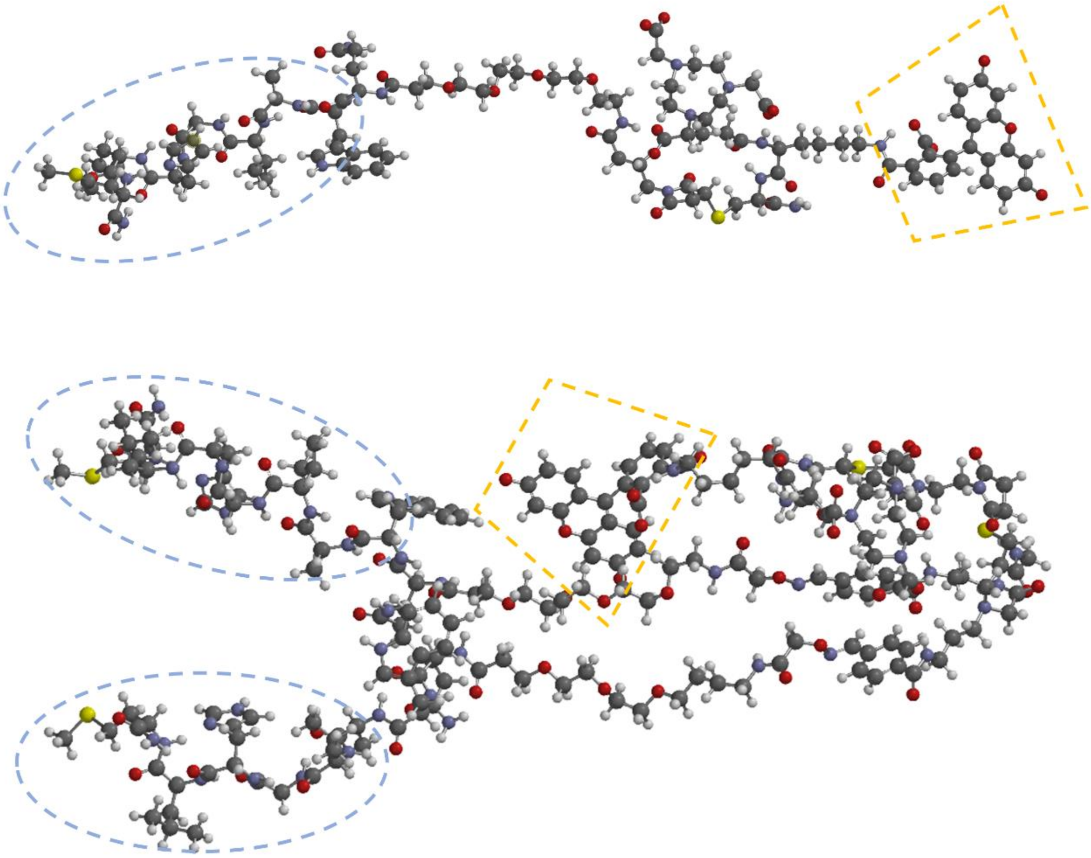

Figure 4.26 Molecular mechanics minimized energy structures of **5 a** (top) and **7 a** (bottom) with highlighted PESIN moieties (light blue) and fluorescein dye (yellow).

This distinct behavior is due to the potential interaction of the MIU with either one of the peptidic moieties of PESIN in compound **7 a**, which takes place during the binding with the receptor as well as when the hybrid compound is in solution (Figure 4.27). The interaction is allowed by the complex structure of the trifunctional linker which connects the imaging unit with the two peptidic residues, causing intramolecular influences between the fluorescent dye and the peptide. Those influences are not otherwise observed in the simpler structure of the corresponding PESIN monomer. As a result, the chelating ability of fluorescein is disrupted, and the cell binding properties of **7 a** are unaffected by the presence of sodium ions, so in line with the charge-cell binding correlation as described in the study which firstly reported this molecule.[91]

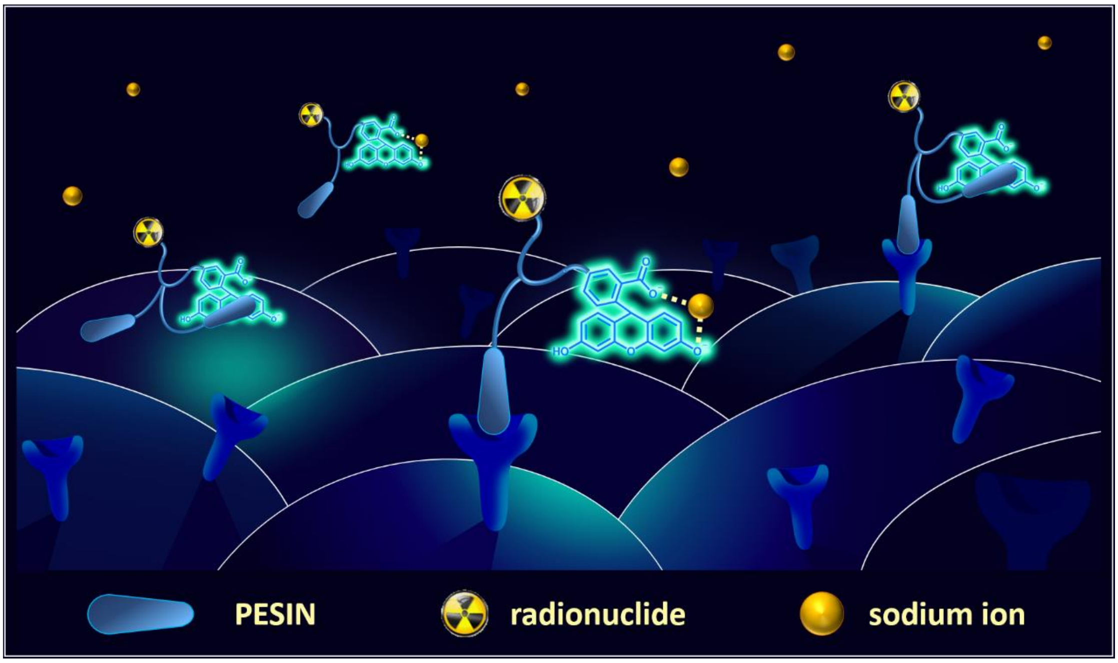

Figure 4.27 Graphical representation of the PESIN monomer-MIU conjugate (**5 a**) and the PESIN dimer-MIU conjugate (**7 a**) interacting with the GRP receptor in presence of sodium ions.

CHAPTER FIVE

Conclusions and perspectives

The work presented in this thesis manuscript aimed at the preparation of radiolabeled organic compounds, to be used as molecular imaging biomarkers for the PET analysis of pathological systems for which suitable radiotracers are not currently available. Two approaches of application of PET were followed.

The first part of the thesis explored this argument with a monomodal approach, developing radiolabeled small molecules targeting the inflammatory process involved in fibrosis. After having identified a suitable biological target and lead compounds for its addressing, the design of a number of radiotracers was performed. Then, different synthetic strategies were studied, resulting in the preparation of both the reference compounds and the cold precursors. Following this stage of "cold synthesis", the precursors were radiolabeled using two strategies: radiofluorination with ^{18}F and radiomethylation with ^{11}C. The optimization of this processes resulted in four radiolabeled compounds, **[^{18}F] 1**, **[^{18}F] 2**, **[^{18}F] 3**, and **[^{11}C] 4** . However, only compounds **[^{18}F] 2** and **[^{11}C] 4** could be obtained with satisfactory radiochemical yield and purity. Thus, these two compounds were selected to be tested with *in vitro* assays, to evaluate their potential as imaging agents. From preliminary tests, it is not clear if compound **[^{18}F] 2** could have a potential application as biomarker, since it seems to develop non-specific interactions with the tested cell lines. On the other hand, compound **[^{11}C] 4** showed suitable characteristics during the blocking experiments, suggesting specific interactions with its biological target in both the tested cell lines, and making it a good candidate to be studied for a possible application in the imaging of the fibrotic process. Future studies on this compound will explore its specificity for the targeted pathology, and will determine its potential use for *in vivo* studies on animal models of fibrosis.

Finally, the second part of the thesis applied a multimodal approach for the synthesis of hybrid dually labeled imaging agents suitable for both PET and optical imaging. This project aimed to test and expand the theory correlating the total net charge of the conjugates with their binding affinity to the respective target. Thus, MIUs comprising a NODA-GA chelator for radiometal labeling and different fluorescent dyes, differing in their charge, were prepare, then introduced into diverse receptor-affine peptides using an efficient click chemistry-based conjugation strategy. By this modular approach, the tailored design and synthesis of hybrid, dually labeled biomolecules for use in PET and OI becomes feasible. The developed GRPR-, MC1R- and integrin $\alpha_v\beta_3$-specific hybrid imaging agents were investigated for their chemical, biological and photophysical properties. Regarding their photophysical and radiochemical properties, it was found that the compounds could be effectively labeled with the positron emitter ^{68}Ga^{3+} under very mild conditions, and the fluorescence characteristics of the bioconjugates were – as expected – not deteriorated.

All developed hybrid dually labeled agents were able to receptor-specifically accumulate in target tumor cells as confirmed by confocal microscopy experiments. Furthermore, also the receptor affinities of the bioconjugates were determined by competitive displacement assays and showed for the GRPR-specific hybrid imaging agents a significant decrease in receptor affinities with increasing number of negative charges introduced by the respective fluorescent dye. These results confirm those obtained before for GRPR-binding peptide dimers and tetramers but showed – as expected – to be more pronounced for the monomeric peptide bioconjugates studied here. This confirms the presumed compensating effect of an increasing number of peptide copies per hybrid molecule on the negative effect of anionic charges.

The clear negative correlation between the number of anionic charges being introduced into the peptide structure by the used fluorescent dye and the observed receptor affinities was furthermore not only found for the GRPR-specific bioconjugates, but also for the other peptides studied and is thus irrespective of the examined peptide-receptor system.

These results confirm that anionic charges negatively influence the in vitro GRPR binding parameters of dually labeled GRPR-specific peptides, and show that this negative effect can be mitigated by peptide multimerization. Moreover, it was shown that the found effects of anionic charges on receptor affinities are not limited at the GRPR and its binders, but is also applicable to other receptor systems such as MC1R and integrin $\alpha_v\beta_3$. However, one of the synthesized monomeric PESIN derivative presenting fluorescein ad fluorescent probe (**5 a**), presented a binding profile apparently didn't fit perfectly in the previously described hypothesis. This aberrant behaviour was explained by illustrating a chelating mechanism on sodium ions of the fluorescein dye moiety of this compound. This hypothesis was supported by both biological results and spectroscopic analysis of the different fluorescein derivatives. Moreover, as comparison set of equally charged conjugates, a series of tartrazine-based PESIN derivatives (**6** – **8 a**) was designed and tested. The introduction of the sodium chelation mechanism allows to include the fluorescein-based monomeric derivative in the theorized correlation, making it the actual exception that proves the rule of the charge-cell binding correlation.

CHAPTER SIX

Side project

LABELED CARNOSINE DERIVATIVES AS INTERNAL STANDARDS

As side project to the main PhD research, the use of non-radioactive isotopes was explored for the preparation of internal standards for the quantitation of carnosine and its derivatives.

Carnosine (L-**1**, Figure 6.1) is an endogenous dipeptide, composed of β-alanine and L-histidine, highly concentrated in skeletal muscle and other excitable tissues. Its physiological roles, based on its biochemical properties, include pH-buffering, metal-ion chelation, antioxidant capacity, as well as the ability to protect against the formation of advanced glycation and lipoxidation end-products.[190] For these reasons, besides its nutritional ergogenic application in the sport community,[191] carnosine supplementation presents a therapeutic potential for the treatment of numerous diseases in which ischemic or oxidative stress are involved, such as diabetes,[192] atherosclerosis,[193] and nephropathy.[194] However, L-carnosine presents limited activity in humans[195] due to the presence of the enzyme human carnosinase (CN1, EC 3.4.13.20), which rapidly hydrolyses the peptide upon absorption.[196]

Besides L-carnosine, most of the animals (except *Homo sapiens*) have also the methylated analogs L-anserine (L-**2**) and/or L-balenine (L-**3**), in which the imidazole ring of L-histidine is methylated at the nitrogen atom closest to the side chain (N^{π}) and away from the side chain (N^{τ}), respectively (Figure 6.1). Although the relative expressions of the methylated forms can vary from species to species, anserine is more frequently observed than balenine.[190]

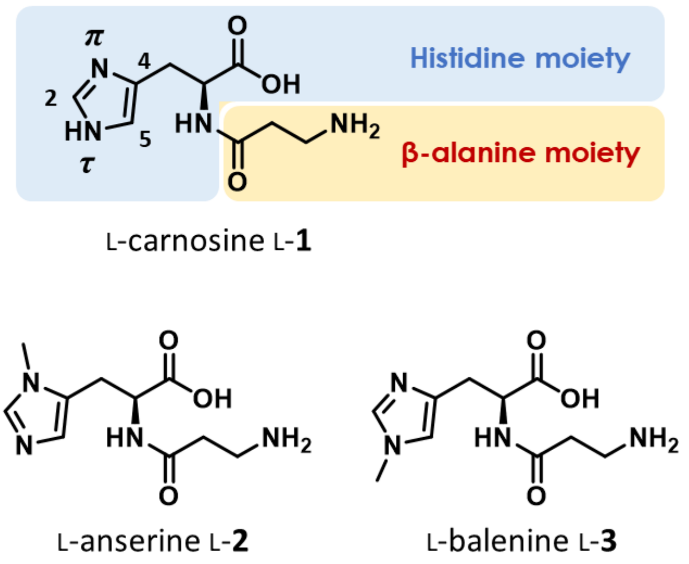

L-carnosine L-**1**

L-anserine L-**2**

L-balenine L-**3**

Figure 6.1 Structure of L-carnosine (L-**1**) and its methylated analogs, L-anserine (L-**2**) and L-balenine (L-**3**).

Quantitation of these histidine dipeptides in biological matrices results to be crucial for their potential applications, therefore several methods have been developed using high performance liquid chromatography coupled to either UV[197-199] or mass spectrometry detectors.[200]

Regarding the detection of carnosine in complex matrices such as biospecimens, mass spectrometry detector is the most used.[192, 201-203] Most of the methods for carnosine quantitation use no internal standard[204] or histidine containing dipeptides (i.e. L-tyrosyl-L-histidine or L-histidyl- L-leucine)[200-202] as internal standard, although isotope dilution (i.e. the use of an analyte isotopologue as internal standard) is the golden standard for mass spectrometry-based methods. This can be explained by the fact that stable isotopologues of carnosine are not available on the market, or the synthesis might be expensive. Isotope dilution mass spectrometry counterbalances spray instability, change of mobile phase solvent composition, background noise, sample interferences and competition from bulk ions.[205-207] This is critical, especially in biological matrices where a lot of compounds are present at different concentration in the samples and ion suppression phenomena can critically influence the output of a quantitative analysis. [205, 208, 209]

However, reliable quantitation data can be obtained with isotope dilution techniques,[210] where a stable isotope of the analyte is used as internal standard. The internal standard, which is characterized by identical physical and chemical properties to the analyte, will elute at the same retention time and undergo to the same phenomena in the ionization process.[211, 212]

On the contrary, the use of an isomer of the analyte is not always suitable since such an internal standard could have a different retention time and even if not so, it will undergo to a different ionization process due to different physical chemical properties of the molecule compared to the analyte.[211]

The use of an internal standard for quantitative analysis has the function of correcting either random or systematic error.[213] To do so, internal standard has to be added as earlier as possible in the sample. Indeed, the longer the sample preparation is, the higher the chance to introduce error. Therefore, having a compound that behaves as the analyte during sample preparation procedure is desirable.

With this side project, two strategies were developed for the preparation of stable isotopologues of carnosine and its derivatives (Figure 6.2):

- Deuterium-based strategy, for the preparation of L-carnosine-D_3;[214]

- Carbon-13-based strategy, for the preparation of ^{13}C-labeled D-isomers of carnosine and its methylated derivatives.[215]

The obtained labeled compounds were used as internal standards for the quantitation of carnosine and its derivatives in complex biological matrices.

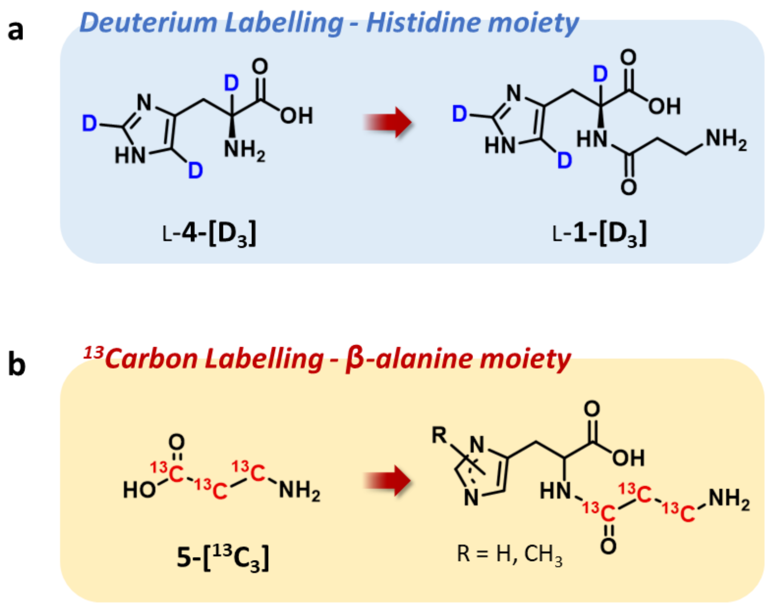

Figure 6.2 Synthetic strategies to obtain stable isotope-labeled carnosine and analogs: a) preparation of L-carnosine-D$_3$ (L-**1-[D$_3$]**) starting from L-histidine-D$_3$ (L-**4-[D$_3$]**), and b) preparation of ^{13}C-labeled carnosine analogs starting from β-alanine-^{13}C$_3$ (**5-[^{13}C$_3$]**). H atoms connected to 13C atoms are omitted for clarity.

The deuterium-based strategy allowed the preparation of L-**1-[D$_3$]** *via* a fast and highly efficient synthetic route (Scheme 6.1) which starts from the commercially available trideuterated L-histidine (α-D$_1$, imidazole-2,5-D$_2$) L-**4-[D$_3$]**. Its esterification was accomplished in the presence of thionyl chloride in methanol under stirring at room temperature for 20 h and provided the methyl ester hydrochloride L-**6-[D$_3$]** in high yield. This intermediate was then coupled to *N*-Boc protected beta-alanine, using the coupling reagent 2-(1*H*-Benzotriazole-1-yl)-1,1,3,3-tetramethylaminium hexafluorophosphate (HBTU) and diisopropylethylamine (DIPEA) as base in acetonitrile at room temperature to obtain the dipeptide intermediate L-**7-[D$_3$]**. Finally, the dipeptide was submitted to a

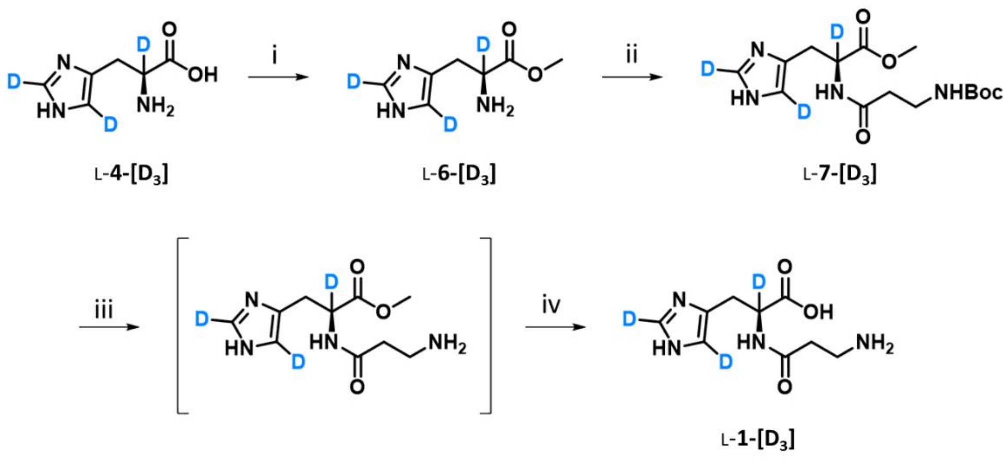

Scheme 6.1 *Reagents and conditions*: i) SOCl$_2$, MeOH, 0°C → rt, 20 h; ii) Boc-β-Ala, HBTU, DIPEA, CH$_3$CN, 0°C → rt, 12 h; iii) TFA, CH$_2$Cl$_2$, 0°C → rt, 1 h; iv) LiOH, H$_2$O/THF (10:1), 0°C → rt, 4 h.

quantitative two-step deprotection sequence. At first, the removal of the Boc group was performed with trifluoroacetic acid in dichloromethane to give the methyl ester derivative, which was not isolated and subjected to hydrolysis using lithium hydroxide in a mixture of tetrahydrofuran/water. The desired product L-**1-[D$_3$]** was obtained after purification on a cation-exchange resin.

This trideuterated analogue of carnosine was used as internal standard to validate a multiple reaction monitoring (MRM) LC-MS/MS method for the measurement of the carnosinase activity in human serum, as well as for the quantitation of carnosine.[214] In comparison to tyrosyl-L-histidine, L-**1-[D$_3$]** resulted to be more effective in correcting error in quantitative data. Tyrosyl-L-histidine has been used as internal standard for carnosine quantitation in many papers in the past.[201, 202] Nevertheless, it has numerous drawbacks such as different retention time than carnosine (depending on the chromatographic gradient developed), and a different intrinsic ionization. Such differences, altogether prevent tyrosyl-L-histidine to be as effective as carnosine isotopologues as internal standard for MS applications.

Figure 6.3 shows the correction efficacy of tyrosyl-L-histidine and L-**1-[D$_3$]** on a calibration curve of carnosine in urine. Each concentration point was done in a single urine sample coming from a different animal, to increase matrix effect differences as much as possible. Carnosine alone does not show a good response linearity, as measured by the goodness of fit (R^2) to a linear model (Figure 6.3 a). The use of tyrosyl-L-histidine as internal standard slightly improved the linearity, although not completely (Figure 6.3 b).

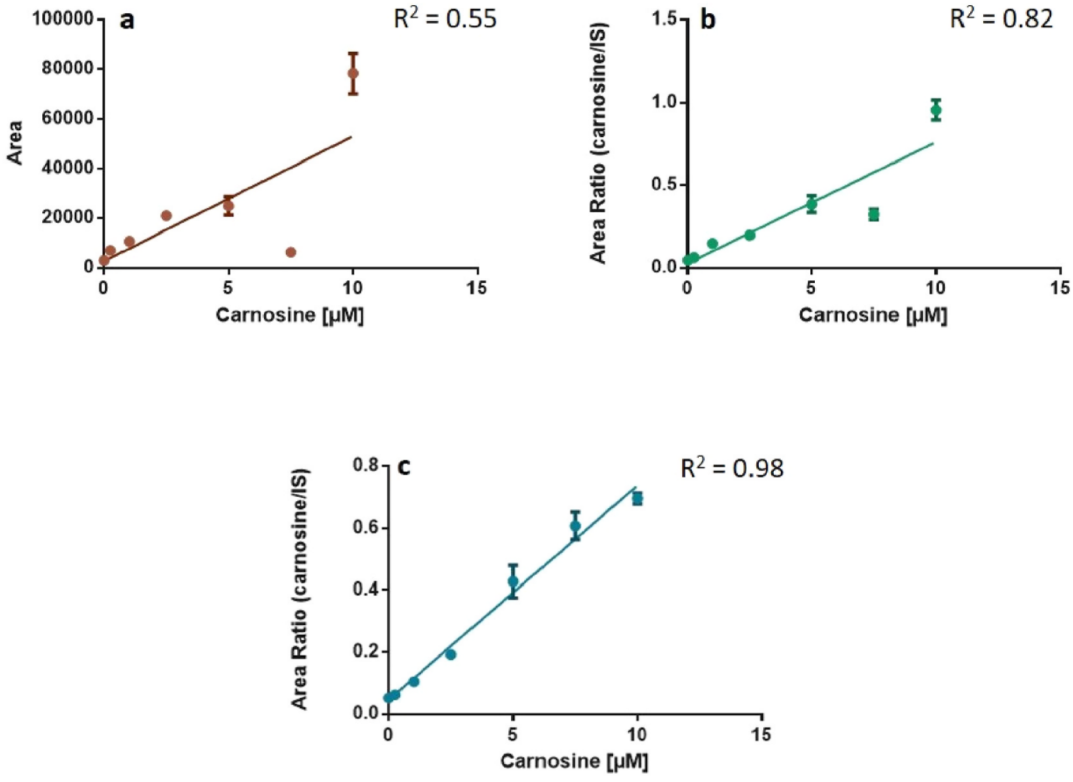

Figure 6.3 Calibration curve in urine of a) carnosine, b) carnosine corrected by tyrosyl-L-histidine, and c) carnosine corrected by L-**1-[D$_3$]**.

Only the correction with L-**1-[D$_3$]** can fully compensate the matrix effect at each concentration point, resulting in a good correlation between sample concentration and peak area (Figure 6.3 c). Such results are expected since matrix effect can be different from sample to sample and affect analyte response in many different ways (e.g. by affection ionization or by affection analyte separation and elution). However, the retention time of the analyte and tyrosyl-L-histidine are different and the matrix impact on their ionization and elution efficiency are not necessarily the same. For this reason, correcting the analyte response by the response of tyrosyl-L-histidine can neither re-establish a linear response to analyte concentration, nor make acceptable the accuracy and precision of the method (Table 6.1).

Table 6.1 Precision and accuracy of carnosine quantitation with and without different internal standards.

	Nominal concentration [a]	Average concentration [b]	SD [c]	CV% [d]	BIAS% [e]
Data not corrected	0.25	0.84	0.20	23.91	237.61
	1	1.58	0.34	21.28	58.30
	2.5	3.61	0.16	4.35	44.44
	5	4.41	0.75	17.02	-11.76
	7.5	0.71	0.21	29.42	-90.56
	10	15.04	1.61	10.69	50.37
Data corrected by tyrosyl-L-histidine internal standard	0.25	0.48	0.07	14.27	91.07
	1	1.64	0.20	12.50	63.66
	2.5	2.32	0.13	5.63	-7.27
	5	4.87	0.69	14.17	-2.50
	7.5	4.02	0.44	10.85	-46.36
	10	12.65	0.82	6.50	26.47
Data corrected by L-**1-[^{13}C$_3$]** internal standard	0.25	0.22	0.18	84.61	-13.68
	1	0.83	0.08	10.06	-16.75
	2.5	2.10	0.07	3.45	-15.92
	5	5.51	0.77	13.99	10.24
	7.5	8.12	0.64	7.90	8.32
	10	9.39	0.25	2.68	-6.07

[a] Nominal concentration is the spiked standard concentration +X = 0 intercept. [b] Average concentration is the concentration calculated from experimental data using regression line. [c] Standard deviation. [d] Coefficient of variation percentage is the intermediate precision of experimental measures. [e] Bias percentage is the accuracy of experimental measures.

Despite this successful result, deuterated standards present disadvantages that can limit the accuracy in quantitation by HPLC-MS. These limitations include:

- loss of deuterium in solution due to deuterium-hydrogen exchange phenomena;
- loss of deuterium under mass spectrometry conditions;
- changes in fragmentation and HPLC retention time compared to the unlabeled compound of interest.

Furthermore, because of the metabolic instability of L-**1-[D$_3$]** due to the action of the carnosinase, the internal standard was not added during the sample preparation but following the blocking of the carnosinase hydrolytic activity.

To outdo these limitations, it was developed a carbon-13 labeling-based strategy for the synthesis of stable isotope carnosine and analogs. Moreover, we decided to prepare the ^{13}C-labeled isotopologues as D-enantiomers to overcome the L-enantiomers instability towards tissue and serum carnosinase degradation. Interestingly, D-carnosine having the D-histidine instead of the L-histidine, displayed a carbonyl quenching activity comparable to that of L-carnosine, but resulted to be stable to the enzymatic hydrolysis.[216, 217] The new ^{13}C-labeled standards suffer from none of the previously mentioned deficiencies and, despite ^{13}C is usually a more expensive labeling technique, they were prepared with a fast and efficient synthetic route which has roughly the same cost as the deuterium-based strategy.

Summing up, this novel approach offers four main advantages over the previous methods. First, ^{13}C labeling has higher isotopic purity (up to 99 %) compared to deuterated compounds, as it is not prone to exchange/loss of label. Second, it is prevented the chromatographic interference due to deuterium atoms, which can influence the retention time of the internal standard.[218] Third, the flexible synthetic pathway developed here allows the synthesis of a ^{13}C-labeled carnosine derivative along with a variety of analogs, such as labeled derivatives of stereoisomers and methylated carnosine analogs (Figure 6.2 b). Finally, the use of a non-physiological D-stereoisomer determines an increased metabolic stability of the labeled compound which therefore can be applied from the beginning of the sample preparation process, resulting to be a more reliable and robust internal standard.[219] On this basis, two novel ^{13}C-labeled analogs of L-carnosine and L-anserine, D-**1-[^{13}C$_3$]** and D-**2-[^{13}C$_3$]** respectively, were prepared, to be used as internal standards for the quantitation of histidine dipeptides in a biological matrix.

This synthetic strategy is based on the application of commercially available β-alanine-^{13}C$_3$ isotope (**5-[^{13}C$_3$]**) and, in contrast with the deuterium-based labelling method, it allows to synthesize d-isomers and methylated analogues of carnosine by simply modifying the histidine moiety before the coupling reaction, saving on the number of reaction steps where the labeled compound is involved.

Initially, histidine moieties D-**6** and its N$^{\pi}$ methylated analogue D-**10** are prepared, starting from the commercial available D-histidine (D-**4**), following the synthetic route depicted in Scheme 6.2. The amino acid D-**4** is treated with thionyl chloride in methanol to give the corresponding methyl ester D-**6**. While different methods were developed to methylate the less reactive N$^{\pi}$ on the imidazole ring,[220-222] it was decided to Boc (*tert*-butyloxycarbonyl)-protect the methyl ester intermediate D-**6** yielding the two N$^{\pi}$ and N$^{\tau}$ Boc imidazole regioisomers, D-**7** and D-**8**, Boc protected also on the primary amine. D-**7** and D-**8** are then separated by silica gel column chromatography and obtained in a 2:8 ratio. Intermediate D-**8** is submitted to N$^{\pi}$ imidazole methylation, which is performed in a two-step reaction, first by treatment of D-**8** with methyl iodide in acetonitrile under reflux condition, and subsequent Boc removal from the imidazole N$^{\tau}$ with potassium carbonate in methanol. This mild deprotection[223] that preserves the primary amine protected allows a convenient chromatographic purification of the methylated compound D-**9**. Subsequent Boc group cleavage from the primary amine of intermediate D-**9** upon treatment with trifluoroacetic acid (TFA) affords compound D-**10**. The desired final ^{13}C labeled compounds D-**1-[^{13}C$_3$]** and D-**2-[^{13}C$_3$]** are obtained as shown in Scheme 6.3. The amino group of β-alanine-^{13}C$_3$ isotope **5-[^{13}C$_3$]** is protected with *tert*-butyloxycarbonyl resulting in **11-[^{13}C$_3$]**. The carboxylic group of **11-[^{13}C$_3$]** is activated using the coupling agent HBTU, and it is then reacted with the previously prepared histidine moieties D-**6** and D-**10**, to afford the protected dipeptides, D-**12-[^{13}C$_3$]** and D-**13-[^{13}C$_3$]**, respectively. The desired labeled compounds D-**1-[^{13}C$_3$]** and D-**2-[^{13}C$_3$]** are finally obtained as pure and neutral derivatives after a two-step deprotection followed by a purification via cation exchange resin. Because of the different solubilities, D-**12-[^{13}C$_3$]** is deprotected in two steps with TFA in

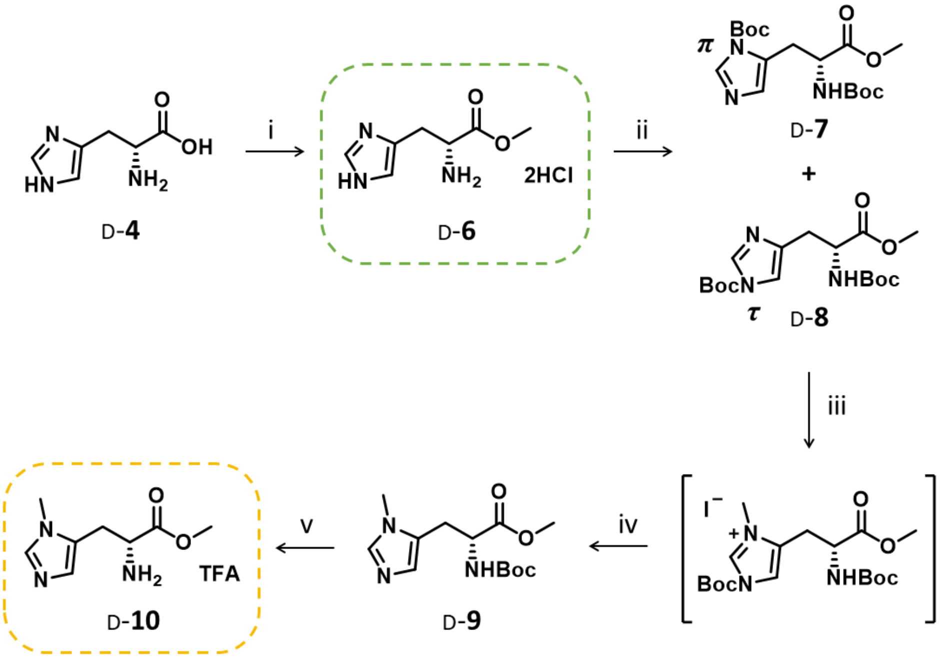

Scheme 6.2 Synthesis of the histidine moieties D-**6** and D-**10**. *Reagents and conditions*: i) MeOH, SOCl$_2$, 0 °C → rt, 12 h; ii) Boc$_2$O, TEA, MeOH, rt, 2 h; iii) MeI, CH$_3$CN, 90 °C, 1.5 h; iv) K$_2$CO$_3$, MeOH, 67 °C, 4 h; v) TFA, DCM, rt, 2 h.

dichloromethane and lithium hydroxide in a tetrahydrofuran/water mixture, whereas D-**13-[$^{13}C_3$]** is treated with sodium hydroxide in methanol followed by hydrochloric acid in water.

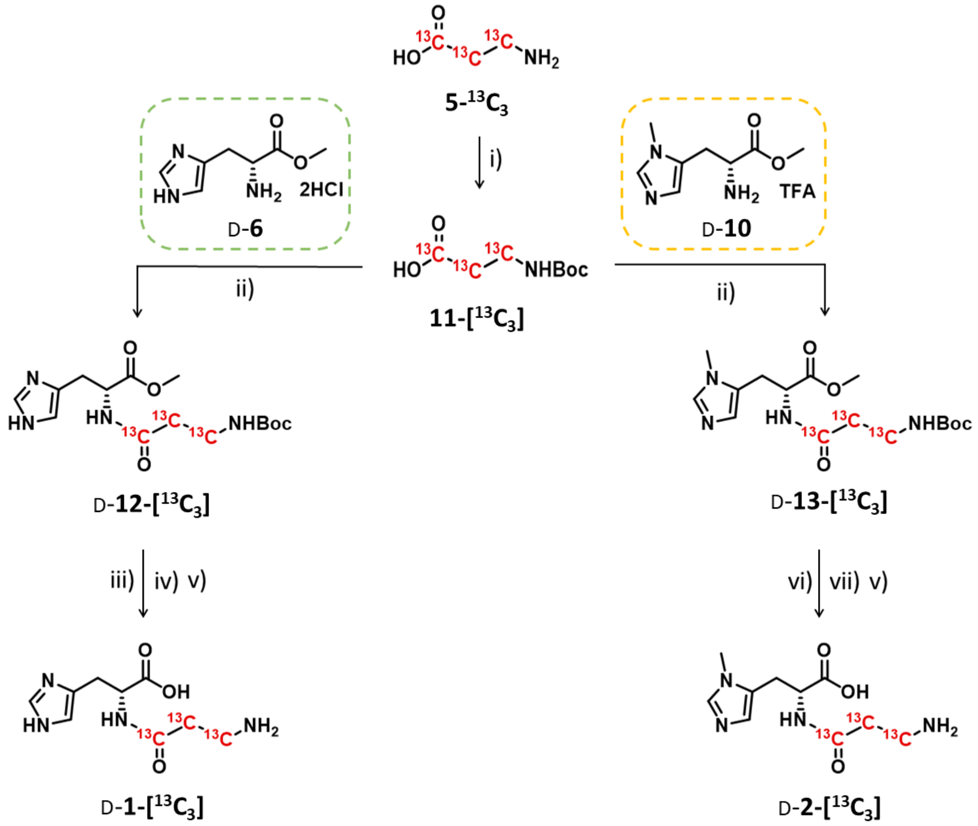

Scheme 6.3 Synthesis of D-**1-[13C3]** and D-**2-[13C3]**. *Reagents and conditions*: i) Boc_2O, NaOH, dioxane/water, 0 °C → rt, 1 h; ii) HBTU, DIPEA, CH_3CN, 0 °C → rt, 3 h; iii) TFA, DCM, rt, 2 h; iv) LiOH, THF/water, 0 °C → rt, 1.5 h; v) DOWEX 50WX2; vi) NaOH, MeOH, rt, 4 h; vii) HCl, water, 0 °C → rt, 12 h.

The two final compounds were obtained with adequate yields and high purity (chemical purity > 99 %). However, when tested *via* enantioselective chromatography, compound D-**2-[$^{13}C_3$]** resulted not to be enantiomerically pure. The most abundant peak detected was the D-enantiomer of anserine, while the L-enantiomer was less abundant. The data of the corresponding peak area were extracted, and the chromatographic enantiomeric excess (ee) was calculated and turned out to be 92%. Presumably, this loss in enantiomeric purity results from the basicity of the imidazole ring of histidine which is highly prone to racemization in mild basic condition. Without the Boc protection the imidazole N^{π} can extract the proton from the chiral center of histidine causing its racemization through the temporary formation of the enolate form.[224] Therefore, the decrease of enantiomeric purity of D-**2-[$^{13}C_3$]** could occur during the Boc-protection of intermediate D-**6** which is subjected to reaction in the presence of triethylamine for 3 h. A similar result was reported by Torikai et al.[225] while Boc-protecting the L-histidine stereoisomer. The cause of racemization was identified in the prolonged exposure of L-histidine methyl ester to basic conditions, and it was possible to increase the enantiomeric excess by reducing the reaction time. However, the enantiomeric impurity of compound D-**2-[$^{13}C_3$]** does not have any impact on the precision and accuracy of the method based on HILIC column, since it co-elutes with the D-enantiomer, and it is detected at the same *m*/*z* ratio.

Finally, compounds D-**1-[$^{13}C_3$]** and D-**2-[$^{13}C_3$]** were employed as internal standards in HPLC-MS analysis for the quantitation of carnosine and anserine, respectively, in mouse muscle (*Tibialis Anterior*) (Figure 6.4). The use of these standard allowed to quantify the corresponding analytes with more precision and accuracy compared to analysis reported in literature.[226] This effect is detectable by a decrease in the coefficient of variation for each point after correcting the analyte peak area by the internal standard (Tables 3 and 4). Looking at the value reported at each calibration curve point, the coefficient of variation percentage (CV%) is too high to consider the analysis acceptable from a precision point of view. This is because a complex matrix such as a tissue homogenate is being analysed. However, the coefficient of variation (CV%) of internal standard peak area across all samples was 15.33 % for D-**1-[$^{13}C_3$]** and 13.45 % for D-**2-[$^{13}C_3$]**. This demonstrates an acceptable fluctuation of signal intensity across samples due to matrix effect.

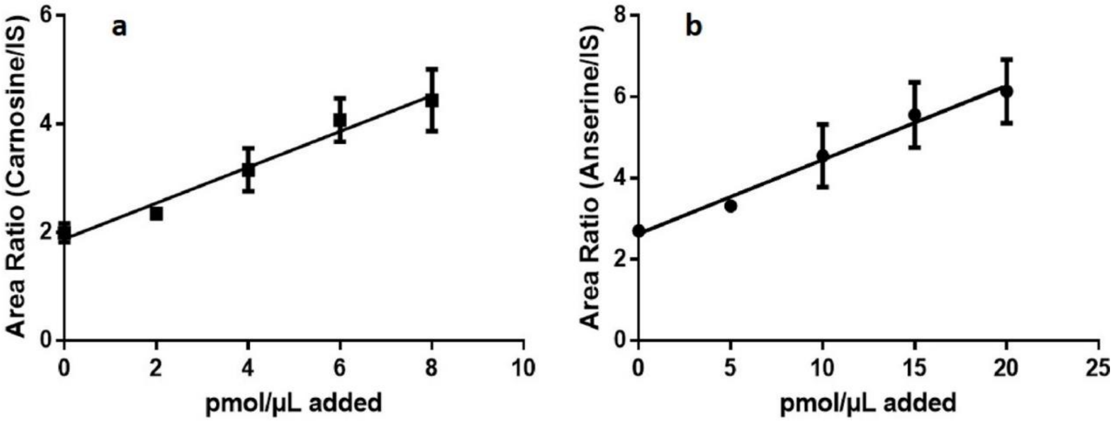

Figure 6.4 Calibration curve in *Tibial Anterior* homogenate of a) carnosine corrected by D-**1-[$^{13}C_3$]** (R^2 = 0.98), and b) anserine corrected by D-**2-[$^{13}C_3$]** (R^2 = 0.98)

To conclude, it was possible to develop fast and convenient synthetic strategies for the preparation of a deuterium labeled carnosine analogue and two additional carbon-13 labeled metabolically stable carnosine analogues, which were used as internal standards for the exact quantitation of carnosine and anserine in biological specimens. The implementation of a stable isotope as internal standard allowed to correct the error of each HPLC-MS course. Mass spectrometry ionization is highly influenced by several uncontrolled factors.[205-207] Our obtained data for carnosine and anserine quantitation show that the use of the stable isotopes as internal standards allows to reduce the impact of these variations, making the analysis more reliable.

Table 6.2 Precision and accuracy of carnosine quantitation with and without D-**1-[^{13}C$_3$]** as internal standard.

CARNOSINE

	Spiked standard	Nominal concentration [a]	Average concentration [b]	SD [c]	CV% [d]	Bias% [e]
Data not corrected	0	4.85	6.00	0.99	16.42	23.65
	2	6.85	7.45	1.13	15.20	8.73
	4	8.85	9.26	1.66	17.94	4.64
	6	10.85	11.88	3.91	32.89	9.52
	8	12.85	13.78	3.23	23.41	7.24
Data corrected by D-**1-[^{13}C$_3$]** internal standard	0	5.67	6.02	0.52	8.59	6.00
	2	7.67	7.10	0.29	4.06	-7.44
	4	9.67	9.53	1.20	12.59	-1.48
	6	11.67	12.31	1.21	9.82	5.46
	⍰	13.67	13.41	1.73	12.87	-1.93

[a] Nominal concentration is the spiked standard concentration +X = 0 intercept. [b] Average concentration is the concentration calculated from experimental data using regression line. [c] Standard deviation. [d] Coefficient of variation percentage is the intermediate precision of experimental measures. [e] Bias percentage is the accuracy of experimental measures.

Table 6.3 Precision and accuracy of anserine quantitation with and without D-**2-[^{13}C$_3$]** as internal standard.

ANSERINE

	Spiked standard	Nominal concentration [a]	Average concentration [b]	SD [c]	CV% [d]	Bias% [e]
Data not corrected	0	13.66	14.85	2.42	16.32	8.67
	5	18.66	19.34	4.02	20.77	3.61
	10	23.66	23.29	5.07	21.77	-1.56
	15	28.66	30.40	9.51	31.30	6.06
	20	33.66	34.32	8.25	24.03	1.94
Data corrected by D-**2-[^{13}C$_3$]** internal standard	0	14.44	14.82	0.69	4.64	2.64
	5	19.44	18.22	0.54	2.97	-6.26
	10	24.44	24.97	4.23	16.94	2.19
	15	29.44	30.50	4.42	14.50	3.60
	20	34.44	33.68	4.29	12.75	-2.20

[a] Nominal concentration is the spiked standard concentration +X = 0 intercept. [b] Average concentration is the concentration calculated from experimental data using regression line. [c] Standard deviation. [d] Coefficient of variation percentage is the intermediate precision of experimental measures. [e] Bias percentage is the accuracy of experimental measures.

EXPERIMENTAL SECTION

All chemicals were purchased from Sigma-Aldrich Srl (Milan, Italy) and Cambridge Isotope Laboratories Inc (Andover, USA) and used without further purification. Anhydrous solvents were purchased in sure seal bottles and used without further drying.

The reactions were monitored by thin-layer chromatography (TLC) on commercial aluminum plates precoated with silica gel 60 (F-254, Merck). Visualization was performed with UV light at 254 nm. Spots were further evidenced by staining with a dilute alkaline potassium permanganate solution or an ethanol solution of ninhydrin and acetic acid. The synthesized compounds were purified on glass chromatography columns packed with silica gel (230–400 mesh particle size, pore size 60 Å, Merck) or DOWEX 50 W × 2 H^+ form resin. ^1H NMR and ^{13}C NMR spectra have been registered with a Varian Mercury 300 instrument (300 MHz and 75 MHz, respectively). Chemical shifts (δ) are expressed in parts-per-million (ppm) and coupling constants (J) in hertz (Hz). Abbreviations used for peak multiplicities are given as follows: s (singlet), bs (broad singlet), d (doublet), dd (doublet of doublets), dd (doublet of doublet of doublets), qd (quadruplet of doublets), dt (doublet of triplets), m (multiplet). Optical rotations were determined with a JASCO P-1010 polarimeter. HPLC-MS analysis was carried out on an ExionLC-100 coupled to an API4000 via Turbo-V ESI source (AB-Sciex, Milan, Italy). Instrument control and data analysis were carried out with Analyst (version 1.6.3; AB-Sciex, Milan, Italy) and Prism (GraphPad, California, USA).

methyl L-histidinate-α,2,5-d_3 dihydrochloride (L-**6-[D_3]**)

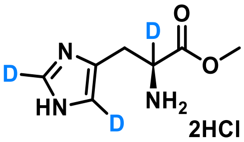

L-**4-[D_3]** (250 mg, 1.61 mmol) is suspended in MeOH (20 mL) and cooled in an ice bath. Thionyl chloride (958 mg, 8.06 mmol) is added dropwise, and the reaction is stirred at room temperature for 12 h. The solvent is removed under reduced pressure, resulting in compound L-**6-[D_3]** as a white powder (390 mg, 99.0 %).

R_f = 0.5 (DCM/MeOH/ammonia solution 8:2:0.1).

^{1}H NMR (300 MHz, CD_3OD) δ ppm 3.36 (d, J = 15.3 Hz, 1H; 1×CH_2CD), 3.45 (d, J = 15.3 Hz, 1H; 1×CH_2CD), 3.86 (s, 3H; OMe).

^{13}C NMR (75 MHz, CD_3OD) δ ppm 25.37 (CH_2CH), 51.64(OMe), 53.09 (CH_2CH), 118.19 (C5 imidazole), 126.74 (C4 imidazole), 134.53 (C2 imidazole), 168.16 (COOMe).

methyl (3-((*tert*-butoxycarbonyl)amino)propanoyl)-L-histidinate-α,2,5-d_3 (L-7-[D$_3$])

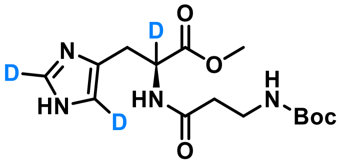

In a two-necked flask flushed with argon, β-alanine (305 mg, 1.61 mmol) is dissolved in dry CH_3CN (5 mL). HBTU (641 mg, 1.69 mmol) is added and the stirring mixture is cooled with an ice bath. DIPEA (452 mg, 3.50 mmol) is added dropwise, and the reaction is stirred for 10 min at 0 °C. L-**6-[D$_3$]** is suspended in dry CH_3CN (15 mL) and added dropwise to the stirring mixture at 0 °C. The reaction is allowed to warm to room temperature and stirred for 12 h. After removal of the solvent under reduced pressure, the residue is diluted with CH_2Cl_2 (15 mL) and washed with saturated aqueous solutions of $NaHCO_3$ (4 mL) and NH_4Cl (4 mL). The organic phase is dried over Na_2SO_4, filtered and concentrated under reduced pressure. The crude was purified via column chromatography (EtOAc/MeOH 75:25), providing L-**7-[D$_3$]** as a white foam (318 mg, 60.5 %).

R_f = 0,6 (EtOAc/MeOH 75:25).

^{1}H NMR (300 MHz, $CDCl_3$) δ ppm 1.36 (s, 9H; Boc), 2.40 – 2.46 (m, 2H; CH_2CO), 3.09 (d, J = 14.2 Hz, 1H; 1×CH_2CD), 3.12 (d, J = 14.2 Hz, 1H; 1×CH_2CD), 3.31 – 3.39 (m, 2H; CH_2N), 3.69 (s, 3H; OMe).

^{13}C NMR (75 MHz, $CDCl_3$) δ ppm 28.26 ($C(CH_3)_3$), 29.34 (CH_2CD), 36.12 (CH_2CO), 37.61 (CH_2NH), 52.58 (OCH_3), 52.93 (CH_2CD), 79.34 ($C(CH_3)_3$), 116.44 (C5 imidazole), 134.22 (C4 imidazole), 135.13 (C2 imidazole), 156.58 (COONH), 172.01 (COOMe), 172.37 (CH_2CONH).

(3-aminopropanoyl)-D-histidine-α,2,5-d_3 (L-**1-[D$_3$]**)

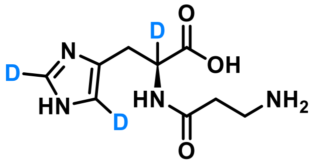

To a stirring solution of L-**7-[D$_3$]** (318 mg, 0.97 mmol) in CH_2Cl_2 (15 mL) was added dropwise TFA (1.13 mL, 14.62 mmol) at 0 °C. The reaction was allowed to warm to room temperature and stirred for 1 h. After removal of the solvent under reduced pressure, the residue was diluted with THF (10 mL) and H_2O (1 mL) and cooled to 0°C. 2 M LiOH aq. solution (2 mL) was added dropwise to the mixture and stirring was continued at room temperature for 4 h. Then the solvent was evaporated under reduced pressure and the crude product was purified via DOWEX 50WX2 resin, providing target compound L-**1-[D$_3$]** as a yellow solid (122 mg, 59 %).

R_f = 0,1 (ACN/MeOH 8:2).

^{1}H NMR (300 MHz, D_2O) δ ppm 2.48 – 2.53 (m, 2H; CH_2CO), 2.81 (d, J = 14.7 Hz, 1H; 1×CH_2CD), 2.98 (d, J = 14.7 Hz, 1H; 1×CH_2CD), 3.04 – 3.09 (m, 2H; CH_2N).

^{13}C NMR (75 MHz, D_2O) δ ppm 27.36 (CH$_2$CD), 32.39 (CH$_2$CO), 35.61 (CH_2NH), 54.55 (CH$_2$$C$D), 117.01 (C5 imidazole), 130.28 (C4 imidazole), 133.72 (C2 imidazole), 171.92 (CONH), 176.74 (COOH).

methyl D-histidinate dihydrochloride (D-**6**)

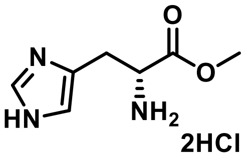

D-**4** (2.00 g, 12.89 mmol) was suspended in MeOH (50 mL) and cooled in an ice bath. Thionyl chloride (7.67 g, 64.45 mmol) was added dropwise, and the reaction was stirred at room temperature for 12 h. The solvent was removed under reduced pressure, resulting in compound D-**6** as a white powder (3.07 g, 98%).

R_f = 0.3 (DCM/MeOH/ammonia solution 8:2:0.1).

$[\alpha]_D^{20}$ = –10.1 (c 0.01, H_2O).

^{1}H NMR (300 MHz, CD_3OD) δ ppm 3.52 – 3.33 (m, 2H; C*H*$_2$CH), 3.86 (s, 3H; OMe), 4.46 (t, *J* = 6.1 Hz, 1H; CH_2C*H*), 7.54 (s, 1H; H5 imidazole), 8.93 (s, 1H; H2 imidazole).

^{13}C NMR (75 MHz, CD_3OD) δ ppm 26.52 (*C*H_2CH), 52.99 (OMe), 53.85 (CH_2*C*H), 119.82 (C5 imidazole), 128.09 (C4 imidazole), 136.05 (C2 imidazole), 169.38 (*C*OOMe).

***tert*-butyl (*R*)-4-(2-((*tert*-butoxycarbonyl)amino)-3-methoxy-3-oxopropyl)-1H-imidazole-1-carboxylate (D-8)**

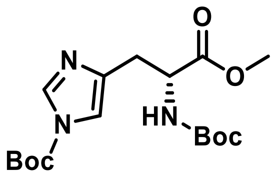

To a stirring suspension of D-**6** (2.00 g, 8.26 mmol) in MeOH (20 mL) was added di-*tert*-butyl dicarbonate (4.00 g, 19.00 mmol). The suspension was cooled in an ice bath, then triethylamine (2.29 mL, 16.52 mmol) was added dropwise and the reaction was stirred at room temperature for 3 h. After completion, the mixture was concentrated under reduced pressure. EtOAc (50 mL) was added, and the formed solution was washed with water (2 x 25 mL). The organic phase was dried over Na_2SO_4 and the solvent was removed under reduced pressure. The crude was purified via column chromatography (cyclohexane/EtOAc 6:4), providing compound D-**8** as a white powder (1.80 g, 59%).

R_f = 0,5 (DCM/MeOH 98:2).

$[\alpha]_D^{20}$ = –4.01 (c 1, MeOH).

^{1}H NMR (300 MHz, $CDCl_3$) δ ppm 1.43 (s, 9H; *Boc*NH), 1.62 (s, 9H; *Boc* imidazole), 3.11 (d, *J* =4.8 Hz, 2H; C*H*$_2$CH), 3.74 (s, 3H; OCH_3), 4.58 (dd, *J* = 5.4 Hz, 1.2 Hz, 1H; CH_2C*H*), 5.70 (d, *J* = 7.3 Hz, 1H; NH), 7.20 (s, 1H; H5 imidazole), 8.11 (s, 1H; H2 imidazole).

^{13}C NMR (75 MHz, $CDCl_3$) δ ppm 28.00 (NHCOOC(*C*H$_3$)$_3$), 28.43 (N$^\tau$COOC(*C*H$_3$)$_3$), 30.39 (*C*H$_2$CH), 52.43 (COO*Me*), 53.30 (CH_2*C*H), 79.90 (NHCOO*C*(CH$_3$)$_3$), 85.75 (N$^\tau$COO*C*(CH$_3$)$_3$), 114.70 (C4 imidazole), 137.05 (C5 imidazole), 138.71 (C2 imidazole), 146.96 (N$^\tau$CO), 155.58 (NHCO), 172.41 (*C*OOMe).

methyl N$^{\alpha}$-(*tert*-butoxycarbonyl)-N$^{\pi}$-methyl-D-histidinate (D-9)

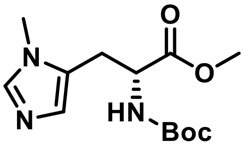

In a flame-dried reaction tube flushed with argon, D-**8** (500 mg, 1.35 mmol) was dissolved in dry CH_3CN (6 mL). Methyl iodide (230 mg, 1.62 mmol) was added dropwise and then the reaction was stirred at 90 °C for 2 h. After completion, the solvent was evaporated under reduced pressure. The resulting yellow solid was dissolved in MeOH (5 mL) and K_2CO_3 (112 mg, 0.81 mmol) was added. After stirring the mixture at 67 °C for 4 h, the solvent was removed under reduced pressure. The crude was purified via column chromatography (DCM/MeOH 100:0 → 95:5), providing compound D-**9** as a white solid (1.80 g, 59%).

R_f = 0.5 (DCM/MeOH 98:2).

$[\alpha]_D^{20}$ = +11.69 (c 1, MeOH).

^{1}H NMR (300 MHz, $CDCl_3$) δ ppm 1.42 (s, 9H; Boc), 3.10 (qd, J = 15.3, 5.8 Hz, 2H; CH_2CH), 3.60 (s, 3H; NMe), 3.74 (s, 3H; OMe), 4.54 dd, J = 11.6, 5.4 Hz, 1H; CH_2C*H*), 5.19 (d, J = 6.5 Hz, 1H; NH), 6.81 (s, 1H; H2 imidazole), 7.53 (s, 1H; H5 imidazole).

^{13}C NMR (75 MHz, $CDCl_3$) δ ppm 27.02 (*C*H_2CH), 28.41 (C(CH_3)$_3$), 31.67 (NMe), 52.76 (OMe), 53.13 (CH_2*C*H), 80.49 (*C*(CH_3)$_3$), 126.89 (C5 imidazole), 127.66 (C4 imidazole), 138.27 (C2 imidazole), 155.18 (*C*OOC(CH_3)$_3$), 171.71 (*C*OOMe).

(*R*)-1-methoxy-3-(1-methyl-1H-imidazol-5-yl)-1-oxopropan-2-aminium 2,2,2-trifluoroacetate (D-10)

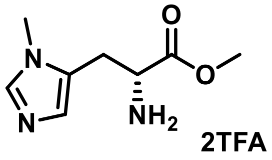

To a stirring solution of D-**9** (60 mg, 0.21 mmol) in DCM (5 mL), trifluoroacetic acid (0.245 mL, 3.18 mmol) was added dropwise. The reaction was stirred at room temperature for 2 h and then the solvent was removed under reduced pressure to afford compound D-**10** as a yellow solid (60 mg, 95%).

R_f = 0,5 (DCM/MeOH 95:5).

$[\alpha]_D^{20}$ = –11.6 (c 1, H_2O).

^{1}H NMR (300 MHz, CD_3OD) δ ppm 3.34 (ddd, *J* = 24,2. 16.4, 6.6 Hz 1H; C*H*$_2$CH), 3.78 (s, 3H; OMe), 3.83 (s, 3H; NMe), 4.40 (t, *J* = 7.1 Hz, 1H; CH$_2$C*H*), 7.42 (s, 1H; H2 imidazole), 8.79 (s, 1H; H5 imidazole).

^{13}C NMR (75 MHz, CD_3OD) δ ppm 28.79 (*C*H$_2$CH), 34.04 (NMe), 52.24 (OMe), 54.14 (CH$_2$*C*H), 120.42 (C5 imidazole), 130.15 (C4 imidazole), 137.73 (C2 imidazole), 169.37 (*C*OOMe).

3-((*tert*-butoxycarbonyl)amino)propanoic acid-$^{13}C_3$ (11-[$^{13}C_3$])

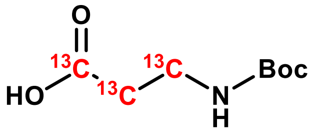

To a stirring solution of **5-[$^{13}C_3$]** (100 mg, 1.12 mmol) in a mixture of dioxane (2 mL) and H_2O (1 mL), 1N NaOH aq. (1 mL) was added dropwise. The mixture was cooled with an ice bath and di-*tert*-butyl dicarbonate (282 mg, 1.29 mmol) was added. After stirring the reaction at room temperature for 1 h, the solvent was concentrated under reduced pressure. The resulting residue was diluted with EtOAc (3.5 mL) and acidified with $NaHSO_4$ aq. (10%) to pH 2-3. The aqueous phase was washed with EtOAc (3 x 1.5 mL). The pooled organic phases were washed with H_2O (2 x 2 mL), dried over Na_2SO_4, filtered and concentrated under reduced pressure to afford compound **11-[$^{13}C_3$]** as a white powder (200 mg, 94%).

R_f = 0.7 (cyclohexane/EtOAc 1:1).

^{1}H NMR (300 MHz, $CdCl_3$) δ ppm 1.39 (s, 9H; Boc). 2.51 (d, J = 124.7 Hz, 2H; $^{13}CO^{13}CH_2$), 3.33 (d, J = 137.8 Hz, 2H; $^{13}CH_2NH$), 5.20 (s, 1H; NH), 10.87 (s, 1H; $^{13}COOH$).

^{13}C NMR (75 MHz, $CdCl_3$) δ ppm 28.40 ($C(CH_3)_3$), 34.44 (dd, J = 53.7, 37.2 Hz; $^{13}CO^{13}CH_2{}^{13}CH_2$), 36.63 (dd, J = 93.1, 37.0 Hz; $^{13}CH_2NH$), 79.76 ($C(CH_3)_3$), 156.16 (CONH), 176.79 (dd, J = 67.2, 55.2 Hz; $^{13}COOH$).

methyl (3-((*tert*-butoxycarbonyl)amino)propanoyl)-D-histidinate-^{13}C3 (D-12-[$^{13}C_3$])

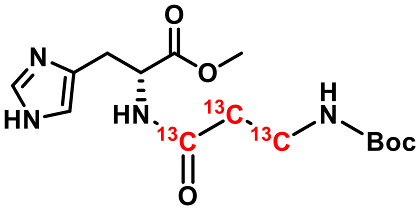

In a two-necked flask flushed with argon, **11-[$^{13}C_3$]** (200 mg, 1.06 mmol) was dissolved in dry CH_3CN (4 mL). HBTU (400 mg, 1.06 mmol) was added and the stirring mixture was cooled with an ice bath. DIPEA (273 mg, 2.12 mmol) was added dropwise, and the reaction was stirred for 10 min at 0 °C. D-**6** is suspended in dry CH_3CN (10 mL) and added dropwise to the stirring mixture at 0 °C. The reaction was allowed to warm to room temperature and stirred for 12 h. After removal of the solvent under reduced pressure, the residue was diluted with CH_2Cl_2 (10 mL) and washed with saturated aqueous solutions of $NaHCO_3$ (4 mL) and NH_4Cl (4 mL). The organic phase was dried over Na_2SO_4, filtered and concentrated under reduced pressure. The crude was purified via column chromatography (EtOAc/MeOH 75:25), providing D-**12-[$^{13}C_3$]** as a white foam (250 mg, 70%).

R_f = 0,6 (EtOAc/MeOH 75:25).

$[\alpha]_D^{26}$ = –19,08 (*c* 0,45, CH_2Cl_2).

^{1}H NMR (300 MHz, $CDCl_3$) δ ppm 1.43 (s, 9H; Boc), 2.25 – 2.19 (m, 1H; $^{13}CO^{13}CH\mathit{H}$), 2.69 – 2.60 (m, 1H; $^{13}CO^{13}C\mathit{H}H$), 3.20 – 3.12 (m, 3H; $^{13}CH\mathit{H}NH$, $C\mathit{H}_2CH$), 3.71 – 3.62 (m, 4H; OCH_3, $^{13}C\mathit{H}HNH$), 4.82 (d, *J* = 4.14, Hz 1H; $CH_2C\mathit{H}$), 5.53 (s, 1H; $^{13}CH_2N\mathit{H}Boc$), 6.80 (s, 1H; H5 imidazole), 7.10 (s, 1H; $CH_2CHN\mathit{H}$), 7.58 (s, 1H; H2 imidazole).

^{13}C NMR (75 MHz, $CDCl_3$) δ ppm 28.44 ($C(\mathit{C}H_3)_3$), 29.15 ($\mathit{C}H_2CH$), 38.04 – 35.73 (m; $^{13}CH_2NH$, $^{13}CO^{13}\mathit{C}H_2{}^{13}CH_2$), 52.41 ($OCH_3$), 52.78 ($CH_2\mathit{C}H$), 79.38 ($\mathit{C}(CH_3)_3$), 116.07 (C5 imidazole), 134.12 (C4 imidazole), 135.22 (C2 imidazole), 156.28 (CONH), 171.80 (d, *J* = 46.3 Hz; ^{13}CONH).

methyl N$^{\alpha}$-(3-((tert-butoxycarbonyl)amino)propanoyl)-N$^{\pi}$-methyl-D-histidinate-^{13}C3 (D-**13-[$^{13}C_3$]**)

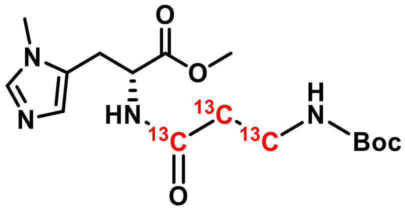

In a two-necked flask flushed with argon, **11-[$^{13}C_3$]** (200 mg, 1.06 mmol) was dissolved in dry CH_3CN (4 mL). HBTU (400 mg, 1.06 mmol) was added and the stirring mixture was cooled with an ice bath. DIPEA (273 mg, 2.12 mmol) was added dropwise, and the reaction was stirred for 10 min at 0 °C. D-**10** is suspended in dry CH_3CN (10 mL) and added dropwise to the stirring mixture at 0 °C. The reaction was allowed to warm to room temperature and stirred for 12 h. After removal of the solvent under reduced pressure, the residue was diluted with CH_2Cl_2 (10 mL) and washed with saturated aqueous solutions of $NaHCO_3$ (4 mL) and NH_4Cl (4 mL). The organic phase was dried over Na_2SO_4, filtered and concentrated under reduced pressure. The crude was purified via column chromatography (EtOAc/MeOH 75:25), providing D-**13-[$^{13}C_3$]** as a white foam (180 mg, 96%).

R_f = 0.34 (EtOAc/MeOH 75:25).

$[\alpha]_D^{26}$ = +7,3 (c 1, MeOH).

^{1}H NMR (300 MHz, $CDCl_3$) δ ppm 1.40 (s, 9H; Boc), 2.17 (d, J = 11.3 Hz, 1H; $^{13}CO^{13}CH\mathit{H}$), 2.59 (d, J = 5.9 Hz, 1H; $^{13}CO^{13}C\mathit{H}H$), 3.08 – 3.04 (m, 3H; $C\mathit{H}_2CH$, $^{13}CH\mathit{H}NH$), 3.55 (s, 4H; OMe, $^{13}C\mathit{H}HNH$), 3.72 (s, 3H; NMe), 4.79 (qd, J = 6.4, 2.9 Hz, 1H; $CH_2C\mathit{H}$), 5.20 (s, 1H; $^{13}CH_2N\mathit{H}Boc$), 6.71 (s, 1H; H5 imidazole),7.06 (bs, 1H; $CHN\mathit{H}$), 7.39 (s, 1H; H2 imidazole).

^{13}C NMR (75 MHz, $CDCl_3$) δ ppm 26.52 ($\mathit{C}H_2CH$), 28.46 ($C(\mathit{C}H_3)_3$), 31.51 (NMe), 37.56 – 35.39 (m; $^{13}CO^{13}\mathit{C}H_2{}^{13}CH_2$, $^{13}CH_2NH$), 51.67 (OMe), 52.72 ($CH_2\mathit{C}H$), 79.38 ($\mathit{C}(CH_3)_3$), 126.65 (C5 imidazole), 127.87 (C4 imidazole), 138.48 (C2 imidazole), 156.12 (CONH), 170.87 ($\mathit{C}OOMe$), 171.65 (d; J = 44.9 Hz; ^{13}CONH).

(3-aminopropanoyl)-D-histidine-^{13}C3 (D-1-[$^{13}C_3$])

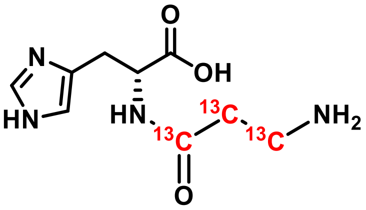

To a stirring solution of D-**12-[$^{13}C_3$]** (90 mg, 0.26 mmol) in CH_2Cl_2 (5 mL) was added dropwise TFA (0.3 mL, 3.97 mmol) at 0 °C. The reaction was allowed to warm to room temperature and stirred for 1 h. After removal of the solvent under reduced pressure, the residue was diluted with THF (5 mL) and H_2O (0.5 mL) and cooled to 0°C. 2 M LiOH aq. solution (2 mL) was added dropwise to the mixture and stirring was continued at room temperature for 4 h. Then the solvent was evaporated under reduced pressure and the crude product was purified via DOWEX 50WX2 resin, providing target compound D-**1-[$^{13}C_3$]** as a yellow solid (57 mg, 95%).

R_f = 0,1 (ACN/MeOH 8:2).

$[\alpha]_D^{26}$ = –20.40 (*c* 0.5, H_2O).

^{1}H NMR (300 MHz, D_2O) δ ppm 2.45 – 2.39 (m, 1H; ^{13}CO^{13}CH*H*), 3.00 – 2.80 (m, 3H; ^{13}CH*H*NH$_2$, CH*H*CH, ^{13}CO^{13}C*H*H), 3.13 (dd, *J* = 15.0, 4.6 Hz, 1H; C*H*HCH), 3.41 (dt, *J* = 11.2, 5.7 Hz, 1H; ^{13}C*H*HNH), 4.46 (ddd, *J* = 8.7, 4.7, 2.8 Hz, 1H; CH$_2$C*H*), 6.94 (s, 1H; H5 imidazole), 7.68 (s, 1H; H2 imidazole).

^{13}C NMR (75 MHz, D_2O) δ ppm 28.95 (*C*H$_2$CH), 32.73 (dd, *J* = 50.2, 35.6 Hz; ^{13}CO^{13}*C*H$_2$^{13}CH$_2$), 35.86 (d, *J* = 36.8 Hz; ^{13}CH$_2$NH), 55.13 (CH$_2$CH), 117.40 (C5 imidazole), 133.27 (C4 imidazole), 135.72 (C2 imidazole), 171.74 (d, *J* = 49.0 Hz; ^{13}CONH), 177.91 (COOH).

HRMS: theoretical m/z = 230.12393, experimental m/z = 230.12397, accuracy = 0.17 ppm.

N$^{\alpha}$-(3-aminopropanoyl)-N$^{\pi}$-methyl-D-histidine-^{13}C3 (D-**2-[$^{13}C_3$]**)

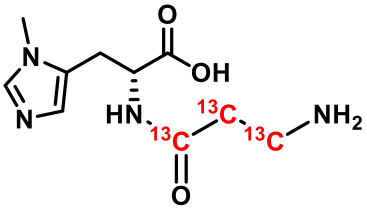

To a solution of D-**13-[$^{13}C_3$]** (180 mg, 0.508 mmol) in MeOH (5 mL) a 1M aqueous solution of NaOH was added dropwise up to pH 13 (1 mL) and the reaction was stirred at room temperature for 4h. After completion, the solvent was evaporated and the residue suspended in H_2O (5 mL). 1M HCl was added dropwise up to pH 1 (2 mL) and the mixture was stirred overnight. The solvent was evaporated under reduced pressure and the crude product was purified via DOWEX 50WX2 resin, providing the final compound D-**2-[$^{13}C_3$]** as a yellow solid (90 mg, 95%).

R_f = 0,5 (DCM/MeOH 98:2).

$[\alpha]_D^{26} = -9.0$ (c 1, H_2O).

^{1}H NMR (300 MHz, D_2O) δ ppm 2.38 – 2.29 (m, 1H; ^{13}CO^{13}CH*H*), 2.94 – 2.74 (m, 3H; ^{13}CH*H*NH, CH*H*CH, ^{13}CO^{13}C*H*H), 3.12 (dd, *J* = 15.5, 4.8 Hz, 1H; C*H*HCH), 3.31 – 3.28 (m, 1H; ^{13}C*H*HNH$_2$), 3.58 (s, 3H; NMe), 4.42 (ddd, *J* = 9.0, 4.8, 2.9 Hz, 1H; CH$_2$C*H*), 6.75 (s, 1H; H5 imidazole), 7.52 (s, 1H; H2 imidazole).

^{13}C NMR (75 MHz, D_2O) δ ppm 26.14 (*C*H$_2$CH), 31.01 (NMe), 33.61 (dd, *J* = 48.8, 36.4 Hz; ^{13}CO^{13}*C*H$_2$^{13}CH$_2$), 36.02 (d, *J* = 36.6 Hz; ^{13}CH$_2$NH), 53.66 (CH$_2$*C*H), 126.02 (C5 imidazole), 128.85 (C4 imidazole), 138.66 (C2 imidazole), 172.00 (d, *J* = 48.5 Hz; ^{13}CONH), 177.29 (COOH).

HRMS: theoretical m/z = 244.13997, experimental m/z = 244.14014, accuracy = 0.69 ppm.

Bibliography

1. Patton, D.D., *Roentgen's moment of discovery: a time for panic.* Radiology, 1996. **198**: p. 497-498.
2. Patton, D.D., *Roentgen and the "New Light"—Roentgen's Moment of Discovery.* Invest. Radiol., 1993. **28**: p. 51-58.
3. Röntgen, W.C., *On a new kind of rays.* Nature, 1896. **53**: p. 274–276.
4. Mould, R.F., *The early history of X-ray diagnosis with emphasis on the contributions of physics 1895-1915.* Phys. Med. Biol. , 1995. **40**: p. 1741-1787.
5. Coolidge, W.D., *A powerful roentgen ray tube with a pure electron discharge.* Phys. Rev., 1913. **2**: p. 409.
6. Levine, M.S. and Rubesin, S.E., *History and Evolution of the Barium Swallow for Evaluation of the Pharynx and Esophagus.* Dysphagia, 2017. **32**: p. 55–72.
7. Hessenbruch, A., *A brief history of x-rays.* Endeavour, 2002. **26**: p. 137-141.
8. Bradley, W.G., *History of Medical Imaging.* P. Am. Philos. Soc., 2008. **152**: p. 349-361.
9. Becquerel, A.H., *Sur les radiations invisibles émises par les corps phosphorescence.* Comp. Rend. Acad. Sci., 1896. **122**: p. 501-503.
10. Curie, M., *Rayons émis par les composés de l'uranium et du thorium.* CR. Acad. Sci., 1898. **126**: p. 1101-1103.
11. Curie, P., Curie, M., and Bémont, G., *Sur une nouvelle substance fortement radioactive contenue dans la pechblende.* CR. Acad. Sci., 1898. **127**: p. 1215-1217.
12. Rosenwald, J.C. and Fridtjof, N., *Marie Curie's contribution to Medical Physics.* Physica Medica, 2013. **29**: p. 423-425.
13. Cohen, M., *Rutherford's curriculum vitae, 1894-1907.* Med. Phys., 1995. **22**: p. 841-859.
14. Rutherford, E., *Uranium radiation and the electrical conduction produced by it.* Phil. Mag. Ser. 5, 1899. **47**: p. 109-163.
15. Rutherford, E. and Soddy, F., *Radioactive change.* Phil. Mag. Ser. 6, 1903. **5**: p. 576-591.
16. Rutherford, E., *The Scattering of α and β Particles by Matter and the Structure of the Atom.* Phil. Mag. Ser. 6, 1911. **21**: p. 669-688.
17. Rutherford, E., *Collision of α particles with light atoms. IV. An anomalous effect in nitrogen.* Phil. Mag. Ser. 6, 1919. **37**: p. 31-37.
18. Bothe, W. and Becker, H., *Künstliche Erregung von Kern-γ-Strahlen* Z. Phys., 1930. **66**: p. 289-306.
19. Curie, I., *Sur le rayonnement γ nucléaire excité dans le glucinium et dans le lithium par les rayons α du polonium.* C. r. hebd. séances Acad. sci. Paris, 1930. **193**: p. 1412.
20. Joliot, F., *Sur l'excitation des rayons γ nucléaires du bore par les particules α. Énergie quantique du rayonnement γ du polonium.* C. r. hebd. séances Acad. sci. Paris, 1931. **193**: p. 1415.
21. Chadwick, J., *Possible existance of a neutron.* Nature, 1932. **129**: p. 312.
22. Curie, I. and Joliot, F., *Un nouveau type de Radioactivité.* C. r. hebd. séances Acad. sci. Paris, 1934. **198**: p. 254-256.
23. Joliot, F. and Curie, I., *Artificial Production of a New Kind of Radio-Element.* Nature, 1934. **133**: p. 201-202.
24. Fermi, E., *Radioactivity Induced by Neutron Bombardment.* Nature, 1934. **133**: p. 757.
25. Niese, S., *George de Hevesy (1885–1966), founder of Radioanalytical Chemistry.* Czech J. Phys., 2006. **56**: p. D3-D11.
26. de Hevesy, G., *The Absorption and Translocation of Lead by Plants.* Biochem. J., 1923. **17**: p. 439.
27. Chiewitz, O. and de Hevesy, G., *Radioactive Indicators in the Study of Phosphorus Metabolism in Rats.* Nature, 1935. **136**: p. 754-755.
28. Lawrence, E., *Method and apparatus for the accelleration of ions.* (U.S. Patent No. 1,948,384), 1934.

29. Livingood, J.J. and Seaborg, G.T., *Radioactive Isotopes of Iodine.* Phys. Rev., 1938. **54**: p. 775-782.
30. Hamilton, J.C. and Soley, M.H., *Studies in iodine metabolism by use of a new radioactive isotope of iodine.* Am. J. Phys., 1939. **127**: p. 557-572.
31. Seidlin, S.M., Marinelli, L.D., and Oshry, E., *Radioactive iodine therapy; effect on functioning metastases of adenocarcinoma of the thyroid.* J. Am. Med. Assoc., 1946. **132**: p. 838-847.
32. Lifton, J.F. and Welch, M.J., *Preparation of glucose labeled with 20-minute half-lived carbon-11.* Radiat. Res., 1971. **45**: p. 35-40.
33. Raichle, M.E., Larson, K.B., Phelps, M.E., Grubb, R.L.J., Welch, M.J., and Ter-Pogossian, M.M., *In vivo measurement of brain glucose transport and metabolism employing glucose- -11C* Am. J. Phys., 1975. **228**: p. 1936-1948.
34. Tobias, C.A. and Lawrence, J.H., *The elimination of carbon monoxide from the human body with reference to the possible conversion of CO to CO_2.* Am. J. Physiol., 1945. **145**: p. 253-263.
35. Snell, A.H., *A New Radioactive Isotope of Fluorine.* Phys. Rev. , 1936. **51**: p. 143.
36. Volker, J.F., Hodge, H.C., Wilson, H.J., and Van Voorhis, S.N., *The absorption of fluoride by enamel, dentin, bone, and hydroxyapatite as shown by the radioactive isotope.* J. Biol. Chem., 1940. **134**: p. 543-548.
37. Reivich, M., Kuhl, D., Wolf, A., Greenberg, J., Phelps, M., Ido, T., Casella, V., Fowler, J., Gallagher, B., Hoffman, E., Alavi, A., and Sokoloff, L., *Measurement of local cerebral glucose metabolism in man with 18F-2-fluoro-2-deoxy-d-glucose* Acta. Neurol. Scand. Suppl., 1977. **64**: p. 190-191.
38. Som, P., Atkins, H.L., Bandoypadhyay, D., Fowler, J.S., MacGregor, R.R., Matsui, K., Oster, Z.H., Sacker, D.F., Shiue, C.Y., Turner, H., Wan, C.N., Wolf, A.P., and Zabinski, S.V., *A fluorinated glucose analog, 2-fluoro-2-deoxy-D-glucose (F-18): nontoxic tracer for rapid tumor detection.* J. Nucl. Med., 1980. **21**: p. 670-675.
39. Cannella, N., Cosa-Linan, A., Roscher, M., Takahashi, T.T., Vogler, N., Wängler, B., and Spanagel, R., *[18F]-Fluorodeoxyglucose-Positron Emission Tomography in Rats with Prolonged Cocaine Self-Administration Suggests Potential Brain Biomarkers for Addictive Behavior.* Front. Psychiatry 2017. **8**: p. 218.
40. Zhang, H.-W., Li, D.-Y., Zhao, J., Guan, Y.-H., Sun, B.-M., and Zuo, C.-T., *Imaging of Deep Brain Stimulation in Anorexia Nervosa. A 18F-FDG PET/CT Study.* Clin. Nucl. Med., 2013. **38**: p. 943-948.
41. Ha, S., Lee, H., Choi, Y., Kang, H., Jeon, S.J., Ryu, J.H., Kim, H.J., Cheong, J.H., Lim, S., Kim, B.-N., and Lee, D.S., *Maturational delay and asymmetric information flow of brain connectivity in SHR model of ADHD revealed by topological analysis of metabolic networks.* Sci. Rep., 2020. **10**: p. 3197-3210.
42. Ishibashi, K., Onishi, A., Wagatsuma, K., Fujiwara, Y., and Ishii, K., *Longitudinal 18F-FDG Images in Patients With Alzheimer Disease Over More Than 9 Years From a Preclinical Stage.* Clin. Nucl. Med., 2020. **45**: p. e185-e189.
43. Peter, J., Houshmand, S., Werner, T.J., Rubello, D., and Alavi, A., *Applications of global quantitative18F-FDG-PET analysis in temporal lobe epilepsy.* Nucl. Med. Commun., 2016. **37**: p. 223-230.
44. Perrier, C. and Segrè, E., *Radioactive Isotopes of Element 43.* Nature, 1937. **140**: p. 193-194.
45. Loc'h, C., Mazièré, B., and Comar, D., *A new generator for ionic gallium-68.* J. Nucl. Med., 1980. **21**: p. 171-173.
46. Hine, G.J., *The inception of photoelectric scitillation detection commemorated after three decades.* J. Nucl. Med., 1977. **18**: p. 867-871.
47. Cassen, B., Curtis, L., and Reed, C.W., *A sensitive directional gamma ray detector.* Nucleonics, 1950. **6**: p. 78-80.

48. Blahd, W.H., *Ben Cassen and the Development of the Rectilinear Scanner.* Semin. Nucl. Med., 1996. **26**: p. 165-170.
49. Brownell, G.L. and Sweet, W.H., *Localization of Brain Tumors with Positron Emitters.* Nucleonics, 1953. **11**: p. 40-45.
50. Sweet, W.H. and Brownell, G.L., *Localization of intracranial lesions by scanning with positron-emitting arsenic.* J. Am. Med. Assoc., 1955. **157**: p. 1183-1188.
51. Nutt, R., *The History of Positron Emission Tomography.* Mol. Imaging. Biol., 2002. **4**: p. 11-26.
52. Mankoff, D., *A Definition of Molecular Imaging.* J. Nucl. Med., 2007. **48**: p. 18N-21N.
53. Piel, M., Vernaleken, I., and Rösch, F., *Positron Emission Tomography in CNS Drug Discovery and Drug Monitoring. .* J. Med. Chem., 2014. **57**: p. 9232-9258.
54. Anderson, C.J. and Lewis, J.S., *Current status and future challenges for molecular imaging.* Phil. Trans. R. Soc. A, 2017. **375**: p. 20170023.
55. Montesi, S.B., Désogère, P., Fuchs, B.C., and Caravan, P., *Molecular imaging in fibrosis: recent advances and future directions.* J. Clin. Invest., 2019. **129**: p. 24-33.
56. Schillaci, O. and Urbano, N., *Personalized medicine: a new option for nuclear medicine and molecular imaging in the third millenium.* Eur. J. Nucl. Med. Mol. Imaging, 2017. **44**: p. 563-566.
57. Caravan, P., Yang, Y., Zachariah, R., Schmitt, A., Mino-Kenudson, M., Chen, H.H., and Lanuti, M., *Molecular Magnetic Resonance Imaging of Pulmonary Fibrosis in Mice.* Am. J. Respir. Cell. Mol. Biol., 2013. **49**: p. 1120-1126.
58. Désogère, P., Tapias, L.F., Hariri, L.P., Rotile, N.J., Rietz, T.A., Probst, C.K., and Caravan, P., *Type I collagen-targeted PET probe for pulmonary fibrosis detection and staging in preclinical models.* Sci. Transl. Med., 2017. **9**: p. eaaf4696.
59. Sanyal, A.J., Brunt, E.M., Kleiner, D.E., Kowdley, K.V., Chalasani, N., Lavine, J.E., and McCullough, A., *Endpoints and clinical trial design for nonalcoholic steatohepatitis.* Lancet, 2011. **385**: p. 956-965.
60. Ley, B., Collard, H.R., and King, T.E., *Clinical course and prediction of survival in idiopathic pulmonary fibrosis.* Am. J. Respir. Crit. Care Med., 2011. **183**: p. 431-440.
61. Collard, H.R., Bradford, W.Z., Cottin, V., Flaherty, K.R., King, T.E., Koch, G.G., and Brown, K.K., *A new era in idiopathic pulmonary fibrosis: considerations for future clinical trials.* Eur. Respir. J., 2015. **46**: p. 243-249.
62. Marcu, L.G., Moghaddasi, L., and Bezak, E., *Imaging of tumour characteristics and molecular pathways with PET: developments over the last decade towards personalised cancer therapy.* Int. J. Radiat. Oncol., 2018. **102**: p. 1165-1182.
63. Derlin, T., Grünwald, V., Steinbach, J., Wester, H.J., and Ross, T.L., *Molecular Imaging in Oncology Using Positron Emission Tomography.* Dtsch. Arztebl. Int., 2018. **115**: p. 175-181.
64. Endo, K., Oriuchi, N., Higuchi, T., Iida, Y., Hanaoka, H., Miyakubo, M., Ishikita, T., and Koyama, K., *PET and PET/CT using 18F-FDG in the diagnosis and management of cancer patients.* Int. J. Clin. Oncol., 2006. **11**: p. 286-296.
65. Judenhofer, M.S., Wehrl, H.F., Newport, D.F., Catana, C., Siegel, S.B., Becker, M., and Pichler, B.J., *Simultaneous PET-MRI: a new approach for functional and morphological imaging.* Nat. Med., 2008. **14**: p. 459-465.
66. Hernot, S., van Manen, L., Debie, P., Mieog, J.S.D., and Vahrmeijer, A.L., *Latest developments in molecular tracers for fluorescence image-guided cancer surgery.* Lancet, 2019. **20**: p. 354-367.
67. van Dam, G.M., Themelis, G., Crane, L.M.A., Harlaar, N.J., Pleijhuis, R.G., Kelder, W., Sarantopoulos, A., de Jong, J.S., Arts, H.J.G., van der Zee, A.G.J., Bart, J., Low, P.S., and Ntziachristos, V., *Intraoperative tumor-specific fluorescence imaging in ovarian cancer by folate receptor-α targeting: first in-human results.* Nat. Med., 2011. **17**: p. 1315-1319.

68. Wang, C., Wang, Z., Zhao, T., Li, Y., Huang, G., Sumer, B.D., and Gao, J., *Optical molecular imaging for tumor detection and image-guided surgery.* Biomaterials, 2017. **157**: p. 62-75.
69. Saeed, M., Xu, Z., De Geest, B.G., Xu, H., and Yu, H., *Molecular Imaging for Cancer Immunotherapy: Seeing Is Believing.* Bioconjugate Chem., 2020. **31**: p. 404-415.
70. Vahrmeijer, A.L., Hutteman, M., van der Vorst, J.R., van de Velde, C.J.H., and Frangioni, J.V., *Image-guided cancer surgery using near-infrared fluorescence.* Nat. Rev. Clin. Oncol., 2013. **10**: p. 507-518.
71. Rieffel, J., Chitgupi, U., and Lovell, J.F., *Recent Advances in Higher-Order, Multimodal, Biomedical Imaging Agents.* Small, 2015. **11**: p. 4445–4461.
72. Ahn, S.H. and Boros, E., *Nuclear and Optical Bimodal Imaging Probes Using Sequential Assembly: A Perspective.* Cancer Biother. Radio., 2018. **33**: p. 308-315.
73. Ni, D., Ehlerding, E.B., and Cai, W., *Multimodality Imaging Agents with PET as the Fundamental Pillar.* . Angew. Chem. Int. Ed. Engl., 2019. **58**: p. 2570-2579.
74. Christensen, A., Juhl, K., Persson, M., Charabi, B.W., Mortensen, J., Kiss, K., Lelkaitis, G., Rubek, N., von Buchwald, C., and Kjær, A., *uPAR-targeted optical near-infrared (NIR) fluorescence imaging and PET for image-guided surgery in head and neck cancer: proof-of-concept in orthotopic xenograft model.* Oncotarget, 2017. **8**: p. 15407-15419.
75. Renard, E., Dancer, P.A., Portal, C., Denat, F., Prignon, A.l., and Goncalves, V., *Design of Bimodal Ligands of Neurotensin Receptor 1 for Positron Emission Tomography Imaging and Fluorescence-Guided Surgery of Pancreatic Cancer.* J. Med. Chem., 2020. **63**: p. 2426−2433.
76. Baranski, A.C., Schäfer, M., Bauder-Wüst, U., Roscher, M., Schmidt, J., Stenau, E., Simpfendörfer, T., Teber, D., Maier-Hein, L., Hadaschik, B., Haberkorn, U., Eder, M., and Kopka, K., *PSMA-11-Derived Dual-Labeled PSMA inhibitors for preoperative PET imaging and precise fluorescence-guided surgery of prostate cancer.* J. Nucl. Med., 2018. **59**: p. 639-645.
77. Kang, N.Y., Lee, J.Y., Lee, S.H., Song, I.H., Hwang, Y.H., Kim, M.J., Phue, W.H., Agrawalla, B.K., Wan, S.Y.D., Lalic, J., Park, S.J., Kim, J.J., Kwon, H.Y., Im, S.H., Bae, M.A., Ahn, J.H., Lim, C.S., Teo, A.K.K., Park, S., Kim, S.E., Lee, B.C., Lee, D.Y., and Chang, Y.T., *Multimodal Imaging Probe Development for Pancreatic βCells: From Fluorescence to PET.* J. Am. Chem. Soc., 2020. **142**: p. 3430-3439.
78. Ahn, S.H., Thach, D., Brett A. Vaughn, Alford, V.M., Preston, A.N., Laughlin, S.T., and Boros, E., *Linear Desferrichrome-Linked Silicon–Rhodamine Antibody Conjugate Enables Targeted Multimodal Imaging of HER2 in Vitro and in Vivo.* Mol. Pharmaceutics, 2019. **16**: p. 1412−1420.
79. Lee, S., Xie, J., and Chen, X., *Peptide-based probes for targeted molecular imaging.* Biochemistry, 2010. **49**: p. 1364-1376.
80. MacPherson, D., Fung, K., Cook, B.E., Francesconi, L., and Zeglis, B.M., *A Brief Overview of Metal Complexes as Nuclear Imaging Agents.* Dalton Trans., 2019. **48**: p. 14547-14565.
81. Boros, E. and Packard, A.B., *Radioactive Transition Metals for Imaging and Therapy.* Chem. Rev., 2019. **119**: p. 870-901.
82. Gioux, S., Choi, H.S., and Frangioni, J.V., *Image-Guided Surgery Using Invisible Near-Infrared Light: Fundamentals of Clinical Translation* mol. imaging., 2010. **9**: p. 237-255.
83. König, S.G. and Krämer, R., *Accessing Structurally Diverse Near-Infrared Cyanine Dyes for Folate Receptor-Targeted Cancer Cell Staining.* Chem. Eur. J., 2017. **23**: p. 9306-9312.
84. Cheng, Z., Wu, Y., Xiong, Z., Gambhir, S.S., and Chen, X., *Near-Infrared Fluorescent RGD Peptides for Optical Imaging of Integrin αvβ3Expression in Living Mice.* Bioconjug. Chem., 2005. **16**: p. 1433-1441.
85. Huang, J., Weinfurter, S., Pinto, P.C., Pretze, M., Kränzlin, B., Pill, J., and Gretz, N., *Fluorescently Labeled Cyclodextrin Derivatives as Exogenous Markers for Real-Time*

Transcutaneous Measurement of Renal Function. Bioconjug. Chem., 2016. **27**: p. 2513-2526.

86. Lu, Y.-J., Hu, D.-P., Zhang, K., Wong, W.-L., and Chow, C.-F., *New pyridinium-based fluorescent dyes: A comparison of symmetry and side-group effects on G-Quadruplex DNA binding selectivity and application in live cell imaging.* Biosens. Bioelectron., 2016. **81**: p. 373-381.

87. Pliquett, J., Dubois, A., Racoeur, C., Mabrouk, N., Amor, S., Lescure, R., and Goze, C., *A promising family of fluorescent water-soluble aza-BODIPY dyes for in vivo molecular imaging.* Bioconjug. Chem., 2019. **30**: p. 1061-1066.

88. Sturzu, A., Sheikh, S., Echner, H., Nägele, T., Deeg, M., Amin, B., and Heckl, S., *Rhodamine-marked bombesin: a novel means for prostate cancer fluorescence imaging.* Invest. New Drugs, 2014. **32**: p. 37-46.

89. Tsaplev, Y.B., Trofimov, A.V., Pershukevich, P.P., Pavich, T.A., Zak, P.P., Trofimova, N.N., and Lapina, V.A., *Tuning Luminescent Converters Based on Coumarins and Their Photostability.* J. Appl. Spectroscop., 2017. **84**: p. 859-865.

90. Zhang, W., Huo, F., and Yin, C., *Recent advances of dicyano-based materials in biology and medicine.* J. Mater. Chem. B, 2018. **6**: p. 6919-6929.

91. Hübner, R., Cheng, X., Wängler, B., and Wängler, C., *Functional Hybrid Molecules for the Visualization of Cancer: PESIN-Homodimers Combined with Multimodal Molecular Imaging Probes for PositronEmission Tomography and Optical Imaging:Suited for Tracking of GRPR-Positive MalignantTissue.* Chem. Eur. J. , 2020. **26**: p. 16349 –16356.

92. Hübner, R., von Kiedrowski, V., Benkert, V., Wängler, B., Schirrmacher, R., Krämer, R., and Wängler, C., *Hybrid Multimodal Imaging Synthons for Chemoselective and Efficient Biomolecule Modification with Chelator and Near-Infrared Fluorescent Cyanine Dye.* Pharmaceuticals, 2020. **13**: p. 250-264.

93. Beer, M., Montani, M., Gerhardt, J., Wild, P.J., Hany, T.F., Hermanns, T., Muntener, M., and Kristiansen, G.P., *Profiling gastrin-releasing peptide receptor in prostate tissues: Clinical implications and molecular correlates.* Prostate, 2012. **72**: p. 318-325.

94. Körner, M., Waser, B., Rehmann, R., and Reubi, J.C., *Early over-expression of GRP receptors in prostatic carcinogenesis.* Prostate, 2014. **74**: p. 217-224.

95. Markwalder, R. and Reubi, J.C., *Gastrin-releasing peptide receptors in the human prostate: Relation to neoplastic transformation.* Cancer Res., 1999. **59**: p. 1152-1159.

96. Dalm, S.U., Martens, J.W., Sieuwerts, A.M., van Deurzen, C.H., Koelewijn, S.J., de Blois, E., Maina, T., Nock, B.A., Brunel, L., and Fehrentz, J.A., *In vitro and in vivo application of radiolabeled gastrin-releasing peptide receptor ligands in breast cancer.* J. Nucl. Med., 2015. **56**: p. 752-757.

97. Gugger, M. and Reubi, J.C., *Gastrin-releasing peptide receptors in non-neoplastic and neoplastic human breast.* Am. J. Pathol., 1999. **155**: p. 2067-2076.

98. Morgat, C., MacGrogan, G., Brouste, V., Velasco, V., Sevenet, N., Bonnefoi, H., Fernandez, P., Debled, M., and Hindie, E.E., *Expression of gastrin-releasing peptide receptor in breast cancer and its association with pathologic, biologic, and clinical parameters: A study of 1432 primary tumors.* J. Nucl. Med., 2017. **58**: p. 1401-1407.

99. Mattei, J., Achcar, R.D., Cano, C.H., Macedo, B.R., Meurer, L., Batlle, B.S., Groshong, S.D., Kulczynski, J.M., Roesler, R., and Dal Lago, L., *Gastrin-releasing peptide receptor expression in lung cancer.* Arch. Pathol. Lab. Med., 2014. **138**: p. 98-104.

100. Reubi, J.C., *Peptide receptor expression in GEP-NET.* Virchows Archiv., 2007. **451**: p. S47-S50.

101. Reubi, J.C., Körner, M., Waser, B., Mazzucchelli, L., and Guillou, L., *High expression of peptide receptors as a novel target in gastrointestinal stromal tumours.* Eur. J. Nucl. Med. Mol. Imaging, 2004. **31**: p. 803-810.

102. Reubi, J.C., Wenger, S., Schmuckli-Maurer, J., Schaer, J.C., and Gugger, M., *Bombesin receptor subtypes in human cancers: Detection with the universal radioligand 125I-*

[dTyr6,beta-Ala11,Phe13,Nle14]bombesin (6–14). Clin. Cancer Res., 2002. **8**: p. 1139-1146.

103. Mansi, R., Nock, B.A., Dalm, S.U., Busstra, M.B., van Weerden, W.M., and Maina, T., *Radiolabeled Bombesin Analogs.* Cancers, 2021. **13**: p. 5766.

104. Fischer, G., Lindner, S., Litau, S., Schirrmacher, R., Wängler, B., and Wängler, C., *Next step towards an optimization of GRP receptor avidities: Determination of the minimal distance between BBN(7-14) units in peptide homodimers.* Bioconjug. Chem., 2015. **26**: p. 1479-1483.

105. Hübner, R., Paretzki, A., von Kiedrowski, V., Maspero, M., Cheng, X., Davarci, G., Braun, D., Damerow, H., Judmann, B., Filippou, V., Dallanoce, C., Schirrmacher, R., Wängler, B., and Wängler, C., *PESIN Conjugates for Multimodal Imaging: Can Multimerization Compensate Charge Influences on Cell Binding Properties? A Case Study.* Pharmaceuticals, 2021. **14**: p. 531-545.

106. Flotats, A. and Carrió, I., *Cardiac neurotransmission SPECT imaging.* J. Nucl. Cardiol., 2004. **11**: p. 587-602.

107. Strafella, A.P., Bohnen, N.I., Perlmutter, J.S., Eidelberg, D., Pavese, N., and Van Eimeren, T., *Molecular imaging to track Parkinson's disease and atypical parkinsonisms: New imaging frontiers.* Mov. Disord., 2017. **32**: p. 181-192.

108. Rockey, D.C., Bell, P.D., and Hill, J.A., *Fibrosis - A Common Pathway to Organ Injury and Failure.* N. Engl. J. Med., 2015. **372**: p. 1138-1149.

109. Weiskirchen, R., Weiskirchen, S., and Tacke, F., *Organ and tissue fibrosis: Molecular signals, cellular mechanisms and translational implications.* Mol. Aspects Med., 2019. **65**: p. 2-15.

110. Parola, M. and Pinzani, M., *Pathophysiology of Organ and Tissue Fibrosis.* Mol. Aspects Med., 2019. **65**: p. 1.

111. Burstein, B. and Nattel, S., *Atrial fibrosis: mechanisms and clinical relevance in atrial fibrillation.* J. Am. Coll. Cardiol., 2008. **51**: p. 802-809.

112. Rieder, F. and Fiocchi, C., *Intestinal fibrosis in inflammatory bowel disease - current knowledge and future perspectives.* J. Crohns Colitis, 2008. **2**: p. 279-290.

113. Whatcott, C.J., Diep, C.H., Jiang, P., Watanabe, A., Lo Bello, J., Sima, C., and Han, H., *Desmoplasia in Primary Tumors and Metastatic Lesions of Pancreatic Cancer.* Clin. Cancer Res., 2015. **21**: p. 3561-3568.

114. Richeldi, L., du Bois, R.M., Raghu, G., Azuma, A., Brown, K.K., Costabel, U., and Collard, H.R., *Efficacy and Safety of Nintedanib in Idiopathic Pulmonary Fibrosis.* N. Engl. J. Med., 2014. **370**: p. 2071-2082.

115. King, T.E., Bradford, W.Z., Castro-Bernardini, S., Fagan, E.A., Glaspole, I., Glassberg, M.K., and Noble, P.W., *A Phase 3 Trial of Pirfenidone in Patients with Idiopathic Pulmonary Fibrosis.* N. Engl. J. Med., 2014. **370**: p. 2083-2092.

116. Raghu, G., Remy-Jardin, M., Myers, J.L., Richeldi, L., Ryerson, C.J., Lederer, D.J., and Wilson, K.C., *Diagnosis of Idiopathic Pulmonary Fibrosis. An Official ATS/ERS/JRS/ALAT Clinical Practice Guideline.* Am. J. Respir. Crit. Care Med. , 2018. **198**: p. e44-e68.

117. Weidemann, F. and Herrmann, S., *Impact of Myocardial Fibrosis in Patients With Symptomatic Severe Aortic Stenosis.* Circulation, 2009. **120**: p. 577-584.

118. Edeling, M., Ragi, G., Huang, S., Pavenstädt, H., and Susztak, K., *Developmental signalling pathways in renal fibrosis: the roles of Notch, Wnt and Hedgehog.* Nat. Rev. Nephrol., 2016. **12**: p. 426-439.

119. Chen, D.Q., Feng, Y.L., Cao, G., and Y., Z.Y., *Natural Products as a Source for Antifibrosis Therapy.* Trends Pharmacol. Sci., 2018. **39**: p. 937-925.

120. Mora, A.L., Rojas, M., Pardo, A., and Selman, M., *Emerging therapies for idiopathic pulmonary fibrosis, a progressive age-related disease.* Nat. Rev. Drug Discov., 2017. **16**: p. 755-772.

121. Wynn, T.A., *Common and unique mechanisms regulate fibrosis in various fibroproliferative diseases.* J. Clin. Invest., 2007. **117**: p. 524-529.

122. Gourdie, R.G., Dimmeler, S., and Kohl, P., *Novel therapeutic strategies targeting fibroblasts and fibrosis in heart disease.* Nat. Rev. Drug Discov., 2016. **15**: p. 620-638.

123. White, E.S., Lazar, M.H., and Thannickal, V.J., *Pathogenetic mechanisms in usual interstitial pneumonia/idiopathic pulmonary fibrosis.* J. Pathol., 2003. **201**: p. 343-354.

124. Thannickal, V.J., Lee, D.Y., White, E.S., Cui, Z., Larios, J.M., Chacon, R., and Thomas, P.E., *Myofibroblast Differentiation by Transforming Growth Factor-β1 Is Dependent on Cell Adhesion and Integrin Signaling via Focal Adhesion Kinase.* J. Biol. Chem, 2003. **278**: p. 12384–12389.

125. Cardoso, A.L., Fernandes, A., Aguilar-Pimentel, J.A., de Angelis, M.H., Guedes, J.R., Brito, M.A., and Trendelenburg, A.-U., *Towards frailty biomarkers: Candidates from genes and pathways regulated in aging and age-related diseases. .* Ageing Res. Rev., 2018. **47**: p. 214-277.

126. Plasschaert, L.W., Žilionis, R., Choo-Wing, R., Savova, V., Knehr, J., Roma, G., and Jaffe, A.B., *A single-cell atlas of the airway epithelium reveals the CFTR-rich pulmonary ionocyte.* Nature, 2018. **560**: p. 377–381.

127. Wang, J., Li, L., Li, L.-Y., Yan, Q., Li, J., and Xu, T., *Emerging role and therapeutic implication of Wnt signaling pathways in liver fibrosis.* Gene, 2018. **674**: p. 57-69.

128. Zhou, D., Fu, H., Zhang, L., Zhang, K., Min, Y., Xiao, L., and Liu, Y., *Tubule-Derived Wnts Are Required for Fibroblast Activation and Kidney Fibrosis.* J. Am. Soc. Nephrol., 2017. **28**: p. 2322-2336.

129. Henderson, W.R., Chi, E.Y., Ye, X., Nguyen, C., Tien, Y.-T., Zhou, B., Borok, Z., Knight, D.A., Kahn, M., and Stork, M., *Inhibition of Wnt/β-catenin/CREB binding protein (CBP) signaling reverses pulmonary fibrosis.* PNAS, 2010. **107**: p. 14309-14314.

130. Cheng, J.H., She, H., Han, Y.-P., Wang, J., Xiong, S., Asahina, K., and Tsukamoto, H., *Wnt antagonism inhibits hepatic stellate cell activation and liver fibrosis.* Am. J. Physiol. Gastrointest. Liver Physiol., 2020. **9141**: p. 39-49.

131. Akcora, B.Ö., Storm, G., and Bansal, R., *Inhibition of canonical WNT signaling pathway by β-catenin/CBP inhibitor ICG-001 ameliorates liver fibrosis in vivo through suppression of stromal CXCL12.* BBA-Mol. Basis. Dis., 2018. **1864**: p. 804-818.

132. Gerona-Navarro, G., Rodríguez, Y., Mujtaba, S., Frasca, A., Patel, J., Zeng, L., and Zhou, M.-M., *Rational Design of Cyclic Peptide Modulators of the Transcriptional Coactivator CBP: A New Class of p53 Inhibitors.* J. Am. Chem. Soc., 2011. **133**: p. 2040–2043.

133. Hay, D.A., Fedorov, O., Martin, S., Singleton, D.C., Tallant, C., Wells, C., Picaud, S., Philpott, M., Monteiro, O.P., Rogers, C.M., Conway, S.J., Rooney, T.P.C., Tumber, A., Yapp, C., Filippakopoulos, P., Bunnage, M.E., Mueller, S., Knapp, S., Schofield, C.J., and Brennan, P.E., *Discovery and Optimization of Small-Molecule Ligands for the CBP/p300 Bromodomains.* J. Am. Chem. Soc., 2014. **136**: p. 9308-9319.

134. He, Z.-X., Wei, B.-F., Zhang, X., Gong, Y.-P., Ma, L.-Y., and Zhao, W., *Current development of CBP / p300 inhibitors in the last decade.* Eur. J. Med. Chem., 2021. **209**: p. 112861.

135. Devipriya, B., Parameswari, A.R., Rajalakshmi, G., Palvannan, T., and Kumaradhas, P., *Exploring the binding affinities of p300 enzyme activators CTPB and CTB using docking method.* Indian J. Biochem. Biophys., 2010. **47**: p. 364-369.

136. Zhou, B. and Liu, Y., *Interactions Between β-Catenin and Transforming Growth Factor-β Signaling Pathways Mediate Epithelial-Mesenchymal Transition and Are Dependent on the Transcriptional Co-activator cAMP-response Element-binding Protein (CREB)-binding Protein (CBP).* J. Biol. Chem., 2012. **287**: p. 7026-7038.

137. Takahara, Y., Takahashi, M., Zhang, Q., Wagatsuma, H., Mori, M., and Tamori, A., *Serial changes in expression of functionally clustered genes in progression of liver fibrosis in hepatitis C patients. .* World J. Gastroenterol., 2008. **14**: p. 2010-2022.

138. Ma, H., Nguyen, C., Lee, K., and Kahn, M., *Differential roles for the coactivators CBP and p300 on TCF / b -catenin-mediated survivin gene expression.* Oncogene, 2005. **24**: p. 3619-3631.
139. Emami, K.H., Nguyen, C., Ma, H., Kim, D.H., Jeong, K.W., Eguchi, M., and Kahn, M., *A small molecule inhibitor of β-catenin CREB-binding protein transcription.* P. Natl. A. Sci., 2004. **101**: p. 12682-12687.
140. Okazaki, H., Sato, S., and Koyama, K., *The novel inhibitor PRI-724 for Wnt/β-catenin/CBP signaling ameliorates bleomycin-induced pulmonary fibrosis in mice.* Exp. Lung Res., 2019. **45**: p. 188-199.
141. Osawa, Y., Oboki, K., and Imamura, J., *Inhibition of Cyclic Adenosine Monophosphate (cAMP)-response Element-binding Protein (CREB)-binding Protein (CBP)β-CateninReduces Liver Fibrosis in Mice.* eBioMedicine, 2015. **2**: p. 1751-1758.
142. Jelley, N.A., *Fundamentals of Nuclear Physics.* Cambridge University Press, 2012. **Chapter 6**: p. 161-215.
143. Pascali, C., Bogni, A., Crippa, F., and Bombardieri, E., *Concetti generali sulla produzione di radiofarmaci emettitori di positroni.* Aretrè Srl, 1999.
144. Powsner, R.A., Palmer, M.R., and Powsner, E.R., *Essentials of Nuclear Medicine Physics and Instrumentation.* Wiley-Blackwell (III edition), 2013.
145. Romig, A. and Lindblom, K., *Discovery of the Radiocarbon Dating.* National Historic Chemical Landmarks program of the American Chemical Society 2016.
146. Lameka, K., Farwell, M.D., and Ichise, M., *Positron Emission Tomography. .* Handbook of Clinical Neurology, Neuroimaging Part 1, 2016. **135**: p. 209-227.
147. Dahl, K., Halldin, C., and Schou, M., *New methodologies for the preparation of carbon-11 labeled radiopharmaceuticals.* Clin. Transl. Imaging, 2017. **5**: p. 275-289.
148. Jacobson, O. and Chen, X., *PET Designated Flouride-18 Production and Chemistry.* Curr. Top. Med. Chem., 2010. **10**: p. 1048-1059.
149. Gamache, R.F., Waldmann, C., and Murphy, J.M., *Copper-mediated oxidative fluorination of aryl stannanes with fluoride.* Org. Lett., 2016. **18**: p. 4522-4525.
150. Nusse, R., *Wnt signaling in disease and in development.* Cell. Res., 2005. **15**: p. 28-32.
151. Behari, J., *The Wnt/beta-catenin signaling pathway in liver biology and disease.* Expert Rev. Gastroenterol. Hepatol., 2010. **4**: p. 745–756.
152. He, W., Dai, C., Li, Y., Zeng, G., Monga, S.P., and Y., L., *Wnt/beta-catenin signaling promotes renal interstitial fibrosis.* J. Am. Soc. Nephrol. , 2009. **20**: p. 765–776.
153. Henderson, W.R.J., Chi, E.Y., Ye, X., Nguyen, C., Tien, Y.T., Zhou, B., Borok, Z., Knight, D.A., and Kahn, M., *Inhibition of Wnt/beta-catenin/CREB binding protein (CBP)signaling reverses pulmonary fibrosis.* Proc. Natl. Acad. Sci. U. S. A. , 2010. **107**: p. 14309–14314.
154. Moon, R.T., Bowerman, B., Boutros, M., and Perrimon, N., *The promise and perils of Wnt signaling through beta-catenin.* Science, 2002. **296**: p. 1644-1646.
155. Wu, X.-L., Zeng, W.-Z., Jiang, M.-D., Qin, J.-P., and Xu, H., *Effect of Oxymatrine on the TGFbeta-Smad signaling pathway in rats with CCl_4-induced hepatic fibrosis* World J. Gastroenterol., 2008. **14**: p. 2100-2105.
156. Nayak, S.K., Panesar, P.S., and Kumar, H., *p53-Induced Apoptosis and Inhibitors of p53* Curr. Med. Chem., 2009. **16**: p. 2627-2640.
157. Maspero, M., Cheng, X., von Kiedrowski, V., Dallanoce, C., Wängler, B., Hübner, R., and Wängler, C., *Synthesis, Characterization and In Vitro Evaluation of Hybrid Monomeric Peptides Suited for Multimodal Imaging by PET/OI: Extending the Concept of Charge—Cell Binding Correlation.* Pharmaceuticals, 2021. **14**: p. 989.
158. Haskell-Luevano, C., Nikiforovich, G., Sharma, S.D., Yang, Y.K., Dickinson, C., Hruby, V.J., and Gantz, I., *Biological and Conformational Examination of Stereochemical Modifications Using the Template Melanotropin Peptide, Ac-Nle-c[Asp-His-Phe-Arg-Trp- Ala-Lys]-NH2, on Human Melanocortin Receptors.* J. Med. Chem., 1997. **40**: p. 1738-1748.

159. Haubner, R., Gratias, R., Diefenbach, B., Goodman, S.L., Jonczyk, A., and Kessler, H., *Structural and Functional Aspects of RGD-Containing Cyclic Pentapeptides as Highly Potent and Selective Integrin αVβ3 Antagonists.* J. Am. Chem. Soc., 1996. **118**: p. 7461-7472.
160. Wellings, D.A. and Atherton, E., *Standard Fmoc Protocols. Method. Enzymol.*, 1997. **289**: p. 44.
161. Hübner, R., Benkert, V., Cheng, X., Wängler, B., Krämerb, R., and Wängler, C., *Probing two PESIN-indocyanine-dye-conjugates: significance of the used fluorophore.* J. Mater. Chem. B, 2020. **8**: p. 1302.
162. von Kiedrowski, V., Hübner, R., Kail, D., Schirrmacher, R., Wängler, C., and Wängler, B., *Synthesis, characterization and optimization of in vitro properties of NIR-fluorescent cyclic a-MSH peptides for melanoma imaging.* J. Mater. Chem. B, 2020. **8**: p. 10602.
163. Cheng, X., Hübner, R., von Kiedrowski, V., Fricker, G., Schirrmacher, R., Wängler, C., and Wängler, B., *Design, Synthesis, In Vitro and In Vivo Evaluation of Heterobivalent SiFAlin-Modified Peptidic Radioligands Targeting Both Integrin αvβ3 and the MC1 Receptor—Suitable for the Specific Visualization of Melanomas?* Pharmaceuticals, 2021. **14**: p. 547.
164. Shao, Y., Molnar, L.F., Jung, Y., Kussmann, J., Ochsenfeld, C., Brown, S.T., Gilbert, A.T.B., Slipchenko, L.V., Levchenko, S.V., O'Neill, D.P., DiStasio, R.A., Lochan, R.C., Wang, T., Beran, G.J.O., Besley, N.A., Herbert, J.M., Lin, C.Y., Van Voorhis, T., Chien, S.H., Sodt, A., Steele, R.P., Rassolov, V.A., Maslen, P.E., Korambath, P.P., Adamson, R.D., Austin, B., Baker, J., Byrd, E.F.C., Dachsel, H., Doerksen, R.J., Dreuw, A., Dunietz, B.D., Dutoi, A.D., Furlani, T.R., Gwaltney, S.R., Heyden, A., Hirata, S., Hsu, C.P., Kedziora, G., Khalliulin, R.Z., Klunzinger, P., Lee, A.M., Lee, M.S., Liang, W., Lotan, I., Nair, N., Peters, B., Proynov, E.I., Pieniazek, P.A., Rhee, Y.M., Ritchie, J., Rosta, E., Sherrill, C.D., Simmonett, A.C., Subotnik, J.E., Woodcock, H.L., Zhang, W., Bell, A.T., Chakraborty, A.K., Chipman, D.M., Keil, F.J., Warshel, A., Hehre, W.J., Schaefer, H.F., Kong, J., Krylov, A.I., Gill, P.M.W., and Head-Gordon, M., *Advances in methods and algorithms in a modern quantum chemistry program package. .* Phys. Chem. Chem. Phys. , 2006. **8**: p. 3172-3191.
165. Stephens, P.J., Devlin, F.J., Chabalowski, C.F., and Frisch, M.J., *Ab-Initio Calculation of Vibrational Absorption and Circular-Dichroism Spectra Using Density-Functional Force-Fields. .* J. Phys. Chem., 1994. **98**: p. 11623-11627.
166. Becke, A.D., *Density-Functional Exchange-Energy Approximation with Correct Asymptotic-Behavior. .* Phys. Rev. A, 1988. **38**: p. 3098-3100.
167. Lee, C.T., Yang, W.T., and Parr, R.G., *Development of the Colle-Salvetti Correlation-Energy Formula into a Functional of the Electron-Density.* Phys. Rev. B 1988. **37**: p. 785-789.
168. Antuganov, D., Zykov, M., Timofeev, V., Timofeeva, K., Antuganova, Y., Orlovskaya, V., and Krasikova, R., *Copper-Mediated Radiofluorination of Aryl Pinacolboronate Esters: A Straightforward Protocol by Using Pyridinium Sulfonates.* Eur. J. Org. Chem., 2019: p. 918-922.
169. Cox, P.A., Reid, M., Leach, A.G., Campbell, A.D., King, E.J., and Lloyd-Jones, G.C., *Base-Catalyzed Aryl-B(OH)$_2$ Protodeboronation Revisited: From Concerted Proton Transfer to Liberation of a Transient Aryl Anion.* JACS, 2017. **139**: p. 13156–13165.
170. Zhao, Z., Yu, Q., Mou, T., and Liu, C., *Supporting information - High Efficient One-Pot Labeling of New Phosphonium Cations with Fluorine-18 as Potential PET Agents for Myocardial Perfusion Imaging.* Mol. Pharm., 2014. **11**: p. 3823-3831.
171. Zischler, J., Kolks, N., Modemann, D., Neumaier, B., and Zlatopolskiy, B.D., *Alcohol-Enhanced Cu-Mediated Radiofluorination.* Chem-Eur. J., 2017. **23**: p. 3251–3256.
172. Tomasch, M., Schwed, J.S., Kuczka, K., dos Santos, S.M., Harder, S., Nüsing, R.M., Paulke, A., and Stark, H., *Fluorescent Human EP3 Receptor Antagonists.* ACS Med. Chem. Lett., 2012. **3**: p. 774–779.
173. Lee, H., Mason, J.C., and Achilefu, S., *Heptamethine Cyanine Dyes with a Robust C-C Bond at the Central Position of the Chromophore.* J. Org. Chem. , 2006. **71**: p. 7862-7865.

174. Nair, D.P., Podgórski, M., Chatani, S., Gong, T., Xi, W., Fenoli, C.R., and Bowman, C.N., *The Thiol-Michael Addition Click Reaction: A Powerful and Widely Used Tool in Materials Chemistry.* Chem. Mater., 2014. **26**: p. 724−744.

175. Wängler, C., Wängler, B., Lehner, S., Elsner, A., Todica, A., Bartenstein, P., Hacker, M., and Schirrmacher, R., *A Universally Applicable 68Ga-Labeling Technique for Proteins.* J. Nucl. Med., 2011. **52**: p. 586–591.

176. Cabelli, D.E. and Bielski, B.H.J., *Kinetics and mechanism for the oxidation of ascorbic acid/ascorbate by HO2/O2- (hydroperoxyl/superoxide) radicals. A pulse radiolysis and stopped-flow photolysis study.* J. Phys. Chem., 1983. **87**: p. 1809-1812.

177. Maspero, M., Dallanoce, C., Wängler, B., Wängler, C., and Hübner, R., *The Exception That Proves the Rule: How Sodium Chelation Can Alter the Charge-Cell Binding Correlation of Fluorescein-Based Multimodal Imaging Agents.* Chem. Med. Chem., 2022. **e202100739**: p. 1-7.

178. Zanker, V. and Peter, W., *Die prototropen Formen des Fluoresceins.* Chem. Ber., 1957. **91**: p. 572–580.

179. Lee, M., Gentry, A.F., Schwartz, R., and Bauman, J., *Tartrazine-containing drugs.* Drug. Intell. Clin. Pharm., 1981. **15**: p. 782-788.

180. Rovina, K., Siddiquee, S., and Shaarani, S.M., *A review of extraction and analytical methods for the determination of Tartrazine (E 102) in foodstuffs.* Crit. Rev. Anal. Chem., 2017. **47**: p. 309-324.

181. Acerbi, F., Cavallo, C., Broggi, M., Cordella, R., Anghileri, E., Eoli, M., Schiariti, M., Broggi, G., and Ferroli, P., *Fluorescein-guided surgery for malignant gliomas: a review.* Neurosurg. Rev., 2014. **37**: p. 547-557.

182. Le Guern, F., Mussard, V., Gaucher, A., Rottman, M., and Prim, D., *Fluorescein Derivatives as Fluorescent Probes for pH Monitoring along Recent Biological Applications.* Int. J. Mol. Sci., 2020. **21**: p. 9217-9240.

183. Sjöback, R., Nygren, J., and Kubista, M., *Absorption and fluorescence properties of fluorescein.* Spectrochim. Acta. A., 1995. **51**: p. L7-L21.

184. Emmart, E.W., *Observations on the Absorption Spectra of Fluorescein, Fluorescein Derivatives and Conjugates.* Arch. Biochem. Biophys., 1958. **73**: p. 1-8.

185. The complete formulation of the assays medium OPTIMEM is proprietary, thus a partial disclosure of the sodium contenent was obtained from direct correspondance with Thermo Fisher Scientific.

186. Swamy, K.M.K., Ko, S.-K., Kwon, S.K., Lee, H.N., Mao, C., Kim, J.-M., Lee, K.-H., Kim, J., Shin, I., and Yoon, J., *Boronic Acid-Linked Fluorescent and Colorimetric Probes for Copper Ions.* Chem. Commun., 2008. **45**: p. 5915–5917.

187. Burdette, S.C., Walkup, G.K., Spingler, B., Tsien, R.Y., and Lippard, S.J., *Fluorescent Sensors for Zn2+ Based on a Fluorescein Platform: Synthesis, Properties and Intracellular Distribution.* J. Am. Chem. Soc. , 2001. **123**: p. 7831-7841.

188. Zhang, P., Li, C., Zhang, H., Li, Y., Yu, X., Geng, X., Wang, Y., Zhen, X., and Ma, Z., *Fluorogenic and chromogenic detection of biologically important fluoride anion in aqueous media with a fluorescein-linked hydrogen-bonding receptor via ''off–on'' approach.* J. Incl. Phenom. Macrocycl. Chem., 2014. **81**: p. 295-300.

189. Minta, A., Kao, J.P.Y., and Tsien, R.Y., *Fluorescent Indicators for Cytosolic Calcium Based on Rhodamine and Fluorescein Chromophore.* J. Biol. Chem, 1989. **264**: p. 8171-8178.

190. Boldyrev, A.A., Aldini, G., and Derave, W., *Physiology and pathophysiology of carnosine.* Physiol. Rev., 2013. **93**: p. 1803-1845.

191. Brisola, G. and Zagatto, A., *Ergogenic effects of β-alanine supplementation on different sports modalities: strong evidence or only incipient findings?* J. Strength Condit. Res., 2019. **33**: p. 253–282.

192. Albrecht, T., Schilperoort, M., Zhang, S., Braun, J.D., Qiu, J., Rodriguez, A., and Hauske, S.J., *Carnosine attenuates the development of both type 2 diabetes and diabetic nephropathy in BTBR ob/ob mice.* Sci. Rep., 2017. **7**: p. 44292.

193. Menini, S., Iacobini, C., Ricci, C., Scipioni, A., Fantauzzi, C.B., Giaccari, A., and Pugliese, G., *D-carnosine octylester attenuates atherosclerosis and renal disease in ApoE null mice fed a Western diet through reduction of carbonyl stress and inflammation.* Brit. J. Pharmacol., 2012. **166**: p. 1344–1356.

194. Janssen, B., Hohenadel, D., Brinkkoetter, P., Peters, V., Rind, N., Fischer, C., and van der Woude, F.J., *Carnosine as a protective factor in diabetic nephropathy: association with a leucine repeat of the carnosinase gene CNDP1.* Diabetes, 2005. **54**: p. 2320–2327.

195. Baye, E., Ukropcova, B., Ukropec, J., Hipkiss, A., Aldini, G., and de Courten, B., *Physiological and therapeutic effects of carnosine on cardiometabolic risk and disease.* Amino Acids, 2016. **48**: p. 1131–1149.

196. Teufel, M., Saudek, V., Ledig, J.-P., Bernhardt, A., Boularand, S., Carreau, A.S., and mirnova, T., *Sequence identification and characterization of human carnosinase and a closely related non-specific dipeptidase.* J. Biol. Chem, 2003. **278**: p. 6521–6531.

197. Mori, M., Mizuno, D., Mizuno, K.K., Sadakane, Y., and Kawahara, M., *Quantitative analysis of carnosine and anserine in foods by performing high performance liquid chromatography.* BR, 2015. **26**: p. 147–152.

198. Mora, L., Sentandreu, M.A., and Toldrá, F., *Hydrophilic chromatographic determination of carnosine, anserine, balenine, creatine, and creatinine.* J. Agric. Food Chem., 2007. **55**: p. 4664–4669.

199. Gil-Agustí, M., Esteve-Romero, J., and Carda-Broch, S., *Anserine and carnosine determination in meat samples by pure micellar liquid chromatography.* J. Chromatogr. A, 2008. **1189**: p. 444–450.

200. Uenoyama, R., Miyazaki, M., Miyazaki, T., Shigeno, Y., Tokairin, Y., Konno, H., and Yamashita, T., *LC-ESI-MS/MS quantification of carnosine, anserine, and balenine in meat samples.* J. Chromatogr. B, 2019. **1132**: p. 121826.

201. Baba, S.P., Hoetker, J.D., Merchant, M., Klein, J.B., Cai, J., Barski, O.A., and Bhatnagar, A., *Role of aldose reductase in the metabolism and detoxification of carnosine-acrolein conjugates.* J. Biol. Chem., 2013. **288**: p. 28163–28179.

202. Yeum, K.-J., Orioli, M., Regazzoni, L., Carini, M., Rasmussen, H., Russell, R.M., and Aldini, G., *Profiling histidine dipeptides in plasma and urine after ingesting beef, chicken or chicken broth in humans.* Amino Acids, 2010. **38**: p. 847–858.

203. Regazzoni, L., de Courten, B., Garzon, D., Altomare, A., Marinello, C., Jakubova, M., and Aldini, G., *A carnosine intervention study in overweight human volunteers: bioavailability and reactive carbonyl species sequestering effect.* Sci. Rep., 2016. **6**: p. 27224.

204. Pandya, V.K., Sonwane, B., Rathore, R., Unnikrishnan, A.G., Kumaran, S., and Kulkarni, M.J., *Development of multiple reaction monitoring assay for quantification of carnosine in human plasm.* RSC Adv., 2020. **10**: p. 763–769.

205. Annesley, T.M., *Ion suppression in mass spectrometry.* Clin. Chem., 2003. **49**: p. 1041–1044.

206. Mallet, C.R., Lu, Z., and Mazzeo, J.R., *A study of ion suppression effects in electrospray ionization from mobile phase additives and solid-phase extracts.* Rapid Commun. Mass Spectrom., 2003. **18**: p. 49-58.

207. Cech, N.B., Krone, J.R., and Enke, C.G., *Predicting electrospray response from chromatographic retention time.* Anal. Chem., 2001. **73**: p. 208–213.

208. Kebarle, P. and Verkerk, U.H., *Electrospray: from ions in solution to ions in the gas phase, what we know now.* Mass Spectrom. Rev., 2009. **28**: p. 898–917.

209. Van Hout, M.W.J., Niederländer, H.A.G., de Zeeuw, R.A., and de Jong, G.J., *Ion suppression in the determination of clenbuterol in urine by solid-phase extraction atmospheric*

pressure chemical ionisation ion-trap mass spectrometry. Rapid Commun. Mass Spectrom., 2002. **17**: p. 245–250.

210. Reddy, N.R., *Stable labeled isotopes as internal standards: a critical review.* Mod. Appl. Pharm. Pharmacol., 2017. **1**: p. 2.
211. Stokvis, E., Rosing, H., López-Lázaro, L., Schellens, J.H.M., and Beijnen, J.H., *Switching from an analogous to a stable isotopically labeled internal standard for the LC-MS/MS quantitation of the novel anticancer drug Kahalalide F significantly improves assay performance.* Biomed. Chromatogr., 2004. **18**: p. 400–402.
212. Rychlik, M. and Asam, S., *Stable isotope dilution assays in mycotoxin analysis.* Anal. Bioanal. Chem., 2007. **390**: p. 617–628.
213. Wieling, J., *LC-MS-MS experiences with internal standards.* Chromatographia, 2002. **55**: p. S107–S113.
214. Gilardoni, E., Gervasoni, S., Maspero, M., Dallanoce, C., Vistoli, G., Carini, M., Aldini, G., and Regazzoni, L., *Development of a direct LC-ESI-MS method for the measurement of human serum carnosinase activity.* J. Pharmaceut. Biomed., 2020. **189**: p. 113440.
215. Maspero, M., Gilardoni, E., Bonfanti, C., Messina, G., Regazzoni, L., De Amici, M., Carini, M., Aldini, G., and Dallanoce, C., *Synthesis and characterization of ^{13}C labeled carnosine derivatives for isotope dilution mass spectrometry measurements in biological matrices. .* Talanta, 2021. **235**: p. 122742.
216. Aldini, G., Orioli, M., Rossoni, G., Savi, F., Braidotti, P., Vistoli, G., and Carini, M., *The carbonyl scavenger carnosine ameliorates dyslipidaemia and renal function in Zucker obese rats.* J. Cell Mol. Med., 2011. **15**: p. 1339–1354.
217. Orioli, M., Vistoli, G., Regazzoni, L., Pedretti, A., Lapolla, A., Rossoni, G., and Aldini, G., *Design, synthesis, ADME properties, and pharmacological activities of β-Alanyl-d-histidine (D-Carnosine) prodrugs with improved bioavailability.* ChemMedChem, 2011. **6**: p. 1269–1282.
218. Wang, S., Cyronak, M., and Yang, E., *Does a stable isotopically labeled internal standard always correct analyte response? A matrix effect study on a LC/MS/MS method for the determination of carvedilol enantiomers in human plasma.* J. Pharmaceut. Biomed. Anal., 2007. **43**: p. 701–707.
219. Stokvis, E., Rosing, H., and Beijnen, J.H., *Stable isotopically labeled internal standards in quantitative bioanalysis uning liquid chromatography/mass spectrometry: necessity or not?* Rapid Commun. Mass Spectrom., 2005. **19**: p. 401-407.
220. Rinderknecht, H., Rebane, T., and Ma, V., *A simple and efficient synthesis of L-carnosine.* J. Org. Chem., 1964. **29**: p. 1968.
221. El-Dakdouki, M.H., Daouk, N., and Abdallah, H., *Synthesis and characterization of a series of orthogonally protected L-carnosine derivatives.* Int. J. Pept. Res. Therapeut., 2019. **25**: p. 379–390.
222. Wiles, C. and Watts, P., *An expedient, scalable synthesis of the natural product l-anserine.* Synthesis, 2007. **17**: p. 2608-2610.
223. Chakrabarty, M., Kundu, T., and Harigaya, Y., *Mild deprotection of tert-butyl carbamates of NH-heteroarenes under basic conditions.* Synthetic Commun., 2006. **36**: p. 2069–2077.
224. Isidro-Llobet, A., Alvarez, M., and Albericio, F., *Amino acid-protecting groups.* Chem. Rev., 109. **109**: p. 2455–2504.
225. Torikai, K., Yanagimoto, R., and Watanabe, L.A., *N(π)-2-Naphthylmethoxymethyl-Protected histidines: scalable, racemization-free building blocks for peptide synthesis.* Org. Process. Res. Dev., 2020. **24**: p. 448–453.
226. Peñafiel, R., Ruzafa, C., Monserrat, F., and Cremades, A., *Gender-related differences in carnosine, anserine and lysine content of murine skeletal muscle.* Amino Acids, 2004. **26**: p. 53-58.